mαcrϕ@ufmg

Universidade Federal de Minas Gerais
Graduate Program in Electrical Engineering
MACRO Research Group - Mecatronics, Control and Robotics

CLOSED-LOOP ADMITTANCE AND MOTION CONTROL STRATEGIES FOR SAFE ROBOTIC MANIPULATION TASKS SUBJECT TO CONTACTS

Mariana de Paula Assis Fonseca

Belo Horizonte, Brazil
2021

Universidade Federal de Minas Gerais

Escola de Engenharia

Programa de Pós-Graduação em Engenharia Elétrica

CLOSED-LOOP ADMITTANCE AND MOTION CONTROL STRATEGIES FOR SAFE ROBOTIC MANIPULATION TASKS SUBJECT TO CONTACTS

Mariana de Paula Assis Fonseca

Tese de Doutorado submetida à Banca Examinadora designada pelo Colegiado do Programa de Pós-Graduação em Engenharia Elétrica da Escola de Engenharia da Universidade Federal de Minas Gerais, como requisito para obtenção do Título de Doutor em Engenharia Elétrica.

Orientador: Prof. Bruno Vilhena Adorno

Belo Horizonte - MG

Março de 2021

Fonseca, Mariana de Paula Assis.
F676c Closed-loop admittance and motion control strategies for safe robotic manipulation task subject to contacts [recurso eletrônico] / Mariana de Paula Assis Fonseca. - 2021.
1 recurso online (xxvi, 160 f. : il., color.) : pdf.

Orientador: Bruno Vilhena Adorno.
Coorientador: Philippe Fraise.

Tese (doutorado) - Universidade Federal de Minas Gerais, Escola de Engenharia.

Apêndices: f. 136-149.
Bibliografia: f.150-160.

Exigências do sistema: Adobe Acrobat Reader.

1. Engenharia elétrica - Teses. 2. Quatérnios – Teses. 3. Robôs – Sistemas de controle – Teses. I. Adorno, Bruno Vilhena. II. Fraisse, Philippe. III. Universidade Federal de Minas Gerais. Escola de Engenharia. IV. Título.

CDU: 621.3(043)

Ficha catalográfica: Biblioteca Prof. Mário Werneck, Escola de Engenharia da UFMG

"Closed-loop Admittance And Motion Control Strategies For Safe Robotic Manipulation Tasks Subject To Contacts"

Mariana de Paula Assis Fonseca

Tese de Doutorado submetida à Banca Examinadora designada pelo Colegiado do Programa de Pós-Graduação em Engenharia Elétrica da Escola de Engenharia da Universidade Federal de Minas Gerais, como requisito para obtenção do grau de Doutor em Engenharia Elétrica.

Aprovada em 01 de março de 2021.

Por:

Prof. Dr. Bruno Vilhena Adorno
DEE (UFMG) - Orientador

Prof. Dr. Philippe Fraisse
Département Robotique (Université de Montpellier, França) - Coorientador

Prof. Dr. Luciano Cunha de Araújo Pimenta
DELT (UFMG)

Prof. Dr. Luiz Chaimowicz
DCC (UFMG)

Prof. Dr. Fernando Cézar Lizarralde
Departamento de Eletrônica (UFRJ)

Prof. Dr. Glauco Augusto de Paula Caurin
Escola de Engenharia de São Carlos (USP)

"Projects we have completed demonstrate what we know - future projects decide what we will learn."
- Dr. Mohsin Tiwana

Acknowledgements

Michael Fishman once said: "Self-made is an illusion. There are many people who played divine roles in you having the life that you have today. Be sure to let them know how grateful you are." And I could not agree more. All this work would not be possible without the help and encouragement of numerous people, and I would like them to know how thankful I am for all the advice, aids, companionship, incentives, support and comprehension. So this section is dedicated to all of you who contributed to this work be the way it is today.

The education that I have now is only possible thanks to the education that I have had all my life, so nothing more fair than to start thanking the people who educated me throughout life: my parents. Mom and dad (Carmen and Alexandre), thank you for all the counsels that you gave me, for all the discipline you imposed on me, and also for all *"ears tugs"*. This project would not be possible without you. Sorry for being in a bad mood due to badly sleeping nights in times of intense study, and thanks for sending me to bed whenever I am start becoming a Zombie.

Also, I would like to thank my little sister (Alessandra) for the opinion on the figures of this text, for all the patience when I did not have time to help her, to also stand my bad mood sometimes, and for the chocolates that I stole from her stock when I was a little bit stressed.

I would like to give a special thanks to Professor Bruno V. Adorno, for accepting me as his student, not only in the Doctorate but also in the Master. Thank you for all the conversations, ideas, tips, help, and inspirations. I am always more motivated after a two-hour conversation in your office. I am very thankful for your guidance throughout all these years.

I would also like to thank Professor Philippe Fraisse, for accepting me as his foreigner student, even without knowing me. My one-year stay in Montpellier was of great value and learning, our meetings, even if just a few, were always inspiring and a great opportunity to practice my French and my English.

To all my friends and family, I would like to leave here a huge thanks for all incentive in my study, for understanding when I did not have so much time to see you, and for all the patience. To all my friends at Jasper, thank you for supporting me and for understanding

when I left the company to follow my dreams. To my friends from MACRO, specially the ones supervised by Bruno Adorno, thank you for all the discussions and for the companionship in all these years. Also, I am grateful to you for holding my lamentations when some simulation did not work properly. To my friends from LIRMM, thank you for all the discussions, the company during lunch time, and also the hiking days and drinking nights that helped me to relax from the intense writing and experiment days, specially in my last months in Montpellier. A special thanks to Benjamin Navarro, for all the help in the experiments with KUKA. To my friends from Pitágoras, thank you so much for being part of my life. I would not have been able to get here without your support. Your excitement for my work always gave me strength to continue, even though you did not understand anything when I explained what I was doing.

For last but not least, I would like to thank all the UFMG's professors, who were part of my learning process. I did learn a lot from you, and I will take your teachings for all my life.

Abstract

This thesis contributes to the field of manipulation regarding tasks involving contact with the environment, focusing on safety. To this end, a control architecture is proposed where there is an admittance controller in an outer-loop, which changes the reference trajectory to the robot end-effector to achieve a desired compliant behavior, and a motion controller in an inner-loop used to track this trajectory.

More specifically, a six-degree-of-freedom task-space admittance controller using dual quaternion logarithmic mapping is developed in order to impose a desired apparent impedance to the robot. The controller couples the translation and rotation impedance in a single mathematical structure, it is designed based on the energy of the system, and the stiffness matrix is built to be consistent with the task geometry. Furthermore, the formulation is free of topological obstruction, and a solution for the unwinding phenomenon based on a switched error function is presented.

Regarding the inner-loop, the choice of the motion controller should take into account the type of actuation of the robot (velocity/position or torque) and the availability of the robot model. On the one hand, if the robot is actuated in torque, appropriate pose controllers for physical interactions are usually based on the robot dynamics as it enables more accurate analyses and helps in the synthesis of the robot dynamic behavior. In those controllers, the ill-conditioning of the joint-space inertia matrix plays an important role. Due to this ill-conditioning, small perturbations in the system can produce large changes in the numerical solutions, which may lead to poor performance or even instability, resulting in unsafe interactions. To overcome these problems, this thesis presents a controller in which the joint-space inertia matrix conditioning is adapted online, consequently enhancing the closed-loop performance. On the other hand, if the robot is actuated in velocity/position, a controller based on the robot kinematics is commonly used. Hence, a kinematic controller based on the dual quaternion logarithmic mapping is also developed.

The algorithms proposed in this thesis are validated in simulation and/or experimentally on a robot manipulator and an extension of the proposed architecture for the whole-body case, considering a bimanual mobile manipulator, is also evaluated in simulation. Furthermore, statistical analyses are used to compare the performance of these controllers to other ones of the state of the art, and the results show that the developed techniques

are at least as good as or outperforms the ones from the literature.

Keywords: tasks subject to contacts, interaction forces, admittance control, adaptive control, whole-body control, dual quaternion.

Resumo

A presente tese contribui para o campo de manipulação de tarefas que envolvem contato com o ambiente, focando em segurança. Para este fim, uma arquitetura de controle é proposta onde há um controlador de admitância em um laço externo, que altera a trajetória de referência do efetuador a fim de atingir o comportamento complacente desejado, e um controlador de movimento em um laço interno, usado para acompanhar esta trajetória.

Mais especificamente, um controlador de admitância de seis graus de liberdade no espaço da tarefa usando o mapeamento logarítmico de quatérnios duais é desenvolvido para impor uma impedância desejada aparente no robô. O controlador acopla a impedância de translação e de rotação em uma única estrutura matemática, ele é projetado baseado na energia do sistema, e a matriz de rigidez é construída para ser consistente com o geometria da tarefa. Além disso, a formulação é livre de obstrução topológica e uma solução para o fenômeno de *unwinding* baseado em uma função chaveada do erro é apresentada.

Em relação ao laço interno, a escolha do controlador de movimento deve levar em conta o tipo de atuação do robô (velocidade/posição ou torque), e a disponibilidade do modelo do robô. Se o robô é atuado em torque, um controlador de pose apropriado para interações físicas é geralmente baseado na dinâmica do robô, uma vez que isso permite uma análise mais precisa e ajuda na sítese do comportamento dinâmico do mesmo. Nesses controladores, o mau condicionamento da matriz de inércia no espaço das juntas tem um papel importante. Devido ao mau condicionamento, pequenas perturbações no sistema podem levar a grandes mudanças nas soluções numéricas, o que pode gerar uma performance ruim do controlador, ou até mesmo instabilidade, resultando em uma interação insegura. Para contornar esses problemas, esta tese apresenta um controlador no qual o condicionamento da matriz de inércia no espaço das juntas é adaptado *online*, consequentemente melhorando a performance do sistema em malha fechada. Se o robô é atuado em velocidade/posição, um controlador baseado no seu modelo cinemático é comumente utilizado. Dessa forma, um controlador cinemático baseado no mapeamento logarítmico de quatérnios duais é desenvolvido.

Os algoritmos propostos nesta tese foram validados em simulação e/ou experimentalmente em um robô manipulador, e uma extensão da arquitetura proposta para o caso de corpo completo, considerando um manipulador móvel bimanual, também foi avaliada em

simulação. Além disso, análises estatísticas foram utilizadas para comparar a performance desses controladores com outros do estado da arte, e os resultados mostraram que as técnicas desenvolvidas são pelo menos tão boas quanto ou melhores do que as da literatura.

Palavras-chave: tarefas sujeitas a contatos, forças de interação, controle de admitância, controle adaptativo, controle de corpo completo, quatérnios duais.

Résumé

Cette thèse contribue au domaine de la manipulation des tâches impliquant le contact avec l'environnement, en se concentrant sur la sécurité. À cette fin, une architecture de commande est proposée où il y a une commande d'admittance dans une boucle externe, qui modifie la trajectoire de référence vers l'effecteur du robot pour obtenir un comportement conforme souhaité, et un contrôleur de mouvement dans une boucle interne utilisé pour suivre cette trajectoire.

Plus spécifiquement, une commande d'admittance d'espace de tâches à six degrés de liberté utilisant une cartographie logarithmique à double quaternion est développée afin d'imposer une impédance apparente souhaitée au robot. La commande couple l'impédance de translation et de rotation dans une structure mathématique unique, il est conçu en fonction de l'énergie du système et la matrice de rigidité est construite pour être cohérente avec la géométrie de la tâche. De plus, la formulation est exempte d'obstruction topologique et une solution pour le phénomène de déroulement basé sur une fonction d'erreur commutée est présentée.

Concernant la boucle interne, le choix de la commande de mouvement doit prendre en compte le type d'actionnement du robot (vitesse/position ou couple) et la disponibilité du modèle du robot. Si le robot est actionné en couple, les commandes de pose appropriées pour les interactions physiques sont généralement basées sur la dynamique du robot car ils permettent des analyses plus précises et aident à la synthèse du comportement dynamique du robot. Dans ces commandes, le mauvais conditionnement de la matrice d'inertie dans l'espace articulaire joue un rôle important. En raison de ce mauvais conditionnement, de petites perturbations dans le système peuvent produire de grands changements dans les solutions numériques, ce qui peut conduire à des performances médiocres ou même à une instabilité, entraînant des interactions dangereuses. Pour surmonter ces problèmes, cette thèse présente une commande dans laquelle le conditionnement de la matrice d'inertie dans l'espace articulaire est adaptée en ligne, améliorant ainsi les performances en boucle fermée. Si le robot est actionné en vitesse/position, une commande basée sur la cinématique du robot est couramment utilisée. Par conséquent, une commande cinématique basée sur la cartographie logarithmique à double quaternion est également développée.

Les algorithmes proposés dans cette thèse sont validés en simulation et/ou expérimen-

talement sur un robot manipulateur et une extension de l'architecture proposée pour le cas du corps entier, considérant un manipulateur mobile bimanuel, est également évaluée en simulation. De plus, des analyses statistiques permettent de comparer les performances de ces contrôleurs à d'autres de l'état de l'art, et les résultats montrent que les techniques développées sont au moins aussi bonnes ou surpassent celles de la littérature.

Mots-clés: interaction homme-robot, forces d'interaction, commande d'admission, commande adaptatif, commande du corps entier, double quaternion.

Contents

List of Figures

List of Tables

Acronyms

AC	Adaptive Controller
ACD	Adaptive Controller with an Arbitrary Positive Definite Matrix
ACM	Adaptive Controller Considering Motors' Inertia
ACIm	Admittance Controller using Imaginary part of rotation quaternion
ACLog	Admittance Controller using Logarithm
BAZAR	Bimanual Agile Zany Anthorpomorphic Robot
CDTS	Cooperative Dual Task-Space
COM	Center of Mass
DFKM	Differential Forward Kinematic Model
DH	Denavit-Hartenberg
DLR	*Deutsches Zentrum für Luft-und Raumfahrt* (German Aerospace Center)
DOF	Degrees of Freedom
DQ	Dual Quaternion
EEG	Electroencephalography
EMG	Electromyography
FKM	Forward Kinematic Model
HERB	Home Exploring Robotic Butler
HRC	Human-Robot Collaboration
HRI	Human-Robot Interaction
HTM	Homogeneous Transformation Matrix

ICAR	International Conference on Advanced Robotics
IDFL	Inverse Dynamics with Feedback Linearization
IMU	Inertia Measurement Unit
ISO	International Organization for Standardization
JINT	Journal of Intelligent & Robotics Systems
JSIM	Joint Space Inertia Matrix
LIRMM	Laboratoire d'Informatique, de Robotique et de Microélectronique de Montpellier
LQR	Linear-Quadratic Regulator
MPS	Multiple-Predictor System
PD	Proportional and Derivative
PI	Proportional and Integral
PID	Proportional, Integral, and Derivative
pHRI	Physical Human-Robot Interaction
PIS	Positive Invariant Set
PR2	Personal Robot 2
QP	Quadratic Programming
RAM	Random Access Memory
ROS	Robot Operating System
SIPP	Safe-Interval Path Planner
SLDS	Switching Linear Dynamic System
TAC	Task-Space Adaptive Controller
TIDFL	Task-Space Inverse Dynamics with Feedback Linearization
TPID	Task-Space Proportional, Integral, and Derivative
UFMG	Universidade Federal de Minas Gerais
V-REP	Virtual Robot Experimentation Platform

Notation

Lowercase bold letters represent vectors or quaternions, such as $\boldsymbol{u} \in \mathbb{R}^n$ and $\boldsymbol{h} \in \mathbb{H}$. Underline lowercase bold letters represent dual quaternions, such as $\underline{\boldsymbol{h}} \in \mathcal{H}$. Upper bold letters represent matrices, such as $\boldsymbol{A} \in \mathbb{R}^{m \times n}$.

The identity matrix is denoted by $\boldsymbol{I}_{n \times n} \in \mathbb{R}^{n \times n}$ and $\boldsymbol{0}_{n \times m} \in \mathbb{R}^{n \times m}$ is a matrix of zeros. The flipper matrix

$$\boldsymbol{I}^{\#} \triangleq \begin{bmatrix} \boldsymbol{0}_{3\times3} & \boldsymbol{I}_{3\times3} \\ \boldsymbol{I}_{3\times3} & \boldsymbol{0}_{3\times3} \end{bmatrix} \tag{1}$$

can be used to reverse the rows of a matrix.

The reducing matrix

$$\bar{\boldsymbol{I}} \triangleq \begin{bmatrix} \boldsymbol{0}_{3\times1} & \boldsymbol{I}_{3\times3} \end{bmatrix} \tag{2}$$

is used to remove the first row of a 4×4 matrix by pre-multiplying it, and its transpose

$$\bar{\boldsymbol{I}}^T = \begin{bmatrix} \boldsymbol{0}_{1\times3} \\ \boldsymbol{I}_{3\times3} \end{bmatrix}$$

can be used to remove the first column by pos-multiplying the 4×4 matrix.

The following notations is also used:

$\hat{\imath}, \hat{\jmath}, \hat{k}$	Imaginary or quaternionic units;
$\mathbb{R}$	Set of real numbers;
$\mathbb{H}$	Set of quaternions;
$\mathbb{H}_p$	set of pure quaternions;
$\mathbb{S}^3$	Set of unit quaternions;
$\mathcal{H}$	Set of dual quaternions;
$\mathcal{H}_p$	Set of pure dual quaternions;
$\underline{\boldsymbol{\mathcal{S}}}$	Unit dual quaternions set;

$O(n)$	Group of $n \times n$ orthogonal matrices;
$GL(n)$	Group of $n \times n$ general linear matrices;
ε	Dual unit;
$\bar{\boldsymbol{H}}_4, \overset{+}{\boldsymbol{H}}_4$	Hamilton operators;
$\bar{\boldsymbol{H}}_8, \overset{+}{\boldsymbol{H}}_8$	Hamilton operators;
vec_4	Operator that maps $\mathbb{H}$ to $\mathbb{R}^4$;
vec_8	Operator that maps $\mathcal{H}$ to $\mathbb{R}^8$;
vec_3	Operator that maps $\mathbb{H}_p$ to $\mathbb{R}^3$;
vec_6	Operator that maps $\mathcal{H}_p$ to $\mathbb{R}^6$;
$\underline{\mathbf{vec}}_4$	Operator that maps $\mathbb{R}^4$ to $\mathbb{H}$;
$\underline{\mathbf{vec}}_8$	Operator that maps $\mathbb{R}^8$ to $\mathcal{H}$;
$\underline{\mathbf{vec}}_3$	Operator that maps $\mathbb{R}^3$ to $\mathbb{H}_p$;
$\underline{\mathbf{vec}}_6$	Operator that maps $\mathbb{R}^6$ to $\mathcal{H}_p$;
$\underline{\boldsymbol{h}}^*$	Dual quaternion conjugate;
$\underline{\boldsymbol{h}}^{\{\lambda\}}$	Unit dual quaternion *geometrical* exponentiation;
$\|\underline{\boldsymbol{h}}\|$	Dual quaternion norm;
$\mathcal{P}(\cdot)$	Primary part of a dual quaternion;
$\mathcal{D}(\cdot)$	Dual part of a dual quaternion;
$\boldsymbol{I}$	Identity matrix;
$\bar{\boldsymbol{I}}$	Reducing matrix;
$\boldsymbol{I}^{\#}$	Flipper matrix;
$\mathcal{F}$	Frame;
$\underline{\boldsymbol{x}}_b^a$	Rigid transformation from $\mathcal{F}_a$ to $\mathcal{F}_b$;
$\underline{\boldsymbol{y}}_b^a$	Logarithm of the unit DQ $\underline{\boldsymbol{x}}_b^a$;
$\text{Ad}(\cdot)$	Adjoint transformation;

$\underline{\boldsymbol{\xi}}$	Dual quaternion twist;
$\underline{\boldsymbol{\psi}}$	Dual quaternion wrench;
$\underline{\boldsymbol{\zeta}}$	Dual quaternion with angular and linear velocities;
$\underline{\boldsymbol{\varsigma}}$	Dual quaternion with force and moment;
$\boldsymbol{J}$	Jacobian matrix;
$\boldsymbol{J}^{+}$	Jacobian matrix pseudo-inverse;
$\boldsymbol{M}$	Inertia matrix;
$\boldsymbol{C}$	Coriolis matrix;
$\boldsymbol{g}$	Gravitational vector;
$\boldsymbol{M}_d$	Desired inertia matrix;
$\boldsymbol{B}_d$	Desired damping matrix;
$\boldsymbol{K}_d$	Desired stiffness matrix.

1 Introduction

For years, society has imagined robots helping humans and interacting with them (Adorno et al., 2011a). This theme has been approached by many science fiction books, films, and animated movies. In fact, the word "robot" was firstly introduced by the fiction work of Karel Capek entitled *R. U. R.* (*Rossum's Universal Robots*, in English), written in 1920 (Bainbridge, 2004). Works like this one have inspired many researchers and now we have the presence of robots interacting with humans in the real world. Service robotics (i.e., robots that help workers) is a growing market. Autonomous robots, for instance, may work together with the military, supply troops with ammunition, do surveillance (Squeo, 2001, apud Hinds et al., 2004), and assist astronauts in the investigation of distant planets (Ambrose et al., 2001, apud Hinds et al., 2004). Some robots already deliver medicine from pharmacies to nursing stations in hospitals, avoiding obstacles as they move (Okie, 2002; Siino & Hinds, 2004, apud Hinds et al., 2004). The field of human-robot cooperation is also growing, where humans and robots work/act together to perform a certain task (Adorno et al., 2011b). In this sense, supervision and cooperation of complex tasks can be performed by humans while robots increase human capabilities in terms of strength, speed, and accuracy.

In some applications that are not fully automated, human-robot cooperation is rewarding, since humans can use their experience, knowledge and perception to perform a given task correctly (Santis, 2007), whereas robots may have skills that complement those of humans. They can go to toxic or unsafe places, tolerate repetitive tasks, and can store large amounts of data (Hinds et al., 2004). Some examples of human-robot interaction

(HRI) are illustrated in Figure 1.1.

Figure 1.1: Examples of robots interacting with humans. [1]

Regardless the task the robot needs to perform, an important point is the intrinsic need for direct interaction between humans and robots in human environments (Santis, 2007). These robots share the same physical space with humans and work closely with them to perform tasks together as part of their daily life (Hinds et al., 2004). Due to this close interaction, it is necessary to impose some rules in the closed-loop controller in order to guarantee safety, which is one of the biggest challenges in the physical interaction between a human being and a robot.

When a robot interacts with the environment, contact wrenches may appear, and for a safe interaction it is crucial to ensure a compliant robot behavior, which can be imposed by controlling its apparent impedance (Caccavale et al., 1999, 2008). Depending on how the robot is actuated (velocity/position or torque), this behavior can be achieved by using an admittance or impedance controller.

Not only the nature of the controller must be defined, but also the type of the robot that is more appropriate to a given task and environment. In order to interact with people and perform tasks in human environments, it is desired for the robot to have anthropomorphic structures since "human tools match human dexterity" (Kemp et al., 2008). This means that human-designed environments are adequate for their physical characteristics, and robots with structures similar to humans are more efficient at performing tasks in these environments (Adorno et al., 2011a). However, these robots present some challenges in

[1] Source: https://www.bbc.com/news/technology-35201183
http://www.about-robots.com/robonaut.html
https://hri.iit.it/research/physical-human-robot-interaction-and-collaboration
https://www.manualdousuario.net/pepper-robo-emotivo/
https://www.ucsf.edu/news/2015/04/125386/higher-tech-and-higher-touch
https://www.nursingtimes.net/archive/experimental-robot-could-help-nurses-of-the-future-lift-patients-27-02-2015/

relation to control since in addition to performing the desired task, humanoid robots must simultaneously perform other tasks such as maintaining balance and controlling gait. Mobile manipulators, on the other hand, combine robotic arm dexterity with mobile base mobility (Adorno, 2011), being a versatile and lower-cost option. The mobile base can take advantage of a large workspace compared to conventional robots arms with fixed base (Borst et al., 2009) and that kind of robotic systems usually do not need balance control since in many cases their base is naturally in equilibrium (Silva, 2017). Moreover, the bimanual manipulators can better perform some manipulation tasks as having two arms increase the manipulation capability in terms of dexterity and load-carrying capacity compared to a single manipulator (Erhart & Hirche, 2015).

Due to the large number of degrees of freedom (DOF) the bimanual mobile manipulators usually have (as they are composed of three smaller robots: two manipulators and a mobile base), they may be redundant with respect to the task (i.e., they have more actuated DOF than it is strictly needed to execute the task) which allows the robot to simultaneously satisfy further tasks (Liegeois, 1977). Furthermore, the use of whole-body control takes advantage of all DOF available, allowing the robot movements to be more smoothly and potentially more human-like (Fonseca & Adorno, 2016).

That being said, different controllers are developed for a robot manipulator, aiming the safety when performing tasks, especially the ones that includes contact, as for example in physical human-robot interaction (pHRI). Moreover, an extension for some of these controllers is done considering the whole-body of a bimanual mobile manipulator.

1.1 Objective and Contributions

Motivated by the great growth and importance of appropriate pHRI, the purpose of this work is to propose control strategies, including a whole-body control for a two-arm mobile manipulator, aiming at a safe closed-loop system for accomplishment of cooperative and contact tasks.

The main contributions of this thesis are the following:

- The development of an admittance controller using the logarithmic mapping of a dual quaternion (DQ), with the following characteristics:
  - the stiffness term is designed to be geometrically consistent with the six-DOF task, which makes the controller have a physical meaning;
  - thanks to the coupling between translation and orientation, a single control law minimizes the error norm as a whole, considering both variables at once, which is simpler to implement when compared to uncoupled strategies, in which usually there are two separate control laws (for position and orientation), as for example the one of Caccavale et al. (1999);

  - it does not have the problem of topological obstruction, as in the work of Caccavale et al. (2008), and a solution for the unwinding phenomenon is proposed based on a switching error function that maps the two positive invariant sets (PIS) of the space of unit DQ into a single PIS in the image of the logarithmic mapping. Moreover, the trajectories of the closed-loop system always converge to that single PIS without exhibiting chattering, which would require a more complex hybrid control strategy (Kussaba et al., 2017);
  - the closed-loop system is proven to be passive and thus stable, considering the inner-loop controller as a double integrator.

- The development of a joint-space and a task-space adaptive controllers that formally ensures the improvement of the joint-space inertia matrix conditioning, which is usually ill-conditioned and affects the closed-loop behavior of the system;

- The development of a first-order and second-order kinematic controllers using the DQ logarithmic mapping that:

  - respects the properties of the unit DQ group;
  - has a dissipative term that prevents the joint velocities to be different from zero if the system is in equilibrium, which can happen when using the second-order controller in redundant robots with respect to the task.

- The combination of the proposed admittance controller and the motion controllers (the kinematic controller when the robot is actuated in position and the adaptive controller when the robot is actuated in torque), aiming at a safe interaction by imposing a desired impedance behavior to the robot while tracking the reference trajectory, as depicted in Figure 1.2.

- The extension of the proposed architecture for a whole-body control of a bimanual mobile manipulator, including the control of external and internal wrenches acting in a manipulated object.

Furthermore, experiments were carried out in a KUKA LWR4+ robot manipulator equipped with one ATI Mini 45 six axis force/torque sensor at the end-effector. Moreover, some simulations were executed using the model of the KUKA robot. The extension for the whole-body control of a bimanual mobile manipulator was also tested in simulation considering the BAZAR model, which consists of two KUKA LWR4+ robot manipulators and a mobile base. [2] The proposed controllers were compared with widely used controllers of the state of art via statistical analyses.

[2] As the robot is available in the LIRMM in France, and the Ph.D. candidate is located in Brazil, with just one year of exchange program in France, some controllers were only tested in simulation.

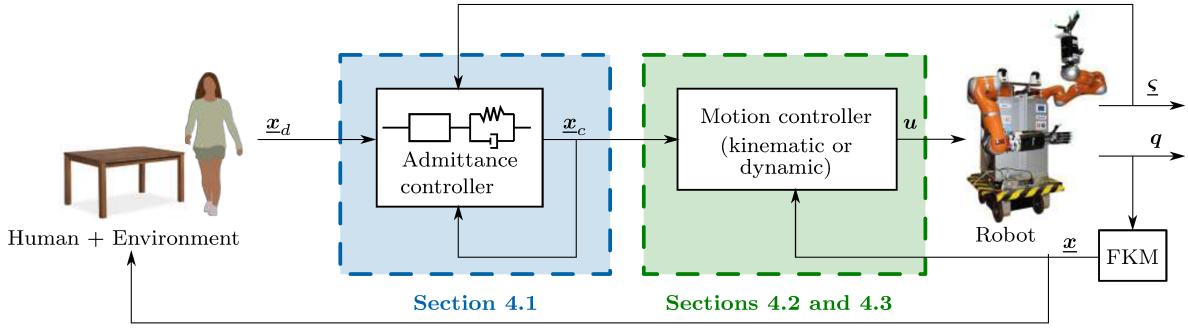

Figure 1.2: Block diagram with the structure and controllers proposed in the thesis. Given a force/torque $\underline{\varsigma}$ at the robot end-effector that appear due to its interaction with the environment, the admittance controller modifies the desired end-effector trajectory $\underline{\boldsymbol{x}}_d$ to achieve a compliant behavior of the robot. The inner motion control loop controls the robot end-effector pose $\underline{\boldsymbol{x}}$ according to this modified trajectory $\underline{\boldsymbol{x}}_c$.

The developments and results reported in this thesis partially appears in two journal papers, two conference papers, and one workshop extended abstract, as depicted in Table 1.1.

Table 1.1: Contributions presented in papers.

Journal Papers	
Fonseca et al., 2020	Sections 3.3.3, 4.1.2, 4.2.2, 5.5
Fonseca et al. 2021	Sections 3.3.3, 4.1, 4.3, 5.4
Conference Papers	
Fonseca et al. 2018	Sections 4.3, 5.2
Fonseca et al. 2019a	Sections 4.3, 5.3
Workshop Ext. Abstract	
Fonseca et al. 2019b	Sections 4.1

1.2 Organization of the Thesis

This text is divided into six chapters, summarized as follows:

Chapter 1 gives a brief introduction about the HRI and the existing needs behind it. It also enumerates the contributions and objectives of the thesis.

Chapter 2 presents some developments related to the control of contact forces and internal forces in the human-robot or robot-robot interaction. Furthermore, this chapter shows some adaptive techniques to compensate the uncertainties introduced by unknown kinematic and specially dynamic models.

Chapter 3 introduces the mathematical background needed to understand all the modeling and controllers used and proposed in this thesis. It also establishes the notation used throughout the text. Moreover, this chapter also presents the whole-body model of a

bimanual mobile manipulator.

Chapter 4 shows the strategies used to control the robot imposing a desired impedance in order to the robot behave compliantly in the presence of contact wrenches. It also presents a kinematic controller using the DQ logarithmic mapping. Furthermore, a solution to mitigate the problems related to control due to the ill-conditioning of the inertia matrix is proposed. All these contributions are summarized in Figure 1.2, where, given a desired pose for the end-effectors, an outer-loop imposes a desired impedance behavior for the robot, so it moves compliantly when there are contact wrenches acting on it, and an inner-loop is responsible to track the reference trajectory of the end-effectors.

Chapter 5 shows the results obtained through simulations and experiments made on the KUKA robot, related to the theory of Chapter 4. Moreover, it presents simulations of the whole-body model of the BAZAR, regarding the extension of some of the controllers described in Chapter 4 for a bimanual mobile manipulator. It also shows an analysis of a robot manipulator behavior, highlighting the dynamic characteristics intrinsic to open serial kinematic chains.

Lastly, Chapter 6 presents the final remarks and the perspectives for future works.

2
Related Works

As previously mentioned, the close interaction between human and robots are becoming more and more frequent each day (Haddadin et al., 2009). In this chapter, some related works of the state of art, considering pHRI and issues related to the dynamic behavior of the robot, are shown.

2.1 Human-Robot Interaction

The fast growing demands for robots in home and industrial workspace led to the growth of the number of activities/tasks involving HRI (Ajoudani et al., 2018). The HRI combines the dexterity, flexibility, and problem-solving abilities of humans with the strength, endurance, and precision of robots (Vanderborght, 2018). Thus, combining the characteristics from humans and robots can bring many advantages, yielding highly effective systems (Badeau et al., 2018). HRI is a research field on the rise, with a lot of researches taking place, but still with much development to be done. In order to illustrate the growth of the area, Figure 2.1 shows the number of publications from year 2000 to 15th June of 2020, according to Google Scholar.[1] The number of articles increased a lot since 2000, going from around 280 in 2000 to 11500 articles in 2019. Still, there is a lot to do in the HRI research field, both in cognitive HRI and in physical interaction.

Human-robot collaboration (HRC) is a specific area of HRI. The latter stands for any

[1]The collected data was the number of articles returned by Google Scholar when searching for the expression "human robot interaction", for a specific year.

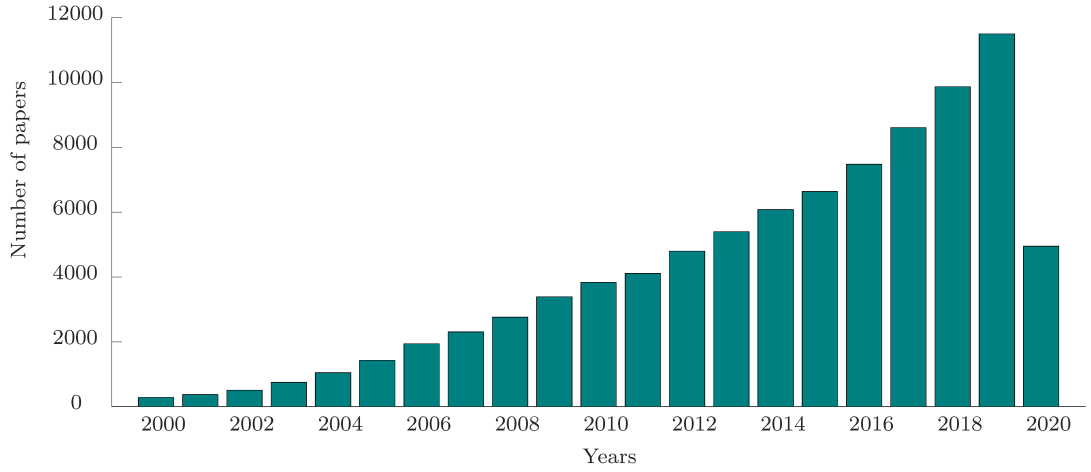

Figure 2.1: Number of publications along the years from 2000 to 2020 (until 15$^{\text{th}}$ June). The data is the number of articles by Google Scholar when searching for the expression "human robot interaction", for a given year.

action that involves a human and a robot, whilst the former means humans working with robots to reach a common goal (Bauer et al., 2008; Ajoudani et al., 2018). However, for simplicity, both situations will be denoted here as HRI.

In HRI, two points must be taken into consideration in order to allow a better interaction (Cherubini et al., 2017):

1. the human intent should be understood by the robot in an easy way;

2. the closed-loop behavior should be safe for both human and robot.

Moreover, according to Goodrich & Schultz (2007), the communication and interaction between the robot and the human can be separated into two categories: remote interaction and proximate interaction, in which in the former the human and the robot are spatially separated, and in the latter they are co-located. In this thesis, the focus is on the controllers for safe robotic manipulation tasks subject to contacts, that is, human-robot interaction in which the participants of the interaction are co-located. Therefore, only works related to the second point are discussed.

2.1.1 Physical Human-Robot Interaction

In many scenarios, as for example robots helping workers in industries or people in domestic environments, or assistance robots making advantage of its payload to carry elderly or people with reduced mobility, the pHRI is evident, either directly (i.e., the robot is in contact with the human) or indirectly (i.e., the robot is in contact with an object that is also in contact with the human partner) and thus safety must be taken into account. According to De Santis et al. (2008), safety is one of the keys to a "successful introduction of robots into human environments".

Safety may include many topics, as for example collision (and self-collision) avoidance, joint limits avoidance, velocity limits, interaction force limit, balance, and physical compliance. However, this thesis focuses on the interaction itself, in which two aspects draw attention: the contact forces and the compliant behavior. Different control approaches can be used to treat these topics, such as force controllers, impedance, and admittance controllers.

2.1.1.1 Force Controllers

Pure motion control is usually insufficient to handle the physical contacts between the robot and the environment, specially if the environment is rigid, because of the large contact wrenches arising from the interactions (Villani & de Schutter, 2008). Therefore, some works have largely relied on the use of force controllers to minimize the interaction forces (Cherubini et al., 2017).

For instance, Uchiyama & Dauchez (1988) propose a hybrid position/force controller for coordination of a dual-arm system. To do that, the authors propose to use a "virtual stick," which is a hypothetical rigid bar fixed between the end-effector of each manipulator and the center of the manipulated object, as illustrated in Figure 2.2 by $\boldsymbol{o}_1$ and $\boldsymbol{o}_2$. This concept helps to define the external and internal wrenches acting on the object, in which the former induce motion and the later do not (Erhart & Hirche, 2015). More specifically, the force $\boldsymbol{F}^0_{\text{tip},i} \in \mathbb{R}^3$ and moment $\boldsymbol{N}^0_{\text{tip},i} \in \mathbb{R}^3$ at the tip of the virtual stick with reference to the inertial frame $\mathcal{F}_0$, with $i = 1, 2$, is given by

$$\begin{aligned} \boldsymbol{F}^0_{\text{tip},i} &= \boldsymbol{F}^0_i, \\ \boldsymbol{N}^0_{\text{tip},i} &= \boldsymbol{N}^0_i + \boldsymbol{F}^0_i \times \boldsymbol{o}_i, \end{aligned}$$

with $\boldsymbol{F}^0_i \in \mathbb{R}^3$ and $\boldsymbol{N}^0_i \in \mathbb{R}^3$ being, respectively, the force and moment acting on each robot end-effector i. The external $\boldsymbol{\mathcal{W}}^0_a \in \mathbb{R}^6$ and internal $\boldsymbol{\mathcal{W}}^0_r \in \mathbb{R}^6$ wrenches are obtained by

$$\begin{aligned} \boldsymbol{\mathcal{W}}^0_a &= \boldsymbol{\mathcal{W}}^0_{\text{tip},1} + \boldsymbol{\mathcal{W}}^0_{\text{tip},2}, \\ \boldsymbol{\mathcal{W}}^0_r &= \frac{1}{2}\left(\boldsymbol{\mathcal{W}}^0_{\text{tip},1} - \boldsymbol{\mathcal{W}}^0_{\text{tip},2}\right), \end{aligned}$$

where $\boldsymbol{\mathcal{W}}^0_{\text{tip},i} = \begin{bmatrix} \boldsymbol{F}^{0T}_{\text{tip},i} & \boldsymbol{N}^{0T}_{\text{tip},i} \end{bmatrix}^T$ is the wrench at the tip of the virtual stick (Uchiyama & Dauchez, 1988). Then, the authors derive the absolute and the relative velocities dual to these wrenches. In their proposed architecture, the authors use a selection matrix to select the force or the position control mode.

Chiaverini & Sciavicco (1993) also propose a position/force controller but, differently from Uchiyama & Dauchez (1988), they do not use a selection matrix. Instead, their

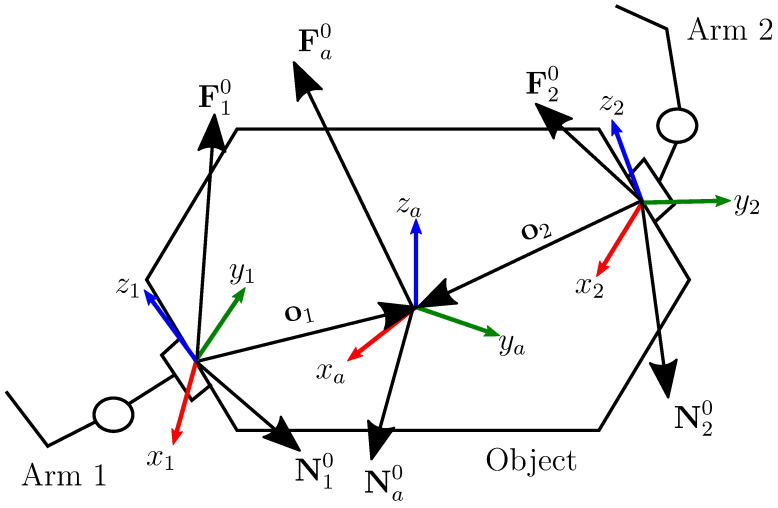

Figure 2.2: Forces $\boldsymbol{F}$ and moments $\boldsymbol{N}$ acting in two robots holding a common object.[2]

approach consists of a parallel architecture where the force controller has a higher priority than the position controller. This priority is set by using a PD for the position and a PI for the force. Simulations considering only translation and linear force were done to analyze the performance of the proposed controller in a rigid, frictionless and elastic environment.

More recently, Alban & Adorno (2017) have used a hybrid force/pose controller using a cascade scheme in order to regulate the interaction forces. The outer-loop is composed of a force controller with the aim of regulating the force applied by the manipulator's end-effector, and an inner-loop that controls the end-effector pose according to the desired pose and the perturbation given by the outer-loop. Alban & Adorno also do not need a selection matrix in their architecture. However, in their work, the authors consider that the force and desired position are always orthogonal, so the proposed controller is not adequate to tasks in which this assumption is not satisfied.

To modulate the interaction forces in HRI, Mitsantisuk et al. (2010) propose a force controller based on an impedance scheme. Moreover, the authors develop a twin direct-drive motor with a wire rope to hand over a "precise force sensation" in HRI. Also aiming at a safe physical interaction, Magrini et al. (2015) extend typical impedance and force controllers to handle generic contact points on the robot, using for this purpose the estimation of contact forces proposed by Magrini et al. (2014).

2.1.1.2 Impedance and Admittance Controllers

Despite the many works regarding force controllers, traditional force controllers tend to increase the robot stiffness to obtain high bandwidth and position accuracy, which may result in poor compliance and even instability (Colgate & Hogan, 1989). Therefore, force

[2]Figure adapted from (Uchiyama & Dauchez, 1988).

controllers are not the best choice for a good and safe interaction (Pratt et al., 2005; Ju et al., 2014). Impedance and admittance controllers, on the other hand, have shown to be more appropriate to handle interactions (Kimmel & Hirche, 2015), ensuring a suitable compliant behavior by controlling the apparent robot impedance. Corroborating this, Ajoudani et al. (2018) present an overview of many works related to HRI and, concerning physical interaction, most of the works used an approach with impedance control.

Differently from the force controllers, the impedance controller does not control the forces acting on the robot, but regulates the relation between the velocity and the force (mechanical impedance). More specific, the Laplace transformation of the mechanical impedance is given by

$$Z(s) = \frac{F_e(s)}{V(s)},$$

where $F_e(s)$ is the external force acting on the robot end-effector, and $V(s)$ is its velocity (Spong et al., 2006).

Hogan (1985) propose the first impedance controller to control dynamic interactions between a manipulator and the environment in cases involving interaction forces that are not orthogonal to motions, in which pure force controllers are not adequate. By changing the robot impedance to match a desired interaction impedance, safety is improved, which has motivated many researchers to use impedance controllers when physical interactions are required.

For instance, Erhart et al. (2013) extend an impedance-based controller to dual-arm mobile manipulators to limit undesired internal forces caused by kinematic errors due to uncertainties in the object geometry and manipulators. In order to accomplish that, the motion of the arms are separated from the motion of the mobile base to decrease the computational cost and also to, using a potential function, minimize the propagation of the base disturbances to the manipulators. Experiments were performed only in the horizontal plane. Lee et al. (2014) also present an impedance controller that considers a dual-arm system as a single manipulator, whose end-effector motion is defined by the relative motion between the two end-effectors. Thus, using a relative Jacobian, the impedance controller is reduced to a single controller for both arms. Two different arms are used to perform a writing task, in which one arm holds a plate while the other writes on it.

Pedro et al. (2013) use an impedance controller, together with a smooth trajectory, to perform the task of unscrewing a bottle cap using an industrial robot. The authors have used a third-order polynomial curve to modify the impedance parameters according to the manipulation phases: when the robot is subject to contact and when it is not. Higa et al. (2019) study the influence of the joint configuration on the passivity of robotic legs controlled using impedance. The authors use an impedance controller because it is appropriate to handle interactions with unknown environments.

In the context of HRI, Sieber et al. (2015) propose the use of an impedance controller in a manipulation task performed by a team composed of a human and multiple robots. In their architecture, the human coordinates the robots formation and the desired trajectory is designed according to the manipulated object geometry. However, small deviations in the trajectory result in internal forces, and thus impedance controllers are used in each manipulator to prevent damages either to the robots or to the object. A major drawback of that work is that only the end-effectors positions are considered, therefore the internal torques due to orientation uncertainties are not explicitly taken into account.

More concerned with multiple tasks, Hoffman et al. (2018) propose a multi-priority impedance controller that considers task priorities inside a Quadratic Programming (QP) optimization framework that allows equality and inequality constraints. This architecture is useful when more than one task must be dealt with simultaneously, such as controlling the end-effectors of a humanoid robot while keeping the balance. Moreover, equality and inequality constrains enables the definition of joint limits, collision avoidance, etc., directly in the control law.

Admittance controllers, which are dual to impedance controllers, have also been used in applications where the manipulator physically interacts with the environment. Throughout the literature, admittance controllers have been called *position-based impedance controllers*, *velocity-based impedance controllers,* or, ambiguously, *impedance controllers* (Keemink et al., 2018). Currently, a more widely accepted definition is that impedance controllers are the ones in which the robot velocity is measured, yielding a wrench as a control signal. Conversely, in admittance controllers, a contact wrench is measured and mapped to a velocity that must be imposed to the robot (Keemink et al., 2018).

The admittance controller is usually used when a high positioning accuracy is desirable since it can achieve smaller steady-state error in the end-effector pose than the impedance controller. It is also more directly applied to robots actuated in velocity or position. However, it does not exclude the use of admittance controllers with torque actuated robots. A drawback of admittance controllers is that it is a challenge to render low inertia, differently from the impedance controller. On the other hand, the impedance controller is more appropriate to handle contacts (Dietrich, 2015; Keemink et al., 2018) and it presents difficulty in dynamically interacting with low inertia (i.e., free motion).

To admittance controlled devices to be able to render low inertia, Keemink et al. (2018) propose a set of design guidelines to ensure coupled stability in this situation. Notwithstanding, the authors consider only a single-DOF system, which is not usually the case in real applications. In the multi-DOF system, the coupling between nonlinear DOF could result in instability because of the effects absent in single-DOF systems.

Instability can also emerge when an admittance-controlled robot interacts with stiff environments. To prevent this, Ferraguti et al. (2019) propose a method for detecting instability and restore a stable behavior using a passivity-base adaptation of the admittance

parameters.

According to Roveda et al. (2016), pure force control works better when there is a compliance in the force/torque sensor (Lange et al., 2012) or in the robot's joints. On the other hand, the impedance controller is easier to tune when the robot performs assembly tasks, for example. Nonetheless, impedance controllers, as well as admittance controllers, do not allow a fine control of the interaction forces, introducing the problem of force peaks during the task execution, specially when the contact starts. Therefore, Roveda et al. (2016) treat the problem with two control structures: an internal, which consists of a pure impedance controller with constants parameters, and an external, which is an admittance controller with adaptive gains calculated online, based on the estimation of the environment stiffness. The admittance gains are calculated as the solution of a linear-quadratic regulator (LQR) problem, and the environment stiffness is estimated through an Extended Kalman Filter.

Thanks to the ability of handling stiff impedances in addition to enabling non-back drivable and heavy robots to have a compliant behavior, admittance controllers are often used in wearable and industrial robots (Keemink et al., 2018; Ferraguti et al., 2019). For instance, Navarro et al. (2016) propose an adaptive damping controller (a special type of admittance controller) that fulfills the ISO10218, a standard that has some requirements to guarantee safety in HRI with industrial robots. Moreover, the authors also limit the tool speed and contact force online. The controller was validated on a manipulator equipped with a robotic hand in a collaborative screwing application. As an improvement of their previous work, Navarro et al. (2018) develop an open-source software to satisfy the safety level imposed by ISO 10218:2011 and ISO/TS 15066, called OpenPHRI, which is also based on a damping control. To guarantee safety, a set of constraints are build to limit the velocities in both task and joint space, because both can lead to undesired behaviors. Force control is also considered in the framework, mapped to a velocity command. Cherubini et al. (2016) develop a collaborative human-robot manufacturing cell for homokinetic joint assembly, in which pre-taught trajectories are deformed to comply with external wrenches using an admittance controller. As a result, the human workload is reduced, and a risk analysis indicates that their approach is compatible with safety standards.

Tarbouriech et al. (2020) propose an admittance controller for a collaborative dual-arm manipulation of bulky objects. Computer vision is used to detect where the human is in contact with the object and an admittance controller makes the bimanual manipulator move according to this information. As the gravity effects are canceled during the manipulation, the human makes an effort only to move the object, without needing to sustain it. Agravante et al. (2014) combine a visual servoing controller to an admittance controller to achieve a human-robot collaborative task of carrying a flat surface while preventing an object on top of it from falling. The authors ensure the human safety by imposing the human's intention through the haptic channel and making the robot more compliant. Since they

used Euler angles to represent orientations, the controller is restricted to small rotations due to representational singularities (Siciliano et al., 2009).

To avoid the representational singularity problem when performing six-DOF impedance and admittance control, Caccavale et al. (1999) propose to use the imaginary part of a unit quaternion to represent rotations, expressing the mutual orientation between the compliant and the desired frames. Moreover, the authors formulate an energy-based impedance equation with a geometrically consistent stiffness for infinitesimal displacements. Notwithstanding, they use two distinct control laws for the position and orientation and their approach presents the topological obstruction problem (Bhat & Bernstein, 1998), which may trap the closed-loop system within an unstable equilibrium set. That work is later extended (Caccavale et al., 2008) to propose a controller in which the stiffness is proved to be geometrically consistent for finite displacements. Caccavale et al. (2008) applied that controller into a dual-arm manipulation, considering internal and external wrenches. Nonetheless, the new controller still carries the topological obstruction issue. The literature still lacks a formulation based on DQ algebra, which has some advantages as, for instance, it has a compact representation, the coefficients of a DQ can be used directly in the control law, and has it has strong algebraic properties. Therefore, this topic is addressed in this thesis.

Some of the aforementioned works do not consider a human in the task, but treat the case of multi-robot for manipulation of a common object. Those works are also important since one of those robots could be substituted by a human partner. In this case, the problem is even more challenging, since the human behavior is usually not controlled as the robot is, and thus the robot must adapt to the human's motion.

When dealing with HRI, mainly the pHRI, another point related to the safety is the control accuracy and also the avoidance of instability. If the control of the end-effector pose is not precise, large interaction wrenches can appear when the robot interacts with highly rigid environments, which may damage the robot or the environment, especially when an impedance or admittance controller is not used. Also, if the system becomes unstable, the robot can also perform movements that would harm the human and cause damage to the environment, which is undesirable. Considering this, it is important to treat an intrinsic problem of serial robot manipulators that can lead to a not precise control and also instability.

2.1.2 Safety Issue: Ill-Conditioning of Open Serial Chains

The joint space inertia matrix (JSIM) of a robot manipulator plays an important role in control and in the analysis of its dynamic behavior. More specifically, the JSIM is specially important in forward dynamics, which is essential for simulation (Featherstone, 2004; Shah et al., 2018), and when designing motion controllers based on Euler-Lagrange equations.

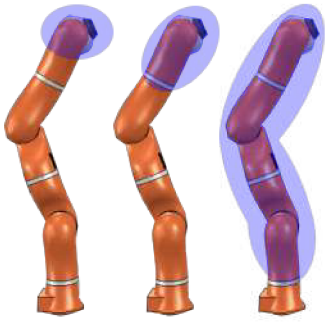

Figure 2.3: The links of a serial manipulator are connected in a way that each link in the kinematic chain is carried by its predecessors while carrying all successive links in the chain, which leads to the ill-conditioning of the inertia matrix.

Although it is well known that the JSIM is positive definite independently of the robot configuration, this property does not guarantee the good conditioning of the matrix (Shen & Featherstone, 2003).

In a multi-link open serial chain, the links are connected to each other in a way that the penultimate link carries the last one, the antepenultimate link carries the last two and so on, and the base link carries all the others, as illustrated in Figure 2.3. As a result, the equivalent inertia of the links are extremely disparate, and this difference increases with the number of links, even if the links are identical to each other (Agarwal et al., 2014), which leads to the ill-conditioning of the JSIM. Moreover, if the links are not all the same size, the condition number can be higher (Featherstone, 2004).

When the JSIM becomes ill-conditioned (i.e., it has a large condition number), small perturbations in the system can produce large changes in the numerical solutions (Agarwal et al., 2014), affecting both the accuracy of simulation results and the control performance (Shen & Featherstone, 2003), which in turn may affect safety. For instance, imprecise end-effector motion control can result in large interaction wrenches when the robot interacts with highly rigid environments, which may result in damage to either the robot or the environment. Also, depending on the control design, especially the ones that rely on the inversion of the JSIM, an ill-conditioned inertia matrix may lead to closed-loop instability, which may yield dangerous movements that would harm the human or cause damage to the environment. Even when there is no inversion, the ill-conditioning can cause some problems. For instance, the controller based on inverse dynamics with feedback linearization (Spong et al., 2006) behaves poorly whenever the JSIM is ill-conditioned. Due to the difference in the singular values of the JSIM, the torque of each joint calculated from the inverse dynamics control law can be very different, even if the joints accelerations are the same. This way, if the inertia along a specific joint is very small, no matter how large the position/velocity error or PD-coefficients are, the correction torque applied on that joint will be still small compared to the dominant torque, which may result in some undesired stationary error in that joint (Shen & Featherstone, 2003).

Despite the fact that this ill-conditioning is intrinsic to serial kinematic chains (Featherstone, 2004), its effects can be mitigated and therefore the control performance can be enhanced. However, this problem is mostly neglected by researchers and just a few have worked on a solution for it (Shen & Featherstone, 2003).

In order to circumvent the ill-conditioning problem, Shen & Featherstone (2003) propose to use a PD controller with gravity compensation, which yields an asymptotically stable closed-loop system if the PD gains are properly chosen. This controller does not use the JSIM directly in the control law, and thus it is not affected by the ill-conditioning of this matrix since it directly converts the joint position/velocity error to the driven torque. Yet, according to the authors, other controllers that have complete knowledge about the robot dynamics should achieve better accuracy.

To benefit from the complete dynamic model in the control law whilst alleviating the effects of the JSIM's ill-conditioning, an alternative is to add a well-conditioned constant positive definite matrix to it in the Euler-Lagrange equation. However, this addition could lead to steady-state error in the closed-loop system due to the introduction of disturbances in the robot model that are not compensated by the control law. Such matrix could be related to the inertia of the actuators, instead of just adding an arbitrary matrix, in order to prevent the introduction of unnecessary inaccuracies to the model (Fonseca et al., 2018). However, if the added actuator's inertia does not correspond to the actual one, the closed-loop system may still present steady-state error.

Many control methods are sensitive to the uncertainties in some parameters in the dynamic model (Ding et al., 2015), as for example, again, the inverse dynamic control with feedback linearization. One could try to use an integrator to remove the steady-state error (Shen & Featherstone, 2003). However, the added disturbance must be constant in order to the integrator to work, which is not always true. Even though the actuator's inertia matrix is usually constant, the disturbance depends on the robot acceleration and therefore is time-varying. More specifically, if the actual robot's inertia matrix is given by $\bar{\boldsymbol{M}} = \boldsymbol{M}(\boldsymbol{q}) + \boldsymbol{M}_m$, where $\boldsymbol{M}(\boldsymbol{q})$ is the nominal robot's inertia matrix and $\boldsymbol{M}_m$ is the actuators' inertia matrix, the actual dynamic model is given by

$$\begin{aligned}\boldsymbol{\tau} &= \bar{\boldsymbol{M}}\ddot{\boldsymbol{q}} + \boldsymbol{C}(\boldsymbol{q}, \dot{\boldsymbol{q}})\dot{\boldsymbol{q}} + \boldsymbol{g}(\boldsymbol{q}) \\ &= \boldsymbol{M}(\boldsymbol{q})\ddot{\boldsymbol{q}} + \boldsymbol{C}(\boldsymbol{q}, \dot{\boldsymbol{q}})\dot{\boldsymbol{q}} + \boldsymbol{g}(\boldsymbol{q}) + \boldsymbol{w},\end{aligned}$$

where $\boldsymbol{w} = \boldsymbol{M}_m\ddot{\boldsymbol{q}}$ is the time-varying disturbance.

An alternative solution to improve the JSIM's conditioning is to use an adaptive controller to compensate for the unknown inertia of the actuators. The basic idea in adaptive control is to estimate the uncertain parameters online based on the measured system signals, and use those estimates in the control input computation (Siciliano & Slotine, 1991).

Another option is to add a positive definite variable matrix that varies according to the JSIM conditioning, without adding excessive inaccuracy to the nominal model. This matrix should be adapted during the robot motion, also motivating the use of an adaptive controller.

2.1.2.1 Adaptive Control

Adaptive controllers can be used to compensate for the unknown parameters of the system model. For instance, Slotine & Li (1987) propose an adaptive control law for robots with dynamics uncertainties and show that although the estimated parameters do not converge to the real parameters, the trajectories of the colsed-loop system converge to the invariant $\left(\tilde{\boldsymbol{q}}, \dot{\tilde{\boldsymbol{q}}}\right) = (\mathbf{0}, \mathbf{0})$, where $\tilde{\boldsymbol{q}}$ is the joint-space error (or to $\left(\tilde{\boldsymbol{x}}, \dot{\tilde{\boldsymbol{x}}}\right) = (\mathbf{0}, \mathbf{0})$, where $\tilde{\boldsymbol{x}}$ is the task-space error, if the controller is in the Cartesian space). The controller consists of a PD feedback together with a full dynamics feed-forward compensation, in which the authors restrict the residual tracking errors to lie on a sliding surface, guaranteeing asymptotic convergence of not only the velocity but also the tracking position while estimating the parameters online. According to the authors, differently from most of the algorithms in the literature, in their architecture there is no need to measure the joint accelerations or to invert the estimated inertia matrix. The paper of Slotine & Li (1987) first addresses the problem in joint space, and then extends the solution to the Cartesian space.

Cheah et al. (2006b,a) extend the work of Slotine & Li (1987) to treat not only dynamics but also kinematics uncertainties. They show that the robot end-effector is able to converge to the desired trajectory despite the uncertain dynamic and kinematic parameters, which are updated online by adaptive laws. Moreover, according to the authors, the proposed controller can be extended to adaptive visual tracking control with uncertain camera parameters. Liu et al. (2006) propose a task-space adaptive Jacobian controller that is asymptotically stable in the Lyapunov sense and consider, besides the dynamics and kinematics, also the actuator dynamics, which was not considered by any of the previous works.

Adaptive controllers as the ones proposed by Slotine & Li (1987); Cheah et al. (2006a,b) are considered passivity-based controllers, which adopt approximate transpose-Jacobian feedback to track the manipulator end-effector (Wang & Xie, 2009). Although these controllers achieve asymptotic stability, their performance is not good over the entire robot configuration space. Since the closed-loop response varies with the manipulator configuration (Wang & Xie, 2009), it is not possible to define fixed gains that results in fixed closed-loop poles. Moreover, this type of controller leads to nonlinear and coupled error dynamics, and thus it is hard to quantify the system performance. Controllers based on the inverse dynamics, on the other hand, yield linear and decoupled error dynamics when the robot parameters are perfectly known. Thus, Wang & Xie (2009) propose an adaptive inverse dynamics controller for robots with unknown dynamic and kinematic parameters.

Notwithstanding, the controller requires the measurement of the joints accelerations, which is not necessary in the passivity-based controllers. As a result, the adaptive inverse dynamics controller is more sensitive to noises.

Both passivity-based and inverse dynamics based adaptive controller use the fact that both kinematic and dynamic models are linear parameterizable and utilize a regressor in the parameter update laws. However, computing the regressor matrix is expensive for manipulators with a high number of DOF. Thus, Hanlei (2010) proposes a computationally efficient adaptive control law based on the Newton-Euler recursive algorithm.

Table 2.1 summarizes the characteristics of passivity-based, recursive passivity-based, and inverse dynamics controllers.

Table 2.1: Characteristics of different types of adaptive controllers.

Adaptive Controller	**Passivity-based**	**Recursive passivity-based**	**Inverse dynamics**
Do not require inversion of inertia matrix	✓	✓	
Do not require measurement of joint accelerations	✓	✓	
Good performance over the entire robot configuration space			✓
Linear error dynamics			✓
Computationally efficient		✓	
Achieve convergence of the position and velocity	✓	✓	✓

Passivity-based controllers have some advantages when compared to inverse dynamics controllers. For example, they do not require the inversion of the estimated inertia matrix. However, those laws usually do not guarantee that the estimated inertia matrix is positive definite, which results in physically inconsistent results, or even well-conditioned (Wang & Xie, 2011). To overcome the lack of positiveness guarantee, one strategy is to ensure that the estimated parameters are positive to obtain a positive definite estimated inertia matrix. This can be done by defining an appropriate convex region, whose interior defines the set of admissible positive parameters, and then using a projection algorithm to ensure that the parameters remain inside that region (Cheah et al., 2006b). Nevertheless, in discrete implementations, the estimated parameters may escape from that region, thus Wang & Xie (2011) propose an approach that guarantees the positiveness of the estimated parameters while retaining stability of the closed-loop system. Still, they observed that when the

parameter update is too fast, the algorithm cannot project the estimated parameters into the region of admissible parameters.

Despite the vast literature on adaptive control, it still lacks works that focus on the improvement of the JSIM conditioning.

2.2 Conclusion

This chapter shows the intrinsic problem of robot manipulators. Although the inertia matrix of a manipulator is positive definite, it can be ill-conditioned, which can lead to bad performance of controllers. To circumvent this problem, an adaptive controller can be used since we can enforce the inertia matrix to be well-conditioned and compensate the added uncertainties in order to have a stable response, as shown in section 4.3. Therefore, the adaptive controller of the literature has been reviewed.

Besides the need to have a stable response, another issue concerning safety is the wrenches acting on the robot and the manipulated object. To limit these wrenches or to enable a compliant robot behavior, force, impedance, and admittance controllers can be used. That being said, a revision of the state of the art concerning these three controllers has also been done.

3

Kinematic and Dynamic Modeling Using Dual Quaternions

This chapter presents the mathematical background and notation used in the whole thesis. Here are the most important concepts needed as well as quaternion and DQ properties and operations. Moreover, the kinematic and dynamic model of robot manipulators are described, including a revision of the cooperative dual task-space and its relation with external and internal wrenches when considering bimanual manipulations. Furthermore, the whole-body kinematic model of a bimanual mobile manipulator is described. The mechanical impedance model is also revised.

3.1 Mathematical Background

When designing task-space controllers, the mathematical representation of rigid motions plays an important role, since a poor choice may lead, for instance, to representational singularities (Siciliano et al., 2009). In the last decades, several works have shown that the DQ algebra presents several advantages over other mathematical tools for robot modeling and control, most notably when the task-space is considered (Adorno & Marinho, 2020).

For instance, the unit DQ has a compact representation, requiring only eight parameters, whereas the homogeneous transformation matrix (HTM) needs twelve if the fourth constant row is discarded, presenting thus a smaller computational cost concerning multiplications and additions. Moreover, the unit DQ does not have representational singularities, as

well as the HTM, and the coefficients of a DQ can be used directly in the control law. This is a great convenience since the use of other traditional methods based on HTM may require the extraction of geometrical parameters, which in turn can lead to representational singularities (Adorno et al., 2010). Another advantage of DQ is the fact that it has strong algebraic properties and can be used to represent, in addition to rigid motions, wrenches, twists, and geometric primitives such as Plücker lines and planes (Adorno, 2017). Also, the extraction of geometric parameters of a given DQ, like translation, rotation axis, and rotation angles is very simple.

Thanks to the aforementioned advantages, the DQ algebra is used throughout this thesis.

3.1.1 Quaternions

Introduced by Hamilton in the XIX century, quaternions can be understood as an extension of imaginary numbers, where the three imaginary components obey the following properties (Hamilton, 1844, apud Adorno, 2011):

$$\hat{\imath}^2 = \hat{\jmath}^2 = \hat{k}^2 = \hat{\imath}\hat{\jmath}\hat{k} = -1. \tag{3.1}$$

The set $\mathbb{H}$ of quaternions is defined as

$$\mathbb{H} \triangleq \left\{ h_1 + \hat{\imath}h_2 + \hat{\jmath}h_3 + \hat{k}h_4 \,:\, h_1, h_2, h_3, h_4 \in \mathbb{R} \right\}.$$

Given $\mathbb{H} \ni \boldsymbol{h} = h_1 + \hat{\imath}h_2 + \hat{\jmath}h_3 + \hat{k}h_4$, the real part of $\boldsymbol{h}$ is $\mathrm{Re}\left(\boldsymbol{h}\right) \triangleq h_1$ and $\mathrm{Im}\left(\boldsymbol{h}\right) \triangleq \hat{\imath}h_2 + \hat{\jmath}h_3 + \hat{k}h_4$ is the imaginary part, such that $\boldsymbol{h} = \mathrm{Re}\left(\boldsymbol{h}\right) + \mathrm{Im}\left(\boldsymbol{h}\right)$, whereas the quaternion conjugate is given by $\boldsymbol{h}^* \triangleq \mathrm{Re}\left(\boldsymbol{h}\right) - \mathrm{Im}\left(\boldsymbol{h}\right)$, and its norm is defined as

$$\|\boldsymbol{h}\| \triangleq \sqrt{\boldsymbol{h}\boldsymbol{h}^*} = \sqrt{\boldsymbol{h}^*\boldsymbol{h}}. \tag{3.2}$$

The subset of pure quaternions is defined as

$$\mathbb{H}_p \triangleq \left\{ \boldsymbol{h} \in \mathbb{H} \,:\, \mathrm{Re}\left(\boldsymbol{h}\right) = 0 \right\},$$

and the subset of unit quaternions is defined as

$$\mathbb{S}^3 \triangleq \left\{ \boldsymbol{h} \in \mathbb{H} \,:\, \|\boldsymbol{h}\| = 1 \right\}.$$

Unit quaternions whose group composition is the standard multiplication form the group $\mathrm{Spin}\left(3\right)$ (Selig, 2005).

The multiplication between real matrices and quaternions is sometimes necessary, and thus appropriate operators are needed. Given $\mathbb{H} \ni \boldsymbol{h} = h_1 + \hat{\imath}h_2 + \hat{\jmath}h_3 + \hat{k}h_4$, the operator

$\text{vec}_4 : \mathbb{H} \to \mathbb{R}^4$ is defined as

$$\text{vec}_4 \boldsymbol{h} \triangleq \begin{bmatrix} h_1 & h_2 & h_3 & h_4 \end{bmatrix}^T,$$

such that, given $\boldsymbol{a}, \boldsymbol{b} \in \mathbb{H}$, the Hamilton operators $\bar{\boldsymbol{H}}_4, \overset{+}{\boldsymbol{H}}_4 : \mathbb{H} \to \mathbb{R}^{4\times 4}$ satisfy (Adorno, 2011)

$$\text{vec}_4 (\boldsymbol{ab}) = \overset{+}{\boldsymbol{H}}_4 (\boldsymbol{a}) \text{vec}_4 \boldsymbol{b} \tag{3.3}$$

$$= \bar{\boldsymbol{H}}_4 (\boldsymbol{b}) \text{vec}_4 \boldsymbol{a}. \tag{3.4}$$

The inverse operation is performed by the operator $\underline{\mathbf{vec}}_4 : \mathbb{R}^4 \to \mathbb{H}$. Thus, given $\boldsymbol{u} = \begin{bmatrix} u_1 & u_2 & u_3 & u_4 \end{bmatrix}^T$,

$$\underline{\mathbf{vec}}_4 \boldsymbol{u} = u_1 + \hat{\imath} u_2 + \hat{\jmath} u_3 + \hat{k} u_4.$$

Moreover, given $\mathbb{H}_p \ni \boldsymbol{h} = \hat{\imath} h_1 + \hat{\jmath} h_2 + \hat{k} h_3$, the operator $\text{vec}_3 : \mathbb{H}_p \to \mathbb{R}^3$ is defined as (Adorno, 2011)

$$\text{vec}_3 \boldsymbol{h} \triangleq \begin{bmatrix} h_1 & h_2 & h_3 \end{bmatrix}^T,$$

and the operator $\underline{\mathbf{vec}}_3 : \mathbb{R}^3 \to \mathbb{H}_p$ is defined as

$$\underline{\mathbf{vec}}_3 \boldsymbol{u} = \hat{\imath} u_1 + \hat{\jmath} u_2 + \hat{k} u_3,$$

where $\boldsymbol{u} = \begin{bmatrix} u_1 & u_2 & u_3 \end{bmatrix}^T$.

Given $\boldsymbol{u}, \boldsymbol{v} \in \mathbb{H}_p$, the cross product can be defined using only quaternion operations (Adorno, 2011), and is given by

$$\boldsymbol{u} \times \boldsymbol{v} \triangleq \frac{\boldsymbol{uv} - \boldsymbol{vu}}{2}.$$

Furthermore, it is related to the skew-symmetric matrix $\boldsymbol{S}(\cdot)$ by

$$\text{vec}_3 (\boldsymbol{u} \times \boldsymbol{v}) = \boldsymbol{S} (\text{vec}_3 \boldsymbol{u}) \text{vec}_3 \boldsymbol{v}. \tag{3.5}$$

3.1.2 Dual Quaternions

Analogously to quaternions, the DQ set is defined as (Adorno, 2011)

$$\mathcal{H} \triangleq \left\{ \boldsymbol{h}_1 + \varepsilon \boldsymbol{h}_2 \,:\, \boldsymbol{h}_1, \boldsymbol{h}_2 \in \mathbb{H},\, \varepsilon \neq 0,\, \varepsilon^2 = 0 \right\},$$

where ε is the nilpotent dual unit (Clifford, 1873). Given $\mathcal{H} \ni \underline{\boldsymbol{h}} = \boldsymbol{h}_1 + \varepsilon \boldsymbol{h}_2$, the primary part is defined as $\mathcal{P}(\underline{\boldsymbol{h}}) \triangleq \boldsymbol{h}_1$ and the dual part is $\mathcal{D}(\underline{\boldsymbol{h}}) = \boldsymbol{h}_2$. Moreover, the real part of $\underline{\boldsymbol{h}}$ is $\operatorname{Re}(\underline{\boldsymbol{h}}) \triangleq \operatorname{Re}(\boldsymbol{h}_1) + \varepsilon \operatorname{Re}(\boldsymbol{h}_2)$, and $\operatorname{Im}(\underline{\boldsymbol{h}}) \triangleq \operatorname{Im}(\boldsymbol{h}_1) + \varepsilon \operatorname{Im}(\boldsymbol{h}_2)$ is the imaginary part. Its conjugate is given by $\underline{\boldsymbol{h}}^* \triangleq \operatorname{Re}(\underline{\boldsymbol{h}}) - \operatorname{Im}(\underline{\boldsymbol{h}})$, and its norm is defined as

$$\|\underline{\boldsymbol{h}}\| \triangleq \sqrt{\underline{\boldsymbol{h}}\underline{\boldsymbol{h}}^*} = \sqrt{\underline{\boldsymbol{h}}^*\underline{\boldsymbol{h}}}.$$

The subset of pure DQ is defined as

$$\mathcal{H}_p \triangleq \{\underline{\boldsymbol{h}} \in \mathcal{H} \,:\, \operatorname{Re}(\underline{\boldsymbol{h}}) = 0\}$$

whereas the set of unit DQ is defined as

$$\underline{\boldsymbol{\mathcal{S}}} \triangleq \{\underline{\boldsymbol{h}} \in \mathcal{H} \,:\, \|\underline{\boldsymbol{h}}\| = 1\}.$$

Unit DQ whose group composition is the standard multiplication form the group $\operatorname{Spin}(3) \ltimes \mathbb{R}^3$ of rigid motions (Selig, 2005).

Similar to quaternions, given $\mathcal{H} \ni \underline{\boldsymbol{a}} = \mathcal{P}(\underline{\boldsymbol{a}}) + \varepsilon \mathcal{D}(\underline{\boldsymbol{a}})$ and $\mathcal{H}_p \ni \underline{\boldsymbol{b}} = \mathcal{P}(\underline{\boldsymbol{b}}) + \varepsilon \mathcal{D}(\underline{\boldsymbol{b}})$, the operators $\operatorname{vec}_8 : \mathcal{H} \to \mathbb{R}^8$ and $\operatorname{vec}_6 : \mathcal{H}_p \to \mathbb{R}^6$ are defined as (Adorno, 2011)

$$\begin{aligned}
\operatorname{vec}_8 \underline{\boldsymbol{a}} &= \begin{bmatrix} (\operatorname{vec}_4 \mathcal{P}(\underline{\boldsymbol{a}}))^T & (\operatorname{vec}_4 \mathcal{D}(\underline{\boldsymbol{a}}))^T \end{bmatrix}^T, \\
\operatorname{vec}_6 \underline{\boldsymbol{b}} &= \begin{bmatrix} (\operatorname{vec}_3 \mathcal{P}(\underline{\boldsymbol{b}}))^T & (\operatorname{vec}_3 \mathcal{D}(\underline{\boldsymbol{b}}))^T \end{bmatrix}^T.
\end{aligned}$$

Given $\boldsymbol{u} = \begin{bmatrix} u_1 & u_2 & u_3 & u_4 & u_5 & u_6 & u_7 & u_8 \end{bmatrix}^T$ and $\boldsymbol{v} = \begin{bmatrix} v_1 & v_2 & v_3 & v_4 & v_5 & v_6 \end{bmatrix}^T$, the inverse mappings $\underline{\mathbf{vec}}_8 : \mathbb{R}^8 \to \mathcal{H}$ and $\underline{\mathbf{vec}}_6 : \mathbb{R}^6 \to \mathcal{H}_p$ are given by

$$\underline{\mathbf{vec}}_8 \boldsymbol{u} = u_1 + \hat{\imath} u_2 + \hat{\jmath} u_3 + \hat{k} u_4 + \varepsilon \left(u_5 + \hat{\imath} u_6 + \hat{\jmath} u_7 + \hat{k} u_8 \right), \tag{3.6}$$

$$\underline{\mathbf{vec}}_6 \boldsymbol{u} = \hat{\imath} u_1 + \hat{\jmath} u_2 + \hat{k} u_3 + \varepsilon \left(\hat{\imath} u_4 + \hat{\jmath} u_5 + \hat{k} u_6 \right). \tag{3.7}$$

Given $\underline{\boldsymbol{a}}, \underline{\boldsymbol{b}} \in \mathcal{H}$, the Hamilton operators $\bar{\boldsymbol{H}}_8, \overset{+}{\boldsymbol{H}}_8 : \mathcal{H} \to \mathbb{R}^{8\times 8}$ are defined such that (Adorno, 2011)

$$\begin{aligned}
\operatorname{vec}_8 (\underline{\boldsymbol{a}}\underline{\boldsymbol{b}}) &= \overset{+}{\boldsymbol{H}}_8 (\underline{\boldsymbol{a}}) \operatorname{vec}_8 \underline{\boldsymbol{b}} \\
&= \bar{\boldsymbol{H}}_8 (\underline{\boldsymbol{b}}) \operatorname{vec}_8 \underline{\boldsymbol{a}}.
\end{aligned}$$

Moreover, the constant matrix $\boldsymbol{C}_8 = \operatorname{diag}(1, -1, -1, -1, 1, -1, -1, -1)$ satisfies

$$\boldsymbol{C}_8 \operatorname{vec}_8 \underline{\boldsymbol{a}} = \operatorname{vec}_8 \underline{\boldsymbol{a}}^*.$$

3.2 Representation of Rigid Movements

Points and translations given by $\begin{bmatrix} p_x & p_y & p_z \end{bmatrix}^T \in \mathbb{R}^3$ can be represented also by a pure quaternion $\boldsymbol{p} \in \mathbb{H}_p$

$$\boldsymbol{p} = \hat{\imath} p_x + \hat{\jmath} p_y + \hat{k} p_z.$$

An unit quaternion $\boldsymbol{r} \in \mathrm{Spin}\,(3)$ given by

$$\boldsymbol{r} = \cos\left(\frac{\phi}{2}\right) + \boldsymbol{n}\sin\left(\frac{\phi}{2}\right)$$

represents the rotation in three-dimensional Euclidean space (Adorno, 2011), where ϕ is the angle of rotation around the unit axis $\boldsymbol{n} = \hat{\imath} n_i + \hat{\jmath} n_y + \hat{k} n_k$, with n_x, n_y, $n_z \in \mathbb{R}$. If $\phi = 0\,\mathrm{rad}$, then $\boldsymbol{r} = 1$ and no rotation is performed.

When rotating a coordinate system $\mathcal{F}_0$, we can reference a point $\boldsymbol{p}^0$ of the original system in the rotated frame $\mathcal{F}_1$. In this case, (Adorno, 2011)

$$\boldsymbol{p}^1 = \mathrm{Ad}\left(\boldsymbol{r}_0^1\right)\boldsymbol{p}^0 \triangleq \boldsymbol{r}_0^1 \boldsymbol{p}^0 \boldsymbol{r}_0^{1*}, \tag{3.8}$$

where the superscript of $\boldsymbol{p}$ denotes the reference frame, and $\mathrm{Ad}\,(\cdot)$ is the adjoint transformation.

Considering a translation $\boldsymbol{p} \in \mathbb{H}_p$ and a rotation $\boldsymbol{r} \in \mathrm{Spin}(3)$, the unit DQ that represents the rigid movement from frame $\mathcal{F}_0$ to frame $\mathcal{F}_1$ is given by (Adorno, 2011)

$$\underline{\boldsymbol{x}}_1^0 \triangleq \boldsymbol{r}_1^0 + \varepsilon\frac{1}{2}\boldsymbol{p}_{01}^0 \boldsymbol{r}_1^0, \tag{3.9}$$

where $\underline{\boldsymbol{x}}_1^0 \in \mathrm{Spin}(3)\ltimes\mathbb{R}^3$ corresponds to the translation $\boldsymbol{p}_{01}^0$ followed by the rotation $\boldsymbol{r}_1^0$, as illustrated in Figure 3.1. Moreover, the composition of rigid motion is given by the multiplication of unit DQ. For instance, the transformation from frame $\mathcal{F}_0$ to frame $\mathcal{F}_4$ is given by (Adorno, 2011)

$$\underline{\boldsymbol{x}}_4^0 = \underline{\boldsymbol{x}}_1^0 \underline{\boldsymbol{x}}_2^1 \underline{\boldsymbol{x}}_3^2 \underline{\boldsymbol{x}}_4^3.$$

The next propositions and definitions regarding DQ are also important.

Proposition 3.1. *Given* $\underline{\boldsymbol{x}} = \boldsymbol{r} + \varepsilon\,(1/2)\,\boldsymbol{p}\boldsymbol{r}$ *a unit DQ with* $\boldsymbol{r} = \cos\,(\phi/2) + \boldsymbol{n}\sin\,(\phi/2)$, $\boldsymbol{n} = \hat{\imath} n_x + \hat{\jmath} n_y + \hat{k} n_z$, *and* $\boldsymbol{p} = \hat{\imath} p_x + \hat{\jmath} p_y + \hat{k} p_z$, *the logarithm of* $\underline{\boldsymbol{x}}$ *is (Adorno, 2011)*

$$\log \underline{\boldsymbol{x}} = \frac{\phi \boldsymbol{n}}{2} + \varepsilon\frac{\boldsymbol{p}}{2},$$

and $\log \underline{\boldsymbol{x}} \in \mathcal{H}_p$.

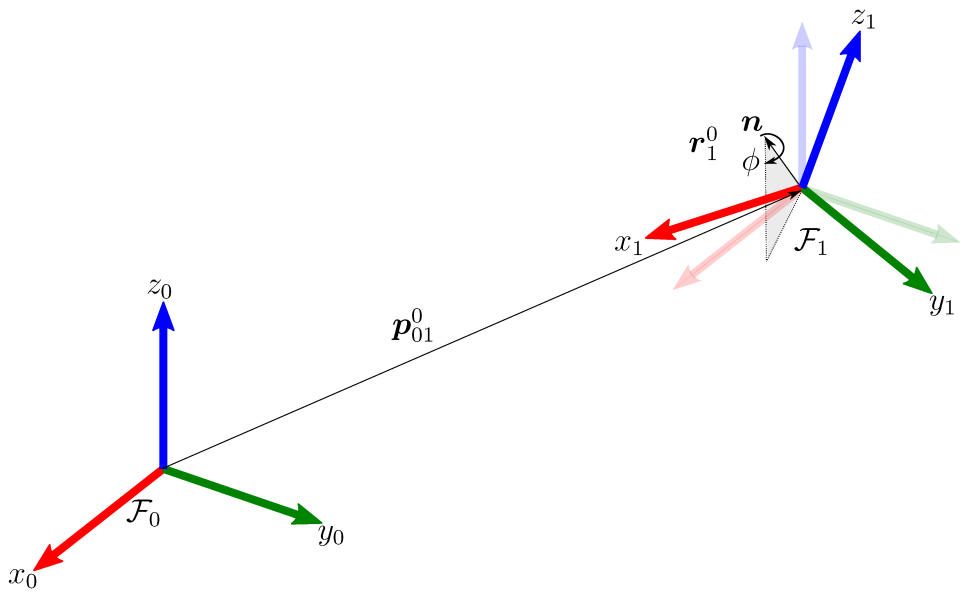

Figure 3.1: Rigid movement from the coordinate system $\mathcal{F}_0$ to $\mathcal{F}_1$.

Proposition 3.2. *Given* $\underline{\boldsymbol{g}} \in \mathcal{H}_p$*, the exponential of* $\underline{\boldsymbol{g}}$ *is (Adorno, 2011)*

$$\exp \underline{\boldsymbol{g}} = \mathcal{P}\left(\exp \underline{\boldsymbol{g}}\right) + \varepsilon\, \mathcal{D}\left(\underline{\boldsymbol{g}}\right) \mathcal{P}\left(\exp \underline{\boldsymbol{g}}\right) \tag{3.10}$$

$$\mathcal{P}\left(\exp \underline{\boldsymbol{g}}\right) = \begin{cases} \cos \left\|\mathcal{P}\left(\underline{\boldsymbol{g}}\right)\right\| + \frac{\sin\left\|\mathcal{P}\left(\underline{\boldsymbol{g}}\right)\right\|}{\left\|\mathcal{P}\left(\underline{\boldsymbol{g}}\right)\right\|} \mathcal{P}\left(\underline{\boldsymbol{g}}\right), & \text{if } \left\|\mathcal{P}\left(\underline{\boldsymbol{g}}\right) \neq 0\right\| \\ 1, & \text{otherwise,} \end{cases} \tag{3.11}$$

and $\exp \underline{\boldsymbol{g}} \in \underline{\boldsymbol{\mathcal{S}}}$.

Definition 3.1. Given the Propositions 3.1 and 3.2, the *geometrical* exponential of $\underline{\boldsymbol{x}} \in \underline{\boldsymbol{\mathcal{S}}}$ is (Adorno, 2011)

$$\begin{aligned} \underline{\boldsymbol{x}}^{\{\lambda\}} &\triangleq \exp\left(\lambda \log \underline{\boldsymbol{x}}\right) \\ &= \boldsymbol{r}^{\{\lambda\}} + \varepsilon \frac{1}{2} \lambda \boldsymbol{p} \boldsymbol{r}^{\{\lambda\}}, \end{aligned}$$

where $\boldsymbol{r}^{\{\lambda\}} = \cos\left(\lambda\phi/2\right) + \boldsymbol{n} \sin\left(\lambda\phi/2\right)$.

3.3 Derivative of (Dual) Quaternions

This section covers the derivative of DQ, showing the relationship between the derivative of a unit DQ with its correspondent twist, as well as the derivative of its logarithm.

3.3.1 Relationship Between the Derivative of Unit Dual Quaternions and Twists

The relationship between the time derivative of an unit quaternion $\boldsymbol{r} \in \mathbb{S}^3$ and the angular velocity $\boldsymbol{\omega} = \hat{\imath}\omega_x + \hat{\jmath}\omega_y + \hat{k}\omega_z$ is given by (Adorno, 2011)

$$\dot{\boldsymbol{r}} = \frac{1}{2}\boldsymbol{\omega}\boldsymbol{r}. \tag{3.12}$$

Now, considering the unit DQ $\underline{\boldsymbol{x}} \triangleq \boldsymbol{r} + \varepsilon\,(1/2)\,\boldsymbol{p}\boldsymbol{r}$, it is related to its twist $\underline{\boldsymbol{\xi}} = \boldsymbol{\omega} + \varepsilon\,(\dot{\boldsymbol{p}} + \boldsymbol{p} \times \boldsymbol{\omega})$ by (Adorno, 2017)

$$\dot{\underline{\boldsymbol{x}}} = \frac{1}{2}\underline{\boldsymbol{\xi}}\underline{\boldsymbol{x}}. \tag{3.13}$$

3.3.2 Relationship Between the Time Derivatives of an Unit Dual Quaternion and its Logarithm

Consider $\underline{\boldsymbol{y}} \triangleq \log\underline{\boldsymbol{x}}$, with $\underline{\boldsymbol{x}} = \boldsymbol{r} + \varepsilon\,(1/2)\,\boldsymbol{p}\boldsymbol{r}$. The relationship between the time derivatives of $\underline{\boldsymbol{x}}$ and $\underline{\boldsymbol{y}}$ is given by (Savino et al., 2020)

$$\operatorname{vec}_8 \dot{\underline{\boldsymbol{x}}} = \boldsymbol{Q}_8\,(\underline{\boldsymbol{x}})\operatorname{vec}_6 \dot{\underline{\boldsymbol{y}}}, \tag{3.14}$$

where

$$\boldsymbol{Q}_8\,(\underline{\boldsymbol{x}}) = \begin{bmatrix} \boldsymbol{Q}_4\,(\boldsymbol{r}) & \boldsymbol{0}_{4\times 3} \\ \frac{1}{2}\overset{+}{\boldsymbol{H}}_4\,(\boldsymbol{p})\,\boldsymbol{Q}_4\,(\boldsymbol{r}) & \overset{-}{\boldsymbol{H}}_4\,(\boldsymbol{r})\,\bar{\boldsymbol{I}}^T \end{bmatrix},$$

with $\boldsymbol{0}_{m\times n} \in \mathbb{R}^{m\times n}$ being a matrix of zeros, $\overset{+}{\boldsymbol{H}}_4\,(\cdot)$ being the Hamilton operator as in Equation (3.3), and $\bar{\boldsymbol{I}}$ is the reducing matrix as in Equation (2). In addition,

$$\boldsymbol{Q}_4\,(\boldsymbol{r}) = \begin{bmatrix} -r_2 & -r_3 & -r_4 \\ \Gamma n_x^2 + \Theta & \Gamma n_x n_y & \Gamma n_x n_z \\ \Gamma n_y n_x & \Gamma n_y^2 + \Theta & \Gamma n_y n_z \\ \Gamma n_z n_x & \Gamma n_z n_y & \Gamma n_z^2 + \Theta \end{bmatrix},$$

where r_i is the i-th component of the quaternion $\boldsymbol{r}$, and

$$\Gamma = r_1 - \Theta, \tag{3.15}$$

$$\Theta = \begin{cases} 1, & \text{if } \phi = 0 \\ \frac{\sin(\phi/2)}{\phi/2}, & \text{otherwise,} \end{cases} \tag{3.16}$$

in which ϕ is the angle of rotation. For the proof, see (Savino et al., 2020).

Moreover, the following relation is also true (Savino et al., 2020):

$$\operatorname{vec}_4 \dot{\boldsymbol{r}} = \boldsymbol{Q}_4(\boldsymbol{r}) \frac{d}{dt} \operatorname{vec}_3 \left(\boldsymbol{n} \frac{\phi}{2} \right). \tag{3.17}$$

3.3.2.1 Second Derivative

The relationship between the second derivatives of an unit DQ and its logarithm is found deriving Equation (3.14). Hence,

$$\operatorname{vec}_8 \ddot{\underline{\boldsymbol{x}}} = \dot{\boldsymbol{Q}}_8(\underline{\boldsymbol{x}}) \operatorname{vec}_6 \dot{\underline{\boldsymbol{y}}} + \boldsymbol{Q}_8(\underline{\boldsymbol{x}}) \operatorname{vec}_6 \ddot{\underline{\boldsymbol{y}}}, \tag{3.18}$$

where

$$\dot{\boldsymbol{Q}}_8(\underline{\boldsymbol{x}}) = \begin{bmatrix} \dot{\boldsymbol{Q}}_4(\boldsymbol{r}) & \boldsymbol{0}_{4\times 3} \\ \frac{1}{2}\boldsymbol{\mathcal{Q}}(\underline{\boldsymbol{x}}, \dot{\underline{\boldsymbol{x}}}) & \bar{\boldsymbol{H}}_4(\dot{\boldsymbol{r}}) \bar{\boldsymbol{I}}^T \end{bmatrix},$$

with $\boldsymbol{\mathcal{Q}}(\underline{\boldsymbol{x}}, \dot{\underline{\boldsymbol{x}}}) \triangleq \overset{+}{\boldsymbol{H}}_4(\dot{\boldsymbol{p}}) \boldsymbol{Q}_4(\boldsymbol{r}) + \overset{+}{\boldsymbol{H}}_4(\boldsymbol{p}) \dot{\boldsymbol{Q}}_4(\boldsymbol{r})$ and

$$\dot{\boldsymbol{Q}}_4(\boldsymbol{r}) = \begin{bmatrix} -\dot{r}_2 & -\dot{r}_3 & -\dot{r}_4 \\ \dot{\Gamma} n_x^2 + \Gamma 2 n_x \dot{n}_x + \dot{\Theta} & \dot{\Gamma} n_x n_y + \Gamma \dot{n}_x n_y + \Gamma n_x \dot{n}_y & \dot{\Gamma} n_x n_z + \Gamma \dot{n}_x n_z + \Gamma n_x \dot{n}_z \\ \dot{\Gamma} n_y n_x + \Gamma \dot{n}_y n_x + \Gamma n_y \dot{n}_x & \dot{\Gamma} n_y^2 + \Gamma 2 n_y \dot{n}_y + \dot{\Theta} & \dot{\Gamma} n_y n_z + \Gamma \dot{n}_y n_z + \Gamma n_y \dot{n}_z \\ \dot{\Gamma} n_z n_x + \Gamma \dot{n}_z n_x + \Gamma n_z \dot{n}_x & \dot{\Gamma} n_z n_y + \Gamma \dot{n}_z n_y + \Gamma n_z \dot{n}_y & \dot{\Gamma} n_z^2 + \Gamma 2 n_z \dot{n}_z + \dot{\Theta} \end{bmatrix},$$

with

$$\dot{\Gamma} = \dot{r}_1 - \dot{\Theta}$$

and

$$\dot{\Theta} = \begin{cases} 0, & \text{if } \phi = 0 \\ \frac{\cos(\phi/2)\left(\dot{\phi}/2\right)(\phi/2) - \sin(\phi/2)\left(\dot{\phi}/2\right)}{(\phi/2)^2}, & \text{otherwise.} \end{cases}$$

3.3.3 Relationship Between the Twist and the Derivative of Logarithm

Considering the variable $\mathcal{H}_p \ni \underline{\boldsymbol{\zeta}} = \boldsymbol{\omega} + \varepsilon \dot{\boldsymbol{p}}$,[1] with $\boldsymbol{\omega} \in \mathbb{H}_p$ being the angular velocity, there exists $\boldsymbol{E}(\underline{\boldsymbol{x}}) \in \mathbb{R}^{6\times 6}$ such that

$$\operatorname{vec}_6 \underline{\boldsymbol{\zeta}} = \boldsymbol{E}(\underline{\boldsymbol{x}}) \operatorname{vec}_6 \underline{\dot{\boldsymbol{y}}}. \tag{3.19}$$

More specifically, using the Equations (3.17) and (3.12), $\boldsymbol{E}(\underline{\boldsymbol{x}})$ is found by inspection:

$$\boldsymbol{E}(\underline{\boldsymbol{x}}) \triangleq \begin{bmatrix} \bar{\boldsymbol{I}}\overline{\boldsymbol{W}}(\boldsymbol{r}) & \boldsymbol{0}_{3\times 3} \\ \boldsymbol{0}_{3\times 3} & 2\boldsymbol{I}_{3\times 3} \end{bmatrix}, \tag{3.20}$$

with $\mathbb{R}^{4\times 3} \ni \overline{\boldsymbol{W}}(\boldsymbol{r}) \triangleq 2\bar{\boldsymbol{H}}_4(\boldsymbol{r}^*)\boldsymbol{Q}_4(\boldsymbol{r})$ and $\bar{\boldsymbol{I}}$ being defined as in Equation (2).

Theorem 3.1. *The matrix of Equation (3.20) is invertible and its inverse is given by*

$$\boldsymbol{E}^{-1}(\underline{\boldsymbol{x}}) \triangleq \begin{bmatrix} \frac{1}{2}\boldsymbol{Q}_4^{+}(\boldsymbol{r})\bar{\boldsymbol{H}}_4(\boldsymbol{r})\bar{\boldsymbol{I}}^T & \boldsymbol{0}_{3\times 3} \\ \boldsymbol{0}_{3\times 3} & \frac{1}{2}\boldsymbol{I}_{3\times 3} \end{bmatrix}, \tag{3.21}$$

where $\boldsymbol{Q}_4^{+}(\cdot)$ is the left pseudo-inverse of $\boldsymbol{Q}_4(\cdot)$.

Proof. By direct calculation of $2\bar{\boldsymbol{H}}_4(\boldsymbol{r}^*)\boldsymbol{Q}_4(\boldsymbol{r})$ (see Lemma C.3),

$$\overline{\boldsymbol{W}}(\boldsymbol{r}) = \begin{bmatrix} \boldsymbol{0}_{1\times 3} \\ \boldsymbol{W}(\boldsymbol{r}) \end{bmatrix}$$

for all $\boldsymbol{r} \in \mathbb{S}^3$, where $\boldsymbol{W}(\boldsymbol{r}) \in \mathbb{R}^{3\times 3}$. Also, since $\operatorname{rank}\bar{\boldsymbol{H}}_4(\boldsymbol{r}^*) = 4$ and $\operatorname{rank}\boldsymbol{Q}_4(\boldsymbol{r}) = 3$ for all $\boldsymbol{r} \in \mathbb{S}^3$ (Savino et al., 2020), from Corollary 2.5.10 of (Bernstein, 2009) the following inequation is true:

$$\operatorname{rank}\bar{\boldsymbol{H}}_4(\boldsymbol{r}^*) + \operatorname{rank}\boldsymbol{Q}_4(\boldsymbol{r}) - 4 \leq \operatorname{rank}\bar{\boldsymbol{H}}_4(\boldsymbol{r}^*)\boldsymbol{Q}_4(\boldsymbol{r}) \leq \min\left\{\operatorname{rank}\bar{\boldsymbol{H}}_4(\boldsymbol{r}^*), \operatorname{rank}\boldsymbol{Q}_4(\boldsymbol{r})\right\}.$$

Hence, $\operatorname{rank}\overline{\boldsymbol{W}}(\boldsymbol{r}) = 3$ for all $\boldsymbol{r} \in \mathbb{S}^3$ and thus $\operatorname{rank}\boldsymbol{W}(\boldsymbol{r}) = 3$. Therefore, $\bar{\boldsymbol{I}}\overline{\boldsymbol{W}}(\boldsymbol{r}) = \boldsymbol{W}(\boldsymbol{r})$ is full rank, which implies that for all $\boldsymbol{r} \in \mathbb{S}^3$ the inverse of $\boldsymbol{W}(\boldsymbol{r})$ exists and is given by

$$\boldsymbol{W}^{-1}(\boldsymbol{r}) = \frac{1}{2}\boldsymbol{Q}_4^{+}(\boldsymbol{r})\bar{\boldsymbol{H}}_4(\boldsymbol{r})\bar{\boldsymbol{I}}^T. \tag{3.22}$$

[1] This is not the twist that satisfies the relation $\underline{\boldsymbol{\xi}}^a = \operatorname{Ad}(\underline{\boldsymbol{x}}_b^a)\underline{\boldsymbol{\xi}}^b$ as in (Adorno, 2017), and sometimes it is called dual velocity (Adorno, 2011).

Indeed, since $\bar{\boldsymbol{I}}^T \bar{\boldsymbol{I}} \overline{\boldsymbol{W}}(\boldsymbol{r}) = \overline{\boldsymbol{W}}(\boldsymbol{r})$ then

$$\boldsymbol{W}^{-1}(\boldsymbol{r})\,\boldsymbol{W}(\boldsymbol{r}) = \frac{1}{2}\boldsymbol{Q}_4^{+}(\boldsymbol{r})\,\bar{\boldsymbol{H}}_4(\boldsymbol{r})\,\bar{\boldsymbol{I}}^T \bar{\boldsymbol{I}} \overline{\boldsymbol{W}}(\boldsymbol{r}) = \boldsymbol{I}_{3\times 3}$$

because $\bar{\boldsymbol{H}}_4(\boldsymbol{r}) = \bar{\boldsymbol{H}}_4^{-1}(\boldsymbol{r}^*)$ and $\boldsymbol{Q}_4^{+}(\boldsymbol{r})\,\boldsymbol{Q}_4(\boldsymbol{r}) = \boldsymbol{I}_{3\times 3}$ (Savino et al., 2020). Moreover, as $\boldsymbol{W}(\boldsymbol{r})$ is square and full rank, the left inverse equals the right inverse (i.e., $\boldsymbol{W}^{-1}(\boldsymbol{r})\,\boldsymbol{W}(\boldsymbol{r}) = \boldsymbol{W}(\boldsymbol{r})\,\boldsymbol{W}^{-1}(\boldsymbol{r}) = \boldsymbol{I}_{3\times 3}$). Consequently, $\boldsymbol{E}(\underline{\boldsymbol{x}})$ is also full rank and thus invertible. □

By inspection, using Equation (3.5), the DQ twist $\underline{\boldsymbol{\xi}}$ is related to $\underline{\boldsymbol{\zeta}}$ by $\boldsymbol{A}(\underline{\boldsymbol{x}}) \in \mathbb{R}^{6\times 6}$ as

$$\operatorname{vec}_6 \underline{\boldsymbol{\xi}} = \boldsymbol{A}(\underline{\boldsymbol{x}}) \operatorname{vec}_6 \underline{\boldsymbol{\zeta}}, \tag{3.23}$$

with

$$\boldsymbol{A}(\underline{\boldsymbol{x}}) \triangleq \begin{bmatrix} \boldsymbol{I}_{3\times 3} & \boldsymbol{0}_{3\times 3} \\ \boldsymbol{S}(\operatorname{vec}_3 \boldsymbol{p}) & \boldsymbol{I}_{3\times 3} \end{bmatrix}, \tag{3.24}$$

where $\boldsymbol{S}(\cdot) \in SO(3)$.

Lemma 3.1. *The inverse of Equation (3.24) exists and is given by*

$$\boldsymbol{A}^{-1}(\underline{\boldsymbol{x}}) \triangleq \begin{bmatrix} \boldsymbol{I}_{3\times 3} & \boldsymbol{0}_{3\times 3} \\ -\boldsymbol{S}(\operatorname{vec}_3 \boldsymbol{p}) & \boldsymbol{I}_{3\times 3} \end{bmatrix}.$$

Proof. Since $\boldsymbol{I}_{3\times 3}$ is invertible, by inspection of Equation (3.24), the matrix $\boldsymbol{A}(\underline{\boldsymbol{x}})$ is invertible, which concludes the proof. □

Therefore, substituting Equation (3.19) in Equation (3.23) yields

$$\operatorname{vec}_6 \underline{\boldsymbol{\xi}} = \underbrace{\boldsymbol{A}(\underline{\boldsymbol{x}})\,\boldsymbol{E}(\underline{\boldsymbol{x}})}_{\boldsymbol{G}_{\log}(\underline{\boldsymbol{x}})} \operatorname{vec}_6 \dot{\underline{\boldsymbol{y}}}, \tag{3.25}$$

and thus $\boldsymbol{G}_{\log}(\underline{\boldsymbol{x}}) \in \mathbb{R}^{6\times 6}$ is given by

$$\boldsymbol{G}_{\log}(\underline{\boldsymbol{x}}) \triangleq \begin{bmatrix} \boldsymbol{W}(\boldsymbol{r}) & \boldsymbol{0}_{3\times 3} \\ \boldsymbol{S}(\operatorname{vec}_3 \boldsymbol{p})\,\boldsymbol{W}(\boldsymbol{r}) & 2\boldsymbol{I}_{3\times 3} \end{bmatrix}. \tag{3.26}$$

Theorem 3.2. *The matrix of Equation (3.26) is invertible and its inverse is given by*

$$\boldsymbol{G}_{\log}^{-1}(\underline{\boldsymbol{x}}) \triangleq \begin{bmatrix} \boldsymbol{W}^{-1}(\boldsymbol{r}) & \boldsymbol{0}_{3\times 3} \\ -\frac{1}{2}\boldsymbol{S}(\operatorname{vec}_3 \boldsymbol{p}) & \frac{1}{2}\boldsymbol{I}_{3\times 3} \end{bmatrix}. \tag{3.27}$$

Proof. By Theorem 3.1, the matrix $\boldsymbol{E}(\underline{\boldsymbol{x}})$ is proven to be invertible. Moreover, by Lemma 3.1, the matrix $\boldsymbol{A}(\underline{\boldsymbol{x}})$ is also invertible. Since $\boldsymbol{G}_{\log}(\underline{\boldsymbol{x}}) = \boldsymbol{A}(\underline{\boldsymbol{x}})\boldsymbol{E}(\underline{\boldsymbol{x}})$, then $\boldsymbol{G}_{\log}^{-1}(\underline{\boldsymbol{x}}) = \boldsymbol{E}^{-1}(\underline{\boldsymbol{x}})\boldsymbol{A}^{-1}(\underline{\boldsymbol{x}})$. Hence, by direct calculation $\boldsymbol{G}_{\log}^{-1}(\underline{\boldsymbol{x}})$ is given by Equation (3.27). □

3.3.3.1 Second Derivative

The relationship between the time derivative of $\underline{\boldsymbol{\zeta}}$ and the second time derivative of the logarithm is given by the derivative of Equation (3.19):

$$\operatorname{vec}_6 \dot{\underline{\boldsymbol{\zeta}}} = \dot{\boldsymbol{E}}(\underline{\boldsymbol{x}}) \operatorname{vec}_6 \dot{\underline{\boldsymbol{y}}} + \boldsymbol{E}(\underline{\boldsymbol{x}}) \operatorname{vec}_6 \ddot{\underline{\boldsymbol{y}}}, \tag{3.28}$$

where the time derivative of Equation (3.20) is given by

$$\dot{\boldsymbol{E}}(\underline{\boldsymbol{x}}) \triangleq \begin{bmatrix} 2\bar{\boldsymbol{I}}\boldsymbol{\mathcal{E}}(\boldsymbol{r}, \dot{\boldsymbol{r}}) & \boldsymbol{0}_{3\times 3} \\ \boldsymbol{0}_{3\times 3} & \boldsymbol{0}_{3\times 3} \end{bmatrix}, \tag{3.29}$$

where

$$\boldsymbol{\mathcal{E}}(\boldsymbol{r}, \dot{\boldsymbol{r}}) = \bar{\boldsymbol{H}}_4(\dot{\boldsymbol{r}}^*)\boldsymbol{Q}_4(\boldsymbol{r}) + \bar{\boldsymbol{H}}_4(\boldsymbol{r}^*)\dot{\boldsymbol{Q}}_4(\boldsymbol{r}, \dot{\boldsymbol{r}}). \tag{3.30}$$

Moreover, from Equation (3.23), the relationship between the time derivatives of $\underline{\boldsymbol{\zeta}}$ and the twist is

$$\operatorname{vec}_6 \dot{\underline{\boldsymbol{\xi}}} = \dot{\boldsymbol{A}}(\underline{\boldsymbol{x}}) \operatorname{vec}_6 \underline{\boldsymbol{\zeta}} + \boldsymbol{A}(\underline{\boldsymbol{x}}) \operatorname{vec}_6 \dot{\underline{\boldsymbol{\zeta}}},$$

with

$$\dot{\boldsymbol{A}}(\underline{\boldsymbol{x}}) \triangleq \begin{bmatrix} \boldsymbol{0}_{3\times 3} & \boldsymbol{0}_{3\times 3} \\ \boldsymbol{S}(\operatorname{vec}_3 \dot{\boldsymbol{p}}) & \boldsymbol{0}_{3\times 3} \end{bmatrix}.$$

Furthermore, from Equation (3.25),

$$\operatorname{vec}_6 \dot{\underline{\boldsymbol{\xi}}} = \dot{\boldsymbol{G}}_{\log}(\underline{\boldsymbol{x}}) \operatorname{vec}_6 \dot{\underline{\boldsymbol{y}}} + \boldsymbol{G}_{\log}(\underline{\boldsymbol{x}}) \operatorname{vec}_6 \ddot{\underline{\boldsymbol{y}}},$$

where

$$\dot{\boldsymbol{G}}_{\log}(\underline{\boldsymbol{x}}) \triangleq \begin{bmatrix} 2\bar{\boldsymbol{I}}\boldsymbol{\mathcal{E}}(\boldsymbol{r}, \dot{\boldsymbol{r}}) & \boldsymbol{0}_{3\times 3} \\ \boldsymbol{\mathcal{G}}(\underline{\boldsymbol{x}}, \dot{\underline{\boldsymbol{x}}}) & \boldsymbol{0}_{3\times 3} \end{bmatrix},$$

with $\boldsymbol{\mathcal{G}}(\underline{\boldsymbol{x}}, \dot{\underline{\boldsymbol{x}}}) \triangleq \boldsymbol{S}(\operatorname{vec}_3 \dot{\boldsymbol{p}})\boldsymbol{W}(\boldsymbol{r}) + 2\boldsymbol{S}(\operatorname{vec}_3 \boldsymbol{p})\bar{\boldsymbol{I}}\boldsymbol{\mathcal{E}}(\boldsymbol{r}, \dot{\boldsymbol{r}})$, where $\boldsymbol{\mathcal{E}}(\boldsymbol{r}, \dot{\boldsymbol{r}})$ is given by Equation (3.30).

3.4 Representation of Wrench

Considering the force and moment acting on a point $\boldsymbol{p}$, they are respectively represented by $\mathbb{H}_p \ni \boldsymbol{f} = \hat{\imath} f_x + \hat{\jmath} f_y + \hat{k} f_z$ and $\mathbb{H}_p \ni \boldsymbol{m} = \hat{\imath} m_x + \hat{\jmath} m_y + \hat{k} m_z$. Hence, the wrench at point $\boldsymbol{p}$ given with respect to frame $\mathcal{F}_a$ is represented by (Adorno, 2011)[2]

$$\underline{\boldsymbol{\varsigma}}^a_{a,a} = \boldsymbol{f}^a_a + \varepsilon \boldsymbol{m}^a_a.$$

In order to change only the point of observation of the wrench from frame $\mathcal{F}_a$ to frame $\mathcal{F}_b$, the adjoint transformation is used as

$$\begin{aligned} \underline{\boldsymbol{\varsigma}}^b_{a,a} &= \mathrm{Ad}\left(\boldsymbol{r}^b_a\right) \underline{\boldsymbol{\varsigma}}^a_{a,a} \\ &= \boldsymbol{f}^b_a + \varepsilon \boldsymbol{m}^b_a. \end{aligned} \tag{3.31}$$

However, if the point of observation is changed, as well as the point of actuation of the wrench, from frame $\mathcal{F}_a$ to frame $\mathcal{F}_b$, the adjoint transformation is used as

$$\begin{aligned} \underline{\boldsymbol{\varsigma}}^b_{b,a} &= \mathrm{Ad}\left(\underline{\boldsymbol{x}}^b_a\right) \underline{\boldsymbol{\varsigma}}^a_{a,a} \\ &= \boldsymbol{f}^b_a + \varepsilon \left(\boldsymbol{m}^b_a + \boldsymbol{p}^b_{ba} \times \boldsymbol{f}^b_a\right), \end{aligned} \tag{3.32}$$

as shown in Figure 3.2.

Remark 3.1. When the point of actuation is changed, that is, when $\mathrm{Ad}\left(\underline{\boldsymbol{x}}\right)$ is used, the resultant wrench takes into consideration the lever arm regarding this new point, which is not true when changing only the point of observation through $\mathrm{Ad}\left(\boldsymbol{r}\right)$. In the latter case, if there is a lever arm in the original wrench, it is kept the same. For reasons of readability, when a new lever arm is taken into consideration, the variable $\underline{\boldsymbol{\psi}}$ is used, otherwise, the variable is $\underline{\boldsymbol{\varsigma}}$ used.

3.4.1 Static Analysis

Using the principle of virtual work,

$$\begin{aligned} \delta\left(\mathrm{vec}_6\, \underline{\boldsymbol{y}}\right)^T \mathrm{vec}_6\, \underline{\boldsymbol{\varsigma}}_{\log} &= \delta\left(\boldsymbol{I}^{\#}\left[\left(\mathrm{vec}_4\, \boldsymbol{r}\right)^T \quad \left(\mathrm{vec}_4\, \boldsymbol{p}\right)^T\right]^T\right)^T \mathrm{vec}_6\, \underline{\boldsymbol{\varsigma}} \\ \lim_{\delta t \to 0} \frac{\delta\left(\mathrm{vec}_6\, \underline{\boldsymbol{y}}\right)^T}{\delta t} \mathrm{vec}_6\, \underline{\boldsymbol{\varsigma}}_{\log} &= \lim_{\delta t \to 0} \frac{\delta\left(\boldsymbol{I}^{\#}\left[\left(\mathrm{vec}_4\, \boldsymbol{r}\right)^T \quad \left(\mathrm{vec}_4\, \boldsymbol{p}\right)^T\right]^T\right)^T}{\delta t} \mathrm{vec}_6\, \underline{\boldsymbol{\varsigma}} \\ \left(\mathrm{vec}_6\, \dot{\underline{\boldsymbol{y}}}\right)^T \mathrm{vec}_6\, \underline{\boldsymbol{\varsigma}}_{\log} &= \left(\boldsymbol{I}^{\#} \mathrm{vec}_6\, \underline{\boldsymbol{\zeta}}\right)^T \mathrm{vec}_6\, \underline{\boldsymbol{\varsigma}}, \end{aligned}$$

[2]The notation used here is the following: the wrench is acting in (first subscript) due to (second subscript) and it is observed by (superscript).

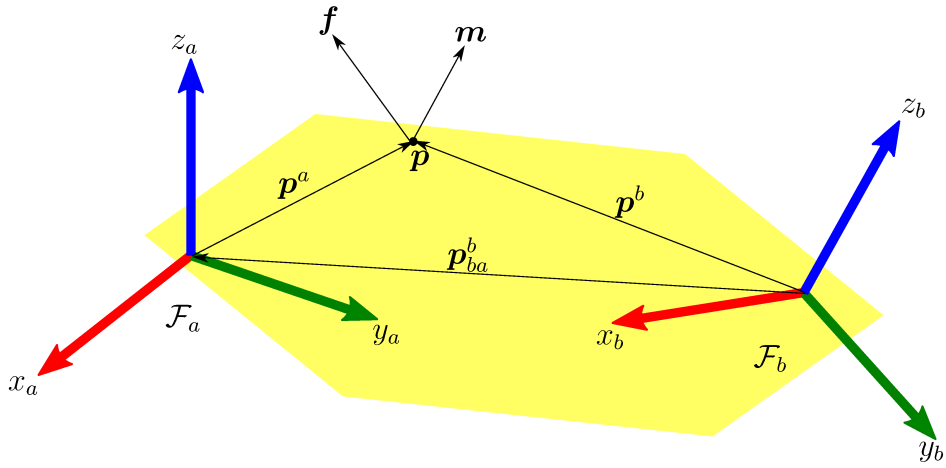

Figure 3.2: Wrench at point $\boldsymbol{p}$, with respect to frame $\mathcal{F}_a$ and frame $\mathcal{F}_b$.

where $\mathcal{H}_p \ni \underline{\boldsymbol{\zeta}} = \boldsymbol{\omega} + \varepsilon \dot{\boldsymbol{p}}$ is the dual velocity, $\mathcal{H}_p \ni \underline{\boldsymbol{\varsigma}} = \boldsymbol{f} + \varepsilon \boldsymbol{m}$ is the wrench, $\underline{\boldsymbol{y}} = \log \underline{\boldsymbol{x}}$, where $\underline{\boldsymbol{x}} \in \mathrm{Spin}(3) \ltimes \mathbb{R}^3$, $\underline{\boldsymbol{\varsigma}}_{\log}$ is the wrench related to the logarithm of a unit DQ, and $\boldsymbol{I}^{\#}$ is the flipper matrix given by Equation (1).

Using Equation (3.19) yields to

$$\begin{aligned} \left(\mathrm{vec}_6\, \dot{\underline{\boldsymbol{y}}}\right)^T \mathrm{vec}_6\, \underline{\boldsymbol{\varsigma}}_{\log} &= \left(\boldsymbol{I}^{\#} \boldsymbol{E}\left(\underline{\boldsymbol{x}}\right) \mathrm{vec}_6\, \dot{\underline{\boldsymbol{y}}}\right)^T \mathrm{vec}_6\, \underline{\boldsymbol{\varsigma}},\ \forall \dot{\underline{\boldsymbol{y}}} \in \mathcal{H}_p, \\ \implies \mathrm{vec}_6\, \underline{\boldsymbol{\varsigma}}_{\log} &= \left(\boldsymbol{I}^{\#} \boldsymbol{E}\left(\underline{\boldsymbol{x}}\right)\right)^T \mathrm{vec}_6\, \underline{\boldsymbol{\varsigma}}. \end{aligned} \tag{3.33}$$

3.5 Dual Quaternion Error

The DQ invariant error $\tilde{\underline{\boldsymbol{x}}}$ can be defined as the spacial difference in $\mathrm{Spin}(3) \ltimes \mathbb{R}^3$ (Figueredo et al., 2013), that is,

$$\tilde{\underline{\boldsymbol{x}}} \triangleq \underline{\boldsymbol{x}}^* \underline{\boldsymbol{x}}_d,$$

where $\underline{\boldsymbol{x}}_d$ is the desired pose and $\underline{\boldsymbol{x}}$ is the current one. Hence, if $\underline{\boldsymbol{x}} = \underline{\boldsymbol{x}}_d$, then $\tilde{\underline{\boldsymbol{x}}} = 1$. In order to have the DQ error translated to the origin, the error $\tilde{\underline{\boldsymbol{x}}}_e$ can be defined as

$$\tilde{\underline{\boldsymbol{x}}}_e \triangleq \tilde{\underline{\boldsymbol{x}}} - 1. \tag{3.34}$$

This way, when a motion controller is designed to asymptotically stabilize the system,

$$\tilde{\underline{\boldsymbol{x}}} \to 1 \iff \tilde{\underline{\boldsymbol{x}}}_e \to 0.$$

The logarithm $\tilde{\underline{\boldsymbol{y}}} \triangleq \log \tilde{\underline{\boldsymbol{x}}}$ can also be used to translate the error to the origin as

$$\tilde{\underline{\boldsymbol{x}}} \to 1 \implies \tilde{\underline{\boldsymbol{y}}} \to 0.$$

3.5.1 Solution to Homogeneous Differential Equations Using Dual Quaternions

Some control laws, as for example the impedance/admittance controllers, are written as differential equations. When using DQ, the solution of these differential equations needs to respect the properties of the unit DQ group, so the result $\underline{\boldsymbol{x}} \in \mathcal{H}$ can still represent a rigid motion. Hence, the choice of the error definition should respect these properties.

For simplicity, consider a first-order homogeneous equation:

$$\dot{\underline{\tilde{\boldsymbol{x}}}}_e(t) + \lambda \underline{\tilde{\boldsymbol{x}}}_e(t) = 0, \tag{3.35}$$

with $\lambda \in (0, \infty)$ constant. The solution to Equation (3.35) is

$$\underline{\tilde{\boldsymbol{x}}}_e(t) = e^{-\lambda t} \underline{\tilde{\boldsymbol{x}}}_e(0).$$

Using Equation (3.34) yields

$$\underline{\tilde{\boldsymbol{x}}}(t) = e^{-\lambda t} [\underline{\tilde{\boldsymbol{x}}}(0) - 1] + 1,$$

which has unit norm only when $t = 0$.

To circumvent this problem, the logarithm of unit DQ can be used, since it is isomorphic to $\mathbb{R}^6$ under addition operations. The first order differential equation, now using the logarithm, is given by

$$\dot{\underline{\tilde{\boldsymbol{y}}}}(t) + \lambda \underline{\tilde{\boldsymbol{y}}}(t) = 0, \tag{3.36}$$

whose solution is $\underline{\tilde{\boldsymbol{y}}}(t) = e^{-\lambda t} \underline{\tilde{\boldsymbol{y}}}(0)$. Therefore,

$$\log \underline{\tilde{\boldsymbol{x}}}(t) = e^{-\lambda t} \log \underline{\tilde{\boldsymbol{x}}}(0) \Longrightarrow \underline{\tilde{\boldsymbol{x}}}(t) = \exp\left\{e^{-\lambda t} \log \underline{\tilde{\boldsymbol{x}}}(0)\right\} = \underline{\tilde{\boldsymbol{x}}}(0)^{\left\{e^{-\lambda t}\right\}},$$

which preserves the DQ unit norm (Adorno, 2011).

3.6 Kinematic and Dynamic Model

This section reviews the kinematic and dynamic modeling of a two-arm robot. First, the forward kinematics of a serial manipulator, using DQ, is presented, followed by the forward kinematics of a two-arm robotic system, and, finally, of a two-arm mobile manipulator. Moreover, the cooperative dual task-space (CDTS) variables are reviewed, which is a way to describe the coordination of a two-arm system using DQ. Then, these variables are related to the internal and external wrenches of a bimanual manipulation task. Finally, the dynamic model of a robot manipulator using the Euler-Lagrange equation, used in

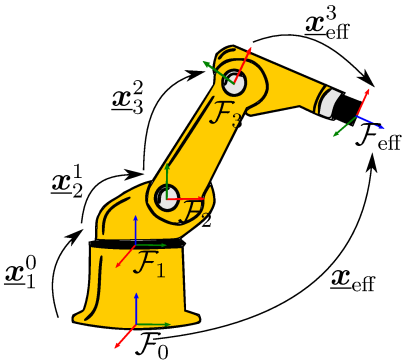

Figure 3.3: Kinematic chain of a robotic arm. The image shows the coordinate system of each joint as well as the transformation of the frame of a joint in relation to the previous one, resulting in the forward kinematics that relates each joint to the effector $\underline{\boldsymbol{x}}_{\text{eff}}$.

many controllers, is presented.

3.6.1 Forward Kinematics

Forward kinematics describes the relationship between each individual joint of the robot and the pose (position and orientation) of the end-effector (Spong et al., 2006). To facilitate this relationship, some conventions can be adopted, such as the standard and modified Denavit-Hartenberg (DH). Once the coordinate system of each joint is defined, the forward kinematics that relates each joint to the end-effector of the kinematic chain can be found.

Given a serial kinematic chain composed of n links, the forward kinematic model (FKM) relates the configuration of the joints to the end-effector pose $\underline{\boldsymbol{x}}_{\text{eff}}$ through the mapping $\underline{\boldsymbol{f}} : \mathbb{R}^n \to \text{Spin}(3) \ltimes \mathbb{R}^3$ such that

$$\underline{\boldsymbol{x}}_{\text{eff}} = \underline{\boldsymbol{f}}\left(\boldsymbol{q}\right), \tag{3.37}$$

where $\boldsymbol{q} = \begin{bmatrix} q_1 & \cdots & q_n \end{bmatrix}^T$ is the vector with the joints' configurations (Adorno, 2011).

Definition 3.2. Considering $\underline{\boldsymbol{x}}_i^{i-1}$ as the unit DQ representing the pose of the frame in the i-th joint related to the one in the $(i-1)$-th joint, the end-effector pose $\underline{\boldsymbol{x}}_{\text{eff}}$ of a robotic arm of n joints is given by (Adorno, 2011)

$$\underline{\boldsymbol{x}}_{\text{eff}} = \underline{\boldsymbol{x}}_{\text{eff}}^0 = \underline{\boldsymbol{x}}_1^0 \underline{\boldsymbol{x}}_2^1 \ldots \underline{\boldsymbol{x}}_{n-1}^{n-2} \underline{\boldsymbol{x}}_n^{n-1}, \tag{3.38}$$

where $\mathcal{F}_0$ is the base of the kinematic chain, as illustrated in Figure 3.3.

3.6.2 Differential Kinematics

Considering a serial kinematic chain of n links, its differential forward kinematic model (DFKM) is given by

$$\text{vec}_8\, \dot{\underline{\boldsymbol{x}}}_{\text{eff}} = \boldsymbol{J}(\boldsymbol{q})\, \dot{\boldsymbol{q}}, \tag{3.39}$$

where $\mathbb{R}^{8\times n} \ni \boldsymbol{J}(\boldsymbol{q}) \triangleq \frac{\partial\, \text{vec}_8\, \underline{\boldsymbol{f}}(\boldsymbol{q})}{\partial \boldsymbol{q}}$ is the analytical Jacobian matrix algebraically derived (Adorno, 2011). Equation (3.39) relates the generalized velocity of the end-effector $\dot{\underline{\boldsymbol{x}}}_{\text{eff}}$ with the velocity of the joints $\dot{\boldsymbol{q}}$.

Moreover, the second order differential kinematics is given by

$$\text{vec}_8\, \ddot{\underline{\boldsymbol{x}}}_{\text{eff}} = \dot{\boldsymbol{J}}(\boldsymbol{q})\, \dot{\boldsymbol{q}} + \boldsymbol{J}(\boldsymbol{q})\, \ddot{\boldsymbol{q}}, \tag{3.40}$$

where $\mathbb{R}^{8\times n} \ni \dot{\boldsymbol{J}}(\boldsymbol{q}) \triangleq \frac{d\boldsymbol{J}(\boldsymbol{q})}{dt}$ is the first order time derivative of the Jacobian matrix.

3.6.3 Cooperative Dual Task-Space

The CDTS was proposed by Adorno et al. (2010) in order to facilitate the bimanual manipulation of robots, being based on the work of Chiacchio et al. (1996). Adorno et al. (2010) propose two variables for this cooperative space, denominated cooperative relative variable and cooperative absolute variable.

Consider two kinematic chains such that $\underline{\boldsymbol{x}}_{\text{right}}$ and $\underline{\boldsymbol{x}}_{\text{left}}$ are the end-effector poses of the right and left chains, respectively, with respect to a common reference. The relative variable $\underline{\boldsymbol{x}}_{\text{rel}}$ is the pose of the left end-effector with respect to the right one, and the absolute variable $\underline{\boldsymbol{x}}_{\text{abs}}$ is the pose represented by a frame located in the middle of the two end-effectors, corresponding to half of the transformation from one to the other. Both variables are formally described by

$$\underline{\boldsymbol{x}}_{\text{rel}} \triangleq \underline{\boldsymbol{x}}^{*}_{\text{right}} \underline{\boldsymbol{x}}_{\text{left}}, \tag{3.41}$$

$$\underline{\boldsymbol{x}}_{\text{abs}} \triangleq \underline{\boldsymbol{x}}_{\text{right}} \underline{\boldsymbol{x}}^{\{1/2\}}_{\text{rel}} \tag{3.42}$$

where $\underline{\boldsymbol{x}}^{\{1/2\}}_{\text{rel}}$ is the transformation corresponding to half of the rotation of the angle θ_{rel} around the $\boldsymbol{n}_{\text{rel}}$ axis of the quaternion $\mathcal{P}(\underline{\boldsymbol{x}}_{\text{rel}}) = \cos(\theta_{\text{rel}}/2) + \boldsymbol{n}_{\text{rel}} \sin(\theta_{\text{rel}}/2)$ and half of the translation from the right to the left end-effector $\boldsymbol{p}^{\text{right}}_{\text{right,left}}$. Figure 3.4 illustrates both cooperative variables $\underline{\boldsymbol{x}}_{\text{rel}}$ and $\underline{\boldsymbol{x}}_{\text{abs}}$.

Similarly to Equation (3.39), the derivative of the relative variable is given by (Adorno

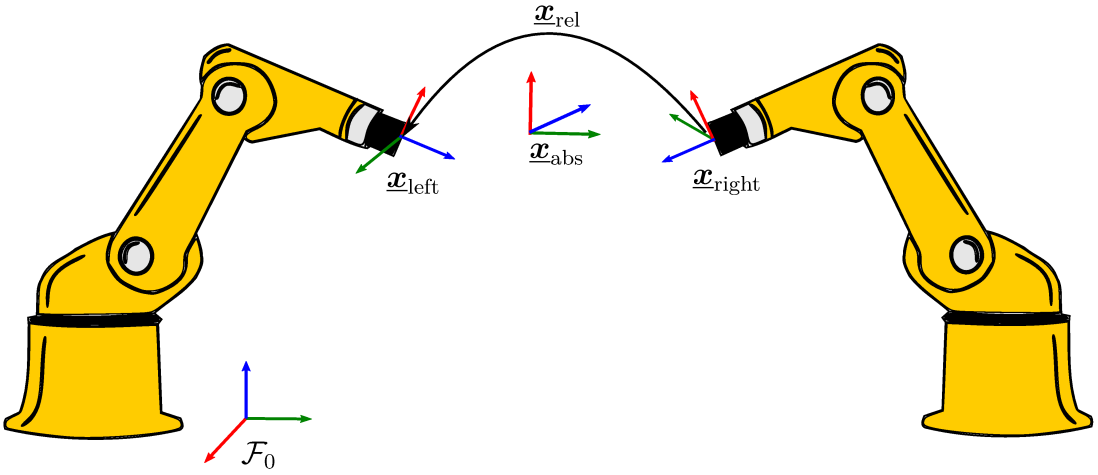

Figure 3.4: Representation of the cooperative dual task-space. The variables $\underline{\boldsymbol{x}}_{\text{rel}}$ and $\underline{\boldsymbol{x}}_{\text{abs}}$ represent the relative and absolute poses, respectively.

et al., 2010)

$$\text{vec}_8\, \dot{\underline{\boldsymbol{x}}}_{\text{rel}} = \boldsymbol{J}_{\text{rel}}\left(\boldsymbol{q}_{\text{arms}}\right) \dot{\boldsymbol{q}}_{\text{arms}}, \tag{3.43}$$

where $\mathbb{R}^{8\times\left(\dim\left(\boldsymbol{q}_{\text{right}}\right)+\dim\left(\boldsymbol{q}_{\text{left}}\right)\right)} \ni \boldsymbol{J}_{\text{rel}}\left(\boldsymbol{q}_{\text{arms}}\right) \triangleq \frac{\partial\, \text{vec}_8\, \underline{\boldsymbol{x}}_{\text{rel}}}{\partial \boldsymbol{q}_{\text{arms}}}$ is the Jacobian matrix related to the relative variable, and $\boldsymbol{q}_{\text{arms}} = \begin{bmatrix}\boldsymbol{q}_{\text{right}}^T & \boldsymbol{q}_{\text{left}}^T\end{bmatrix}^T$, with $\boldsymbol{q}_{\text{right}}$ and $\boldsymbol{q}_{\text{left}}$ being the right and left arm joints, respectively.

Analogously, the DFKM for $\underline{\boldsymbol{x}}_{\text{abs}}$ is

$$\text{vec}_8\, \dot{\underline{\boldsymbol{x}}}_{\text{abs}} = \boldsymbol{J}_{\text{abs}}\left(\boldsymbol{q}_{\text{arms}}\right) \dot{\boldsymbol{q}}_{\text{arms}},$$

where $\mathbb{R}^{8\times\left(\dim\left(\boldsymbol{q}_{\text{right}}\right)+\dim\left(\boldsymbol{q}_{\text{left}}\right)\right)} \ni \boldsymbol{J}_{\text{abs}}\left(\boldsymbol{q}_{\text{arms}}\right) \triangleq \frac{\partial\, \text{vec}_8\, \underline{\boldsymbol{x}}_{\text{abs}}}{\partial \boldsymbol{q}_{\text{arms}}}$ is the Jacobian matrix related to the absolute variable (Adorno et al., 2010).

The main advantage of using the CDTS is that the motion of two kinematic chains working cooperatively can be described by only two variables (Adorno et al., 2010). Furthermore, the control laws using the CDTS take in consideration the whole robot kinematic chain, and the two cooperative variables offer an abstraction whose focus is the bimanual manipulation.

3.6.4 Mobile Base Kinematic Model

A holonomic mobile base can be parameterized as $\boldsymbol{q}_{\text{base}} = \begin{bmatrix}x & y & \phi\end{bmatrix}^T$ (see Figure 3.5), which means that its pose can be represented as a function of the Cartesian coordinates (x, y) and the angle ϕ of the base as (Adorno, 2011)

$$\underline{\boldsymbol{x}}_{\text{base}} = \boldsymbol{r}_{\text{base}} + \frac{1}{2}\varepsilon \boldsymbol{p}_{\text{base}} \boldsymbol{r}_{\text{base}}, \tag{3.44}$$

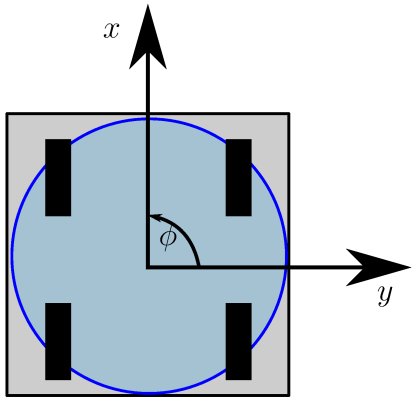

Figure 3.5: Holonomic mobile base, which can be represented as a function of the Cartesian coordinates (x, y) and the angle ϕ of the base.

with $\boldsymbol{p}_{\text{base}} = \hat{\imath}x + \hat{\jmath}y$ and $\boldsymbol{r}_{\text{base}} = \cos(\phi/2) + \hat{k}\sin(\phi/2)$. Thus, the FKM of the mobile base is given by

$$\text{vec}_8\, \dot{\underline{\boldsymbol{x}}}_{\text{base}} = \boldsymbol{J}_{\text{base}}(\boldsymbol{q}_{\text{base}})\, \dot{\boldsymbol{q}}_{\text{base}}, \tag{3.45}$$

where

$$\boldsymbol{J}_{\text{base}}(\boldsymbol{q}_{\text{base}}) = \begin{bmatrix} 0 & 0 & -\frac{1}{2}\sin\frac{\phi}{2} \\ 0 & 0 & 0 \\ 0 & 0 & 0 \\ 0 & 0 & \frac{1}{2}\cos\frac{\phi}{2} \\ 0 & 0 & 0 \\ \frac{1}{2}\cos\frac{\phi}{2} & \frac{1}{2}\sin\frac{\phi}{2} & \frac{1}{4}\left(-x\sin\frac{\phi}{2} + y\cos\frac{\phi}{2}\right) \\ -\frac{1}{2}\sin\frac{\phi}{2} & \frac{1}{2}\cos\frac{\phi}{2} & \frac{1}{4}\left(x\cos\frac{\phi}{2} - y\sin\frac{\phi}{2}\right) \\ 0 & 0 & 0 \end{bmatrix}$$

is the Jacobian matrix of the base (Adorno, 2011).

3.6.5 Whole-Body Kinematic Model of Bimanual Mobile Robots

Bimanual mobile manipulators consist of a two-arm robot manipulator attached to a mobile base. One example of bimanual mobile robot is BAZAR, which is the robot used in the simulations performed for this thesis. The BAZAR (Bimanual Agile Zany Anthorpomorphic Robot) platform shown in Figure 3.6 was designed at LIRMM,[3] in France, and is composed of two Kuka LWR4+ arms, a Neobotix MPO700 mobile base, Shadow

[3]Laboratoire d'Informatique, de Robotique et de Microélectronique de Montpellier (LIRMM) http://www.lirmm.fr/

Figure 3.6: BAZAR robot.[4]

Hands, and cameras (Navarro et al., 2017). This robot has been used in the European Project H2020 VERSATILE (2017- 2020) to address the industrial case studies proposed by PSA Peugeot Citroën, Airbus, and BIC, and is provided with the last generation of sensors and actuators.

Since BAZAR does not have an articulated torso, the whole-body model is presented here without considering it. Moreover, although BAZAR is equipped with a Neobotix MPO 700, which is an omni-directional non-holonomic mobile base with four steerable wheels, its internal controller can receive a control signal of type $\dot{\boldsymbol{q}}_{\text{base}} = \begin{bmatrix} \dot{x} & \dot{y} & \dot{\phi} \end{bmatrix}^T$, which allows us to control it in a high level, considering it as a holonomic base.

Considering the robot as a holonomic mobile base with two robot manipulators attached to it, three limbs need to be modeled. Each limb can be considered as an independent kinematic chain (Adorno, 2011). Thus, the FKM and the DFKM of each arm is given by Equations (3.38) and (3.39), respectively, and for the base is given by Equations (3.44) and (3.45). With the FKM and the DFKM of each limb, two or more limbs can be serialized with the objective of unify them as a single body, using all DOF available in the combination of the multiple kinematic chains.

Considering the whole-body, that is, the base and the two arms, the serialization is done with the absolute variable, as shown in Figure 3.7, which yields (Adorno, 2011)

$$\underline{\boldsymbol{x}}_{\text{ba}} = \underline{\boldsymbol{x}}_{\text{base}} \underline{\boldsymbol{x}}_{\text{abs}}^{\text{base}}, \tag{3.46}$$

[4]Source: (Navarro et al., 2017)

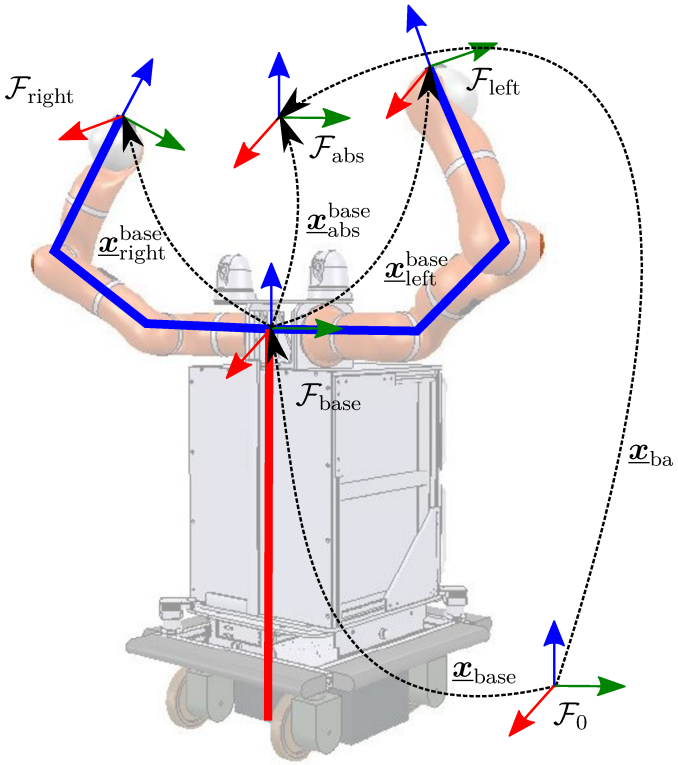

Figure 3.7: Serialization of the mobile base and both arms of the robot, using for this the absolute variable.

and

$$\operatorname{vec}_8 \dot{\underline{\boldsymbol{x}}}_{\text{ba}} = \underbrace{\left[\bar{\boldsymbol{H}}_8\left(\underline{\boldsymbol{x}}^{\text{base}}_{\text{abs}}\right)\boldsymbol{J}_{\text{base}}\left(\boldsymbol{q}_{\text{base}}\right) \;\vdots\; \overset{+}{\boldsymbol{H}}_8\left(\underline{\boldsymbol{x}}_{\text{base}}\right)\boldsymbol{J}^{\text{base}}_{\text{abs}}\left(\boldsymbol{q}_{\text{abs}}\right)\right]}_{\boldsymbol{J}_{\text{ba}}(\boldsymbol{q}_{\text{wb}})}\dot{\boldsymbol{q}}_{\text{wb}} \tag{3.47}$$

with $\boldsymbol{J}_{\text{ba}}\left(\boldsymbol{q}_{\text{wb}}\right) \in \mathbb{R}^{8\times\left(\dim(\boldsymbol{q}_{\text{base}})+\dim\left(\boldsymbol{q}_{\text{right}}\right)+\dim(\boldsymbol{q}_{\text{left}})\right)}$ being the whole-body Jacobian matrix and $\boldsymbol{q}_{\text{wb}} = \begin{bmatrix}\boldsymbol{q}^T_{\text{base}} & \boldsymbol{q}^T_{\text{arms}}\end{bmatrix}^T$ is the joint vector of the whole-body.

3.6.6 Wrenches in the Cooperative Dual Task-Space

In bimanual manipulation of objects, the uncertainties in the object and/or the robot geometries can lead to undesirable forces and moments that do not contribute to the movement of the object, and therefore are called internal forces (Uchiyama & Dauchez, 1988). Suppose, for example, a bimanual manipulator holding a rigid object. In this situation there is a constraint imposed by the object that is given by

$$d\left(\boldsymbol{x}_{\text{eff}_1} - \boldsymbol{x}_{\text{eff}_2}\right) = \text{const.}, \tag{3.48}$$

where $\boldsymbol{x}_{\text{eff}_1}$ and $\boldsymbol{x}_{\text{eff}_2}$ are the poses of the end-effector 1 and 2, respectively, and $d\left(\boldsymbol{x}_{\text{eff}_1} - \boldsymbol{x}_{\text{eff}_2}\right)$ is a distance function between them. If this constraint is not obeyed, internal forces appear

(Erhart et al., 2013). The constraint of Equation (3.48) also arises when the object is firmly grasped by humans and robots, as illustrated by Figure 3.8.

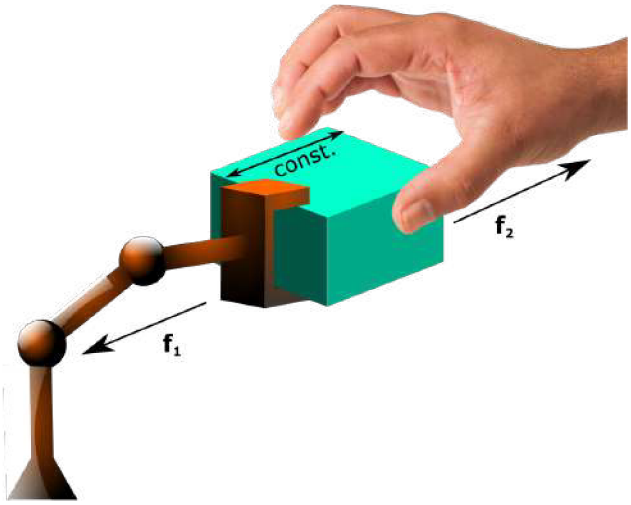

Figure 3.8: Human and robotic arm manipulating a common object. If $\boldsymbol{f}_1 = -\boldsymbol{f}_2$, there is no motion but the object will suffer an internal stress.

Therefore, when considering bimanual manipulation of an object it is necessary to treat not only external forces and moments but also internal ones. In this context, consider $\underline{\boldsymbol{\varsigma}}^{\mathrm{eff}_i}_{\mathrm{eff}_i,\mathrm{eff}_i}$ the wrench applied on the i-th end-effector with respect to the same frame $\mathcal{F}_{\mathrm{eff}_i}$. The wrench $\underline{\boldsymbol{\psi}}^{\mathrm{abs}}_{\mathrm{abs},\mathrm{eff}_i} \triangleq \underline{\boldsymbol{\varsigma}}^{\mathrm{abs}}_{\mathrm{abs},\mathrm{eff}_i}$ acting on the absolute reference frame $\mathcal{F}_{\mathrm{abs}}$ due to the i-th end-effector is given by

$$\underline{\boldsymbol{\psi}}^{\mathrm{abs}}_{\mathrm{abs},\mathrm{eff}_i} = \mathrm{Ad}\left(\underline{\boldsymbol{x}}^{\mathrm{abs}}_{\mathrm{eff}_i}\right) \underline{\boldsymbol{\varsigma}}^{\mathrm{eff}_i}_{\mathrm{eff}_i,\mathrm{eff}_i}. \tag{3.49}$$

This transformation is equivalent to the idea of the "virtual stick" proposed by Uchiyama & Dauchez (1988), and discussed in section 2.1.1.1.

Transformations like Equation (3.49) can be also used to transform the measured wrench to any other reference frame. For instance, following Equation (3.32), the wrench acting on the inertia reference frame $\mathcal{F}_0$ and with respect to this frame $\mathcal{F}_0$ is given by

$$\underline{\boldsymbol{\psi}}^{0}_{0,\mathrm{eff}_i} = \mathrm{Ad}\left(\underline{\boldsymbol{x}}^{0}_{\mathrm{abs}}\right) \underline{\boldsymbol{\psi}}^{\mathrm{abs}}_{\mathrm{abs},\mathrm{eff}_i}.$$

Thus, the external wrench with respect to the inertia reference frame is given by (Adorno, 2011)

$$\underline{\boldsymbol{\psi}}^{0}_{\mathrm{ext}} = \underline{\boldsymbol{\psi}}^{0}_{0,\mathrm{eff}_1} + \underline{\boldsymbol{\psi}}^{0}_{0,\mathrm{eff}_2}, \tag{3.50}$$

and the internal wrench is given by

$$\underline{\boldsymbol{\psi}}^{0}_{\mathrm{int}} = \frac{1}{2}\left(\underline{\boldsymbol{\psi}}^{0}_{0,\mathrm{eff}_1} - \underline{\boldsymbol{\psi}}^{0}_{0,\mathrm{eff}_2}\right). \tag{3.51}$$

3.6.7 Dynamic Model

The derivation of the dynamic model has a key role in simulation of robot motion, as well as in the design of control laws that take into account the inertial parameters of the system (Siciliano et al., 2009). Both Euler-Lagrange equations and the Newton-Euler formulation (Spong et al., 2006) are methods that model the dynamic of a robot and lead to the same final torque applied in the robot's joints. Although the second one has a recursive algorithm, most of the control laws are designed based on the Euler-Lagrange equation. Therefore, the Euler-Lagrange equation is used in the present text.

The dynamic model of a n-link serial manipulator using the Euler-Lagrange equation is given by (Spong et al., 2006)

$$\boldsymbol{M}(\boldsymbol{q})\ddot{\boldsymbol{q}} + \boldsymbol{C}(\boldsymbol{q},\dot{\boldsymbol{q}})\dot{\boldsymbol{q}} + \boldsymbol{g}(\boldsymbol{q}) = \boldsymbol{\tau}, \tag{3.52}$$

in which $\boldsymbol{M}(\boldsymbol{q}) \in \mathbb{R}^{n\times n}$ is the inertia matrix, $\boldsymbol{C}(\boldsymbol{q},\dot{\boldsymbol{q}}) \in \mathbb{R}^{n\times n}$ contains the Coriolis and centrifugal terms, $\boldsymbol{g}(\boldsymbol{q}) \in \mathbb{R}^n$ is the gravity vector, $\boldsymbol{q} = \begin{bmatrix} q_1 \cdots & q_n \end{bmatrix}^T$ is the vector of joints configuration, and $\boldsymbol{\tau} \in \mathbb{R}^n$ is the torque applied to the joints.

3.6.7.1 Euler-Lagrange Equation with Actuators' Dynamics

Usually the actuators' dynamics are negligible compared to the dynamics of the rigid multi-link robot (Shen & Featherstone, 2003), hence the inertia matrix usually takes into consideration only the inertia of the links. However, sometimes it is useful to explicitly consider the inertia of the actuators, as they can help in improving the condition number of the resultant inertia matrix.

Considering a robot whose links are connected through revolute joints, and assuming that the motion of each link is transmitted via a set of gears, its kinetic energy is the sum of the kinetic energies of the links and those of the rotors (Kelly et al., 2005; Siciliano et al., 2009); that is,[5]

$$\mathcal{K}\left(\boldsymbol{q},\dot{\boldsymbol{q}},\dot{\boldsymbol{\theta}}\right) = \frac{1}{2}\dot{\boldsymbol{q}}^T\boldsymbol{M}(\boldsymbol{q})\dot{\boldsymbol{q}} + \frac{1}{2}\dot{\boldsymbol{\theta}}^T\boldsymbol{N}\dot{\boldsymbol{\theta}},$$

where $\boldsymbol{N} = \operatorname{diag}(\eta_1,\ldots,\eta_n)$ is a diagonal positive definite matrix, whose elements are the rotors' moments of inertia. When considering just the "spinning" rotor velocity, the angular velocity of the axes after the set of gears is given by $\dot{\boldsymbol{\theta}} = \begin{bmatrix} \vartheta_1\dot{q}_1 & \cdots & \vartheta_n\dot{q}_n \end{bmatrix}$, with ϑ_i being the gear ratio of the i-th actuator. Therefore, the dynamic model that explicitly

[5] In this model, coupling effects between rotors and links are neglected. According to Siciliano et al. (2009), some couplings in joints' dynamics may be reduced or eliminated when designing the structure in order to simplify the control problem. One way of doing that is to choose the motor axis collinear with the joint axis.

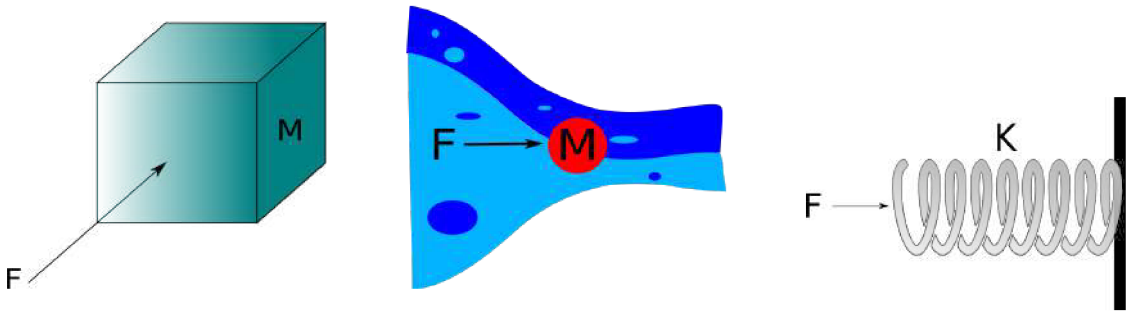

Inertial

$Z(s) = Ms$

Resistive

$Z(s) = Ms + B$

Capacitive

$Z(s) = {}^{K}/_{s}$

Figure 3.9: Mechanical impedance model of each type of environment.

takes into consideration the actuators' inertia is given by

$$[\boldsymbol{M}(\boldsymbol{q}) + \boldsymbol{M}_m]\,\ddot{\boldsymbol{q}} + \boldsymbol{C}(\boldsymbol{q}, \dot{\boldsymbol{q}})\,\dot{\boldsymbol{q}} + \boldsymbol{g}(\boldsymbol{q}) = \boldsymbol{\tau}, \tag{3.53}$$

where $\boldsymbol{M}_m = \text{diag}\,(\eta_1\vartheta_1^2, \ldots, \eta_n\vartheta_n^2)$.

3.7 Mechanical Impedance Model

Impedance is the relationship between the effort and the flow variables (Spong et al., 2006). Thus, considering the effort as the force F and the flow as the velocity V, the impedance in the Laplace domain is given by

$$Z(s) = \frac{F(s)}{V(s)}.$$

Different environments have different impedances. Figure 3.9 shows three types of environments with different impedance.

The impedance equation, in the time domain, of a system considering mass, damper, and spring behavior is given by

$$\boldsymbol{M}\ddot{\boldsymbol{x}} + \boldsymbol{B}\dot{\boldsymbol{x}} + \boldsymbol{K}\boldsymbol{x} = -\boldsymbol{f}, \tag{3.54}$$

where $\boldsymbol{M}$, $\boldsymbol{B}$, $\boldsymbol{K} \in \mathbb{R}^{6\times6}$ are the inertia, damping, and stiffness matrices, respectively, and $\boldsymbol{f} \in \mathbb{R}^6$ is an external wrench. The variable $\boldsymbol{x}$ is the vector with the pose of the object in question, that can be the end-effector of a robot manipulator or the pose of an object, for example. This model will be useful when controlling the interaction forces (both external as internal).

3.8 Conclusion

This chapter presented the basic concepts related to quaternions and DQ, as well as the use of unit DQ to represent rigid motions; and pure DQ to represent twists and wrenches. The use of DQ brings several advantages, and thanks to those advantages, the DQ algebra is used throughout the development of this work, both in the modeling part and in the proposed controllers.

The forward and differential kinematics using DQ were also reviewed in this chapter, including the whole-body kinematic model and a revision of the CDTS, used to facilitate the coordination of two parallel kinematic chains. Moreover, the internal and external wrenches that appears in bimanual manipulation were also related to the cooperative dual task-space. Furthermore, the joint space dynamic model was also described here.

Both kinematic and dynamic models are used to design control laws in order to control manipulators and bimanual mobile manipulators in manipulation tasks, with or without physical human interaction. Regarding this last topic, controlling the impedance of the system is important to avoid harm to any agent involved in the interaction task, which reveals the necessity of revising the mechanical impedance model.

4

Control Strategies

Considering the physical interaction between robots and the environment, the closed-loop behavior should be safe for all involved (Cherubini et al., 2017), whether objects, humans, or even the robot itself, which means that it is crucial to control 1) how the robot responds to the interaction and also 2) its dynamic behavior when moving itself to accomplish a given task.

As seen in Chapter 2, an impedance/admittance controller (Hogan, 1985) is appropriate for a safe interaction (Kimmel & Hirche, 2015), since by controlling the robot apparent impedance we are able to impose a suitable compliant behavior to it (Caccavale et al., 1999, 2008). Moreover, in industrial robot manipulators, admittance controllers are frequently used since those robots are usually characterized by a stiff and non-backdrivable mechanical structure (Landi et al., 2017), in which an admittance controller ensures better performance than impedance controllers (Keemink et al., 2018). Therefore, in order to have a closed-loop control that guarantees a compliant behavior while achieving good end-effector pose accuracy, we propose a control architecture that consists of an admittance controller in the outer-loop that modifies the desired end-effector pose $\underline{\boldsymbol{x}}_d \in \mathrm{Spin}(3) \ltimes \mathbb{R}^3$ according to the external wrench, which is measured at the robot end-effector, and outputs a compliant pose $\underline{\boldsymbol{x}}_c$ that satisfies the desired apparent impedance; and a motion controller in the inner-loop, to track this modified trajectory, as illustrated in Figure 4.1. The design of the proposed admittance controller, which uses the DQ algebra thanks to the advantages mentioned in Chapter 3, as for example the direct use of coefficients of DQ in the proposed control law, is described in this chapter.

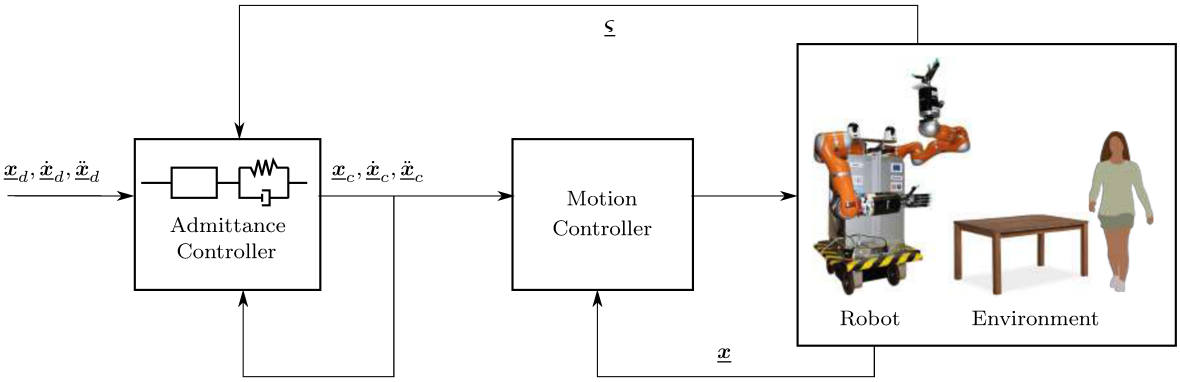

Figure 4.1: Scheme illustrating the control law composed of an outer-loop with an impedance behavior and an-inner loop with a motion controller. The wrench $\underline{\varsigma}$ measured by the force/torque sensor at the robot end-effector is a result of the interaction with the environment.

Depending on how the robot is actuated (position, velocity, or torque) different controllers can be used. For instance, a controller based on its kinematic model or one based on its dynamic model. Considering the first case, a kinematic controller based on the DQ logarithmic mapping is proposed, in which the error definition respects the properties of the unit DQ group. In the second case, the ill-conditioning of the JSIM plays an important role, being related to the robot dynamic behavior, which is also important for safety. Thus, this chapter also shows some motion controllers based on the robot dynamic model, and an adaptive controller to control the end-effector pose while improving the conditioning of the robot inertia matrix is proposed, improving the safety in the manipulation tasks subject to contacts.

4.1 Admittance Controller

An admittance controller regulates the apparent inertia, as well as the damping and stiffness of the robot through the feedback of the interaction wrenches with the environment. Since the idea here is to design an admittance controller using DQ, the definition of an error that obeys the properties of the unit DQ group is important. Since the use of the DQ logarithmic mapping in differential equations allows their solutions to respect those properties (see section 3.5.1), the DQ logarithm is used in the designed controller, namely ACLogOnly.

Given a desired pose $\underline{\boldsymbol{x}}_d \in \mathrm{Spin}(3) \ltimes \mathbb{R}^3$ of a robot end-effector that interacts with the environment, another (compliant) reference frame specified by $\underline{\boldsymbol{x}}_c \in \mathrm{Spin}(3) \ltimes \mathbb{R}^3$ is considered such that a desired apparent impedance can be imposed on the pose displacement between $\underline{\boldsymbol{x}}_d$ and $\underline{\boldsymbol{x}}_c$ (Caccavale et al., 1999). Thus, the desired apparent impedance is achieved by imposing the closed-loop dynamics given by

$$\boldsymbol{M}_d \operatorname{vec}_6 \ddot{\underline{\boldsymbol{y}}}_d^c + \boldsymbol{B}_d \operatorname{vec}_6 \dot{\underline{\boldsymbol{y}}}_d^c + \boldsymbol{K}_d \operatorname{vec}_6 \underline{\boldsymbol{y}}_d^c = -\operatorname{vec}_6 \underline{\varsigma}_{\log}^c, \tag{4.1}$$

where $\boldsymbol{M}_d, \boldsymbol{B}_d, \boldsymbol{K}_d \in \mathbb{R}^{6\times 6}$ are the apparent desired inertia, damping, and stiffness positive definite matrices, $\operatorname{vec}_6 \underline{\boldsymbol{y}}_d^c \triangleq \operatorname{vec}_6 (\log \underline{\boldsymbol{x}}_d^c)$, with $\underline{\boldsymbol{x}}_d^c \triangleq \underline{\boldsymbol{x}}_c^* \underline{\boldsymbol{x}}_d$, and $\operatorname{vec}_6 \underline{\boldsymbol{\varsigma}}_{\log}^c \triangleq \left(\boldsymbol{I}^{\#} \boldsymbol{E}\left(\underline{\boldsymbol{x}}_d^c\right)\right)^T \operatorname{vec}_6 \underline{\boldsymbol{\varsigma}}_{\text{eff,eff}}^c$ is the external generalized wrench, with respect to frame $\mathcal{F}_c$, transformed to be consistent with the logarithmic mapping according to Equation (3.33). Since the wrench $\underline{\boldsymbol{\varsigma}}_{\text{eff,eff}}^{\text{eff}} \in \mathcal{H}_p$ measured by the force/torque sensor at the robot end-effector is given with respect to the end-effector frame, the coordinate transformation to express it in the compliant frame $\mathcal{F}_c$ is given by Equation (3.31). Hence,

$$\underline{\boldsymbol{\varsigma}}_{\text{eff,eff}}^c = \operatorname{Ad}\left(\boldsymbol{r}_{\text{eff}}^c\right) \underline{\boldsymbol{\varsigma}}_{\text{eff,eff}}^{\text{eff}},$$

where $\boldsymbol{r}_{\text{eff}}^c = \boldsymbol{r}_c^* \boldsymbol{r}_{\text{eff}}$, with $\boldsymbol{r}_{\text{eff}} \in \mathbb{S}^3$ being the orientation of the end-effector with respect to a fixed reference frame.

The admittance controller is dual to the impedance controller. As in the former the contact wrench is measured and the controller output is the acceleration, the admittance control law is given by

$$\operatorname{vec}_6 \ddot{\underline{\boldsymbol{y}}}_d^c = \boldsymbol{M}_d^{-1}\left(-\boldsymbol{B}_d \operatorname{vec}_6 \dot{\underline{\boldsymbol{y}}}_d^c - \boldsymbol{K}_d \operatorname{vec}_6 \underline{\boldsymbol{y}}_d^c - \operatorname{vec}_6 \underline{\boldsymbol{\varsigma}}_{\log}^c\right). \tag{4.2}$$

4.1.1 Trajectory Generation

In order to use the admittance control signal $\operatorname{vec}_6 \ddot{\underline{\boldsymbol{y}}}_d^c$ in the inner motion control loop, we first generate the trajectory $\ddot{\underline{\boldsymbol{y}}}_d^c \mapsto \left(\underline{\boldsymbol{x}}_c(t), \dot{\underline{\boldsymbol{x}}}_c(t), \ddot{\underline{\boldsymbol{x}}}_c(t)\right)$ as follows. The displacement $\underline{\boldsymbol{x}}_d^c$ and its first and second time derivatives are found by integrating $\operatorname{vec}_6 \ddot{\underline{\boldsymbol{y}}}_d^c$ twice and using the Equations (3.14) and (3.18), and the exponential of a pure DQ given by Equation (3.10). More specifically,

$$\begin{aligned}
\underline{\boldsymbol{x}}_d^c &= \exp \underline{\boldsymbol{y}}_d^c, \\
\dot{\underline{\boldsymbol{x}}}_d^c &= \underline{\mathbf{vec}}_8\left(\boldsymbol{Q}_8\left(\underline{\boldsymbol{x}}_d^c\right) \operatorname{vec}_6 \dot{\underline{\boldsymbol{y}}}_d^c\right), \\
\ddot{\underline{\boldsymbol{x}}}_d^c &= \underline{\mathbf{vec}}_8\left(\dot{\boldsymbol{Q}}_8\left(\underline{\boldsymbol{x}}_d^c\right) \operatorname{vec}_6 \dot{\underline{\boldsymbol{y}}}_d^c + \boldsymbol{Q}_8\left(\underline{\boldsymbol{x}}_d^c\right) \operatorname{vec}_6 \ddot{\underline{\boldsymbol{y}}}_d^c\right).
\end{aligned}$$

Hence, the compliant pose $\underline{\boldsymbol{x}}_c(t)$ and its time derivatives $\dot{\underline{\boldsymbol{x}}}_c(t)$ and $\ddot{\underline{\boldsymbol{x}}}_c(t)$ are given by

$$\underline{\boldsymbol{x}}_c = \underline{\boldsymbol{x}}_d \underline{\boldsymbol{x}}_d^{c*}, \tag{4.3}$$

$$\dot{\underline{\boldsymbol{x}}}_c = \dot{\underline{\boldsymbol{x}}}_d \underline{\boldsymbol{x}}_{\text{d}}^{c*} + \underline{\boldsymbol{x}}_d \dot{\underline{\boldsymbol{x}}}_{\text{d}}^{c*}, \tag{4.4}$$

$$\ddot{\underline{\boldsymbol{x}}}_c = \ddot{\underline{\boldsymbol{x}}}_d \underline{\boldsymbol{x}}_{\text{d}}^{c*} + 2\dot{\underline{\boldsymbol{x}}}_d \dot{\underline{\boldsymbol{x}}}_{\text{d}}^{c*} + \underline{\boldsymbol{x}}_d \ddot{\underline{\boldsymbol{x}}}_{\text{d}}^{c*}. \tag{4.5}$$

Remark 4.1. In the absence of interaction forces, the compliant pose $\underline{\boldsymbol{x}}_c$ is equal to the desired pose $\underline{\boldsymbol{x}}_d$. However, when in contact with the environment, interaction forces appear as a consequence. Hence, in order to keep the desired (apparent) mass, damping, and stiffness matrices of the robot, the pose $\underline{\boldsymbol{x}}_c$ may differ from $\underline{\boldsymbol{x}}_d$.

4.1.2 Physically Meaningful Admittance Controller (ACLog)

Although simple and satisfying the properties of the DQ group, the controller of Equation (4.2) is not the most appropriate, since it presents two known problems:

1. it presents the unwinding phenomenon;
2. its impedance matrices are not proven to have a physical meaning.

Notwithstanding, another controller also using the DQ logarithmic mapping, namely ACLog, is designed with the objective of circumventing these problems. In this case, in order to impose the desired apparent impedance behavior to the robot, an admittance control law that is physically meaningful and a stiffness matrix that is consistent with the task geometry are defined. Similarly to what Caccavale et al. (1999, 2008) have proposed, here we also derive the impedance equation based on the energy of the system, but using elements of the DQ algebra.

Consider a desired constant positive definite inertia matrix $\boldsymbol{M}_d = \operatorname{diag}\left(\boldsymbol{\mathcal{I}}^c_{3\times3}, m\boldsymbol{I}^c_{3\times3}\right)$, where m is the mass and $\boldsymbol{\mathcal{I}}^c_{3\times3} \in \mathbb{R}^{3\times3}$ is the inertia tensor. Let us assume that the kinetic energy of the desired closed-loop system is given by

$$\mathcal{K} = \frac{1}{2}\left(\operatorname{vec}_6 \underline{\boldsymbol{\zeta}}^c_{cd}\right)^T \boldsymbol{M}_d \operatorname{vec}_6 \underline{\boldsymbol{\zeta}}^c_{cd}, \tag{4.6}$$

where $\underline{\boldsymbol{\zeta}}^c_{cd} = \boldsymbol{\omega}^c_{cd} + \varepsilon \boldsymbol{v}^c_{cd}$ is the DQ containing the angular and linear velocities from frame $\mathcal{F}_c$ to $\mathcal{F}_d$, with respect to frame $\mathcal{F}_c$.

To obtain the power, one can take the time derivative of Equation (4.6), which is given by

$$\dot{\mathcal{K}} = \left(\operatorname{vec}_6 \underline{\boldsymbol{\zeta}}^c_{cd}\right)^T \boldsymbol{I}^{\#} \operatorname{vec}_6 \underline{\boldsymbol{\varsigma}}^c_I, \tag{4.7}$$

where

$$\operatorname{vec}_6 \underline{\boldsymbol{\varsigma}}^c_I \triangleq \boldsymbol{I}^{\#} \boldsymbol{M}_d \operatorname{vec}_6 \dot{\underline{\boldsymbol{\zeta}}}^c_{cd} \tag{4.8}$$

is the inertial wrench with respect to the frame $\mathcal{F}_c$.

A dissipative damping wrench is also considered, given by

$$\operatorname{vec}_6 \underline{\boldsymbol{\varsigma}}^c_D \triangleq \boldsymbol{I}^{\#} \boldsymbol{B}_d \operatorname{vec}_6 \underline{\boldsymbol{\zeta}}^c_{cd}, \tag{4.9}$$

with $\mathbb{R}^{6\times6} \ni \boldsymbol{B}_d > 0$.

Now a special attention is given to the stiffness matrix regarding geometric consistency. Considering a positive definite stiffness matrix $\boldsymbol{K} \in \mathbb{R}^{6\times6}$, it can be decomposed as $\boldsymbol{K} = \boldsymbol{U}\boldsymbol{\Gamma}\boldsymbol{U}^T$ (Chen, 1999), with $\boldsymbol{\Gamma} = \operatorname{diag}(\gamma_1, \cdots, \gamma_6)$ in which γ_i, with $i \in \{1, \ldots, 6\}$ represent the stiffnesses along the principal axes $\boldsymbol{u}_i$, which are the column vectors of the orthogonal matrix $\boldsymbol{U} \in \mathrm{O}(6)$. Therefore, the stiffness matrix can be specified with respect

to a frame with the origin at the center of stiffness (i.e., the equilibrium point when there is no deformation), in terms of the stiffness parameters γ_i and principal axes $\boldsymbol{u}_i$ (Caccavale et al., 2008).

Furthermore, the potential energy function of an ideal stiffness depends only on the relative pose of the two attached bodies and is port symmetric (Caccavale et al., 2008), which means that the potential energy is the same whether seen from either $\mathcal{F}_c$ or $\mathcal{F}_d$. Considering the positive definite matrices $\boldsymbol{K}_\phi \in \mathbb{R}^{3\times3}$ and $\boldsymbol{K}_p \in \mathbb{R}^{3\times3}$ that represent the rotational and translational stiffness matrices, respectively, and that there is no coupling between translation and rotation, the elastic potential energy is given by

$$\mathcal{U} = \left(\operatorname{vec}_6 \underline{\boldsymbol{y}}_d^c\right)^T \boldsymbol{K}_d \operatorname{vec}_6 \underline{\boldsymbol{y}}_d^c, \tag{4.10}$$

with $\boldsymbol{K}_d = 2\text{blk}\operatorname{diag}\left(\boldsymbol{K}_\phi, \boldsymbol{K}'_p\right)$, where[1]

$$\boldsymbol{K}'_p \triangleq \frac{1}{2}\boldsymbol{K}_p + \frac{1}{2}\boldsymbol{R}_d^c \boldsymbol{K}_p \boldsymbol{R}_d^{cT}, \tag{4.11}$$

with $\boldsymbol{R}_d^c = \bar{\boldsymbol{I}}\overset{+}{\boldsymbol{H}}_4\left(\boldsymbol{r}_d^c\right)\bar{\boldsymbol{H}}_4\left(\boldsymbol{r}_d^{c*}\right)\bar{\boldsymbol{I}}^T$ (Lemma C.2) being the rotation matrix from frame $\mathcal{F}_c$ to $\mathcal{F}_d$, which guarantees that the potential energy is port symmetric (see Lemma C.4).

Deriving Equation (4.10), the power is given by[2]

$$\dot{\mathcal{U}} = 2\left(\operatorname{vec}_6 \dot{\underline{\boldsymbol{y}}}_d^c\right)^T \boldsymbol{K}_d \operatorname{vec}_6 \underline{\boldsymbol{y}}_d^c + 2\left(\operatorname{vec}_6 \underline{\boldsymbol{y}}_d^c\right)^T \frac{\dot{\boldsymbol{K}}_d}{2} \operatorname{vec}_6 \underline{\boldsymbol{y}}_d^c, \tag{4.12}$$

where

$$\frac{\dot{\boldsymbol{K}}_d}{2} = \begin{bmatrix} \boldsymbol{0}_{3\times3} & \boldsymbol{0}_{3\times3} \\ \boldsymbol{0}_{3\times3} & \dot{\boldsymbol{R}}_d^c \boldsymbol{K}_p \boldsymbol{R}_d^{cT} \end{bmatrix}.$$

Using Equation (3.19) in Equation (4.12) yields

$$\begin{aligned}\dot{\mathcal{U}} &= 2\left(\boldsymbol{E}^{-1}(\underline{\boldsymbol{x}}_d^c)\operatorname{vec}_6 \underline{\boldsymbol{\zeta}}_{cd}^c\right)^T \boldsymbol{K}_d \operatorname{vec}_6 \underline{\boldsymbol{y}}_d^c + 2\left(\operatorname{vec}_6 \underline{\boldsymbol{y}}_d^c\right)^T \frac{\dot{\boldsymbol{K}}_d}{2} \operatorname{vec}_6 \underline{\boldsymbol{y}}_d^c \\ &= 2\left\{\left(\operatorname{vec}_6 \underline{\boldsymbol{\zeta}}_{cd}^c\right)^T \boldsymbol{E}^{-T}(\underline{\boldsymbol{x}}_d^c)\boldsymbol{K}_d + \left(\operatorname{vec}_6 \underline{\boldsymbol{y}}_d^c\right)^T \frac{\dot{\boldsymbol{K}}_d}{2}\right\} \operatorname{vec}_6 \underline{\boldsymbol{y}}_d^c.\end{aligned}$$

Since $\operatorname{vec}_6 \underline{\boldsymbol{y}}_d^c = \begin{bmatrix}\left(\operatorname{vec}_3 \frac{\boldsymbol{n}_{cd}^c \phi}{2}\right)^T & \left(\operatorname{vec}_3 \frac{\boldsymbol{p}_{cd}^c}{2}\right)^T\end{bmatrix}^T$ and using the fact that $\dot{\boldsymbol{R}}_d^c = \boldsymbol{S}\left(\operatorname{vec}_3 \boldsymbol{\omega}_{cd}^c\right)\boldsymbol{R}_d^c$

[1] This transformation is only needed for translation because $\log \boldsymbol{r}_d^c = -\log \boldsymbol{r}_c^d$, but $\log \underline{\boldsymbol{x}}_d^c \neq -\log \underline{\boldsymbol{x}}_c^d$.

[2] It can be verified by direct calculation that $\dot{\boldsymbol{R}}_d^c \boldsymbol{K}_p \boldsymbol{R}_d^{cT}$ is a symmetric matrix.

(Spong et al., 2006), we obtain

$$\dot{\mathcal{U}} = 2\left\{\left(\operatorname{vec}_6 \underline{\boldsymbol{\zeta}}^c_{cd}\right)^T \boldsymbol{E}^{-T}(\underline{\boldsymbol{x}}^c_d)\boldsymbol{K}_d + \begin{bmatrix}\mathbf{0}_{1\times 3} & \left(\operatorname{vec}_3 \frac{\boldsymbol{p}^c_{cd}}{2}\right)^T \boldsymbol{S}\left(\operatorname{vec}_3 \boldsymbol{\omega}^c_{cd}\right)\boldsymbol{R}^c_d\boldsymbol{K}_p\boldsymbol{R}^{cT}_d\end{bmatrix}\right\}\operatorname{vec}_6 \underline{\boldsymbol{y}}^c_d.$$

As

$$\left(\operatorname{vec}_3 \frac{\boldsymbol{p}^c_{cd}}{2}\right)^T \boldsymbol{S}\left(\boldsymbol{\omega}^c_{cd}\right) = -\left(\operatorname{vec}_3 \frac{\boldsymbol{\omega}^c_{cd}}{2}\right)^T \boldsymbol{S}\left(\operatorname{vec}_3 \boldsymbol{p}^c_{cd}\right) = \left(\operatorname{vec}_3 \frac{\boldsymbol{\omega}^c_{cd}}{2}\right)^T \boldsymbol{S}^T\left(\operatorname{vec}_3 \boldsymbol{p}^c_{cd}\right),$$

thus

$$\begin{aligned}\dot{\mathcal{U}} &= 2\left\{\left(\operatorname{vec}_6 \underline{\boldsymbol{\zeta}}^c_{cd}\right)^T \boldsymbol{E}^{-T}(\underline{\boldsymbol{x}}^c_d)\boldsymbol{K}_d + \begin{bmatrix}\mathbf{0}_{1\times 3} & \left(\operatorname{vec}_3 \boldsymbol{\omega}^c_{cd}/2\right)^T \boldsymbol{S}^T\left(\operatorname{vec}_3 \boldsymbol{p}^c_{cd}\right)\boldsymbol{R}^c_d\boldsymbol{K}_p\boldsymbol{R}^{cT}_d\end{bmatrix}\right\}\operatorname{vec}_6 \underline{\boldsymbol{y}}^c_d \\ &= 2\left\{\left(\operatorname{vec}_6 \underline{\boldsymbol{\zeta}}^c_{cd}\right)^T \boldsymbol{E}^{-T}(\underline{\boldsymbol{x}}^c_d)\boldsymbol{K}_d + \left(\operatorname{vec}_6 \underline{\boldsymbol{\zeta}}^c_{cd}\right)^T \begin{bmatrix}\mathbf{0}_{3\times 3} & \frac{1}{2}\boldsymbol{K}''_p \\ \mathbf{0}_{3\times 3} & \mathbf{0}_{3\times 3}\end{bmatrix}\right\}\operatorname{vec}_6 \underline{\boldsymbol{y}}^c_d,\end{aligned}$$

with

$$\boldsymbol{K}''_p = \boldsymbol{S}^T\left(\operatorname{vec}_3 \boldsymbol{p}^c_{cd}\right)\boldsymbol{R}^c_d\boldsymbol{K}_p\boldsymbol{R}^{cT}_d, \tag{4.13}$$

and therefore

$$\dot{\mathcal{U}} = \left(\operatorname{vec}_6 \underline{\boldsymbol{\zeta}}^c_{cd}\right)^T \left\{\boldsymbol{E}^{-T}\left(\underline{\boldsymbol{x}}^c_d\right)2\boldsymbol{K}_d + \begin{bmatrix}\mathbf{0}_{3\times 3} & \boldsymbol{K}''_p \\ \mathbf{0}_{3\times 3} & \mathbf{0}_{3\times 3}\end{bmatrix}\right\}\operatorname{vec}_6 \underline{\boldsymbol{y}}^c_d. \tag{4.14}$$

Substituting Equation (3.21) in Equation (4.14) yields

$$\dot{\mathcal{U}} = \left(\operatorname{vec}_6 \underline{\boldsymbol{\zeta}}^c_{cd}\right)^T \boldsymbol{I}^{\#}\operatorname{vec}_6 \underline{\boldsymbol{\varsigma}}^c_E, \tag{4.15}$$

where

$$\operatorname{vec}_6 \underline{\boldsymbol{\varsigma}}^c_E \triangleq \boldsymbol{I}^{\#}\boldsymbol{K}'_d \operatorname{vec}_6 \underline{\boldsymbol{y}}^c_d \tag{4.16}$$

is the elastic wrench with respect to $\mathcal{F}_c$, with

$$\boldsymbol{K}'_d = \begin{bmatrix}\boldsymbol{K}'_\phi & \boldsymbol{K}''_p \\ \mathbf{0}_{3\times 3} & 2\boldsymbol{K}'_p\end{bmatrix}, \tag{4.17}$$

where

$$\boldsymbol{K}'_\phi = 2\bar{\boldsymbol{I}}\bar{\boldsymbol{H}}_4\left(\boldsymbol{r}^{c*}_d\right)\boldsymbol{Q}^{+T}_4\left(\boldsymbol{r}^c_d\right)\boldsymbol{K}_\phi. \tag{4.18}$$

Hence, using Equations (4.8), (4.9), and (4.16), the impedance equation is given by

$\operatorname{vec}_6 \underline{\boldsymbol{\varsigma}}_I^c + \operatorname{vec}_6 \underline{\boldsymbol{\varsigma}}_D^c + \operatorname{vec}_6 \underline{\boldsymbol{\varsigma}}_E^c = -\operatorname{vec}_6 \underline{\boldsymbol{\varsigma}}_{\text{eff,eff}}^c$, which leads to

$$\boldsymbol{M}_d \operatorname{vec}_6 \dot{\underline{\boldsymbol{\zeta}}}_{cd}^c + \boldsymbol{B}_d \operatorname{vec}_6 \underline{\boldsymbol{\zeta}}_{cd}^c + \boldsymbol{K}'_d \operatorname{vec}_6 \underline{\boldsymbol{y}}_d^c = -\boldsymbol{I}^{\#} \operatorname{vec}_6 \underline{\boldsymbol{\varsigma}}_{\text{eff,eff}}^c, \tag{4.19}$$

where $\underline{\boldsymbol{\varsigma}}_{\text{eff,eff}}^c = \operatorname{Ad}(\boldsymbol{r}_c^*)\, \underline{\boldsymbol{\varsigma}}_{\text{eff,eff}}$ is the external wrench acting on the robot end-effector expressed with reference to $\mathcal{F}_c$.

The dual of the impedance equation is the admittance equation (Hogan, 1985), which is given by

$$\operatorname{vec}_6 \dot{\underline{\boldsymbol{\zeta}}}_{cd}^c = \boldsymbol{M}_d^{-1} \left(-\boldsymbol{I}^{\#} \operatorname{vec}_6 \underline{\boldsymbol{\varsigma}}_{\text{eff,eff}}^c - \boldsymbol{B}_d \operatorname{vec}_6 \underline{\boldsymbol{\zeta}}_{cd}^c - \boldsymbol{K}'_d \operatorname{vec}_6 \underline{\boldsymbol{y}}_d^c \right). \tag{4.20}$$

Lemma 4.1. *The matrix $\boldsymbol{K}'_d$ in Equation (4.17) is invertible.*

Proof. To prove that $\boldsymbol{K}'_d$ is invertible, it is sufficient to prove that $\boldsymbol{K}'_\phi$ (Equation (4.18)) and $\boldsymbol{K}'_p$ (Equation (4.11)) are full rank. Since $\boldsymbol{K}_p$ is positive definite, then $\boldsymbol{R}_d^c \boldsymbol{K}_p \boldsymbol{R}_d^{cT}$ is also positive definite. Also, the sum of two positive-definite matrices is also positive-definite, therefore $\boldsymbol{K}'_p$ is positive definite and thus has full rank (Chen, 1999). By Equations (4.18) and (3.22), $\boldsymbol{K}'_\phi = 4\boldsymbol{W}^{-T}(\boldsymbol{r}_d^c)\, \boldsymbol{K}_\phi$ and since $\boldsymbol{W}(\boldsymbol{r}_d^c)$ and $\boldsymbol{K}_\phi$ are full rank, so it is $\boldsymbol{K}'_\phi$ (Bernstein, 2009). Hence, the matrix in Equation (4.17) is full rank and thus invertible. □

Theorem 4.1. *Assuming that the inner-loop dynamics is not taken into account (i.e., the inner motion controller accurately tracks the trajectory generated by the admittance controller in the outer-loop) the closed-loop system given by Equation (4.19) is passive mapping from $-\boldsymbol{I}^{\#} \operatorname{vec}_6 \underline{\boldsymbol{\varsigma}}_{\text{eff,eff}}^c$ to $\operatorname{vec}_6 \underline{\boldsymbol{\zeta}}_{cd}^c$, hence stable. Moreover, when in free-motion, the only equilibrium point is given by $\underline{\boldsymbol{y}}_d^c = 0$, which implies that $\underline{\boldsymbol{x}}_c = \underline{\boldsymbol{x}}_d$.*

Proof. Given the Hamiltonian $\mathcal{E} = \mathcal{K} + \mathcal{U} \geq 0$, Equations (4.7), (4.15), and (4.19) are used to obtain

$$\begin{aligned} \dot{\mathcal{E}} &= \dot{\mathcal{K}} + \dot{\mathcal{U}} \\ &= -\left(\operatorname{vec}_6 \underline{\boldsymbol{\zeta}}_{cd}^c\right)^T \boldsymbol{I}^{\#} \operatorname{vec}_6 \underline{\boldsymbol{\varsigma}}_{\text{eff,eff}}^c - \left(\operatorname{vec}_6 \underline{\boldsymbol{\zeta}}_{cd}^c\right)^T \boldsymbol{B}_d \operatorname{vec}_6 \underline{\boldsymbol{\zeta}}_{cd}^c, \end{aligned}$$

where $\mathcal{E}$ is the stored energy, $-\boldsymbol{I}^{\#} \operatorname{vec}_6 \underline{\boldsymbol{\varsigma}}_{\text{eff,eff}}^c$ is the system input, $\operatorname{vec}_6 \underline{\boldsymbol{\zeta}}_{cd}^c$ is the output, and $\left(\operatorname{vec}_6 \underline{\boldsymbol{\zeta}}_{cd}^c\right)^T \boldsymbol{B}_d \operatorname{vec}_6 \underline{\boldsymbol{\zeta}}_{cd}^c \geq 0$. Therefore, the system represents a passive mapping from $-\boldsymbol{I}^{\#} \operatorname{vec}_6 \underline{\boldsymbol{\varsigma}}_{\text{eff,eff}}^c$ to $\operatorname{vec}_6 \underline{\boldsymbol{\zeta}}_{cd}^c$ and is, hence, stable (Slotine & Li, 1991). Moreover, it is dissipative, with the dissipative power given by $\left(\operatorname{vec}_6 \underline{\boldsymbol{\zeta}}_{cd}^c\right)^T \boldsymbol{B}_d \operatorname{vec}_6 \underline{\boldsymbol{\zeta}}_{cd}^c$.

Furthermore, in the case of free motion (i.e., $\operatorname{vec}_6 \underline{\boldsymbol{\varsigma}}_{\text{eff,eff}}^c = \boldsymbol{0}$), $\dot{\mathcal{E}} = 0$ if and only if $\operatorname{vec}_6 \underline{\boldsymbol{\zeta}}_{cd}^c = \boldsymbol{0}$. Also, because the system is dissipative, if $\operatorname{vec}_6 \underline{\boldsymbol{\varsigma}}_{\text{eff,eff}}^c = \boldsymbol{0}$ and $\operatorname{vec}_6 \underline{\boldsymbol{\zeta}}_{cd}^c = \boldsymbol{0}$, then $\operatorname{vec}_6 \dot{\underline{\boldsymbol{\zeta}}}_{cd}^c = \boldsymbol{0}$. Therefore, from Equation (4.19) ,

$$\boldsymbol{K}'_d \operatorname{vec}_6 \underline{\boldsymbol{y}}_d^c = \boldsymbol{0}, \tag{4.21}$$

which implies that $\underline{\boldsymbol{y}}_d^c = 0$ is the only equilibrium point since, by Lemma 4.1, $\boldsymbol{K}'_d$ is invertible. Moreover, $\underline{\boldsymbol{y}}_d^c = 0 \implies \underline{\boldsymbol{x}}_d^c = 1 \implies \underline{\boldsymbol{x}}_c = \underline{\boldsymbol{x}}_d$. □

Remark 4.2. The restriction that $\boldsymbol{K}_p$ and $\boldsymbol{K}_\phi$ are positive-definite matrices can be relaxed so they can be positive semi-definite. In this case, $\boldsymbol{K}'_d$ is not invertible and thus there is a set of infinite stable points that satisfies Equation (4.21). In this case, for some equilibrium points, $\underline{\boldsymbol{x}}_d \neq \underline{\boldsymbol{x}}_c$. For instance, see Example 4.1.

Example 4.1. Consider $\boldsymbol{K}_\phi = 80\boldsymbol{I}_{3\times 3}$ and

$$\boldsymbol{K}_p = \begin{bmatrix} 0 & 0 & 0 \\ 0 & 80 & 0 \\ 0 & 0 & 80 \end{bmatrix},$$

so $\boldsymbol{K}_p$ is a positive semi-definite matrix. Moreover, consider the situation where $\boldsymbol{r}_d^c = 1$, and $\boldsymbol{p}_{cd}^c = 0.1\hat{\imath}$, which gives

$$\underline{\boldsymbol{y}}_d^c = \log\left(\boldsymbol{r}_d^c + \varepsilon\frac{1}{2}\boldsymbol{p}_{cd}^c\boldsymbol{r}_d^c\right) = \log\left(1 + \varepsilon 0.1\hat{\imath}\right) = \varepsilon 0.05\hat{\imath}$$

and thus

$$\operatorname{vec}_6 \underline{\boldsymbol{y}}_d^c = \begin{bmatrix} 0 & 0 & 0 & 0.05 & 0 & 0 \end{bmatrix}^T. \tag{4.22}$$

In this case, $\boldsymbol{K}'_\phi = 2\boldsymbol{K}_\phi$, $\boldsymbol{K}'_p = \boldsymbol{K}_p$, and $\boldsymbol{K}''_p = \boldsymbol{S}^T\left(\operatorname{vec}_3 \boldsymbol{p}_{cd}^c\right)\boldsymbol{K}_p$. Hence,

$$\begin{aligned} \boldsymbol{K}'_d &= \begin{bmatrix} 2\boldsymbol{K}_\phi & \boldsymbol{S}^T\left(\operatorname{vec}_3 \boldsymbol{p}_{cd}^c\right)\boldsymbol{K}_p \\ \boldsymbol{0}_{3\times 3} & 2\boldsymbol{K}_p \end{bmatrix} \\ &= \begin{bmatrix} 160 & 0 & 0 & 0 & 0 & 0 \\ 0 & 160 & 0 & 0 & 0 & 8 \\ 0 & 0 & 160 & 0 & -8 & 0 \\ 0 & 0 & 0 & 0 & 0 & 0 \\ 0 & 0 & 0 & 0 & 160 & 0 \\ 0 & 0 & 0 & 0 & 0 & 160 \end{bmatrix}, \end{aligned} \tag{4.23}$$

which has rank $\boldsymbol{K}'_d = 5$ and thus is not invertible. The multiplication of Equation (4.23) by Equation (4.22) satisfies Equation (4.21), which ensures that the trajectory of the closed-loop system converges to the invariant $\left\{\underline{\boldsymbol{y}}_d^c \in \mathcal{H}_p : \dot{\underline{\boldsymbol{\zeta}}}_{cd}^c = 0\right\}$ even though $\underline{\boldsymbol{y}}_d^c \neq 0$.

4.1.2.1 Unwinding Problem

Although the only equilibrium point is $\underline{\boldsymbol{y}}_d^c = 0 \implies \underline{\boldsymbol{x}}_d^c = 1$, both $\underline{\boldsymbol{x}}_d^c = 1$ and $\underline{\boldsymbol{x}}_d^c = -1$ represent the same pose (Kussaba et al., 2017). Considering the closed-loop of Equation

(4.19), if $\underline{\boldsymbol{x}}_d^c = -1$ the robot will move to reach $\underline{\boldsymbol{x}}_d^c = 1$, which is undesirable (this unnecessary motion is called unwinding). To prevent this situation, a new definition of $\underline{\boldsymbol{y}}_d^c$ is proposed to be used in the impedance equation; that is,

$$\underline{\boldsymbol{y}}_d^c \triangleq \begin{cases} \log \underline{\boldsymbol{x}}_d^c, & \text{if } \left\|\underline{\boldsymbol{x}}_d^c - 1\right\|_2 \leq \left\|\underline{\boldsymbol{x}}_d^c + 1\right\|_2, \\ \log\left(-\underline{\boldsymbol{x}}_d^c\right), & \text{otherwise.} \end{cases} \tag{4.24}$$

Therefore, $\underline{\boldsymbol{y}}_d^c$ is zero when $\underline{\boldsymbol{x}}_d^c = 1$ and $\underline{\boldsymbol{x}}_d^c = -1$, and the closed-loop system trajectories will always follow the smallest spatial distance to the stable points 1 and -1, thus preventing the unwinding problem.

Theorem 4.2. *The closed-loop system given by Equation (4.19), with $\underline{\boldsymbol{y}}_d^c$ defined as in Equation (4.24), is stable. Furthermore, it has two stable equilibrium points: $\underline{\boldsymbol{x}}_d^c$ and $-\underline{\boldsymbol{x}}_d^c$.*

Proof. Considering $\underline{\boldsymbol{y}}_d^c = \log \underline{\boldsymbol{a}}$, by Theorem 4.1 the system is in equilibrium when $\underline{\boldsymbol{a}} = 1$. Since according to Equation (4.24) $\underline{\boldsymbol{a}} \in \underline{\boldsymbol{\mathcal{S}}}$ can be $\underline{\boldsymbol{x}}_d^c$ or $-\underline{\boldsymbol{x}}_d^c$, this means that there are two equilibrium points, $\underline{\boldsymbol{x}}_d^c$ and $-\underline{\boldsymbol{x}}_d^c$, both stable:

Case 1: If $\left\|\underline{\boldsymbol{x}}_d^c - 1\right\|_2 \leq \left\|\underline{\boldsymbol{x}}_d^c + 1\right\|_2$, then $\underline{\boldsymbol{y}}_d^c = \log \underline{\boldsymbol{x}}_d^c$. Therefore, the equilibrium point is given by $\underline{\boldsymbol{y}}_d^c = 0 \implies \underline{\boldsymbol{x}}_d^c = 1$.

Case 2: If $\left\|\underline{\boldsymbol{x}}_d^c - 1\right\|_2 > \left\|\underline{\boldsymbol{x}}_d^c + 1\right\|_2$, then $\underline{\boldsymbol{y}}_d^c = \log\left(-\underline{\boldsymbol{x}}_d^c\right)$. Thus, the equilibrium is achieve when $\underline{\boldsymbol{y}}_d^c = 0 \implies -\underline{\boldsymbol{x}}_d^c = 1$. □

Remark 4.3. The admittance controller requires the use of force/torque sensors at the robot, whether at the end-effector or at the joints. Usually there is a force/torque sensor at the end-effector, and thus the robot only reacts to wrenches applied at it. Notwithstanding, if the robot is equipped with torque sensors at the joints, the joint torques $\boldsymbol{\tau}$ may be projected onto the end-effector by using the well-known relationship $\boldsymbol{\tau} = \boldsymbol{J}_G^T(\boldsymbol{q}) \operatorname{vec}_6 \underline{\boldsymbol{\varsigma}}$,[3] where $\boldsymbol{J}_G(\boldsymbol{q})$ is the geometric Jacobian, and $\underline{\boldsymbol{\varsigma}}$ is the wrench applied at the end-effector. Hence, the admittance controller can be used to encompass compliant motions with distributed contacts (Navarro, 2017).

4.1.2.2 Topological Obstruction Problem

A similar problem that exists in some controllers, as for example the one described in Appendix D, is the topological obstruction (Bhat & Bernstein, 1998). In this case, when the initial state of the closed-loop system is within an unstable equilibrium set, the control signal is zero, trapping the system in that set (see Appendix D). Although a small perturbation around the unstable equilibrium set may remove the system from it (Caccavale et al., 1999), it would be still near to an unstable equilibrium point, and thus

[3] Notice that in this case those torques are added to the normal wrenches at the impedance control law, therefore gravity is already compensated in the original control law.

Figure 4.2: Cooperative tasks in which the robot has to pour beverage into the person's cup. Since the cup may be tilted, it is likely that the hand holding the bottle will have to be rotated by angles near to π rad.

the closed-loop error would decay much slower than when the system is far from this set. Such situations may occurs, for instance:

- in cooperative tasks, in which the robot needs to perform a large rotation (sometimes even very close to π rad) in relation to its partner, such as when the robot must pour a beverage into the person's cup (Figure 4.2);
- in bimanual manipulations of an object, in which the end-effectors may be symmetric to the manipulated object, with an initial rotation angle of π rad, and have to align themselves, such as the tasks of folding a sheet of paper, closing or opening a bottle, hence being also near the unstable equilibrium set (Figure 4.3);
- and even when rotating a crank by π rad or using a screwdriver (Figure 4.4).

An advantage of our proposed controller, given by Equation (4.20), over the one proposed by (Caccavale et al., 2008), given by Equation (D.1), is the absence of this problem.

4.1.2.3 Trajectory Generation

Similarly to Equation (4.2), the reference $\operatorname{vec}_6 \dot{\underline{\boldsymbol{\zeta}}}^c_{cd}$ from Equation (4.20) is numerically integrated (Euler approximation) once and transformed into the reference trajectory given by $(\underline{\boldsymbol{x}}_c(t), \dot{\underline{\boldsymbol{x}}}_c(t), \ddot{\underline{\boldsymbol{x}}}_c(t))$ using the Equations (3.19), (3.14), and their derivatives given by Equations (3.28) and (3.18), and the exponential operation described in Equation (3.10). More specifically,

$$\begin{aligned}
\operatorname{vec}_6 \dot{\underline{\boldsymbol{y}}}^c_d &= \boldsymbol{E}^{-1}\left(\underline{\boldsymbol{x}}^c_d\right) \operatorname{vec}_6 \underline{\boldsymbol{\zeta}}^c_{cd}, \\
\operatorname{vec}_6 \ddot{\underline{\boldsymbol{y}}}^c_d &= \boldsymbol{E}^{-1}\left(\underline{\boldsymbol{x}}^c_d\right) \left(\operatorname{vec}_6 \dot{\underline{\boldsymbol{\zeta}}}^c_{cd} - \dot{\boldsymbol{E}}\left(\underline{\boldsymbol{x}}^c_d\right) \operatorname{vec}_6 \dot{\underline{\boldsymbol{y}}}^c_d\right),
\end{aligned}$$

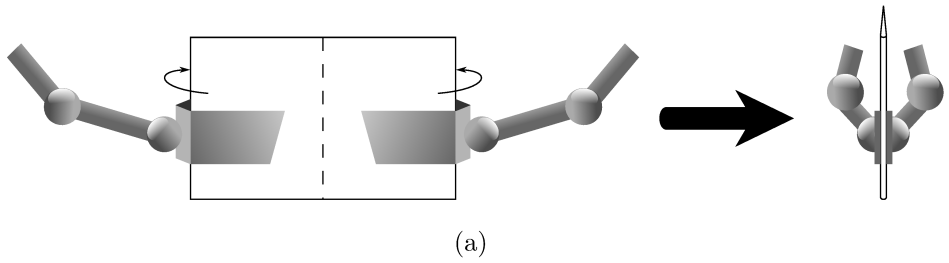

(a)

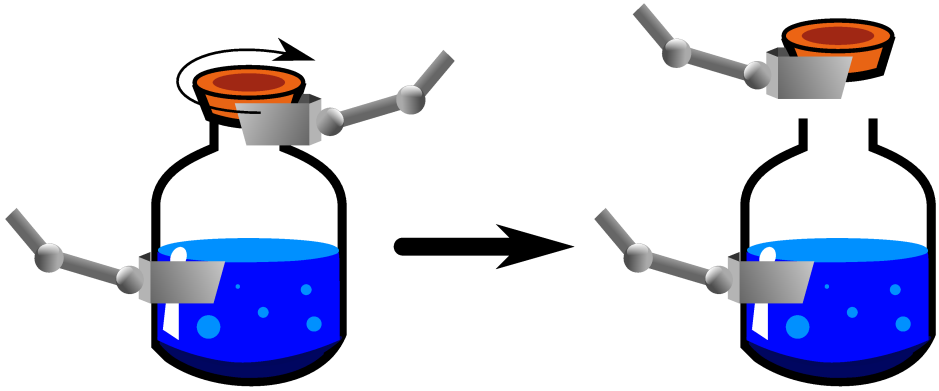

(b)

Figure 4.3: Bimanual tasks of a robot *(a)* folding a sheet of paper and *(b)* closing or opening a bottle. In those bimanual manipulations, the end-effectors may be symmetric to the manipulated object with an initial rotation angle close to π rad, and have to align themselves to perform the manipulation, being thus also near the unstable equilibrium set.

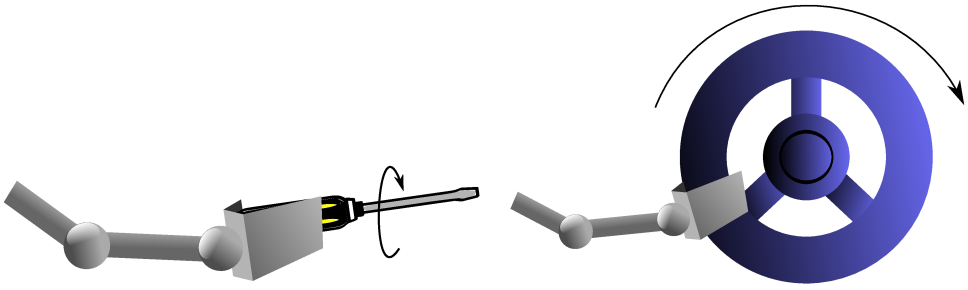

(a) (b)

Figure 4.4: Tasks involving arbitrarily large initial rotations: *(a)* using a screwdriver and *(b)* turning a crank.

then $\operatorname{vec}_6 \dot{\underline{\boldsymbol{y}}}_d^c$ is integrated to obtain $\operatorname{vec}_6 \underline{\boldsymbol{y}}_d^c$, and knowing that $\underline{\boldsymbol{y}}_d^c = \underline{\mathbf{vec}}_6 \left(\operatorname{vec}_6 \underline{\boldsymbol{y}}_d^c\right)$ yields

$$\begin{aligned}
\underline{\boldsymbol{x}}_d^c &= \exp \underline{\boldsymbol{y}}_d^c, \\
\dot{\underline{\boldsymbol{x}}}_d^c &= \underline{\mathbf{vec}}_8 \left(\boldsymbol{Q}_8 \left(\underline{\boldsymbol{x}}_d^c\right) \operatorname{vec}_6 \dot{\underline{\boldsymbol{y}}}_d^c\right), \\
\ddot{\underline{\boldsymbol{x}}}_d^c &= \underline{\mathbf{vec}}_8 \left(\dot{\boldsymbol{Q}}_8 \left(\underline{\boldsymbol{x}}_d^c\right) \operatorname{vec}_6 \dot{\underline{\boldsymbol{y}}}_d^c + \boldsymbol{Q}_8 \left(\underline{\boldsymbol{x}}_d^c\right) \operatorname{vec}_6 \ddot{\underline{\boldsymbol{y}}}_d^c\right).
\end{aligned}$$

Therefore, the trajectory $(\underline{\boldsymbol{x}}_c(t), \dot{\underline{\boldsymbol{x}}}_c(t), \ddot{\underline{\boldsymbol{x}}}_c(t))$ is retrieved using the Equations (4.3)–(4.5).

4.1.3 Admittance Controller Using Dual Quaternion Twist

The previous controller has a physical meaning and a stiffness term that is consistent with the six-DOF task geometry. However, it does not tackle the effects of the existent lever arms in the system. Using the DQ twist $\underline{\boldsymbol{\xi}}_{cd}^c = \boldsymbol{\omega}_{cd}^c + \varepsilon \left(\dot{\boldsymbol{p}}_{cd}^c + \boldsymbol{p}_{cd}^c \times \boldsymbol{\omega}_{cd}^c\right)$, instead of the the variable $\underline{\boldsymbol{\zeta}}_{cd}^c = \boldsymbol{\omega}_{cd}^c + \varepsilon \dot{\boldsymbol{p}}_{cd}^c$, contemplates all characteristics of the previous controller and also the effects of the lever arms.

From Equation (4.7) and using Equation (3.23),

$$\dot{\mathcal{K}} = \left(\boldsymbol{A}^{-1} \left(\underline{\boldsymbol{x}}_d^c\right) \operatorname{vec}_6 \underline{\boldsymbol{\xi}}_{cd}^c\right)^T \boldsymbol{M}_d \operatorname{vec}_6 \dot{\underline{\boldsymbol{\zeta}}}_{cd}^c.$$

Using

$$\operatorname{vec}_6 \underline{\boldsymbol{\zeta}}_{cd}^c = \boldsymbol{A}^{-1} \left(\underline{\boldsymbol{x}}_d^c\right) \operatorname{vec}_6 \underline{\boldsymbol{\xi}}_{cd}^c \implies \operatorname{vec}_6 \dot{\underline{\boldsymbol{\zeta}}}_{cd}^c = \frac{d}{dt}\left(\boldsymbol{A}^{-1} \left(\underline{\boldsymbol{x}}_d^c\right)\right) \operatorname{vec}_6 \underline{\boldsymbol{\xi}}_{cd}^c + \boldsymbol{A}^{-1} \left(\underline{\boldsymbol{x}}_d^c\right) \operatorname{vec}_6 \dot{\underline{\boldsymbol{\xi}}}_{cd}^c$$

yields

$$\begin{aligned}
\dot{\mathcal{K}} &= \left(\boldsymbol{A}^{-1} \left(\underline{\boldsymbol{x}}_d^c\right) \operatorname{vec}_6 \underline{\boldsymbol{\xi}}_{cd}^c\right)^T \boldsymbol{M}_d \left(\frac{d}{dt}\left(\boldsymbol{A}^{-1} \left(\underline{\boldsymbol{x}}_d^c\right)\right) \operatorname{vec}_6 \underline{\boldsymbol{\xi}}_{cd}^c + \boldsymbol{A}^{-1} \left(\underline{\boldsymbol{x}}_d^c\right) \operatorname{vec}_6 \dot{\underline{\boldsymbol{\xi}}}_{cd}^c\right) \\
&= \left(\operatorname{vec}_6 \underline{\boldsymbol{\xi}}_{cd}^c\right)^T \boldsymbol{A}^{-T} \left(\underline{\boldsymbol{x}}_d^c\right) \boldsymbol{M}_d \left(\frac{d}{dt}\left(\boldsymbol{A}^{-1} \left(\underline{\boldsymbol{x}}_d^c\right)\right) \operatorname{vec}_6 \underline{\boldsymbol{\xi}}_{cd}^c + \boldsymbol{A}^{-1} \left(\underline{\boldsymbol{x}}_d^c\right) \operatorname{vec}_6 \dot{\underline{\boldsymbol{\xi}}}_{cd}^c\right) \\
&= \left(\operatorname{vec}_6 \underline{\boldsymbol{\xi}}_{cd}^c\right)^T \left(\boldsymbol{A}^{-T} \left(\underline{\boldsymbol{x}}_d^c\right) \boldsymbol{M}_d \frac{d}{dt}\left(\boldsymbol{A}^{-1} \left(\underline{\boldsymbol{x}}_d^c\right)\right) \operatorname{vec}_6 \underline{\boldsymbol{\xi}}_{cd}^c + \boldsymbol{A}^{-T} \left(\underline{\boldsymbol{x}}_d^c\right) \boldsymbol{M}_d \boldsymbol{A}^{-1} \left(\underline{\boldsymbol{x}}_d^c\right) \operatorname{vec}_6 \dot{\underline{\boldsymbol{\xi}}}_{cd}^c\right) \\
&= \left(\operatorname{vec}_6 \underline{\boldsymbol{\xi}}_{cd}^c\right)^T \left(\boldsymbol{A}^{-T} \left(\underline{\boldsymbol{x}}_d^c\right) \boldsymbol{M}_d \frac{d}{dt}\left(\boldsymbol{A}^{-1} \left(\underline{\boldsymbol{x}}_d^c\right)\right) \operatorname{vec}_6 \underline{\boldsymbol{\xi}}_{cd}^c + \boldsymbol{A}^{-T} \left(\underline{\boldsymbol{x}}_d^c\right) \boldsymbol{M}_d \boldsymbol{A}^{-1} \left(\underline{\boldsymbol{x}}_d^c\right) \operatorname{vec}_6 \dot{\underline{\boldsymbol{\xi}}}_{cd}^c\right).
\end{aligned}$$

Therefore,

$$\dot{\mathcal{K}} = \left(\operatorname{vec}_6 \underline{\boldsymbol{\xi}}_{cd}^c\right)^T \boldsymbol{I}^{\#} \operatorname{vec}_6 \underline{\boldsymbol{\psi}}_I^c,$$

where

$$\operatorname{vec}_6 \underline{\boldsymbol{\psi}}_I^c \triangleq \boldsymbol{I}^{\#}\left(\boldsymbol{A}^{-T}\left(\underline{\boldsymbol{x}}_d^c\right)\boldsymbol{M}_d\frac{d}{dt}\left(\boldsymbol{A}^{-1}\left(\underline{\boldsymbol{x}}_d^c\right)\right)\operatorname{vec}_6\underline{\boldsymbol{\xi}}_{cd}^c+\boldsymbol{A}^{-T}\left(\underline{\boldsymbol{x}}_d^c\right)\boldsymbol{M}_d\boldsymbol{A}^{-1}\left(\underline{\boldsymbol{x}}_d^c\right)\operatorname{vec}_6\dot{\underline{\boldsymbol{\xi}}}_{cd}^c\right) \tag{4.25}$$

is the inertial DQ wrench with respect to the frame $\mathcal{F}_c$, where

$$\frac{d}{dt}\left(\boldsymbol{A}^{-1}\left(\underline{\boldsymbol{x}}_d^c\right)\right)=\begin{bmatrix}\boldsymbol{0}_{3\times3} & \boldsymbol{0}_{3\times3}\\ -\boldsymbol{S}\left(\operatorname{vec}_3\dot{\boldsymbol{p}}\right) & \boldsymbol{I}_{3\times3}\end{bmatrix}.$$

Following the same approach and using Equation (3.23) and the fact that the damping power is given by $\left(\operatorname{vec}_6\underline{\boldsymbol{\zeta}}_{cd}^c\right)^T\boldsymbol{I}^{\#}\operatorname{vec}_6\underline{\boldsymbol{\varsigma}}_I^c$, where $\operatorname{vec}_6\underline{\boldsymbol{\varsigma}}_I^c$ is given by Equation (4.9), the dissipative damping wrench is given by

$$\operatorname{vec}_6\underline{\boldsymbol{\psi}}_D^c\triangleq\boldsymbol{I}^{\#}\boldsymbol{A}^{-T}\left(\underline{\boldsymbol{x}}_d^c\right)\boldsymbol{B}_d\boldsymbol{A}^{-1}\left(\underline{\boldsymbol{x}}_d^c\right)\operatorname{vec}_6\underline{\boldsymbol{\xi}}_{cd}^c, \tag{4.26}$$

with $\mathbb{R}^{6\times6}\ni\boldsymbol{B}_d>0$.

Regarding the stiffness term, using Equation (4.15) gives

$$\begin{aligned}\dot{\mathcal{U}}&=\left(\boldsymbol{A}^{-1}\left(\underline{\boldsymbol{x}}_d^c\right)\operatorname{vec}_6\underline{\boldsymbol{\xi}}_{cd}^c\right)^T\boldsymbol{K}_d'\operatorname{vec}_6\underline{\boldsymbol{y}}_d^c\\&=\left(\operatorname{vec}_6\underline{\boldsymbol{\xi}}_{cd}^c\right)^T\boldsymbol{A}^{-T}\left(\underline{\boldsymbol{x}}_d^c\right)\boldsymbol{K}_d'\operatorname{vec}_6\underline{\boldsymbol{y}}_d^c\\&=\left(\operatorname{vec}_6\underline{\boldsymbol{\xi}}_{cd}^c\right)^T\boldsymbol{I}^{\#}\operatorname{vec}_6\underline{\boldsymbol{\psi}}_E^c\end{aligned}$$

where

$$\operatorname{vec}_6\underline{\boldsymbol{\psi}}_E^c\triangleq\boldsymbol{I}^{\#}\boldsymbol{A}^{-T}\left(\underline{\boldsymbol{x}}_d^c\right)\boldsymbol{K}_d'\operatorname{vec}_6\underline{\boldsymbol{y}}_d^c \tag{4.27}$$

is the elastic wrench with respect to $\mathcal{F}_c$.

Hence, the impedance equation is given by $\operatorname{vec}_6\underline{\boldsymbol{\psi}}_I^c+\operatorname{vec}_6\underline{\boldsymbol{\psi}}_D^c+\operatorname{vec}_6\underline{\boldsymbol{\psi}}_E^c=-\operatorname{vec}_6\underline{\boldsymbol{\psi}}_{c,\text{eff}}^c$, which, using Equations (4.25), (4.26), and (4.27), leads to

$$\boldsymbol{M}_{d_{\underline{\boldsymbol{\xi}}}}\operatorname{vec}_6\dot{\underline{\boldsymbol{\xi}}}_{cd}^c+\boldsymbol{B}_{d_{\underline{\boldsymbol{\xi}}}}\operatorname{vec}_6\underline{\boldsymbol{\xi}}_{cd}^c+\boldsymbol{K}_{d_{\underline{\boldsymbol{\xi}}}}\operatorname{vec}_6\underline{\boldsymbol{y}}_d^c=-\boldsymbol{I}^{\#}\operatorname{vec}_6\underline{\boldsymbol{\psi}}_{c,\text{eff}}^c,$$

where

$$\boldsymbol{M}_{d_{\underline{\boldsymbol{\xi}}}}\triangleq\boldsymbol{A}^{-T}\left(\underline{\boldsymbol{x}}_d^c\right)\boldsymbol{M}_d\boldsymbol{A}^{-1}\left(\underline{\boldsymbol{x}}_d^c\right), \tag{4.28}$$

$$\boldsymbol{B}_{d_{\underline{\boldsymbol{\xi}}}}\triangleq\boldsymbol{A}^{-T}\left(\underline{\boldsymbol{x}}_d^c\right)\boldsymbol{M}_d\frac{d}{dt}\left(\boldsymbol{A}^{-1}\left(\underline{\boldsymbol{x}}_d^c\right)\right)+\boldsymbol{A}^{-T}\left(\underline{\boldsymbol{x}}_d^c\right)\boldsymbol{B}_d\boldsymbol{A}^{-1}\left(\underline{\boldsymbol{x}}_d^c\right), \tag{4.29}$$

$$\boldsymbol{K}_{d_{\underline{\boldsymbol{\xi}}}}\triangleq\boldsymbol{A}^{-T}\left(\underline{\boldsymbol{x}}_d^c\right)\boldsymbol{K}_d', \tag{4.30}$$

and $\underline{\boldsymbol{\psi}}_{c,\text{eff}}^c=\operatorname{Ad}\left(\underline{\boldsymbol{x}}_{\text{eff}}^c\right)\underline{\boldsymbol{\varsigma}}_{\text{eff},\text{eff}}^{\text{eff}}$ is the external wrench acting on the robot end-effector with

reference to $\mathcal{F}_c$, and $\underline{\boldsymbol{\varsigma}}^{\text{eff}}_{\text{eff,eff}}$ is the wrench measured by the force/torque sensor at the end-effector.

Thus, the admittance equation is given by

$$\operatorname{vec}_6 \dot{\underline{\boldsymbol{\xi}}}^c_{cd} = \boldsymbol{M}^{-1}_{d_{\underline{\boldsymbol{\xi}}}} \left(-\boldsymbol{I}^{\#} \operatorname{vec}_6 \underline{\boldsymbol{\psi}}^c_{c,\text{eff}} - \boldsymbol{B}_{d_{\underline{\boldsymbol{\xi}}}} \operatorname{vec}_6 \underline{\boldsymbol{\xi}}^c_{cd} - \boldsymbol{K}_{d_{\underline{\boldsymbol{\xi}}}} \operatorname{vec}_6 \underline{\boldsymbol{y}}^c_d \right). \tag{4.31}$$

The unwinding solution of Equation (4.24) is also applied in the control law of Equation (4.31).

4.1.3.1 Trajectory Generation

Similarly to Equations (4.2) and (4.20), the reference $\operatorname{vec}_6 \dot{\underline{\boldsymbol{\xi}}}^c_{cd}$ from Equation (4.31) is numerically integrated once and transformed into the reference trajectory given by $(\underline{\boldsymbol{x}}_c(t), \dot{\underline{\boldsymbol{x}}}_c(t), \ddot{\underline{\boldsymbol{x}}}_c(t))$ using the Equations (3.19) and (3.14) and their derivatives given by Equations (3.28) and (3.18), and the exponential operation given by Equation (3.10). More specifically,

$$\begin{aligned}
\operatorname{vec}_6 \dot{\underline{\boldsymbol{y}}}^c_d &= \boldsymbol{G}^{-1}_{\log} \left(\underline{\boldsymbol{x}}^c_d \right) \operatorname{vec}_6 \underline{\boldsymbol{\xi}}^c_{cd}, \\
\operatorname{vec}_6 \ddot{\underline{\boldsymbol{y}}}^c_d &= \boldsymbol{G}^{-1}_{\log} \left(\underline{\boldsymbol{x}}^c_d \right) \left(\operatorname{vec}_6 \dot{\underline{\boldsymbol{\xi}}}^c_{cd} - \dot{\boldsymbol{G}}_{\log} \left(\underline{\boldsymbol{x}}^c_d \right) \operatorname{vec}_6 \dot{\underline{\boldsymbol{y}}}^c_d \right),
\end{aligned}$$

then $\operatorname{vec}_6 \dot{\underline{\boldsymbol{y}}}^c_d$ is integrated to obtain $\operatorname{vec}_6 \underline{\boldsymbol{y}}^c_d$, and knowing that $\underline{\boldsymbol{y}}^c_d = \underline{\mathbf{vec}}_6 \left(\operatorname{vec}_6 \underline{\boldsymbol{y}}^c_d \right)$ yields

$$\begin{aligned}
\underline{\boldsymbol{x}}^c_d &= \exp \underline{\boldsymbol{y}}^c_d, \\
\dot{\underline{\boldsymbol{x}}}^c_d &= \underline{\mathbf{vec}}_8 \left(\boldsymbol{Q}_8 \left(\underline{\boldsymbol{x}}^c_d \right) \operatorname{vec}_6 \dot{\underline{\boldsymbol{y}}}^c_d \right), \\
\ddot{\underline{\boldsymbol{x}}}^c_d &= \underline{\mathbf{vec}}_8 \left(\dot{\boldsymbol{Q}}_8 \left(\underline{\boldsymbol{x}}^c_d \right) \operatorname{vec}_6 \dot{\underline{\boldsymbol{y}}}^c_d + \boldsymbol{Q}_8 \left(\underline{\boldsymbol{x}}^c_d \right) \operatorname{vec}_6 \ddot{\underline{\boldsymbol{y}}}^c_d \right).
\end{aligned}$$

Therefore, the trajectory $(\underline{\boldsymbol{x}}_c(t), \dot{\underline{\boldsymbol{x}}}_c(t), \ddot{\underline{\boldsymbol{x}}}_c(t))$ is retrieved using the Equations (4.3)–(4.5).

Remark 4.4. The controller of Equation (4.31) can also be used when considering the whole-body robot. The whole-body control takes advantage of all available degrees of freedom for a better interaction with the environment during the execution of the tasks. For instance, consider a bimanual mobile manipulator, with the base and both arms serialized. In this case, the compliant and desired frames are the ones related to the absolute variable, that is, $\underline{\boldsymbol{x}}_{\text{ba}}$, as in Equation (3.46). Therefore, $\underline{\boldsymbol{x}}^c_d$ becomes $\underline{\boldsymbol{x}}^{\text{ba}_c}_{\text{ba}_d} \triangleq \underline{\boldsymbol{x}}^*_{\text{ba}_c} \underline{\boldsymbol{x}}_{\text{ba}_d}$. The wrench related to the absolute frame is the external one, given by Equation (3.50). Thus, $\underline{\boldsymbol{\psi}}^c_{c,\text{eff}}$ becomes $\operatorname{Ad}\left(\underline{\boldsymbol{x}}^*_{\text{ba}_c} \right) \underline{\boldsymbol{\psi}}^0_{\text{ext}}$. Moreover, one could use the relative variables and the internal wrenches as well, given by Equations (3.41) and (3.51), respectively. In this case, $\underline{\boldsymbol{x}}^c_d$ would be $\underline{\boldsymbol{x}}^{\text{rel}_c}_{\text{rel}_d} \triangleq \underline{\boldsymbol{x}}^*_{\text{rel}_c} \underline{\boldsymbol{x}}_{\text{rel}_d}$ and the wrench would be $\operatorname{Ad}\left(\underline{\boldsymbol{x}}^*_{\text{rel}_c} \right) \underline{\boldsymbol{\psi}}^0_{\text{int}}$.

4.1.4 Extension for bimanual mobile manipulator

Considering the bimanual manipulation of an object, both external and internal wrenches must be taken into account in the admittance controller described by Equation (4.31), and, consequently, the cooperative variables must be used. In order for both wrenches to be tackled with the same priority, a vector concatenating both variables is used. More specifically, the wrench vector used in the whole-body situation is given by[4]

$$\boldsymbol{\psi}^c_{\text{wb}} = \left[\left(\boldsymbol{I}^{\#} \operatorname{vec}_6 \left(\operatorname{Ad} \left(\underline{\boldsymbol{x}}^*_{\text{abs}_c} \right) \underline{\boldsymbol{\psi}}^0_{\text{ext}} \right) \right)^T \quad \left(\boldsymbol{I}^{\#} \operatorname{vec}_6 \left(\operatorname{Ad} \left(\underline{\boldsymbol{x}}^*_{\text{rel}_c} \right) \underline{\boldsymbol{\psi}}^0_{\text{int}} \right) \right)^T \right]^T,$$

where $\underline{\boldsymbol{\psi}}^0_{\text{ext}}$, $\underline{\boldsymbol{\psi}}^0_{\text{int}} \in \mathcal{H}_p$ are the external and internal wrenches, respectively, with respect to the inertial frame $\mathcal{F}_0$, as defined in Equations (3.50)-(3.51). Similarly, the vectors with the DQ twist and the logarithm are given by

$$\boldsymbol{\xi}^c_{cd_{\text{wb}}} = \left[\left(\operatorname{vec}_6 \underline{\boldsymbol{\xi}}^{\text{abs}_c}_{\text{abs}_c,\text{abs}_d} \right)^T \quad \left(\operatorname{vec}_6 \underline{\boldsymbol{\xi}}^{\text{rel}_c}_{\text{rel}_c,\text{rel}_d} \right)^T \right]^T$$

and

$$\boldsymbol{y}^c_{d_{\text{wb}}} = \left[\left(\operatorname{vec}_6 \underline{\boldsymbol{y}}^{\text{abs}_c}_{\text{abs}_d} \right)^T \quad \left(\operatorname{vec}_6 \underline{\boldsymbol{y}}^{\text{rel}_c}_{\text{rel}_d} \right)^T \right],$$

respectively, where $\underline{\boldsymbol{y}}^{\text{abs}_c}_{\text{abs}_d} \triangleq \log \underline{\boldsymbol{x}}^{\text{abs}_c}_{\text{abs}_d}$, $\underline{\boldsymbol{y}}^{\text{rel}_c}_{\text{rel}_d} \triangleq \log \underline{\boldsymbol{x}}^{\text{rel}_c}_{\text{rel}_d}$, with $\underline{\boldsymbol{x}}^{\text{abs}_c}_{\text{abs}_d} \triangleq \underline{\boldsymbol{x}}^*_{\text{abs}_c} \underline{\boldsymbol{x}}_{\text{abs}_d}$and $\underline{\boldsymbol{x}}^{\text{rel}_c}_{\text{rel}_d} \triangleq \underline{\boldsymbol{x}}^*_{\text{rel}_c} \underline{\boldsymbol{x}}_{\text{rel}_d}$, and $\operatorname{vec}_6 \underline{\boldsymbol{\xi}}^{\text{abs}_c}_{\text{abs}_c,\text{abs}_d} \triangleq \boldsymbol{G}_{\log} \left(\underline{\boldsymbol{x}}^{\text{abs}_c}_{\text{abs}_d} \right) \operatorname{vec}_6 \underline{\dot{\boldsymbol{y}}}^{\text{abs}_c}_{\text{abs}_d}$ and $\operatorname{vec}_6 \underline{\boldsymbol{\xi}}^{\text{rel}_c}_{\text{rel}_c,\text{rel}_d} \triangleq \boldsymbol{G}_{\log} \left(\underline{\boldsymbol{x}}^{\text{rel}_c}_{\text{rel}_d} \right) \operatorname{vec}_6 \underline{\dot{\boldsymbol{y}}}^{\text{rel}_c}_{\text{rel}_d}$. The impedance matrices are redefined as

$$\boldsymbol{M}_{d_{\text{wb}}} = \begin{bmatrix} \boldsymbol{M}_{d_{\text{abs}}} & \boldsymbol{0}_{6\times 6} \\ \boldsymbol{0}_{6\times 6} & \boldsymbol{M}_{d_{\text{rel}}} \end{bmatrix},$$

$$\boldsymbol{B}_{d_{\text{wb}}} = \begin{bmatrix} \boldsymbol{B}_{d_{\text{abs}}} & \boldsymbol{0}_{6\times 6} \\ \boldsymbol{0}_{6\times 6} & \boldsymbol{B}_{d_{\text{rel}}} \end{bmatrix},$$

$$\boldsymbol{K}_{d_{\text{wb}}} = \begin{bmatrix} \boldsymbol{K}_{d_{\text{abs}}} & \boldsymbol{0}_{6\times 6} \\ \boldsymbol{0}_{6\times 6} & \boldsymbol{K}_{d_{\text{rel}}} \end{bmatrix},$$

where $\boldsymbol{M}_{d_{\text{abs}}}, \boldsymbol{M}_{d_{\text{rel}}}, \boldsymbol{B}_{d_{\text{abs}}}, \boldsymbol{B}_{d_{\text{rel}}}, \boldsymbol{K}_{d_{\text{abs}}}, \boldsymbol{K}_{d_{\text{rel}}} \in \mathbb{R}^{12\times 12}$ are defined according to Equations (4.28), (4.29), and (4.30), where $\underline{\boldsymbol{x}}^c_d$ in those equations are changed to $\underline{\boldsymbol{x}}^{\text{abs}_c}_{\text{abs}_d}$ and $\underline{\boldsymbol{x}}^{\text{rel}_c}_{\text{rel}_d}$ accordingly.

Therefore, the whole-body admittance controller is given by

$$\dot{\boldsymbol{\xi}}^c_{cd_{\text{wb}}} = \boldsymbol{M}^{-1}_{d_{\text{wb}}} \left(-\boldsymbol{I}^{\#} \boldsymbol{\psi}^c_{\text{wb}} - \boldsymbol{B}_{d_{\text{wb}}} \boldsymbol{\xi}^c_{cd_{\text{wb}}} - \boldsymbol{K}_{d_{\text{wb}}} \boldsymbol{y}^c_{d_{\text{wb}}} \right).$$

[4] Although the acronym *abs* is used here, since we are considering the whole-body, the *abs* stands for the absolute cooperative variable considering the serialization of the mobile base and both arms of the BAZAR, which is the same as the $\underline{\boldsymbol{x}}_{ba}$ defined in Equation (3.46).

4.2 Kinematic Controllers

As the proposed architecture includes a motion control law in the inner-loop, it is necessary to define a motion controller that accurately tracks the reference trajectory $(\underline{\boldsymbol{x}}_c(t), \dot{\underline{\boldsymbol{x}}}_c(t), \ddot{\underline{\boldsymbol{x}}}_c(t))$ to ensure the apparent admittance in the outer-loop and, as consequence, guarantee safety. Since a large class of robots is actuated in velocity, two kinematic controllers are proposed to track a desired end-effector trajectory. Both controllers are design using the DQ logarithmic mapping, but the first one is a first order kinematic controller, and the second one is a second order kinematic controller.

Remark 4.5. The designed kinematic controllers can be used in the inner-loop of the proposed architecture to track the compliant trajectory $(\underline{\boldsymbol{x}}_c(t), \dot{\underline{\boldsymbol{x}}}_c(t), \ddot{\underline{\boldsymbol{x}}}_c(t))$ or, alternatively, it can be the only controller, as for example in cases where there is no interaction. The following developments consider the desired trajectory as $(\underline{\boldsymbol{x}}_d(t), \dot{\underline{\boldsymbol{x}}}_d(t), \ddot{\underline{\boldsymbol{x}}}_d(t))$. If the controllers are used in the architecture as in Figure 4.1, $\underline{\boldsymbol{x}}_d$ and its derivatives should be replaced by $\underline{\boldsymbol{x}}_c$ and its derivatives.

4.2.1 First Order Kinematic Controller

Considering the error $\tilde{\underline{\boldsymbol{x}}} = \underline{\boldsymbol{x}}^* \underline{\boldsymbol{x}}_d$, with $\underline{\boldsymbol{x}}, \underline{\boldsymbol{x}}_d \in \mathrm{Spin}(3) \ltimes \mathbb{R}^3$ being the current and desired poses, respectively, its time derivative is given by

$$\mathrm{vec}_8 \, \dot{\tilde{\underline{\boldsymbol{x}}}} = \bar{\boldsymbol{H}}_8 \left(\underline{\boldsymbol{x}}_d \right) \boldsymbol{C}_8 \, \mathrm{vec}_8 \, \dot{\underline{\boldsymbol{x}}} + \overset{+}{\boldsymbol{H}}_8 \left(\underline{\boldsymbol{x}}^* \right) \mathrm{vec}_8 \, \dot{\underline{\boldsymbol{x}}}_d. \tag{4.32}$$

Substituting Equation (3.14) in the left side of Equation (4.32), and Equation (3.39) in the right side of Equation (4.32), imposing an exponential decay to the error $\tilde{\underline{\boldsymbol{y}}} \triangleq \log \tilde{\underline{\boldsymbol{x}}}$ by defining the desired closed-loop task error dynamics as

$$\boldsymbol{v}_y \triangleq \mathrm{vec}_6 \, \dot{\tilde{\underline{\boldsymbol{y}}}} = -\boldsymbol{K}_P \, \mathrm{vec}_6 \, \tilde{\underline{\boldsymbol{y}}}, \tag{4.33}$$

where $\boldsymbol{K}_P \in \mathbb{R}^{6 \times 6}$ is a positive definite gain matrix. We solve for $\dot{\boldsymbol{q}}$ to obtain the control law

$$\boldsymbol{u} \triangleq \dot{\boldsymbol{q}} = \boldsymbol{N}^+ \left(\boldsymbol{Q}_8 \left(\tilde{\underline{\boldsymbol{x}}} \right) \boldsymbol{v}_y + \boldsymbol{z}_1 \right), \tag{4.34}$$

where, $\boldsymbol{N} \triangleq \bar{\boldsymbol{H}}_8 \left(\underline{\boldsymbol{x}}_d \right) \boldsymbol{C}_8 \boldsymbol{J} \left(\boldsymbol{q} \right)$ (Figueredo et al., 2013), $\boldsymbol{z}_1 \triangleq -\overset{+}{\boldsymbol{H}}_8 \left(\underline{\boldsymbol{x}}^* \right) \mathrm{vec}_8 \, \dot{\underline{\boldsymbol{x}}}_d$.

4.2.2 Second Order Kinematic Controller

Similarly to the first order controller, considering Equation (3.14), the time derivative of Equation (4.32), and defining the desired closed-loop task error dynamics as

$$\boldsymbol{a}_y \triangleq \operatorname{vec}_8 \ddot{\underline{\boldsymbol{y}}} = -\boldsymbol{K}_D \operatorname{vec}_8 \dot{\underline{\boldsymbol{y}}} - \boldsymbol{K}_P \operatorname{vec}_8 \underline{\tilde{\boldsymbol{y}}}, \tag{4.35}$$

with $\mathbb{R}^{6\times 6} \ni \boldsymbol{K}_D, \boldsymbol{K}_P > 0$, the second order kinematic control law is given by

$$\boldsymbol{u}_{\text{nom}} \triangleq \ddot{\boldsymbol{q}} = \boldsymbol{N}^{+} \left(\boldsymbol{Q}_8 \left(\underline{\tilde{\boldsymbol{x}}} \right) \boldsymbol{a}_y + \boldsymbol{z}_2 \right), \tag{4.36}$$

where $\boldsymbol{z}_2 \triangleq \dot{\boldsymbol{Q}}_8 \left(\underline{\tilde{\boldsymbol{x}}} \right) \operatorname{vec}_6 \dot{\underline{\tilde{\boldsymbol{y}}}} - \dot{\boldsymbol{Z}} \operatorname{vec}_8 \underline{\boldsymbol{x}} - \boldsymbol{Z}\boldsymbol{J}\left(\boldsymbol{q}\right)\dot{\boldsymbol{q}} - \dot{\boldsymbol{N}}\dot{\boldsymbol{q}}$, and $\boldsymbol{Z} \triangleq \bar{\boldsymbol{H}}_8 \left(\underline{\dot{\boldsymbol{x}}}_d \right) \boldsymbol{C}_8$.

Remark 4.6. In case of redundant robots, the joint velocities can be different from zero even if the end-effector is in the desired pose. To prevent that situation, a dissipative term is added as $\boldsymbol{u}_{\text{dis}} = k_{\text{dis}} \left(\boldsymbol{1}_n \left\| \operatorname{vec}_6 \dot{\underline{\tilde{\boldsymbol{y}}}} \right\| - \dot{\boldsymbol{q}} \right)$, where $\boldsymbol{1}_n$ is an n-dimensional column vector of ones and $k_{\text{dis}} \in (0, \infty)$ (Quiroz-Omana & Adorno, 2019). Thus, the control law becomes

$$\boldsymbol{u} = \boldsymbol{u}_{\text{nom}} + \boldsymbol{u}_{\text{dis}}. \tag{4.37}$$

Remark 4.7. The solution given by Equation (4.24) to the unwinding problem can also be applied to the kinematic controller given by Equation (4.37) by using $\underline{\tilde{\boldsymbol{y}}}$ and $\underline{\tilde{\boldsymbol{x}}}$ instead of $\underline{\boldsymbol{y}}_d^c$ and $\underline{\boldsymbol{x}}_d^c$, respectively.

4.2.3 Extension for bimanual mobile manipulator

Similarly to the admittance controller, the kinematic controller of Equation (4.37) also suffers modifications when considering the whole-body of a bimanual mobile manipulator. More specifically, the whole-body kinematic control law, considering the absolute and relative poses are given by

$$\boldsymbol{u}_{\text{nom}_{\text{wb}}} \triangleq \ddot{\boldsymbol{q}}_{\text{wb}} = \boldsymbol{N}_{\text{wb}}^{+} \left(\boldsymbol{Q}_{8_{\text{wb}}} \boldsymbol{a}_{y_{\text{wb}}} + \boldsymbol{z}_{2_{\text{wb}}} \right),$$

where $\boldsymbol{q}_{\text{wb}} = \begin{bmatrix} \boldsymbol{q}_{\text{base}}^T & \boldsymbol{q}_{\text{right}}^T & \boldsymbol{q}_{\text{left}}^T \end{bmatrix}^T$ is the vector of joints,

$$\boldsymbol{N}_{\text{wb}} \triangleq \begin{bmatrix} \boldsymbol{N}_{\text{abs}} \\ \begin{bmatrix} \boldsymbol{0}_{8\times\dim(\boldsymbol{q}_{\text{base}})} & \boldsymbol{N}_{\text{rel}} \end{bmatrix} \end{bmatrix}$$

is the whole-body modified Jacobian matrix, where $\mathbb{R}^{8\times\left(\dim(\boldsymbol{q}_{\text{base}})+\dim\left(\boldsymbol{q}_{\text{right}}\right)+\dim(\boldsymbol{q}_{\text{left}})\right)} \ni \boldsymbol{N}_{\text{abs}} \triangleq \bar{\boldsymbol{H}}_8 \left(\underline{\boldsymbol{x}}_{\text{abs}_c} \right) \boldsymbol{C}_8 \boldsymbol{J}_{\text{abs}}$ and $\mathbb{R}^{8\times\left(\dim\left(\boldsymbol{q}_{\text{right}}\right)+\dim(\boldsymbol{q}_{\text{left}})\right)} \ni \boldsymbol{N}_{\text{rel}} \triangleq \bar{\boldsymbol{H}}_8 \left(\underline{\boldsymbol{x}}_{\text{rel}_c} \right) \boldsymbol{C}_8 \boldsymbol{J}_{\text{rel}}$ are the absolute and relative modified Jacobian matrices, respectively. The matrix $\boldsymbol{Q}_{8_{\text{wb}}} \in \mathbb{R}^{16\times 12}$

is given by

$$\boldsymbol{Q}_{8_{\text{wb}}} \triangleq \begin{bmatrix} \boldsymbol{Q}_8\left(\tilde{\underline{\boldsymbol{x}}}_{\text{abs}}\right) & \boldsymbol{0}_{8\times 6} \\ \boldsymbol{0}_{8\times 6} & \boldsymbol{Q}_8\left(\tilde{\underline{\boldsymbol{x}}}_{\text{rel}}\right) \end{bmatrix},$$

and the vector representing the desired dynamics is given by

$$\boldsymbol{a}_{y_{\text{wb}}} \triangleq -\boldsymbol{K}_{D_{\text{wb}}}\dot{\tilde{\boldsymbol{y}}}_{\text{wb}} - \boldsymbol{K}_{P_{\text{wb}}}\tilde{\dot{\boldsymbol{y}}}_{\text{wb}},$$

with

$$\boldsymbol{K}_{D_{\text{wb}}} \triangleq \begin{bmatrix} \boldsymbol{K}_{D_{\text{abs}}} & \boldsymbol{0}_{6\times 6} \\ \boldsymbol{0}_{6\times 6} & \boldsymbol{K}_{D_{\text{rel}}} \end{bmatrix}$$

an

$$\boldsymbol{K}_{P_{\text{wb}}} \triangleq \begin{bmatrix} \boldsymbol{K}_{P_{\text{abs}}} & \boldsymbol{0}_{6\times 6} \\ \boldsymbol{0}_{6\times 6} & \boldsymbol{K}_{P_{\text{rel}}} \end{bmatrix}$$

being the whole-body derivative and proportional gain matrices, where $\boldsymbol{K}_{D_{\text{abs}}}, \boldsymbol{K}_{D_{\text{rel}}}, \boldsymbol{K}_{P_{\text{abs}}}, \boldsymbol{K}_{P_{\text{rel}}} \in \mathbb{R}^{6\times 6}$ are the derivative and proportional gains related to the absolute and relative variables, respectively. The vector with the logarithm is defined as

$$\tilde{\boldsymbol{y}}_{\text{wb}} \triangleq \begin{bmatrix} \left(\text{vec}_6\, \tilde{\underline{\boldsymbol{y}}}_{\text{abs}}\right)^T & \left(\text{vec}_6\, \tilde{\underline{\boldsymbol{y}}}_{\text{rel}}\right)^T \end{bmatrix}^T,$$

with $\tilde{\underline{\boldsymbol{y}}}_{\text{abs}} \triangleq \log \tilde{\underline{\boldsymbol{x}}}_{\text{abs}}$ and $\tilde{\underline{\boldsymbol{y}}}_{\text{rel}} \triangleq \log \tilde{\underline{\boldsymbol{x}}}_{\text{rel}}$, where$\tilde{\underline{\boldsymbol{x}}}_{\text{abs}} \triangleq \underline{\boldsymbol{x}}^*_{\text{abs}}\underline{\boldsymbol{x}}_{\text{abs}_c}$ and $\tilde{\underline{\boldsymbol{x}}}_{\text{rel}} \triangleq \underline{\boldsymbol{x}}^*_{\text{rel}}\underline{\boldsymbol{x}}_{\text{rel}_c}$. The additional terms are given by$\boldsymbol{z}_{2_{\text{wb}}} \triangleq \dot{\boldsymbol{Q}}_{8_{\text{wb}}}\dot{\tilde{\boldsymbol{y}}}_{\text{wb}} - \dot{\boldsymbol{Z}}_{\text{wb}}\boldsymbol{x}_{\text{wb}} - \boldsymbol{Z}_{\text{wb}}\boldsymbol{J}_{\text{wb}}\dot{\boldsymbol{q}}_{\text{wb}} - \dot{\boldsymbol{N}}_{\text{wb}}\dot{\boldsymbol{q}}_{\text{wb}}$, where

$$\boldsymbol{Z}_{\text{wb}} \triangleq \begin{bmatrix} \bar{\boldsymbol{H}}_8\left(\dot{\underline{\boldsymbol{x}}}_{\text{abs}_c}\right)\boldsymbol{C}_8 & \boldsymbol{0}_{8\times 8} \\ \boldsymbol{0}_{8\times 8} & \bar{\boldsymbol{H}}_8\left(\dot{\underline{\boldsymbol{x}}}_{\text{rel}_c}\right)\boldsymbol{C}_8 \end{bmatrix},$$

$\boldsymbol{x}_{\text{wb}} \triangleq \begin{bmatrix} \left(\text{vec}_8\, \underline{\boldsymbol{x}}_{\text{abs}}\right)^T & \left(\text{vec}_8\, \underline{\boldsymbol{x}}_{\text{rel}}\right)^T \end{bmatrix}^T$, and the Jacobian matrix is given by

$$\boldsymbol{J}_{\text{wb}} \triangleq \begin{bmatrix} \boldsymbol{J}_{\text{abs}} \\ \begin{bmatrix} \boldsymbol{0}_{8\times 3} & \boldsymbol{J}_{\text{rel}} \end{bmatrix} \end{bmatrix},$$

where $\boldsymbol{J}_{\text{abs}} \in \mathbb{R}^{8\times\left(\dim(\boldsymbol{q}_{\text{base}})+\dim\left(\boldsymbol{q}_{\text{right}}\right)+\dim(\boldsymbol{q}_{\text{left}})\right)}$ and $\boldsymbol{J}_{\text{rel}} \in \mathbb{R}^{8\times\left(\dim\left(\boldsymbol{q}_{\text{right}}\right)+\dim(\boldsymbol{q}_{\text{left}})\right)}$ are the absolute and relative Jacobian matrices, defined as in Equations (3.47) and (3.43). Finally, the dissipative function is given by

$$\boldsymbol{u}_{\text{dis}_{\text{wb}}} = k_{\text{dis}}\left(\boldsymbol{1}_n\left\|\dot{\tilde{\boldsymbol{y}}}_{\text{wb}}\right\| - \dot{\boldsymbol{q}}_{\text{wb}}\right).$$

4.3 Dynamic Controllers

Many robots have joints actuators whose drivers have an implemented velocity control loop. When this velocity control loop has very good performance, we can consider that the control inputs of the manipulator are the joints velocities. In this case, we say that the robot is "velocity-actuated" or "actuated in velocity". However, other robots have joints actuated in torque (Siciliano et al., 2009). In the latter case, the most appropriate controller is the one based on the robot dynamics, as it enables more accurate analyses and helps in the synthesis of the robot dynamic behavior (Yang et al., 2016). Assuming complete knowledge of the robot dynamic model, the motion control laws proposed in this section are based on it. In this case, the inertia matrix plays an important role, as it influences the control of the robot's dynamic behavior. Despite the fact that the inertia matrix is positive definite independently of the robot configuration, its good conditioning is not guaranteed (Shen & Featherstone, 2003).

This section first presents some well-known controllers and discusses their behaviors regarding the error dynamics and also the steady-state error with respect to the conditioning of the JSIM. Then, it presents two adaptive controllers, based on the ones proposed by Slotine & Li (1987) and Cheah et al. (2006b,a), in order to control a serial robot manipulator while solving the problem introduced by the ill-conditioning of the inertia matrix. Moreover, the choice of the appropriate parameter vector to be estimated by the adaptive controller is presented in order to guarantee a resultant matrix with a condition number smaller than the original one. The controllers are presented first considering the joint-space, and then the task-space.

Remark 4.8. As for the kinematic controllers (see Remark 4.5), the dynamic controllers can also be used purely or together with the admittance controller, in the proposed architecture illustrated in 4.1. The following developments consider the desired trajectory as $(\underline{\boldsymbol{x}}_d(t), \dot{\underline{\boldsymbol{x}}}_d(t), \ddot{\underline{\boldsymbol{x}}}_d(t))$, which should be replaced by $(\underline{\boldsymbol{x}}_c(t), \dot{\underline{\boldsymbol{x}}}_c(t), \ddot{\underline{\boldsymbol{x}}}_c(t))$ if the objective is to follow the compliant trajectory returned by the admittance controller.

4.3.1 Joint-Space Controllers

4.3.1.1 Inverse Dynamics with Feedback Linearization (IDFL)

A common technique to control a robot manipulator modeled by Equation (3.52) is to design a control law based on the inverse dynamics with feedback linearization (Spong et al., 2006). This type of control law is divided into two loops, where the inner-loop is composed of the linearized system and the outer-loop receives the desired trajectory, as shown in Figure 4.5.

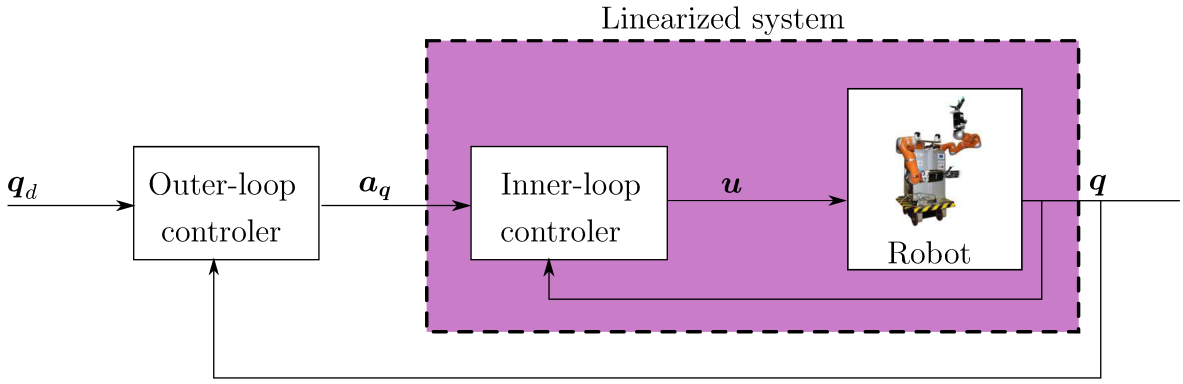

Figure 4.5: Inner-loop/outer-loop control architecture. Adapted from (Spong et al., 2006).

Thus, the control law is given by

$$\boldsymbol{u} = \boldsymbol{M}(\boldsymbol{q})\,\boldsymbol{a}_q + \boldsymbol{C}(\boldsymbol{q}, \dot{\boldsymbol{q}})\,\dot{\boldsymbol{q}} + \boldsymbol{g}(\boldsymbol{q}), \tag{4.38}$$

where the control input $\boldsymbol{u} \triangleq \boldsymbol{\tau} \in \mathbb{R}^n$ is applied to the joints and $\boldsymbol{a}_q \triangleq \ddot{\boldsymbol{q}} \in \mathbb{R}^n$ is the control input designed to stabilize the linearized closed-loop system.

One can define an additional control law as (Kelly et al., 2005)

$$\boldsymbol{a}_q = \ddot{\boldsymbol{q}}_d - \boldsymbol{K}_D\dot{\tilde{\boldsymbol{q}}} - \boldsymbol{K}_P\tilde{\boldsymbol{q}} - \boldsymbol{K}_I\int_0^t \tilde{\boldsymbol{q}}(t)\,dt, \tag{4.39}$$

where $\boldsymbol{K}_D, \boldsymbol{K}_P, \boldsymbol{K}_I \in \mathbb{R}^{n\times n}$ are positive definite design matrices and $\tilde{\boldsymbol{q}} \triangleq \boldsymbol{q} - \boldsymbol{q}_d$ denotes the joints error, with $\boldsymbol{q}_d \in \mathbb{R}^n$ being the desired joint configuration. This control law leads to the following dynamics in closed-loop:

$$\ddot{\tilde{\boldsymbol{q}}} + \boldsymbol{K}_D\dot{\tilde{\boldsymbol{q}}} + \boldsymbol{K}_I\tilde{\boldsymbol{q}} + \boldsymbol{K}_I\int_0^t \tilde{\boldsymbol{q}}(t)\,dt = \boldsymbol{0}. \tag{4.40}$$

Shen & Featherstone (2003) show that the control law in Equation (4.38) may behave poorly whenever the matrix $\boldsymbol{M}(\boldsymbol{q})$ is ill-conditioned. Due to the difference in the singular values of $\boldsymbol{M}(\boldsymbol{q})$, the torque of each joint calculated from Equation (4.38) can be very disparate, even if the joints accelerations are the same. To see that, let us consider the control law of Equation (4.38), and decompose it in the singular values:

$$\begin{aligned}\boldsymbol{u} &= \boldsymbol{M}(\boldsymbol{q})\,\boldsymbol{a}_q + \overbrace{\boldsymbol{C}(\boldsymbol{q},\dot{\boldsymbol{q}})\,\dot{\boldsymbol{q}} + \boldsymbol{g}(\boldsymbol{q})}^{\boldsymbol{f}(\boldsymbol{q},\dot{\boldsymbol{q}})} \\ &= \boldsymbol{U}\begin{bmatrix}\sigma_1 & & \\ & \ddots & \\ & & \sigma_n\end{bmatrix}\boldsymbol{V}^T\boldsymbol{a}_q + \boldsymbol{f}(\boldsymbol{q},\dot{\boldsymbol{q}}) \\ &= \sum_{i=1}^{n} \boldsymbol{u}_i\sigma_i\boldsymbol{v}_i^T\boldsymbol{a}_{\boldsymbol{q}} + \boldsymbol{f}(\boldsymbol{q},\dot{\boldsymbol{q}}),\end{aligned}$$

where σ_i is the i-th singular value, and $\begin{bmatrix}\boldsymbol{u}_1 & \cdots & \boldsymbol{u}_n\end{bmatrix} = \boldsymbol{U} \in O(n)$ and $\begin{bmatrix}\boldsymbol{v}_1 & \cdots & \boldsymbol{v}_n\end{bmatrix} = \boldsymbol{V} \in O(n)$ are orthogonal matrices. Therefore, if the configuration-dependent inertia along a specific joint is very small, no matter how large the position/velocity error or PID-coefficients are, the correction torque applied on that joint will be still small compared to the dominant torque, which may result in some undesired stationary error.

4.3.1.2 PID-Controller with Gravity Compensation (PID)

To circumvent the ill-conditioning of the JSIM, Shen & Featherstone (2003) proposed to use a PD controller with gravity compensation, which is yields an asymptotically stable closed-loop system if the PD gains are properly chosen (Kelly et al., 2005), as it directly converts the joint-space error to the joint torques, without using the JSIM, and therefore it is not affected by its ill-conditioning. If an integral term is used, as well as a feed-forward term, the control law is given by

$$\boldsymbol{u} = \boldsymbol{a}_q + \boldsymbol{g}(\boldsymbol{q}), \tag{4.41}$$

with $\boldsymbol{a}_q$ given by Equation (4.39).

Shen & Featherstone (2003) emphasizes that, although controllers such as in Equation (4.41) do not use the JSIM, which mitigates the problem caused by the JSIM ill-conditioning, a controller that takes into consideration the whole robot dynamic model should achieve better accuracy.

4.3.1.3 Adaptive Controller (AC)

Targeting a control law that is able to achieve a good accuracy by using torque inputs, and assuming knowledge of the robot kinematic and dynamic model, an adequate alternative to the previously widely used control structures is to use an adaptive controller in which a positive definite matrix $\boldsymbol{\mathcal{A}}$ is added to the JSIM, in the Euler-Lagrange equation (Equation (3.52)), and compensating the uncertainties introduced by this matrix in order to improve its conditioning without adding excessive inaccuracy to the nominal model. Since the inertia matrix depends on the robot configuration, it is difficult to choose $\boldsymbol{\mathcal{A}}$

beforehand and thus it should be adapted during the robot motion, which motivates the use of an adaptive controller.

Two solutions are proposed in this section. The first one considers the sum of the matrix corresponding to motors' inertia $\boldsymbol{M}_m$, which is positive definite, an thus it has a physical meaning. However, since the estimated parameters by the adaptation law do not always converge to the real ones, and the controller is able to compensate the added uncertainties, there is no necessity of considering an added matrix with physical meaning. Thus, a second solution is proposed by carefully choosing a positive definite matrix $\bar{\boldsymbol{D}} \in \mathbb{R}^{n \times n}$ to the JSIM, which is designed to improve its conditioning without adding excessive inaccuracy to the model. Therefore, the Euler-Lagrange equation given by Equation (3.52) becomes

$$\left[\boldsymbol{M}\left(\boldsymbol{q}\right) + \boldsymbol{\mathcal{A}}\right]\ddot{\boldsymbol{q}} + \boldsymbol{C}\left(\boldsymbol{q}, \dot{\boldsymbol{q}}\right)\dot{\boldsymbol{q}} + \boldsymbol{g}\left(\boldsymbol{q}\right) = \boldsymbol{\tau}, \tag{4.42}$$

where $\boldsymbol{\mathcal{A}} \in \left\{\boldsymbol{M}_m, \bar{\boldsymbol{D}}\right\}$ is the added positive definite matrix.

A typical adaptive controller is composed of a control law and an adaptation law. Regarding the control law, a sliding vector is defined to restrict the error to a sliding surface, which is required to eliminate the steady-state position error (Slotine & Li, 1987). In the joint space, the adaptive sliding vector is defined as

$$\boldsymbol{s} \triangleq \dot{\boldsymbol{q}} - \dot{\boldsymbol{q}}_r, \tag{4.43}$$

where $\dot{\boldsymbol{q}}_r = \dot{\boldsymbol{q}}_d - \alpha\left(\boldsymbol{q} - \boldsymbol{q}_d\right)$, with α being a positive constant and $\boldsymbol{q}_d$ is the vector of desired joints configurations.

Substituting Equation (4.43) and its derivative in Equation (4.42) yields

$$\left[\boldsymbol{M}\left(\boldsymbol{q}\right) + \boldsymbol{\mathcal{A}}\right]\dot{\boldsymbol{s}} + \boldsymbol{C}\left(\boldsymbol{q}, \dot{\boldsymbol{q}}\right)\boldsymbol{s} + \boldsymbol{g}\left(\boldsymbol{q}\right) + \left[\boldsymbol{M}\left(\boldsymbol{q}\right) + \boldsymbol{\mathcal{A}}\right]\ddot{\boldsymbol{q}}_r + \boldsymbol{C}\left(\boldsymbol{q}, \dot{\boldsymbol{q}}\right)\dot{\boldsymbol{q}}_r = \boldsymbol{\tau}. \tag{4.44}$$

To ensure the JSIM's positiveness, a control law based on the one proposed by Cheah et al. (2006a) is proposed for the purpose of finding a suitable matrix $\boldsymbol{\mathcal{A}}$.

Assuming that the dynamic parameters of the links are known with sufficient accuracy, only the matrix $\boldsymbol{\mathcal{A}}$ needs to be estimated. In addition, as the robot dynamic model is linear in a set of physical parameters and its linear combinations (Cheah et al., 2006a), it is possible to rewrite the last three terms of Equation (4.44) as

$$\left[\boldsymbol{M}\left(\boldsymbol{q}\right) + \boldsymbol{\mathcal{A}}\right]\ddot{\boldsymbol{q}}_r + \boldsymbol{C}\left(\boldsymbol{q}, \dot{\boldsymbol{q}}\right)\dot{\boldsymbol{q}}_r + \boldsymbol{g}\left(\boldsymbol{q}\right) = \boldsymbol{Y}\boldsymbol{a} + \boldsymbol{v}\left(\boldsymbol{q}, \dot{\boldsymbol{q}}, \dot{\boldsymbol{q}}_r, \ddot{\boldsymbol{q}}_r\right), \tag{4.45}$$

where $\boldsymbol{v}\left(\boldsymbol{q}, \dot{\boldsymbol{q}}, \dot{\boldsymbol{q}}_r, \ddot{\boldsymbol{q}}_r\right) \in \mathbb{R}^n$ is a vector containing the known dynamic model (i.e., $\boldsymbol{v}\left(\boldsymbol{q}, \dot{\boldsymbol{q}}, \dot{\boldsymbol{q}}_r, \ddot{\boldsymbol{q}}_r\right) = \boldsymbol{M}\left(\boldsymbol{q}\right)\ddot{\boldsymbol{q}}_r + \boldsymbol{C}\left(\boldsymbol{q}, \dot{\boldsymbol{q}}\right)\dot{\boldsymbol{q}}_r + \boldsymbol{g}\left(\boldsymbol{q}\right)$), the matrix $\boldsymbol{Y} \in \mathbb{R}^{n \times n}$ is the regressor that depends on the choice of $\boldsymbol{\mathcal{A}}$ and on the parameter vector $\hat{\boldsymbol{a}} \in \mathbb{R}^n$ to be estimated.

Therefore, the adaptive control law is given by

$$\boldsymbol{u} \triangleq \boldsymbol{\tau} = \boldsymbol{a}_q + \boldsymbol{v}\left(\boldsymbol{q}, \dot{\boldsymbol{q}}, \dot{\boldsymbol{q}}_r, \ddot{\boldsymbol{q}}_r\right) + \boldsymbol{Y}\hat{\boldsymbol{a}}, \tag{4.46}$$

with $\boldsymbol{a}_q$ defined as in Equation (4.39).

The estimated parameter $\hat{\boldsymbol{a}}$ is adapted by the adaptation law given by

$$\dot{\hat{\boldsymbol{a}}} = -\boldsymbol{L}\boldsymbol{Y}^T\boldsymbol{s}, \tag{4.47}$$

where $\operatorname{diag}(\gamma_1, \ldots, \gamma_n) = \boldsymbol{L} \in \mathbb{R}^{n\times n}$ is a diagonal positive-definite matrix that determines the convergence rate of the adaptive parameters.

Remark 4.9. Considering only the proportional and derivative terms (i.e., $\boldsymbol{K}_I = \boldsymbol{0}$), and the nominal adaptation law as described by Equation (4.47), the trajectory of the closed-loop system when using the control law Equation (4.46) converges to the invariant $(\boldsymbol{q}, \dot{\boldsymbol{q}}) = (\boldsymbol{0}, \boldsymbol{0})$, as proved by Fonseca et al. (2018). We can also use an argument based on passivity theory to prove this convergence, as done by Leite & Lizarralde (2016).

Considering the Motors' Inertia (ACM) When considering the motor's inertia, that is, $\boldsymbol{\mathcal{A}} \triangleq \boldsymbol{M}_m$, the regressor is given by $\boldsymbol{Y} \triangleq \boldsymbol{Y}_m(\ddot{\boldsymbol{q}}_r) = \operatorname{diag}(\ddot{\boldsymbol{q}}_r)$ and $\boldsymbol{a} \triangleq \boldsymbol{a}_m = \begin{bmatrix}\eta_1\vartheta_1^2 & \cdots & \eta_n\vartheta_n^2\end{bmatrix}^T$ is the (constant) parameter vector. [5]

Assuming $\boldsymbol{u} \triangleq \boldsymbol{\tau}$, the closed-loop dynamics is obtained by combining Equations (4.44) and (4.45) and making it equal to Equation (4.46), which results in

$$\left[\boldsymbol{M}(\boldsymbol{q}) + \boldsymbol{M}_m\right]\dot{\boldsymbol{s}} + \boldsymbol{C}(\boldsymbol{q}, \dot{\boldsymbol{q}})\,\boldsymbol{s} - \boldsymbol{a}_q + \boldsymbol{Y}_m(\ddot{\boldsymbol{q}}_r)\,\Delta\boldsymbol{a}_m = \boldsymbol{0} \tag{4.48}$$

where $\Delta\boldsymbol{a}_m = \boldsymbol{a}_m - \hat{\boldsymbol{a}}_m$.

Although the adaptive controller proposed by Cheah et al. ensures asymptotic stability of $\begin{bmatrix}\tilde{\boldsymbol{q}}^T & \dot{\tilde{\boldsymbol{q}}}^T\end{bmatrix}^T = \boldsymbol{0}$, there is no guarantee that the estimated parameters are positive. However, in order to have a physical meaning, the inertia matrix must be positive definite. To guarantee that, the matrix $\boldsymbol{M}_m$ added to the JSIM must also be positive definite, since the sum of two positive definite matrices is also positive definite, which is not always true when the added matrix is not positive definite, as shown in Example 4.2. Therefore, an algorithm based on the one proposed by Wang & Xie (2011) is developed in the next paragraph to ensure that all estimated parameters remain positive.

Example 4.2. Consider a positive definite matrix $\boldsymbol{A} \in GL(2)$, and a negative definite

[5] Since $\boldsymbol{Y}_m(\ddot{\boldsymbol{q}}_r)$ is a diagonal matrix, each element $\dot{\hat{a}}_i$ of $\dot{\hat{\boldsymbol{a}}}_m$ in Equation (4.47) is given by $\dot{\hat{a}}_i = -\gamma_i\ddot{q}_{ri}s_i$, where $\ddot{\boldsymbol{q}}_r = \begin{bmatrix}\ddot{q}_{r1} & \cdots & \ddot{q}_{rn}\end{bmatrix}^T$ and $\boldsymbol{s} = \begin{bmatrix}s_1 & \cdots & s_n\end{bmatrix}$.

matrix $\boldsymbol{B} \in GL(2)$, such that

$$\boldsymbol{A} = \begin{bmatrix} 3 & 0 \\ 0 & 1 \end{bmatrix}, \ \boldsymbol{B} = \begin{bmatrix} -1 & 0 \\ 0 & -1 \end{bmatrix}.$$

Therefore,

$$\begin{aligned} \boldsymbol{C} = \boldsymbol{A} + \boldsymbol{B} &= \begin{bmatrix} 3 & 0 \\ 0 & 1 \end{bmatrix} + \begin{bmatrix} -1 & 0 \\ 0 & -1 \end{bmatrix} \\ &= \begin{bmatrix} 2 & 0 \\ 0 & 0 \end{bmatrix} \notin GL(2) \end{aligned}$$

Besides, the condition numbers[6] of each matrix are $\text{cond}(\boldsymbol{A}) = 3$, $\text{cond}(\boldsymbol{B}) = 1$ and $\text{cond}(\boldsymbol{C}) = \infty$, which indicates that the even adding a better conditioned matrix ($\boldsymbol{B}$) to a positive definite one ($\boldsymbol{A}$) can worsen the matrix conditioning.

Estimation of Positive Parameters In order to guarantee the positive definiteness of the estimated matrix $\boldsymbol{M}_m$ in Equation (3.53), a convex region is defined for the parameter space that correspond to the admissible parameter set (Wang & Xie, 2011), and ensure that the estimated parameters are always projected onto this set. Since the goal here is to compensate for uncertainties in the inertia of the joints, the parameter vector is given by $\boldsymbol{a}_m \triangleq \begin{bmatrix} a_1 & \cdots & a_n \end{bmatrix}^T$, where $a_i = \eta_i \vartheta_i^2$ and the convex region for each joint i is defined as

$$\Omega_i \triangleq \{\hat{a}_i \geq \beta, \ \beta \in (0, \infty)\}, \tag{4.49}$$

where β is the lower bound for all the estimated parameters $\hat{a}_1, \ldots, \hat{a}_n$. If each estimated parameter a_i is positive, then the matrix $\boldsymbol{M}_m$ in Equation (3.53) is positive definite. Therefore, if $\hat{a}_i \in \Omega_i, \ \forall i$ then $\boldsymbol{M}_m > 0$.

Once the convex region is defined, a function $f_i(\hat{a}_i)$ can be designed such that $f_i(\hat{a}_i) \leq 0$ and

$$f_i(\hat{a}_i) = -\hat{a}_i + \beta, \tag{4.50}$$

where i corresponds to the i-th joint. When $f_i(\hat{a}_i) \leq 0$, the estimated parameter is inside the convex region (or on its boundary), and hence positive. If $f_i(\hat{a}_i) > 0$ the parameter $\hat{a}_i$ is outside the admissible parameter set, and then it is necessary to project it onto the set Ω_i. Figure 4.6 illustrates those situations.

In order to ensure the estimation of positive parameters, Equation (4.47) is redefined

[6]Condition number is defined as σ_1/σ_n, where σ_1 is the largest singular value and σ_n is the smallest one. The best conditioning occurs when $\sigma_1/\sigma_n = 1$.

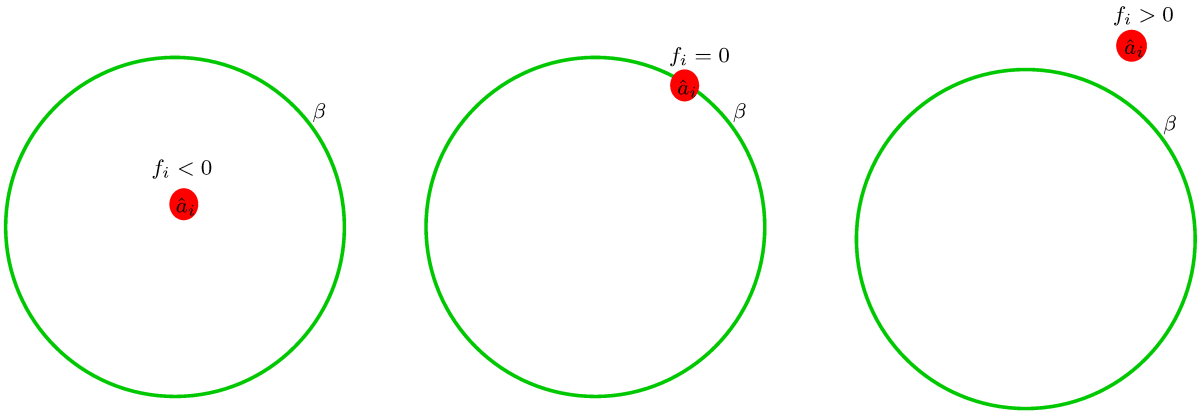

Figure 4.6: The convex region is illustrated by the circles. When the parameters $\hat{a}_i$ are inside the region, $\hat{a}_i > \beta$, and thus $\hat{a}_i > 0$. When they are on the border, $\hat{a}_i = \beta$, and thus $\hat{a}_i > 0$. When the parameters are outside the convex region, $\hat{a}_i < \beta$ and $\hat{a}_i$ may be negative, which is undesired. In this situation, all parameters outside the region must be projected onto the region.

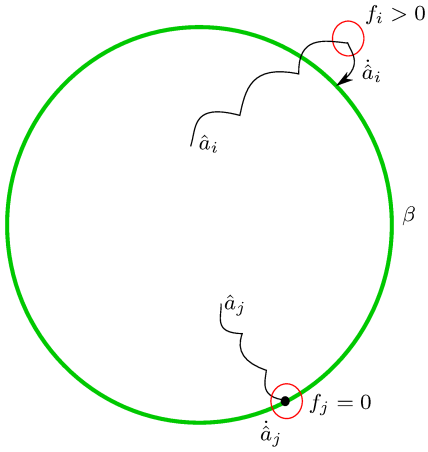

Figure 4.7: If the parameter $\hat{a}_i$ is on the border of the region Ω_i, $f_i = 0$ (or outside it, $f_i > 0$), and the update $\dot{\hat{a}}_i$ makes it leave the region (or remain outside), then the parameter will be projected onto the border of the region.

as (Wang & Xie, 2011)

$$\dot{\hat{a}}_i = \begin{cases} -\gamma_i \lambda \nabla f_{i,\hat{a}_i}, & \text{if } f_i \geq 0 \text{ and } \nu_i \nabla f_{i,\hat{a}_i} \geq 0 \\ \nu_i, & \text{otherwise,} \end{cases} \tag{4.51}$$

where $\nu_i \triangleq -\gamma_i \ddot{q}_{ri} s_i$ is the i-th element of the *nominal* adaptation vector $\dot{\boldsymbol{a}}_m$ in Equation (4.47), γ_i is the i-th element of the diagonal of $\boldsymbol{L}$, $\ddot{q}_{ri}$ is the i-th element of $\ddot{\boldsymbol{q}}_r$, s_i is the i-th element of $\boldsymbol{s}$, the scalar λ is a positive value and $\nabla f_{i,\hat{a}_i} = {}^{df_i}/_{d\hat{a}_i} = -1$.

Equation (4.51) guarantees that, if the parameter $\hat{a}_i$ is on the border of the region Ω_i (or outside it), and the update $\dot{\hat{a}}_i$ makes it leave the region (or remain outside), then the parameter will be projected onto the border of the region, as illustrated in Figure 4.7.

Adding an Arbitrary Positive Definite Matrix (ACD) The solution proposed in section 4.3.1.3 guarantees that the estimated parameters remain positive, and thus the added matrix is positive definite, as well as the result of the sum. nitializing the parameters with values such that the resultant matrix starts better conditioned than the original JSIM, according to Theorem 4.3 below, and considering that the condition number does not change significantly along the simulation, the resultant matrix will be better conditioned than the pure JSIM. However, there is no guarantee that the better conditioning will persist at all time. Therefore, it is proposed here another solution where the positive definite matrix $\bar{\boldsymbol{D}} \in GL(n)$ is carefully chosen to be added to the JSIM in order to ensure the improvement of its conditioning. To accomplish that, it is necessary to find the desired characteristics of $\bar{\boldsymbol{D}}$ in order to the sum $\left(\boldsymbol{M} + \bar{\boldsymbol{D}}\right)$ be, besides positive definite, also better conditioned than $\boldsymbol{M} \triangleq \boldsymbol{M}(\boldsymbol{q})$.

Theorem 4.3. *For the condition number of the sum $\left(\boldsymbol{M} + \bar{\boldsymbol{D}}\right)$, where $\boldsymbol{M}$ is the joint-space inertia matrix and $\bar{\boldsymbol{D}}$ is a positive definite matrix with the same left singular vectors of $\boldsymbol{M}$, be smaller than the one of $\boldsymbol{M}$, the matrix $\bar{\boldsymbol{D}}$ must be better conditioned than $\boldsymbol{M}$.*

Proof. Since the condition number of $\boldsymbol{M}$ is given by

$$\operatorname{cond}(\boldsymbol{M}) = \frac{\sigma_{1_{\boldsymbol{M}}}}{\sigma_{n_{\boldsymbol{M}}}},$$

where $\sigma_{1_{\boldsymbol{M}}}$ and $\sigma_{n_{\boldsymbol{M}}}$ are the maximum and minimum singular values of $\boldsymbol{M}$, respectively, we can decrease the condition number by chosen an appropriate matrix $\bar{\boldsymbol{D}}$ such that $\operatorname{cond}\left(\boldsymbol{M} + \bar{\boldsymbol{D}}\right) < \operatorname{cond}(\boldsymbol{M})$. Since $\boldsymbol{M}$ can be decomposed into $\boldsymbol{M} = \boldsymbol{U}\boldsymbol{S}\boldsymbol{U}^T$, where each column $\boldsymbol{u}_i$, with $i \in \{1, \ldots, n\}$, of $\boldsymbol{U} \in O(n)$ contains the left singular vectors of $\boldsymbol{M}$ and $\boldsymbol{S} \in \mathbb{R}^{n \times n}$ contains the singular values of $\boldsymbol{M}$ (Chen, 1999), $\bar{\boldsymbol{D}} = \boldsymbol{U}\boldsymbol{D}\boldsymbol{U}^T$ is defined as a positive definite matrix, where $\mathbb{R}^{n \times n} \ni \boldsymbol{D} = \operatorname{diag}\left(\sigma_{1_{\bar{\boldsymbol{D}}}}, \ldots, \sigma_{n_{\bar{\boldsymbol{D}}}}\right)$ is a suitable diagonal matrix. Then,

$$\begin{aligned} \boldsymbol{M} + \bar{\boldsymbol{D}} &= \boldsymbol{U}(\boldsymbol{S} + \boldsymbol{D})\boldsymbol{U}^T \\ &= \boldsymbol{U}\left(\begin{bmatrix} \sigma_{1_{\boldsymbol{M}}} + \sigma_{1_{\bar{\boldsymbol{D}}}} & & \\ & \ddots & \\ & & \sigma_{n_{\boldsymbol{M}}} + \sigma_{n_{\bar{\boldsymbol{D}}}} \end{bmatrix}\right)\boldsymbol{U}^T. \end{aligned} \tag{4.52}$$

Therefore,

$$\operatorname{cond}\left(\boldsymbol{M} + \bar{\boldsymbol{D}}\right) = \frac{\sigma_{1_{\boldsymbol{M}+\bar{\boldsymbol{D}}}}}{\sigma_{n_{\boldsymbol{M}+\bar{\boldsymbol{D}}}}} = \frac{\sigma_{1_{\boldsymbol{M}}} + \sigma_{1_{\bar{\boldsymbol{D}}}}}{\sigma_{n_{\boldsymbol{M}}} + \sigma_{n_{\bar{\boldsymbol{D}}}}}.$$

In order to $\operatorname{cond}\left(\boldsymbol{M} + \bar{\boldsymbol{D}}\right) < \operatorname{cond}(\boldsymbol{M})$,

$$\frac{\sigma_{1_{\boldsymbol{M}}} + \sigma_{1_{\bar{\boldsymbol{D}}}}}{\sigma_{n_{\boldsymbol{M}}} + \sigma_{n_{\bar{\boldsymbol{D}}}}} < \frac{\sigma_{1_{\boldsymbol{M}}}}{\sigma_{n_{\boldsymbol{M}}}} \Longrightarrow \frac{\sigma_{1_{\bar{\boldsymbol{D}}}}}{\sigma_{n_{\bar{\boldsymbol{D}}}}} < \frac{\sigma_{1_{\boldsymbol{M}}}}{\sigma_{n_{\boldsymbol{M}}}} \Longrightarrow \operatorname{cond}\left(\bar{\boldsymbol{D}}\right) < \operatorname{cond}(\boldsymbol{M}). \tag{4.53}$$

Therefore, for $\text{cond}\left(\boldsymbol{M}+\bar{\boldsymbol{D}}\right) < \text{cond}\left(\boldsymbol{M}\right)$, it is necessary that $\text{cond}\left(\bar{\boldsymbol{D}}\right) < \text{cond}\left(\boldsymbol{M}\right)$. □

As the condition number of $\bar{\boldsymbol{D}}$ is directly linked to $\boldsymbol{D}$, it is easier to choose a diagonal matrix $\boldsymbol{D}$ to meet the property showed in Equation (4.53). Using Equation (4.45) and $\boldsymbol{\mathcal{A}} \triangleq \bar{\boldsymbol{D}}$ yields

$$\left[\boldsymbol{M}\left(\boldsymbol{q}\right)+\bar{\boldsymbol{D}}\right]\ddot{\boldsymbol{q}}_r+\boldsymbol{C}\left(\boldsymbol{q},\dot{\boldsymbol{q}}\right)\dot{\boldsymbol{q}}_r+\boldsymbol{g}\left(\boldsymbol{q}\right)=\boldsymbol{Y}_\sigma\left(\boldsymbol{q},\ddot{\boldsymbol{q}}_r\right)\boldsymbol{a}_\sigma+\boldsymbol{v}\left(\boldsymbol{q},\dot{\boldsymbol{q}},\dot{\boldsymbol{q}}_r,\ddot{\boldsymbol{q}}_r\right), \tag{4.54}$$

which yields $\boldsymbol{Y} \triangleq \boldsymbol{Y}_\sigma\left(\boldsymbol{q},\ddot{\boldsymbol{q}}_r\right)\boldsymbol{a}_\sigma = \bar{\boldsymbol{D}}\ddot{\boldsymbol{q}}_r$, where $\boldsymbol{a}_\sigma = \begin{bmatrix}\sigma_{1_{\overline{\boldsymbol{D}}}} & \cdots & \sigma_{n_{\overline{\boldsymbol{D}}}}\end{bmatrix}^T$ is the vector with the singular values of $\bar{\boldsymbol{D}}$. Since

$$\begin{aligned}
\bar{\boldsymbol{D}}\ddot{\boldsymbol{q}}_r &= \boldsymbol{U}\boldsymbol{D}\boldsymbol{U}^T\ddot{\boldsymbol{q}}_r \\
&= \boldsymbol{U}\begin{bmatrix}\sigma_{1_{\bar{\boldsymbol{D}}}} & & \\ & \ddots & \\ & & \sigma_{n_{\bar{\boldsymbol{D}}}}\end{bmatrix}\boldsymbol{U}^T\ddot{\boldsymbol{q}}_r \\
&= \sum_{i=1}^{n}\underbrace{\boldsymbol{u}_i\boldsymbol{u}_i^T\ddot{\boldsymbol{q}}_r}_{\boldsymbol{y}_{\sigma_i}}\sigma_{i_{\overline{\boldsymbol{D}}}} \\
&= \begin{bmatrix}\boldsymbol{y}_{\sigma_1} & \cdots & \boldsymbol{y}_{\sigma_n}\end{bmatrix}\begin{bmatrix}\sigma_{1_{\overline{\boldsymbol{D}}}} \\ \vdots \\ \sigma_{n_{\overline{\boldsymbol{D}}}}\end{bmatrix} \\
&= \boldsymbol{Y}_\sigma\left(\boldsymbol{q},\ddot{\boldsymbol{q}}_r\right)\boldsymbol{a}_\sigma,
\end{aligned}$$

the regressor is given by $\boldsymbol{Y}_\sigma\left(\boldsymbol{q},\ddot{\boldsymbol{q}}_r\right) = \begin{bmatrix}\boldsymbol{y}_1 & \cdots & \boldsymbol{y}_n\end{bmatrix}$, where $\boldsymbol{y}_i = \boldsymbol{u}_i\boldsymbol{u}_i^T\ddot{\boldsymbol{q}}_r$. In Equation (4.46), the vector $\hat{\boldsymbol{a}} \triangleq \hat{\boldsymbol{a}}_\sigma$ contains the estimated values of $\boldsymbol{a}_\sigma$, and thus the goal is to enforce $\boldsymbol{Y}_\sigma\left(\boldsymbol{q},\ddot{\boldsymbol{q}}_r\right)\hat{\boldsymbol{a}}_\sigma = \bar{\boldsymbol{D}}\ddot{\boldsymbol{q}}_r$.

Assuming $\boldsymbol{u} \triangleq \boldsymbol{\tau}$, the closed-loop dynamics is analogous to Equation (4.48) and is given by

$$\left[\boldsymbol{M}\left(\boldsymbol{q}\right)+\bar{\boldsymbol{D}}\right]\dot{\boldsymbol{s}}+\boldsymbol{C}\left(\boldsymbol{q},\dot{\boldsymbol{q}}\right)\boldsymbol{s}-\boldsymbol{a}_q+\boldsymbol{Y}_\sigma\left(\boldsymbol{q},\ddot{\boldsymbol{q}}_r\right)\Delta\boldsymbol{a}_\sigma=\boldsymbol{0} \tag{4.55}$$

where $\Delta\boldsymbol{a}_\sigma = \boldsymbol{a}_\sigma - \hat{\boldsymbol{a}}_\sigma$.

Estimation of Positive Parameters In order to enforce the estimated parameters in $\hat{\boldsymbol{a}}_\sigma$ to be positive and also to have a matrix $\bar{\boldsymbol{D}}$ that fulfills condition Equation (4.53), a convex region corresponding to the admissible parameter set is defined (Wang & Xie, 2011). Thus, variable lower ($\beta_{\min}$) and upper ($\beta_{\max}$) bounds are defined as a function of the singular values of the JSIM such that $\sigma_{n_{\boldsymbol{M}}} < \beta_{\min} \neq \beta_{\max} < \sigma_{1_{\boldsymbol{M}}}$. Therefore, the

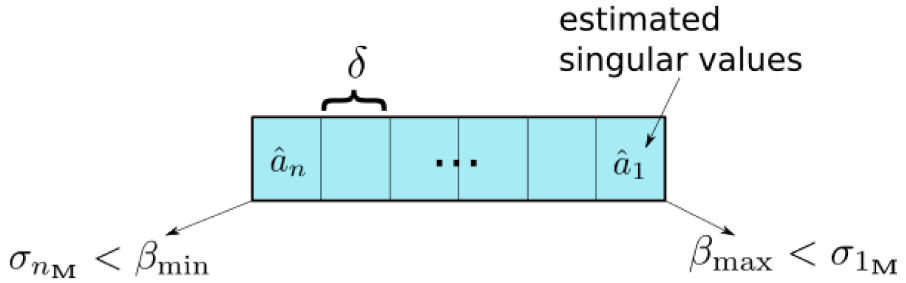

Figure 4.8: Region $\boldsymbol{\Omega}$ with its lower and upper bounds $\beta_{\min}$ and $\beta_{\max}$. The estimated singular values are decreasingly ordered inside the subregions of size δ.

convex region of admissible parameters is defined as

$$\boldsymbol{\Omega} \triangleq \{\boldsymbol{\eta}_{\min} \leq \hat{\boldsymbol{a}} \leq \boldsymbol{\eta}_{\max}\},$$

where

$$\begin{aligned}\boldsymbol{\eta}_{\max} &\triangleq \mathbf{1}_n\beta_{\max} - \operatorname{diag}(0,\ldots,n-1)\,\mathbf{1}_n\delta,\\ \boldsymbol{\eta}_{\min} &\triangleq \mathbf{1}_n\beta_{\max} - \operatorname{diag}(1,\ldots,n)\,\mathbf{1}_n\delta,\end{aligned}$$

with $\mathbf{1}_n$ being an n-dimensional vector of ones, and $\delta \triangleq (\beta_{\max} - \beta_{\min})/n$; therefore, the estimated singular values are decreasingly ordered and between the upper and lower bounds. The region with the estimated parameters are illustrated in Figure 4.8.

The adaptation law is defined as

$$\dot{\hat{\boldsymbol{a}}}_\sigma \triangleq \boldsymbol{P}\boldsymbol{\upsilon} + (\boldsymbol{I}_{n\times n} - \boldsymbol{P})\boldsymbol{L}\boldsymbol{\Lambda}\boldsymbol{\rho}, \tag{4.56}$$

where $\boldsymbol{\upsilon}$ is the nominal adaptive law Equation (4.47) and $\boldsymbol{I}_{n\times n} \in \mathbb{R}^{n\times n}$ is the identity matrix. The matrix $\boldsymbol{P} = \operatorname{diag}(p_1,\ldots,p_n)$, where

$$p_i = \begin{cases} 0, & \text{if } (\hat{a}_i < \eta_{\min,i} \wedge \upsilon_i \leq 0) \vee (\hat{a}_i > \eta_{\max,i} \wedge \upsilon_i \geq 0),\\ 1, & \text{otherwise,}\end{cases}$$

is used to determine if a given parameter shall be projected onto the border of the region, $\boldsymbol{\Lambda} = \operatorname{diag}(\lambda_1,\ldots,\lambda_n)$ with $\lambda_i \in (0,\infty)$ is used to accelerate the convergence of each parameter to the boundary of $\boldsymbol{\Omega}$, and $\boldsymbol{\rho} = [\rho_1,\ldots,\rho_n]^T$ with $\rho_i = \operatorname{sgn}(\eta_{\min,i} - \hat{a}_i)$ is used to choose the direction of convergence, as illustrated in Figure 4.9.

4.3.2 Task-Space Controllers

A given task is typically described in terms of the desired pose of the end-effector, in which the use of a task-space controller is thus more appropriate since it does not need

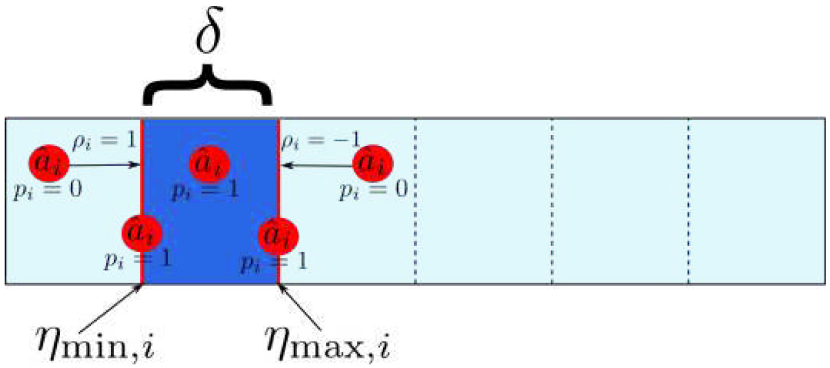

Figure 4.9: Projection of the parameter into the region. If the estimated parameter $\hat{a}_i$ is outside the region and the update υ_i makes it to remain outside, then $p_i = 0$ and the parameter will be projected onto the border of the region. The direction of the projection is defined by ρ_i, which is changed whenever $\hat{a}_i$ is smaller or larger than $\eta_{\min,i}$. If $p_i = 1$, then the nominal adaptation law is used.

the inverse kinematics in order to find the joint trajectory. Therefore, the same dynamic controllers are described here but now in task-space. The two classic task-space motion controllers, namely the task-space inverse dynamics with feedback linearization (TIDFL) and task-space PID controller with gravity compensation (TPID), are adapted to use the unit DQ to represent the end-effector pose, which offers some advantages, as discussed in section 3.1.

4.3.2.1 Task-Space Inverse Dynamics with Feedback Linearization (TIDFL)

As previously discussed, one common controller for torque-actuated robots is based on the inverse dynamics with feedback linearization (Spong et al., 2006); that is,

$$\boldsymbol{u} = \boldsymbol{M}(\boldsymbol{q})\,\boldsymbol{a}_q + \boldsymbol{C}(\boldsymbol{q}, \dot{\boldsymbol{q}})\,\dot{\boldsymbol{q}} + \boldsymbol{g}(\boldsymbol{q}), \tag{4.57}$$

where the control input $\boldsymbol{u} \triangleq \boldsymbol{\tau} \in \mathbb{R}^n$ is applied to the joints and $\boldsymbol{a}_q \triangleq \ddot{\boldsymbol{q}} \in \mathbb{R}^n$ is the control law designed to stabilize the linearized closed-loop system.

Seeking a task-space controller, the control law for the linearized closed-loop system is defined as

$$\boldsymbol{a}_q = \boldsymbol{J}^{+}\left(\boldsymbol{a}_x - \dot{\boldsymbol{J}}\dot{\boldsymbol{q}}\right), \tag{4.58}$$

where $\boldsymbol{J}^{+}$ is the Moore–Penrose pseudoinverse of the Jacobian matrix $\boldsymbol{J} \in \mathbb{R}^{8\times n}$ and $\boldsymbol{a}_x \triangleq \operatorname{vec}_8 \ddot{\underline{\boldsymbol{x}}}$ is given by

$$\boldsymbol{a}_x = \operatorname{vec}_8 \ddot{\underline{\boldsymbol{x}}}_d - \boldsymbol{K}_D \operatorname{vec}_8 \dot{\underline{\boldsymbol{x}}}_e - \boldsymbol{K}_P \operatorname{vec}_8 \underline{\boldsymbol{x}}_e - \boldsymbol{K}_I \int_0^t \operatorname{vec}_8 \underline{\boldsymbol{x}}_e dt, \tag{4.59}$$

where $\boldsymbol{K}_D, \boldsymbol{K}_P, \boldsymbol{K}_I \in \mathbb{R}^{8\times 8}$ are positive definite gain matrices and $\underline{\boldsymbol{x}}_e \triangleq \underline{\boldsymbol{x}} - \underline{\boldsymbol{x}}_d$ denotes

the end-effector error, with $\underline{\boldsymbol{x}}_d \in \underline{\boldsymbol{\mathcal{S}}}$ being the desired end-effector pose.

4.3.3 Task-Space PID Controller with Gravity Compensation (TPID)

The PID controller with gravity compensation in task-space and using the DQ to represent the end-effector pose is given by

$$\boldsymbol{u} = \boldsymbol{J}^{+}\boldsymbol{a}_x + \boldsymbol{g}\left(\boldsymbol{q}\right), \tag{4.60}$$

with $\boldsymbol{a}_x$ given by Equation (4.59).

4.3.4 Task-Space Adaptive Controller (TAC)

The adaptive control law in task-space is given by

$$\boldsymbol{u} = \boldsymbol{J}^{T}\boldsymbol{a}_x + \boldsymbol{v}\left(\boldsymbol{q}, \dot{\boldsymbol{q}}, \dot{\boldsymbol{q}}_r, \ddot{\boldsymbol{q}}_r\right) + \boldsymbol{Y}_{\sigma}\left(\boldsymbol{q}, \ddot{\boldsymbol{q}}_r\right)\hat{\boldsymbol{a}}_{\sigma}, \tag{4.61}$$

where $\boldsymbol{a}_x$ is given by Equation (4.59), $\boldsymbol{v}\left(\boldsymbol{q}, \dot{\boldsymbol{q}}, \dot{\boldsymbol{q}}_r, \ddot{\boldsymbol{q}}_r\right) \in \mathbb{R}^n$ is the vector containing the known dynamic model (i.e., $\boldsymbol{v}\left(\boldsymbol{q}, \dot{\boldsymbol{q}}, \dot{\boldsymbol{q}}_r, \ddot{\boldsymbol{q}}_r\right) = \boldsymbol{M}\left(\boldsymbol{q}\right)\ddot{\boldsymbol{q}}_r + \boldsymbol{C}\left(\boldsymbol{q}, \dot{\boldsymbol{q}}\right)\dot{\boldsymbol{q}}_r + \boldsymbol{g}\left(\boldsymbol{q}\right)$), where

$$\begin{aligned}
\dot{\boldsymbol{q}}_r &= \boldsymbol{J}^{+}\operatorname{vec}_8 \dot{\underline{\boldsymbol{x}}}_r, \\
\ddot{\boldsymbol{q}}_r &= \boldsymbol{J}^{+}\left(\operatorname{vec}_8 \ddot{\underline{\boldsymbol{x}}}_r - \dot{\boldsymbol{J}}\dot{\boldsymbol{q}}_r\right),
\end{aligned}$$

in which

$$\begin{aligned}
\operatorname{vec}_8 \dot{\underline{\boldsymbol{x}}}_r &= \operatorname{vec}_8 \dot{\underline{\boldsymbol{x}}}_d - \alpha \operatorname{vec}_8 \underline{\boldsymbol{x}}_e, \\
\operatorname{vec}_8 \ddot{\underline{\boldsymbol{x}}}_r &= \operatorname{vec}_8 \ddot{\underline{\boldsymbol{x}}}_d - \alpha \operatorname{vec}_8 \dot{\underline{\boldsymbol{x}}}_e,
\end{aligned}$$

with $\alpha \in (0, \infty)$.

The adaptation law is equal to the ones used in the joint-space, that is, Equation (4.51) and Equation (4.56).

4.4 Conclusion

The admittance controllers are appropriate when dealing with interaction wrenches since they allow the control of the robot apparent impedance. When performing human-robot cooperation tasks, specially manipulation tasks, one has to control not only the impedance but also the robot end-effector pose. For this purpose, we use an admittance controller together with a motion controller, which can be a kinematic or a dynamic controller,

depending if the robot joints are actuated in position/velocity or torque. Therefore, this chapter covered the design of an admittance controller using DQ, as well as the design of kinematics controllers, in addition to a discussion about some known dynamic motion control laws and a proposed solution to improve the conditioning of manipulators' JSIM using an adaptive controller.

Using the structure proposed by Caccavale & Villani (2000); Caccavale et al. (2008) and de Gea & Kirchner (2008), the whole controller consists of an admittance controller that, given a desired pose $\underline{\boldsymbol{x}}_d$ and an interaction wrench $\underline{\varsigma}$, returns a compliant reference pose $\underline{\boldsymbol{x}}_c$. This reference pose is the one passed to the motion controller, which drives the end-effector pose to the compliant one.

5

Simulation and Experimental Results

This chapter presents some simulation and experimental results related to both admittance and motion controllers, which were discussed in Chapter 4. In order to evaluate the proposed techniques, simulations were executed on MATLAB R2015a[1] using the DQ Robotics library (Adorno & Marinho, 2020) in a machine running Windows 7 Home Premium 64 bits, 6Gb of RAM, and an Intel(R) Core(TM) i5-2410M CPU @ 2.30GHz processor. The model used for the first simulations is the one of the KUKA LBR4+ robot (see Appendix A), available in V-REP (Rohmer et al., 2013), and for the other simulations, the model of the KUKA LWR4+ is used (see Appendix B).[2]Moreover, experiments were run on a KUKA LWR4+ robot manipulator, equipped with a computer with two Intel Xeon 2.4 GHz hexacore processors with 32 Gb of RAM each, and a 64-bit Anarchy Linux version 1.4 (Linux 4.19.50-rt22-2-rt-lts) using the C++ version of DQ Robotics and the pid framework.[3] The KUKA LWR4+ used in the experiments is part of the BAZAR robot and is equipped with one ATI Mini 45 force/torque sensor at its end-effector (Cherubini et al., 2019). Hence, it only reacts to wrenches applied at the end-effector.

First, some simulations were run in order to corroborate the discussion done in section 2.1.2. For this, the KUKA LBR4+ robot model was used to analyze its behavior under zero torque on its joints. Furthermore, to see the effect of the number of links in the JSIM's conditioning, two other robot models were created by locking the last robot's

[1]1http://www.mathworks.com/products/matlab/

[2]By the time these simulations were run, the dynamic model of the real robot KUKA LWR4+ was not available for us. Due to this fact, some simulations were run with the V-REP model.

[3]http://pid.lirmm.net/pid-framework/

joints, resulting in a robot with fewer links.

Still using the KUKA LBR4+ model, simulations were run to compare the values of the estimated parameters of the adaptive controller and the adaptive controller with the projection to the convex region, as described in section 4.3.1.3. The goal is to see the effect of the sampling time on the estimated parameters, and to compare the performance of the three dynamic controllers described in Chapter 4, that is, the IDFL, the PID, and the ACM, all in joint-space.

Still considering the joint-space controllers, we performed experiments to compare the three controllers, but the adaptive controller is run with the algorithm that guarantees the improvement of the JSIM conditioning (ACD). Lastly, we show the dynamic controllers in task-space, together with the admittance controller using the DQ logarithmic mapping given by Equation (4.2).

Also, experiments were performed using the controller of Equation (4.20), which improves upon the controller of Equation (4.2) by providing a physical meaning to the parameters. Moreover, a comparison was done with one of the state-of-art controllers. All these experiments were executed using the second order kinematic controller of Equation (4.37) in the inner-loop, and the admittance controller in the outer-loop.

In order to show the unwinding phenomenon present when using the controller in Equation (4.20), we performed a simulation using a free-flying rigid body. Furthermore, the same simulation was done with Equation (4.20) plus the solution in Equation (4.24), to show that the problem disappears.

Lastly, simulations with the admittance controller considering the lever-arm effect were done considering the whole-body of BAZAR.

5.1 Dynamic Analysis of a Robot Manipulator

To guarantee safety in manipulation tasks subject to contacts, besides regulating the contact forces, it is important to design a motion controller that ensures stability, or better, asymptotic stability of the closed-loop system. Considering a manipulator, some unexpected behaviors may arise owing to the ill-conditioning of the inertia matrix, when using the dynamic model of the robot, as shown in section 2.1.2. Thus, in order to better understand the influence of this ill-conditioning, some simulations were performed to analyze the dynamic behavior of the KUKA LBR4+.

First, no torque was applied to the complete model of KUKA LBR4+, with 7 DOF. After, some modifications were made to the robot model to observe its behavior with less links.

The simulations were run with a sample time of $T = 25\,\text{ms}$.

5.1.1 Behavior of KUKA LBR4+ In the Absence of Torque

Using the dynamic model of the KUKA LBR4+ (see Appendix A), Equation (3.52) was used to obtain the joints' acceleration and then to obtain the joints' velocities and positions by integration:

$$\begin{aligned}
\ddot{\boldsymbol{q}}\left[k+1\right] &= \boldsymbol{M}^{-1}\left(\boldsymbol{q}\left[k\right]\right)\left[\boldsymbol{\tau} - \boldsymbol{C}\left(\boldsymbol{q}\left[k\right], \dot{\boldsymbol{q}}\left[k\right]\right)\dot{\boldsymbol{q}}\left[k\right] - \boldsymbol{g}\left(\boldsymbol{q}\left[k\right]\right) - \boldsymbol{\tau}_{\text{friction}}\left[k\right]\right], \\
\dot{\boldsymbol{q}}\left[k+1\right] &= \dot{\boldsymbol{q}}\left[k\right] + T\ddot{\boldsymbol{q}}\left[k+1\right], \\
\boldsymbol{q}\left[k+1\right] &= \boldsymbol{q}\left[k\right] + T\dot{\boldsymbol{q}}\left[k+1\right],
\end{aligned} \tag{5.1}$$

where the torque $\boldsymbol{\tau}$ is always zero and $\boldsymbol{\tau}_{\text{friction}}\left[k\right] = 0.01\dot{\boldsymbol{q}}\left[k\right]$ is an added friction to make the robot dissipate energy. The initial configuration was

$$\boldsymbol{q}\left[0\right] = \begin{bmatrix} 0.3207 & -2.2062 & 0.3014 & 0 & 0 & 0 & 0 \end{bmatrix}^T$$

and both initial velocity and acceleration were zero.

When some friction is considered during the simulation, it is expected that the robot moves until all the energy is dissipated. However, the manipulator moved while increasing its velocity, until a very high velocity be obtained, as showed in Figure 5.1, which leads to unstable behavior.

As shown in Chapter 2, there is an intrinsic problem to open kinematic serial chains, which is the ill-conditioning of their inertia matrices. Indeed, as presented in Figure 5.3, the condition number of the robot's inertia matrix $\boldsymbol{M}\left(\boldsymbol{q}\right)$ is very high, reaching values close to 15×10^3. This ill-conditioning explains the observed behavior. Although the matrix $\boldsymbol{M}\left(\boldsymbol{q}\right)$ is invertible, the Frobenius norm of $\boldsymbol{M}\left(\boldsymbol{q}\right)^{-1}$ may be high $\left(\text{e.g. } \left\|\boldsymbol{M}\left(\boldsymbol{q}\left[0\right]\right)^{-1}\right\|_F = 3.8901 \times 10^3\right)$, which means that, when using Equation (5.1) to simulate the robot, the joints' accelerations are also very high, and thus its velocity, which leads to an unstable behavior due to numerical ill-conditioning caused by the high condition number of the inertia matrix, as observed.

5.1.2 Behavior of a Modified KUKA LBR4+ Under Zero Torque

In order to verify that the ill-conditioning of the inertia matrix was due to the difference between the size and number of links (Featherstone, 2004), other two simulations were run. The last joints of KUKA LBR4+ were locked in such a manner that the modified robot would have less links than the original one, as shown in Figure 5.2.

For both simulations, Equation (5.1) was also used, with $\boldsymbol{\tau} = \boldsymbol{0}$ and $\boldsymbol{\tau}_{\text{friction}} = 0.01\dot{\boldsymbol{q}}$. The initial configuration for the 3-link robot was $\boldsymbol{q}_3\left[0\right] = \begin{bmatrix} 0.3207 & -2.2062 & 0.3014 \end{bmatrix}^T$, while $\boldsymbol{q}_5\left[0\right] = \begin{bmatrix} 0.3207 & -2.2062 & 0.3014 & 0 & 0 \end{bmatrix}^T$ was used for the 5-link robot. Both initial velocity and acceleration were zero.

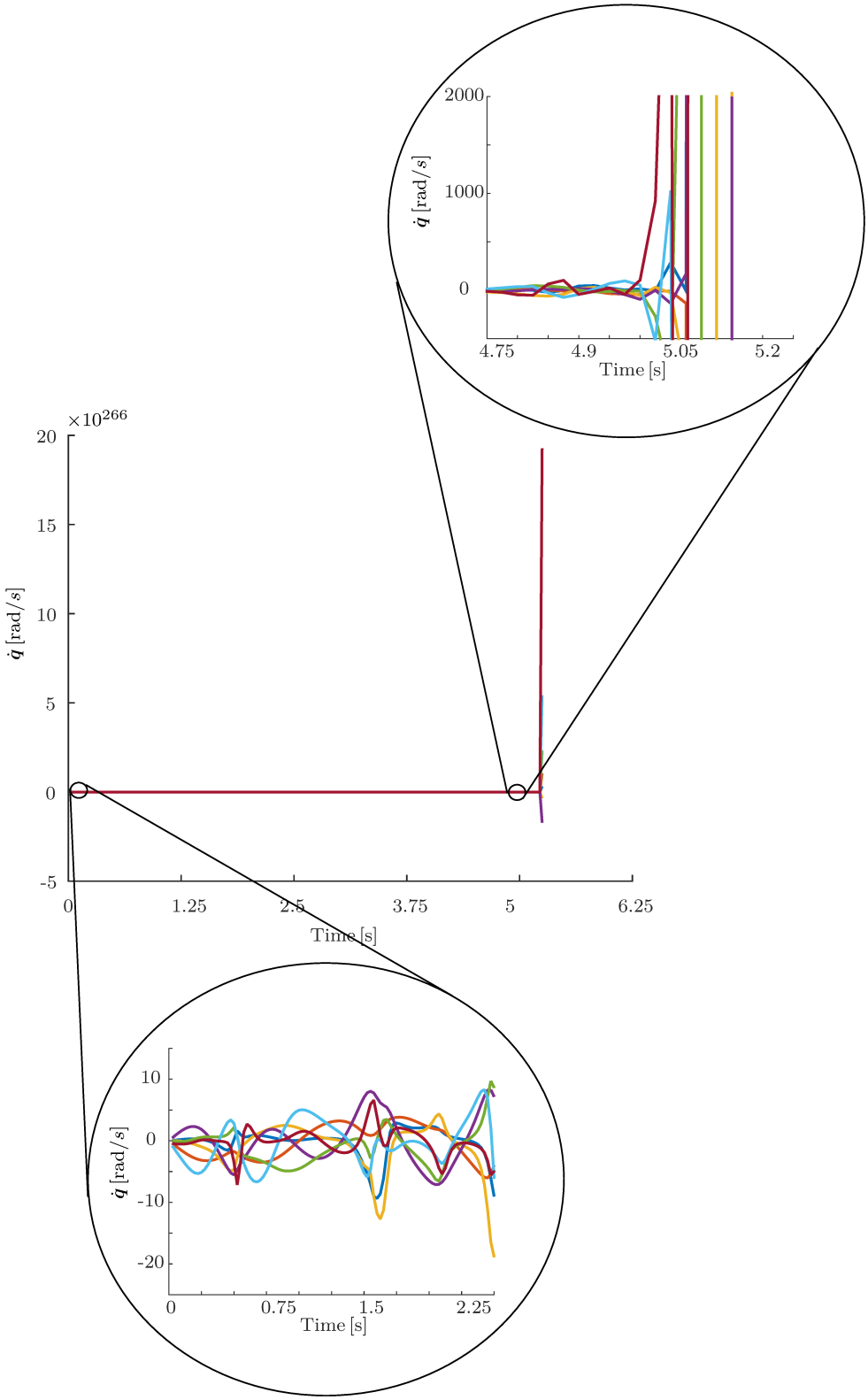

Figure 5.1: Velocity of the robot's joints. After 5 s, the velocity increases rapidly due to numerical ill-conditioning caused by the high condition number of the inertia matrix. Thus, the robot becomes unstable.

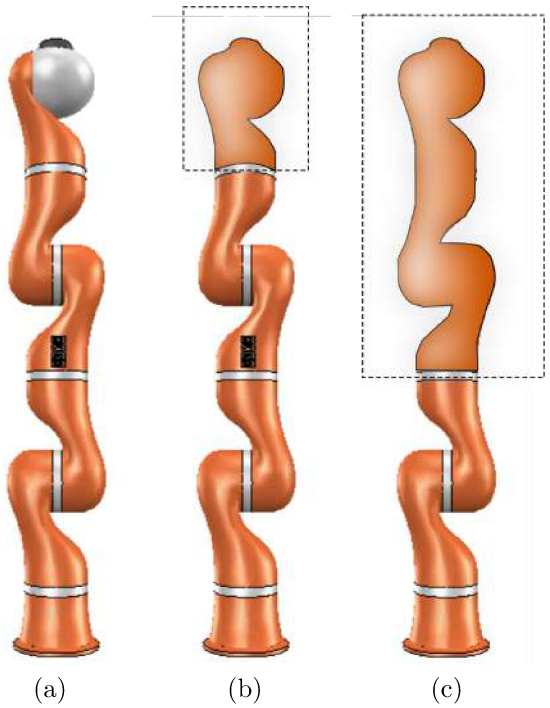

Figure 5.2: Original KUKA LBR4+ and its modifications. *(a)* Original KUKA with 7 DOF. *(b)* KUKA with the last three joints locked, resulting in 5 DOF. *(c)* KUKA with the last five joints locked, resulting in 3 DOF. The coupled links are highlighted by the dashed rectangles.

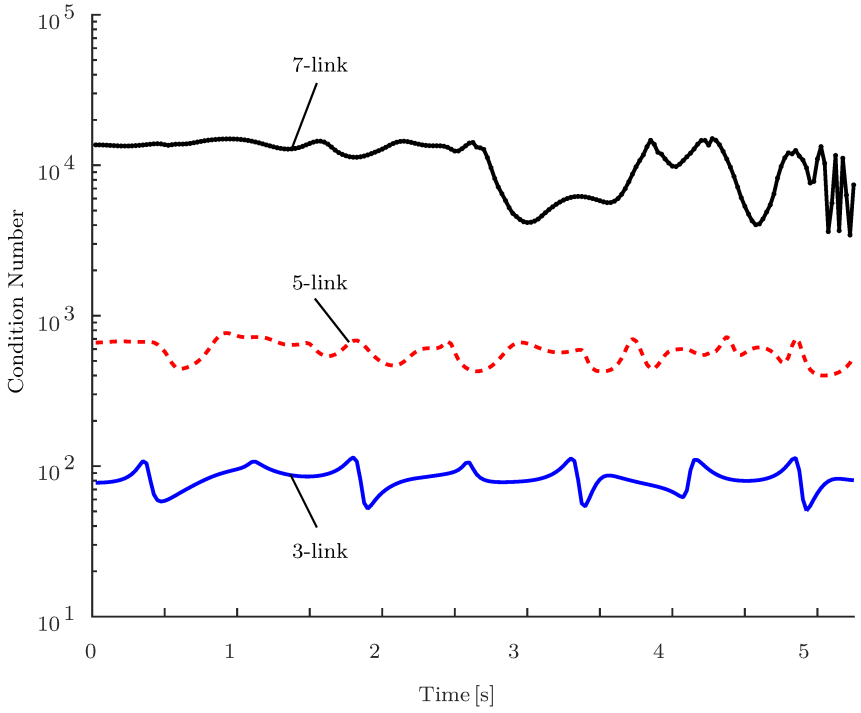

Figure 5.3: Condition number of the inertia matrix of KUKA LBR4+ (original and modified) in logarithm scale. The condition number is very high, depending on the robot configuration, which shows its ill-conditioning.

Comparing the results of the robot with five and three links, the inertia matrix for both cases were better conditioned than the KUKA LBR4+ (Figure 5.3), and that the condition number of the robot with three links was even better than the one with five.

5.2 Simulation Results of Dynamic Joint-Space Controllers

Since serial manipulators have an intrinsic problem that leads to the ill-conditioning of the JSIM, it is important to choose a motion control law that mitigates the effects of this problem. To evaluate the proposed technique and also to compare the motion control laws described in section 4.3, three simulations were run with a seven-link KUKA LBR4+ robot (see Appendix A):

1. In the first simulation, a comparison between the behavior of the AC (Equations (4.46) and (4.47)) and the ACM (Equations (4.46) and (4.51)) was made, concerning the values of the estimated parameters;

2. in the second simulation, the effect of the sampling time was evaluated on the parameter estimation in ACM;

3. last, the third simulation was performed in order to compare the ACM to both PID and IDFL.

For the sake of simulation, two models were considered. The first one, given by Equation (3.52), does not consider the actuators' model and was used as the nominal model. The second one, given by Equation (3.53), explicitly takes into account the actuators' model and was used as the "real" robot.

The simulation sampling time was 25 ms for simulations 1 and 3, whereas simulation 2 used different sampling times. The gain values for all control laws were $\boldsymbol{K}_P = 9\boldsymbol{I}_{7\times7}$, $\boldsymbol{K}_D = 6\boldsymbol{I}_{7\times7}$, and $\boldsymbol{K}_I = 0\boldsymbol{I}_{7\times7}$. For the adaptive controller, $\alpha = 1.5$, $\boldsymbol{L} = 0.15\boldsymbol{I}_{7\times7}$, $\beta = 0.015$, and $\hat{\boldsymbol{a}}_m(0) = \begin{bmatrix}0.1 & 0.05 & 0.04 & 0.03 & 0.02 & 0.02 & 0.02\end{bmatrix}^T$ was the initial estimated parameters vector. The values of the gains, as well as the lower bound β, were chosen empirically. The initial values for the estimated parameters were also chosen empirically; however, it was taken into account the fact that the motors at the base of a serial manipulator are usually larger and heavier than the ones closer to the end-effector, and hence have larger inertia. Therefore, the first values of $\hat{\boldsymbol{a}}_m(0)$ are larger than the last ones.

The robot's initial and desired configurations were $\boldsymbol{q}(0) = \begin{bmatrix}0 & \pi/6 & 0 & -5\pi/9 & 0 & 0 & 0\end{bmatrix}^T$ and $\boldsymbol{q}_d = \begin{bmatrix}0 & \pi/2 & -\pi/2 & -5\pi/9 & 0 & 0 & 0\end{bmatrix}^T$, respectively, as shown in Figure 5.4 and were used in all simulations. In addition, the simulations were executed in 2000 iterations,

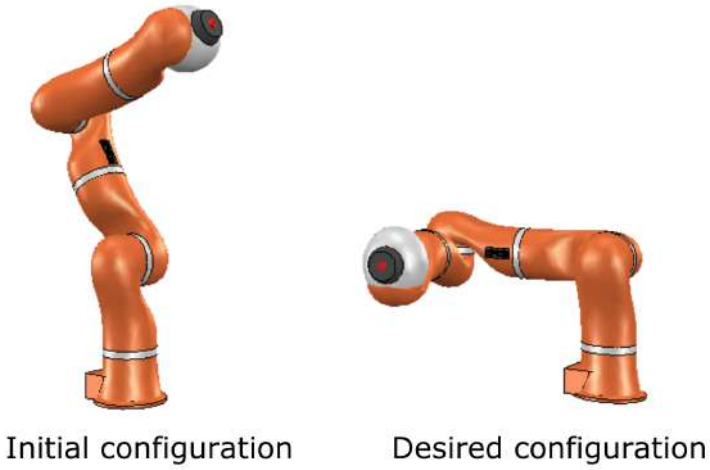

Figure 5.4: Initial and desired configuration of KUKA LBR4+.

which was sufficient for all controllers, except for the IDFL, to achieve steady-state (i.e., $\left\|\dot{\tilde{\boldsymbol{q}}}\right\| \leq 10^{-6}$).

5.2.1 Comparison of Estimated Parameters

The first comparison was done to asses the behavior of the AC (Equations (4.46) and (4.47)) and of the ACM (Equations (4.46) and (4.51)) concerning the values of the estimated parameters.

Figure 5.5a shows that two estimated parameters in the AC have negative values, which is undesirable because the estimated parameters should represent the joints' inertia and gear ratio; consequently they must have positive values. On the other hand, Figure 5.5b shows that all estimated parameters in ACM have positive values, as the theory predicts, which is consistent with the physical meaning of the estimated vector $\hat{\boldsymbol{a}}_m$.

5.2.2 Discretization Effect in Parameters Updating

The discrete form of the algorithm (Equations (4.46) and (4.51)) is necessary when implementing it in a digital computer. Therefore, the Euler integration was used to update the parameters $\hat{a}_i$ in Equation (4.51) according to

$$\hat{\boldsymbol{a}}_m[k+1] = \hat{\boldsymbol{a}}_m[k] + \dot{\hat{\boldsymbol{a}}}_m[k]\,T,$$

where T is the sampling period. The value of λ is determined by the solution to the equation

$$f_i(\hat{a}_i[k+1]) = f_i(\hat{a}_i[k] - \gamma_i \lambda \nabla f_{i,\hat{a}_i} T) = 0, \tag{5.2}$$

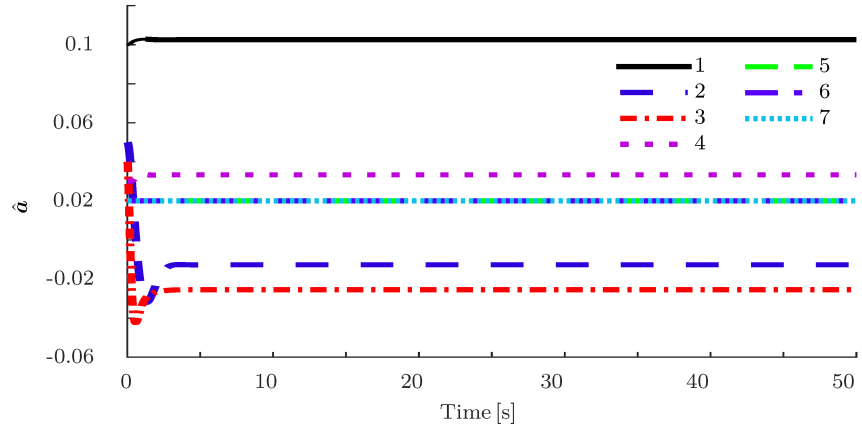

(a) Estimated parameters 2 and 3 are negative, which is undesired.

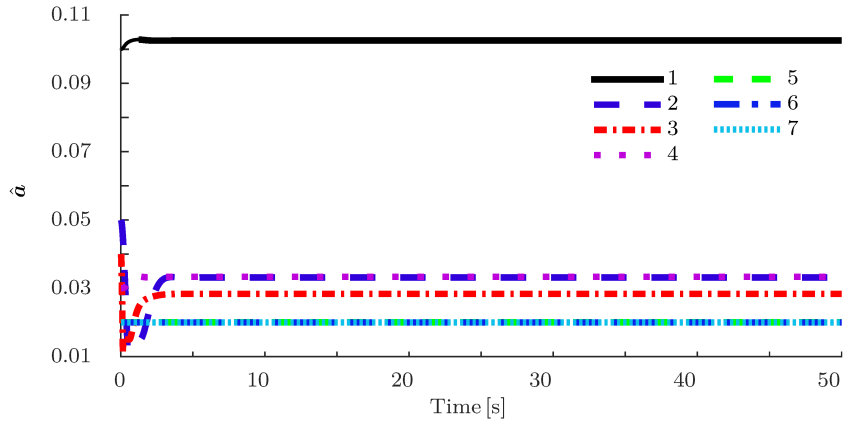

(b) All estimated parameters are positive, as desired. The estimated parameters are the diagonal elements of the matrix $\boldsymbol{M}_m$.

Figure 5.5: Estimated parameters for the (a) AC, and for the (b) ACM.

and indicates the value necessary to project the parameter onto the boundary of Ω_i in one step. From Equation (4.50) and (5.2), it is possible to find a expression for λ:

$$-\left(\hat{a}_i\left[k\right] - \gamma_i \lambda \nabla f_{i,\hat{a}_i} T\right) + \beta = 0,$$

which implies

$$\lambda = \frac{-\hat{a}_i\left[k\right] + \beta}{\gamma_i T}$$

since $\nabla f_{i,\hat{a}_i} = -1$.

Remark 5.1. If the sampling period T is not small enough, some estimated parameters may become temporarily negative until the projection Equation (4.51) is applied in the next step. However, in those situations the resultant matrix $(\boldsymbol{M} + \boldsymbol{M}_m)$ can be temporarily not positive definite, which can be overcome by increasing the value of β or decreasing the sampling period.

Thus, a second simulation was performed using Equations (4.46) and (4.51) to evaluate the effect of the sampling time on the parameter estimation in ACM. Figure 5.6 shows that all estimated parameters are positive in steady-state, although for some values of β and T the parameters can become negative in the transient state. For instance, if $\beta = 10^{-3}$ and $\hat{\boldsymbol{a}}_m\left[0\right] = \left[\begin{array}{ccccccc} 0.05 & 0.05 & 0.05 & 0.05 & 0.05 & 0.05 & 0.05 \end{array}\right]^T$, some parameters can become negative if the sampling time T is not small enough. However, there is a value T for which all parameters are always positive, as shown in Figure 5.6.

5.2.3 Comparison Between Different Motion Controllers

Last, a third simulation was performed in order to compare the ACM to both PID and IDFL. Figure 5.7 shows the error norm of all control laws. Although the error norm decreases for all controllers, the IDFL presents an oscillatory behavior, takes longer to reach the stability point, and exhibits a steady-state error. The PID controller presents a smaller oscillation than the IDFL and reaches the equilibrium point faster and without steady-state error, but the oscillation at the beginning is substantial. The ACM is smoother than both the PID and the IDFL, and the equilibrium point is reached even before the PID controller, also without steady-state error.

Figure 5.8 shows that, for the IDFL, the first four joints reached the desired configurations, but the fifth one took a long time to reach the desired set-point and the last two did not even reach it. This is explained by the difference in the singular values of the inertia matrix, as shown in Figure 5.9. Since the smallest values are almost zero, the correction torques applied to the corresponding joints are much smaller than the dominant one (i.e., the one corresponding to the largest singular value), hence the stationary error is

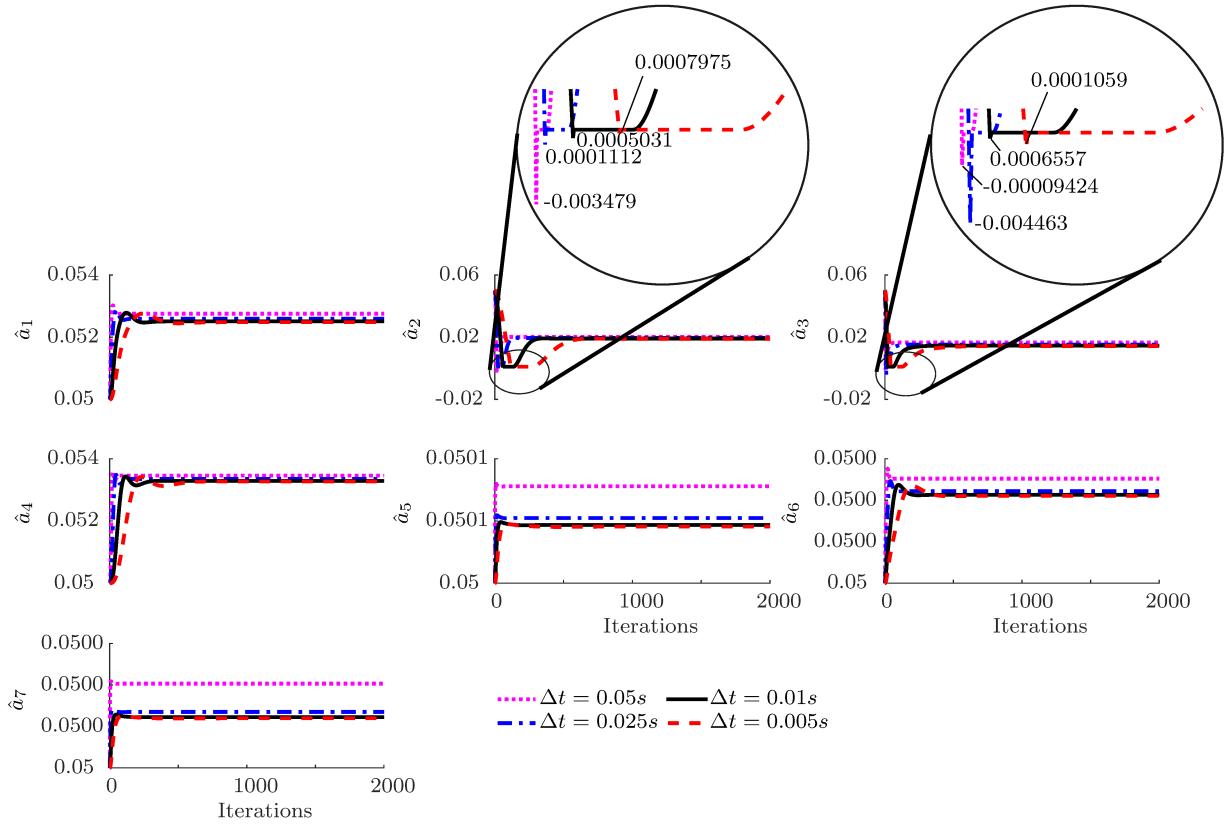

Figure 5.6: Estimated parameters in ACM for four different sampling periods. For $T = 0.05\,\mathrm{s}$ there are two negative parameters, for $T = 0.025\,\mathrm{s}$ there is one negative parameter, and for $T = 0.01\,\mathrm{s}$ and T=0.005 s all parameters are positive.

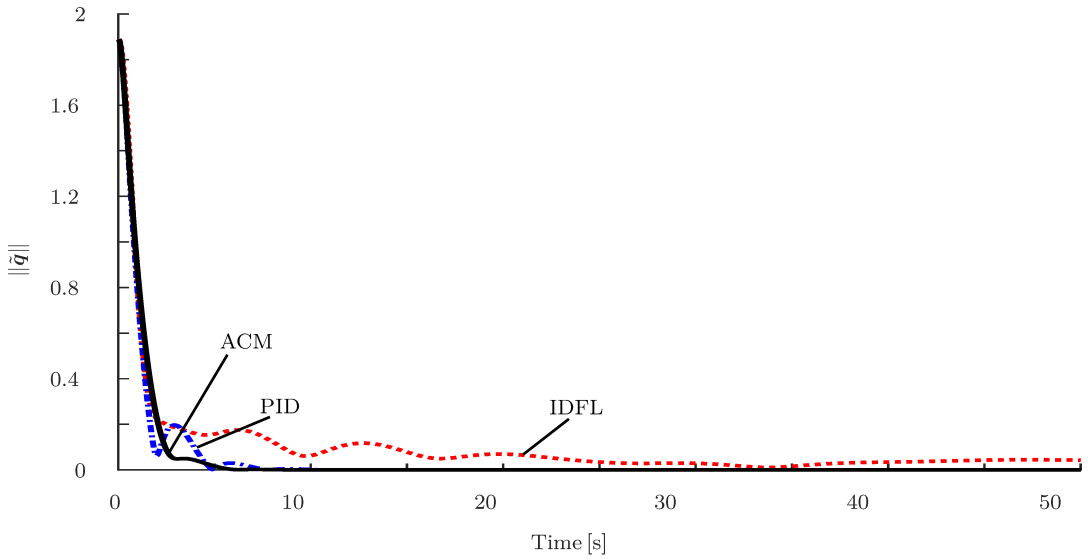

Figure 5.7: Norm of the vector of joints error. The adaptive controller with positive parameters (ACM) presents the smoothest decay among all compared controllers.

observed in those joints, as predicted by Shen & Featherstone (2003). Furthermore, the first and fourth joints have slower time response and larger overshoot for the ACM when compared to the PID controller, although the ACM has smoother overall error dynamics, as previously discussed, and they both achieve steady state at approximately the same time.

Besides the problem due to the difference in the singular values, the IDFL control law has another problem. A perfect feedback linearization only occurs when the model is identical to the real robot, which is not the case. In the simulated case, the model is given by Equation (3.52) whilst the "real" robot is given by Equation (3.53). Although the model is as close as possible to the real robot, uncertainties exist and lead to stationary error in a steady-state.

Figure 5.10 shows that the condition number of the resultant inertia matrix (i.e., $\boldsymbol{M}(\boldsymbol{q}) + \boldsymbol{M}_m$) in the ACM is much smaller than the condition number of the inertia matrix of the nominal model (i.e., $\boldsymbol{M}(\boldsymbol{q})$), which implies that $\boldsymbol{M}(\boldsymbol{q}) + \boldsymbol{M}_m$ is better conditioned than $\boldsymbol{M}(\boldsymbol{q})$. Without considering the estimated parameters, the condition number of the JSIM is close to 8×10^3, whereas the condition number of the resultant inertia matrix is close to 100. Although there is only a formal guarantee that the estimated inertia matrix is always positive definite, Figure 5.10 indicates that the ACM is capable of improving the conditioning of the robot inertia matrix.

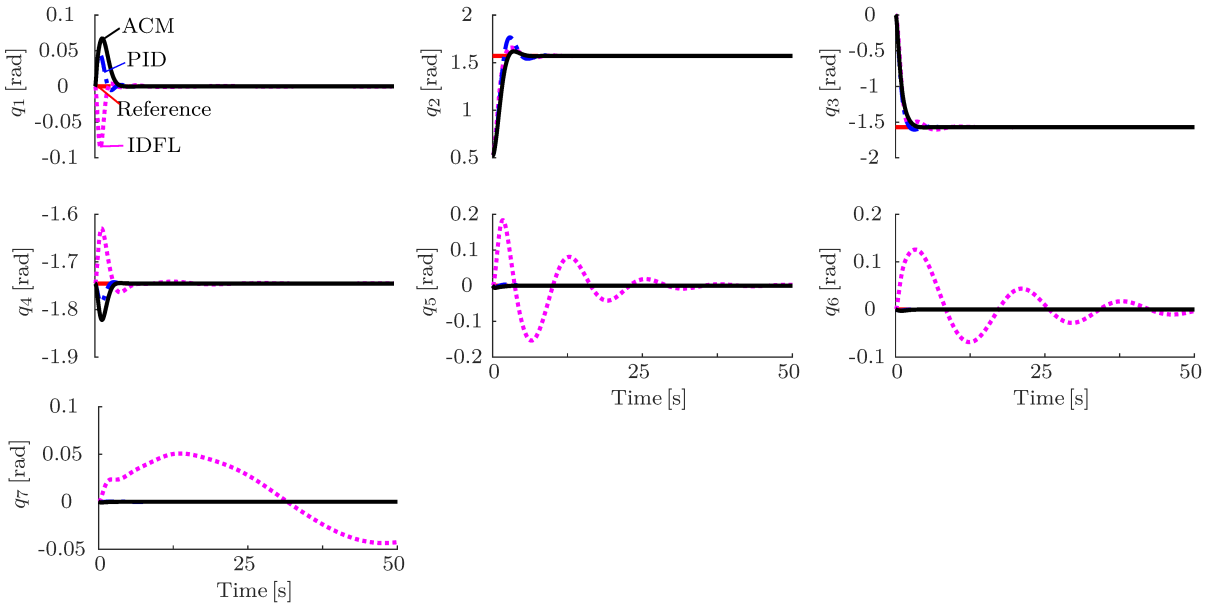

Figure 5.8: Joints configurations during simulation. For the IDFL, the last two joints did not reach the desired values due to the difference in the singular values of the JSIM (i.e., JSIM had a large condition number near the desired configuration).

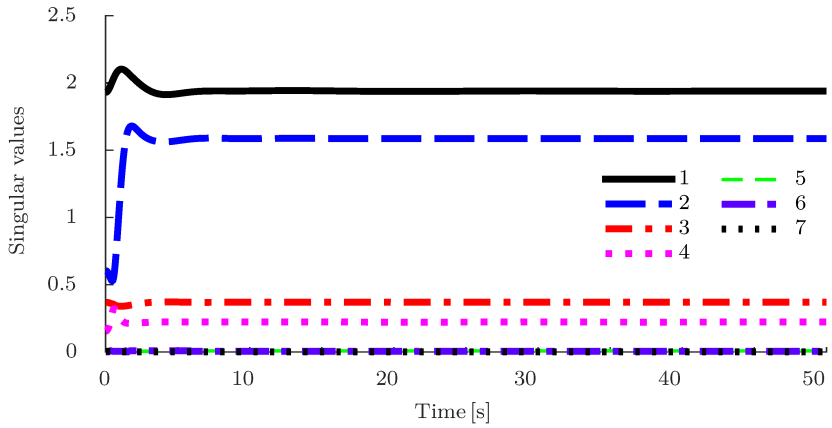

Figure 5.9: Singular values related to each robot's joint during the simulation of the IDFL.

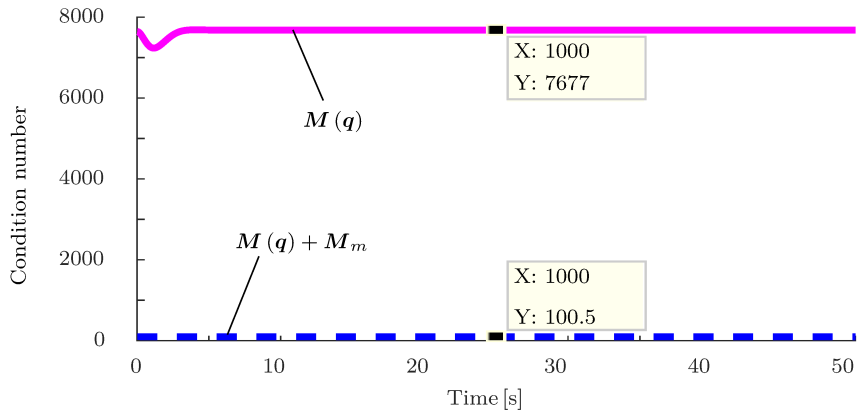

Figure 5.10: Condition number of the nominal JSIM ($\boldsymbol{M}$) and of the resultant JSIM ($\boldsymbol{M}(\boldsymbol{q}) + \boldsymbol{M}_m$).

5.3 Experimental Results of Dynamic Joint-Space Controllers

Despite good results obtained in simulation, the ACM has no formal guarantee that the estimation of the inertia of the actuators improves the JSIM's conditioning, differently from the ACD. Therefore, we run experiments in a KUKA LWR4+ (BAZAR's right arm) robot manipulator using the ACD instead of the ACM to compare it with the other controllers. Although the KUKA LWR4+ has no "torque control" mode available, it can be achieved by using its joint impedance control mode, which is given by

$$\boldsymbol{\tau}^* = \boldsymbol{K}_j\tilde{\boldsymbol{q}} + \boldsymbol{b}\left(\boldsymbol{d}_j\right) + \boldsymbol{\tau}_{\text{dynamics}}\left(\boldsymbol{q}, \dot{\boldsymbol{q}}, \ddot{\boldsymbol{q}}, \boldsymbol{g}\right) + \boldsymbol{\tau}_{\text{FRI}},$$

in which $\boldsymbol{\tau}^* \in \mathbb{R}^7$ are the command torques sent to the actuators, $\boldsymbol{K}_j \in \mathbb{R}^{7\times7}$ is a diagonal matrix of stiffness parameters, $\boldsymbol{b}\left(\boldsymbol{d}_j\right) \in \mathbb{R}^7$ is a vector relative to damping torques parametrized by $\boldsymbol{d}_j \in [0,1]^7$, $\tilde{\boldsymbol{q}} = \boldsymbol{q}_d - \boldsymbol{q} \in \mathbb{R}^7$ is the tracking error, $\boldsymbol{\tau}_{\text{dynamics}} \in \mathbb{R}^7$ is the embedded dynamic model, and $\boldsymbol{\tau}_{\text{FRI}} \in \mathbb{R}^7$ is the additional input torque sent to the robot by the Fast Research Interface (FRI)[4](Navarro, 2017). Making $\boldsymbol{K}_j = \boldsymbol{0}$ and $\boldsymbol{b}\left(\boldsymbol{d}_j\right) = \boldsymbol{0}$, and choosing $\boldsymbol{\tau}_{\text{dynamics}}\left(\boldsymbol{q}, \dot{\boldsymbol{q}}, \ddot{\boldsymbol{q}}, \boldsymbol{g}\right)$ to compensate for the gravity, the final torque sent to the joints is $\boldsymbol{\tau}^* = \boldsymbol{g}\left(\boldsymbol{q}\right) + \boldsymbol{\tau}_{\text{FRI}}$, in which $\boldsymbol{\tau}_{\text{FRI}}$ is the input control (Equations (4.57),(4.41), or (4.46)) minus the gravity vector, that is, $\boldsymbol{\tau}_{\text{FRI}} = \boldsymbol{u} - \boldsymbol{g}\left(\boldsymbol{q}\right)$.

Since the KUKA LWR4+ provides measurements only of current joint angles, the joint velocity and acceleration vectors were calculated by numerical differentiation (backward differencing). Furthermore, to prevent chattering in the control signal due to noise increased by the differentiation, a discrete first-order low-pass filter is implemented as

$$\hat{\boldsymbol{q}}[k] = \alpha_{\text{filter}}\boldsymbol{q}[k] + (1 - \alpha_{\text{filter}})\hat{\boldsymbol{q}}[k-1],$$

where $\hat{\boldsymbol{q}} \in \mathbb{R}^7$ is the vector of filtered joints angles and $\alpha_{\text{filter}} \in [0,1]$. The value $\alpha_{\text{filter}} = 0.3$ was used in the experiments and it was chosen empirically. In addition, to prevent the wind-up effect, a saturation was imposed on the integral term in Equation (4.39), limiting its value into the interval $[-1,1]$.

The experiments were run with a sampling time of 2 ms, and the gain matrices were chosen empirically as $\boldsymbol{K}_P = 100\boldsymbol{I}_{7\times7}$, $\boldsymbol{K}_D = 20\boldsymbol{I}_{7\times7}$, and $\boldsymbol{K}_I = 50\boldsymbol{I}_{7\times7}$, for all controllers (IDFL, PID, ACD). For the adaptive controller, given by Equations (4.46) and (4.56), $\alpha = 0.5$, $\beta_{\min} = \sigma_{n_M} + \Delta\sigma$ and $\beta_{\max} = \sigma_{1_M} - \Delta\sigma$, with $\Delta\sigma = \left(\sigma_{n_M} + \sigma_{1_M}\right)/10$, and $\boldsymbol{L} = 0.1\boldsymbol{I}_{7\times7}$. The initial estimated parameters were $\hat{\boldsymbol{a}}\left(0\right) = \begin{bmatrix} 0.1 & 0.05 & 0.04 & 0.03 & 0.02 & 0.02 & 0.02 \end{bmatrix}^T$, and the robot dynamic model was obtained from (Katsumata et al., 2019) (see Appendix B).

As a way to verify if there is a significant difference between the performance of the

[4]available at http://cs.stanford.edu/people/tkr/fri/html/

three controllers (Equations (4.57),(4.41), and (4.46)-(4.56)), statistical analyses were performed, which consisted of:

1. analysis of the error in steady-state;
2. analysis of the control signal;
3. analysis of the difference between the desired error's dynamics and the experimental one.

5.3.1 Statistical Methodology

In the statistical analyses presented in the next sections, the following definitions are used:

- *p-value*, which is the lowest significance level that would lead to the rejection of the null-hypothesis H_0. This means that the null-hypothesis is rejected if and only if the p-value is smaller than the significance level α_{analysis}, which is the probability of occurrence of a false positive;
- *power* of the test, which is given by $(1 - \beta_{\text{analysis}})$, where β_{analysis} is the probability of occurrence of a false negative;
- *minimally interesting effect*, which is the smallest difference between the controllers we are interested in detecting, regarding each one of the analyses 1, 2 and 3.

The null-hypothesis we want to verify is if the controllers are statistically equivalent (by comparing their population distribution means) concerning the control signal effort and especially the error decay. A false negative is a result that indicates the controllers are statistically equivalent when they are not. A false positive occurs when the null-hypothesis is rejected even if it is true. All statistical analyses are made in R (Peng, 2016).

To perform statistical analysis, we used two types of tests. The first one, the Kruskal-Wallis test (Hollander et al., 1999), is a nonparametric statistical test that assesses the differences among three or more independently sampled groups on a single, non-normally distributed variable. In this test, the null hypothesis and the alternative one are defined as

$$\begin{cases} H_0: & \kappa_1 = \cdots = \kappa_k, \\ H_1: & \kappa_1, \ldots, \kappa_k \text{ not all equal}, \end{cases}$$

where κ_i are the effects, that is, a unique parameter to the population distribution, such as the average, maximum value, etc. If this test shows a difference among the groups, which means that the null hypothesis is rejected, the Pairwise Wilcoxon Rank Sum Test (Hollander et al., 1999) is run, which calculates pairwise comparisons between the different

Table 5.1: Minimally interesting effect for each analysis.

Error in steady-state	Control signal	Error discrepancy
$\delta_{\|\tilde{\boldsymbol{q}}\|} = 0.05$	$\delta_{\mu_{\|\boldsymbol{u}\|}} = 5$	$\delta_{\mu_{\|\boldsymbol{e}-\tilde{\boldsymbol{q}}\|}} = 0.05$
	$\delta_{\max(\|\boldsymbol{u}\|)} = 50$	$\delta_{\max(\|\boldsymbol{e}-\tilde{\boldsymbol{q}}\|)} = 0.9$

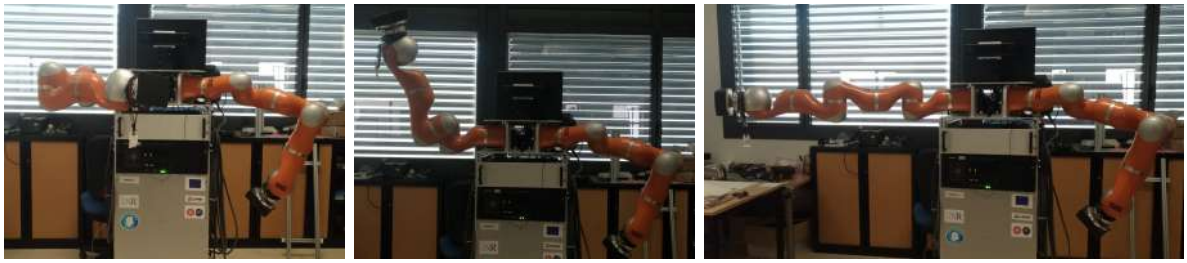

Figure 5.11: Initial configurations for the KUKA LWR4+ (right arm).

types of controllers, with corrections for multiple testing (necessary to keep the overall false positive rate controlled at a given level), to see which pairs of groups are different.

The desired characteristics for the analyses were chosen as:

- significance level of $\alpha_{\text{analysis}} = 0.01$;
- power of 0.85;
- and the minimally interesting effect as shown in Table table 5.1, where $\delta_{\|\tilde{\boldsymbol{q}}\|}$,$\delta_{\mu_{\|.\|}}$, and $\delta_{\max(\|.\|)}$ are, respectively, the norm of the steady-state error, the mean and the maximum values of the control signal and the difference between the desired error's dynamics and the experimental one.

Because the number of samples necessary to run the statistical analysis is based on the variance of the data, which was unknown *a priori*, each of the three controllers was initially run 30 times. In order to generate these 30 pairs of initial/final configurations, three different initial configurations (Figure 5.11) were arbitrarily chosen and, for each initial configuration $\boldsymbol{q}_0$, ten desired joint positions were generated by a normal distribution $\mathcal{N}(\boldsymbol{q}_0, 0.5)$. We calculated the variance of the runs for each type of analysis described in Table 5.1. For each analysis, the number of samples were calculated using the Power Anova Test, available in R, considering the calculated variance, the desired chosen parameters, the number of controllers to be compared (three), and the between group variance, that is calculated as

$$\sigma^2_{\text{between}} = \text{Var}\left(\begin{bmatrix}\frac{\delta}{3} & \frac{\delta}{3} & -\frac{2\delta}{3}\end{bmatrix}\right),$$

where δ is the minimally interesting effect of Table 5.1. The results were values lower than 30, so the analyses were made with the 30 samples already collected.

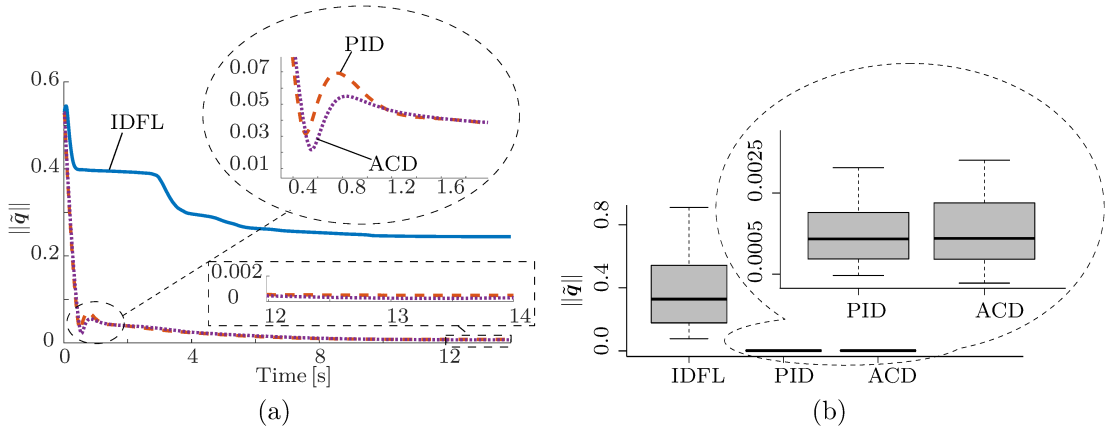

(a) (b)

Figure 5.12: Error norm for each controller *(a)* for one execution and *(b)* boxplot for all executions, but considering only the steady-state.

Table 5.2: Pairwise comparisons for the error norm, using the Wilcoxon rank sum test.

	IDFL	PID
PID	$\mathbf{4.5 \times 10^{-11}}$	-
ACD	$\mathbf{4.5 \times 10^{-11}}$	0.70

5.3.2 Statistical Analysis of the Steady-State Error

Figure 5.12a shows the error norm for one execution of each controller. The IDFL has a much larger steady-state error norm than the other controllers, whereas the PID and the ACD have similar behavior. This is corroborated by the boxplot in Figure 5.12b, which shows that the IDFL presented the worst performance since *all* values are larger than the ones for the other controllers. On the other hand, the results for the PID and the ACD were quite the same and there was no significant difference in the box plot. To further analyze if there was any relevant difference between the controllers, we first performed the Kruskal-Wallis test, as the data turned out to be not normally distributed, which resulted in p-value $= 1.256 \times 10^{-13} < \alpha_{\text{analysis}}$, indicating that the null hypothesis was rejected, confirming that at least one controller had different performance than the others. To see which pair of controllers are different, the Wilcoxon test was performed and the result is shown in Table 5.2. When compared to all other controllers, the values for the IDFL are the only ones smaller than α_{analysis}, indicating that it is the only controller with different performance among the three controllers. Therefore, the PID and the ACD are equivalent with respect to the error norm.

5.3.3 Statistical Analysis of the Control Signal

We first analyze the control effort of each controller, which is given by $\sqrt{\int_0^{t_{\text{end}}} \|\boldsymbol{u}(t)\|^2 \, dt}$, with $t_{\text{end}} = 14\,\text{s}$. According to Figure 5.13a, the IDFL presented the largest effort, but the difference to the other controllers was not so large as in the error norm. The resultant

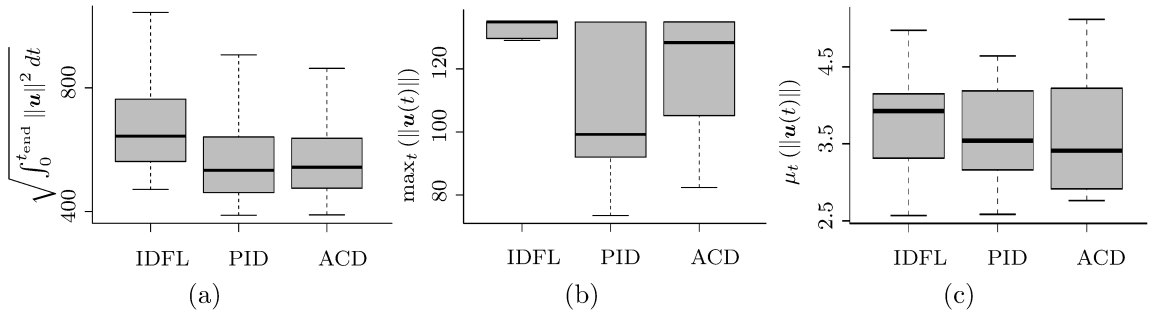

Figure 5.13: Boxplot of the *(a)* control effort, *(b)* maximum control signal, and *(c)* mean control signal for each controller.

Table 5.3: Pairwise comparisons for the control effort and maximum control signal using the Wilcoxon rank sum test.

	Control effort		Maximum control signal	
	IDFL	PID	IDFL	PID
PID	$\mathbf{3.90 \times 10^{-3}}$	-	$\mathbf{2.40 \times 10^{-4}}$	-
ACD	$\mathbf{3.90 \times 10^{-3}}$	7.17×10^{-1}	$\mathbf{5.48 \times 10^{-3}}$	3.50×10^{-2}

p-value from the Kruskal-Wallis test was 0.001887, which is smaller than α_{analysis}, indicating the rejection of the null hypothesis at a significant level of 0.01. Table 5.3 shows that, again, the IDFL was the only one to present a significant difference with respect to all other controllers, regarding the control effort, when compared two-by-two by using the Wilcoxon rank sum test.

Regarding the maximum value of the norm of the control signal ($\max_t(\|\boldsymbol{u}(t)\|)$), Figure 5.13b shows that the IDFL had the largest median, followed by the ACD, and then the PID. Since the Kruskal-Wallis test indicated the rejection of the null hypothesis (p-value $= 9.504 \times 10^{-5}$) we performed the Wilcoxon rank sum test to compare all controllers pairwise, which is summarized in Table 5.3. The only controller that has a different performance from the others is, again, the IDFL.

A similar analysis was done for the mean value of the norm of the control signal ($\mu_t(\|\boldsymbol{u}(t)\|)$). Figure 5.13c shows that the IDFL has the largest median value, followed by the PID, and then the ACD. Notwithstanding, the values are statistically equivalent, which is confirmed by the Kruskal-Wallis test (p-value $= 0.397 > \alpha_{\text{analysis}}$).

5.3.4 Statistical Analysis of the Error Dynamics

Lastly, in order to see how different is the experimental result from the theoretical design regarding the error dynamics, we compared the integral of the difference between the theoretical error[5] $\boldsymbol{e}(t)$ and the measured error $\tilde{\boldsymbol{q}}(t)$, during the motion, namely

[5]The variable $\boldsymbol{e}(t)$ is the solution to the differential equation $\ddot{\tilde{\boldsymbol{q}}} + \boldsymbol{K}_D\dot{\tilde{\boldsymbol{q}}} + \boldsymbol{K}_P\tilde{\boldsymbol{q}} + \boldsymbol{K}_I\int_0^t \tilde{\boldsymbol{q}}(t)dt = \boldsymbol{0}$.

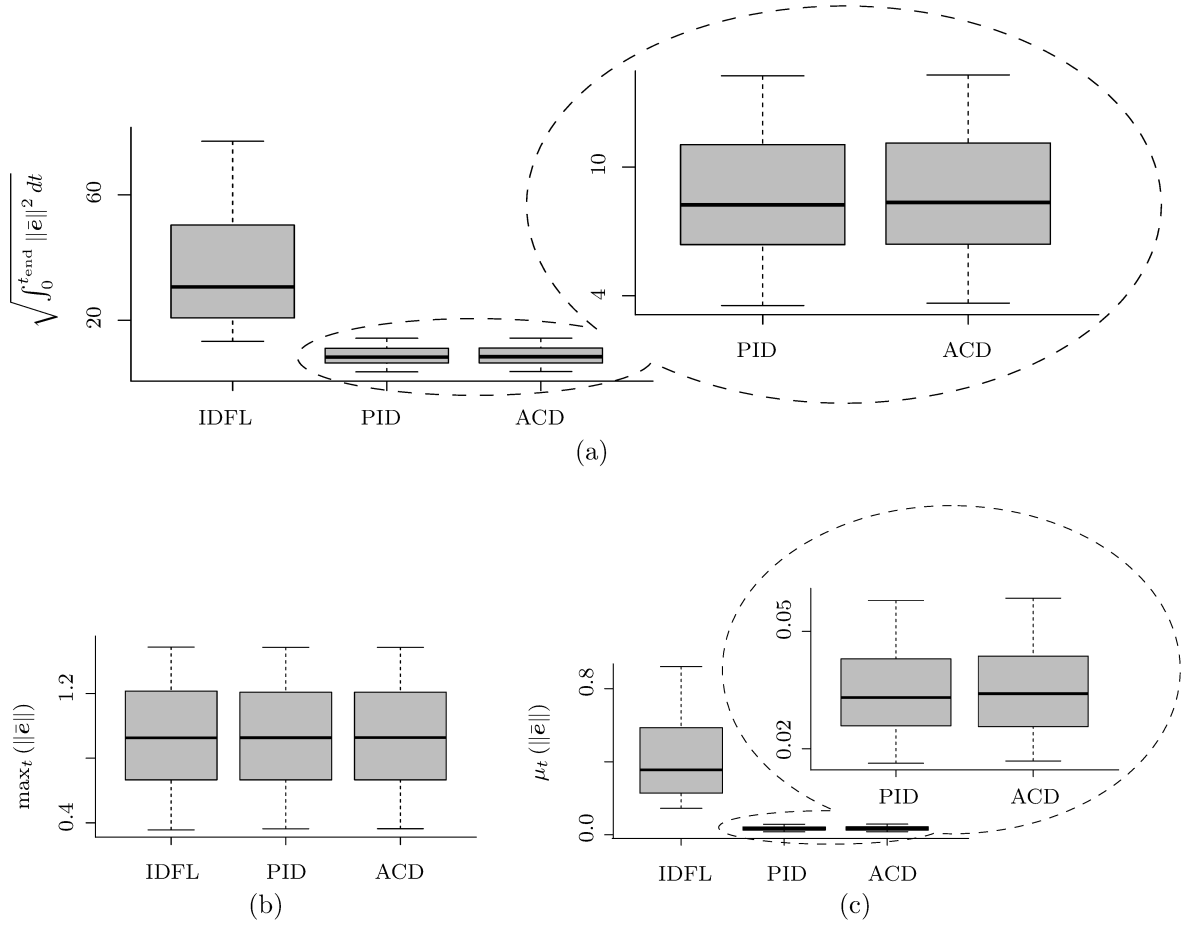

Figure 5.14: Boxplot of the *(a)* integral of the difference between the theoretical error and the experimental one along the motion, *(b)* maximum value of this difference, and *(c)* its mean for each controller, where $\bar{\boldsymbol{e}} = \boldsymbol{e}(t) - \tilde{\boldsymbol{q}}(t)$.

$\sqrt{\int_0^{t_{\text{end}}} \|\boldsymbol{e}(t) - \tilde{\boldsymbol{q}}(t)\|^2 \, dt}$. We also analyzed the maximum difference, $\max_t(\|\boldsymbol{e}(t) - \tilde{\boldsymbol{q}}(t)\|)$, and the mean value, $\mu_t(\|\boldsymbol{e}(t) - \tilde{\boldsymbol{q}}(t)\|)$. Figure 5.14 shows the boxplots for each one of the aforementioned metrics. For the maximum value, all controllers are statistically equivalent (p-value = 0.9605 obtained with the Kruskal-Wallis test). However, regarding the integral of the difference between the desired and actual error dynamics and its mean value, the Kruskal-Wallis test pointed differences between the controllers (p-value was 2.44×10^{-13} and 1.22×10^{-13} for the integration and mean value, respectively). The IDFL presented again the worst result and the performances of the other controllers were very similar between them, as corroborated by Table 5.4, which shows the results of the Wilcoxon test.

5.3.5 Improvement of JSIM Conditioning

In order to show that the adaptation law of the ACD always improves the condition number of the inertia matrix, Figure 5.15 presents the condition number of the JSIM ($\text{cond}(\boldsymbol{M})$) for the IDFL, and the condition of the resultant matrix ($\text{cond}\left(\boldsymbol{M} + \bar{\boldsymbol{D}}\right)$) for the ACD, for one of the 30 executions. Since the worse the conditioning is, the larger is the

Table 5.4: Pairwise comparisons for the integral of the difference between the theoretical error and the experimental one along the whole motion and its mean value using the Wilcoxon rank sum test.

	Integration		Mean	
	IDFL	PID	IDFL	PID
PID	$\mathbf{7.5 \times 10^{-11}}$	-	$\mathbf{4.5 \times 10^{-11}}$	-
ACD	$\mathbf{7.5 \times 10^{-11}}$	0.73	$\mathbf{4.5 \times 10^{-11}}$	0.59

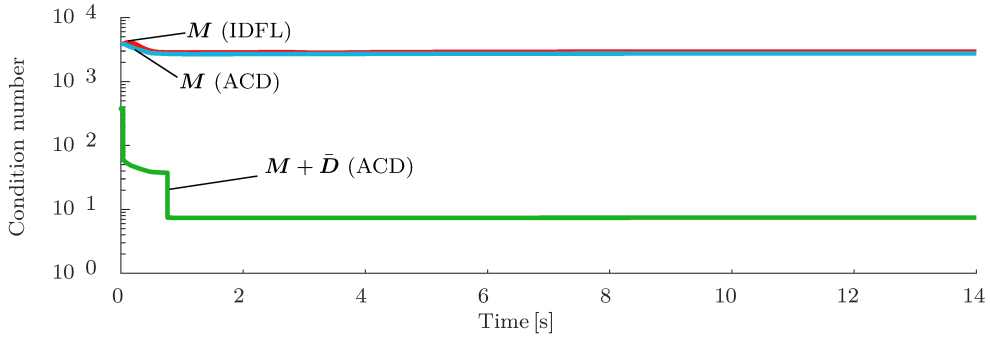

Figure 5.15: Condition number of the nominal $\boldsymbol{M}$ for the IDFL and the ACD, and of the resultant matrix $\boldsymbol{M} + \bar{\boldsymbol{D}}$, for one execution.

condition number, it is possible to see, from Figure 5.15, that the conditioning of $\boldsymbol{M} + \bar{\boldsymbol{D}}$ was always better than the conditioning of the nominal inertia matrix $\boldsymbol{M}$. Furthermore, since the trajectories generated by the ACD may be different from the ones generated by the IDFL, Figure 5.15 also shows the condition number of the nominal $\boldsymbol{M}$, where the nominal inertia matrix was calculated by using the actual joints configurations for the trajectories generated by the ACD. The result shown in Figure 5.15 was also observed in all the 30 executions for each controller.

5.4 Experimental Results of Dynamic Task-Space Controllers

The previous sections showed the results of the dynamic controllers in joint-space. However, most of the tasks are defined in the task-space. Moreover, considering manipulation tasks subject to contacts, and considering the aim to guarantee safety, it is important to put together the admittance controller and the dynamic controllers. With this aim, we compare here the behavior of the three task-space dynamic controllers shown in section 4.3.2 together with the admittance controller of Equation (4.2). This situation is depicted in Figure 4.1, where the motion controller is each of the three task-space dynamic controllers of section 4.3.2.

Similar to the last experiments, since the KUKA LWR4+ API used provides only the current joint angle, the velocity was calculated by numerical differentiation (backward

differencing). In addition, to prevent the wind-up effect, saturation was imposed on the integral term in Equation (4.59), limiting the value for the first four coefficients into the interval $[-1, 1]$ while the last four coefficients were limited into the interval $[-0.06, 0.06]$. These intervals were chosen empirically.

The experiments were run with a sampling time of 5 ms. The parameters of the adaptive controller, given by Equations (4.46) and (4.56), were $\alpha = 0.5$, $\beta_{\min} = \sigma_{n_{\boldsymbol{M}}} + \Delta\sigma$ and $\beta_{\max} = \sigma_{1_{\boldsymbol{M}}} - \Delta\sigma$, with $\Delta\sigma = \left(\sigma_{n_{\boldsymbol{M}}} + \sigma_{1_{\boldsymbol{M}}}\right)/10$, and $\boldsymbol{L} = 0.1\boldsymbol{I}_{7\times7}$. The initial estimated parameters were $\hat{\boldsymbol{a}}\,(0) = \begin{bmatrix} 0.1 & 0.05 & 0.04 & 0.03 & 0.02 & 0.02 & 0.02 \end{bmatrix}^T$, and the robot dynamic model was obtained from Katsumata et al. (2019) (See Appendix B). For the outer-loop, the matrices in Equation (4.2) were chosen empirically as $\boldsymbol{M}_d = 1.5\boldsymbol{I}_{6\times6}$, $\boldsymbol{B}_d = 300\boldsymbol{I}_{6\times6}$, and $\boldsymbol{K}_d = 100\boldsymbol{I}_{6\times6}$. The Equation (4.2) was chosen over the Equation (4.20) because the former is simpler and, for the tasks executed, presents similar results as the latter, as seen in section 5.4.4.

5.4.1 Choice of Gain Matrices

Since manipulation tasks are typically described in the task-space, that is, in terms of physical entities related to the end-effector (e.g., pose, wrench, twist), task-space motion controllers are more appropriate than joint-space motion controllers because no explicit inverse kinematics is required. However, the choice of gains for a task-space motion controller, when based on the transpose of the Jacobian matrix, as in Equation (4.61), is not straightforward, because the closed-loop response tends to be very abrupt for large errors and extremely slow for small errors (Pham et al., 2018). Therefore, a variable gain matrix is desirable to ensure a more uniform behavior.

Since there is a relationship between the task-space and the joint-space closed-loop gains (Pham et al., 2018), one strategy is to define the desired dynamic behavior in joint-space (e.g., exponential decay) and use that relationship to ensure a similar performance in the task-space, regardless if the transpose of the Jacobian matrix is used, as in Equation (4.61), or if the pseudoinverse of the Jacobian matrix is used, as in Equations (4.58) and (4.60). When using the latter, this transformation is given by

$$\boldsymbol{K} = \boldsymbol{J}^{+}\boldsymbol{K}_q\boldsymbol{J}, \tag{5.3}$$

whereas when using the former, the relation is given by

$$\boldsymbol{K} = \boldsymbol{J}^{+T}\boldsymbol{K}_q\boldsymbol{J}^{+}, \tag{5.4}$$

where $\boldsymbol{K}$ and $\boldsymbol{K}_q$ are the task-space and joint-space gain matrices, respectively (Pham

et al., 2018).

Suppose we consider the desired *equivalent* joint-space error dynamics as

$$\ddot{\tilde{\boldsymbol{q}}} + \boldsymbol{K}_{D_q}\dot{\tilde{\boldsymbol{q}}} + \boldsymbol{K}_{P_q}\tilde{\boldsymbol{q}} = 0, \tag{5.5}$$

where $\tilde{\boldsymbol{q}}$ is the joint-space error and $\boldsymbol{K}_{D_q} = \text{diag}\left(k_{D_{q_1}}, \ldots, k_{D_{q_n}}\right)$ and $\boldsymbol{K}_{P_q} = \text{diag}\left(k_{P_{q_1}}, \ldots, k_{P_{q_n}}\right)$ are the derivative and proportional positive-definite joint-space gain matrices, respectively. Since the gain matrices are diagonal, the desired equivalent closed-loop system is uncoupled with n independent characteristic equations such as

$$r_i{}^2 + k_{D_{q_i}} r_i + k_{P_{q_i}} = 0,$$

for all $i \in \{1, \ldots, n\}$, with two roots given by

$$r_{i_{1,2}} = \frac{-k_{D_{q_i}} \pm \sqrt{k_{D_{q_i}}^2 - 4k_{P_{q_i}}}}{2}.$$

If $k_{D_{q_i}}^2 = 4k_{P_{q_i}}$, then $r_{i1} = r_{i2} = -k_{D_{q_i}}/2$ and thus the solution to Equation (5.5) is given by

$$\tilde{q}_i(t) = c_{i_1} e^{r_i t} + c_{i_2} t e^{r_i t},$$

with $c_{i_1}, c_{i_2} \in \mathbb{R}$. Hence, the error decreases exponentially.

Thus, we have chosen the equivalent joint-space gains as $\boldsymbol{K}_{D_q} = 10\boldsymbol{I}_{7\times 7}$ and $\boldsymbol{K}_{P_q} = 25\boldsymbol{I}_{7\times 7}$, for all torque controllers, which satisfy the relation $k_{D_{q_i}}^2 = 4k_{P_{q_i}}$, for all $i \in \{1, \ldots, n\}$ and the integral gain has been chosen empirically as $\boldsymbol{K}_{I_q} = 10\boldsymbol{I}_{7\times 7}$. Consequently, as we wish a dynamic behavior equivalent to Equation (5.5), the gains $\boldsymbol{K}_P$, $\boldsymbol{K}_I$, and $\boldsymbol{K}_D$ for the controllers of Equations (4.57)-(4.59) and (4.60) are found by using the transformation of Equation (5.3). Similarly, the equivalent task-space gains for the controller given by Equations (4.46)- and (4.56) are found according to the transformation given by Equation (5.4).

5.4.2 Experiments with an External Wrench

We performed experiments with an external wrench acting at the robot end-effector to show that the robot behaves compliantly, and also to compare its behavior when different inner motion controllers are used, namely the TIDFL (Equation (4.57)), the TPID (Equation (4.60)), and the TAC (Equation (4.61)). Consider $\underline{\boldsymbol{x}}_c(0) = \underline{\boldsymbol{x}}_d(0) = \underline{\boldsymbol{x}}(0)$, where $\underline{\boldsymbol{x}}(0)$ is the initial robot end-effector pose and the robot initial configuration $\boldsymbol{q}(0) = \begin{bmatrix} 0 & 0.5 & \pi/2 & -\pi/2 & 0 & 0 & 0 \end{bmatrix}^T$ is shown in Figure 5.16a. At the beginning, an

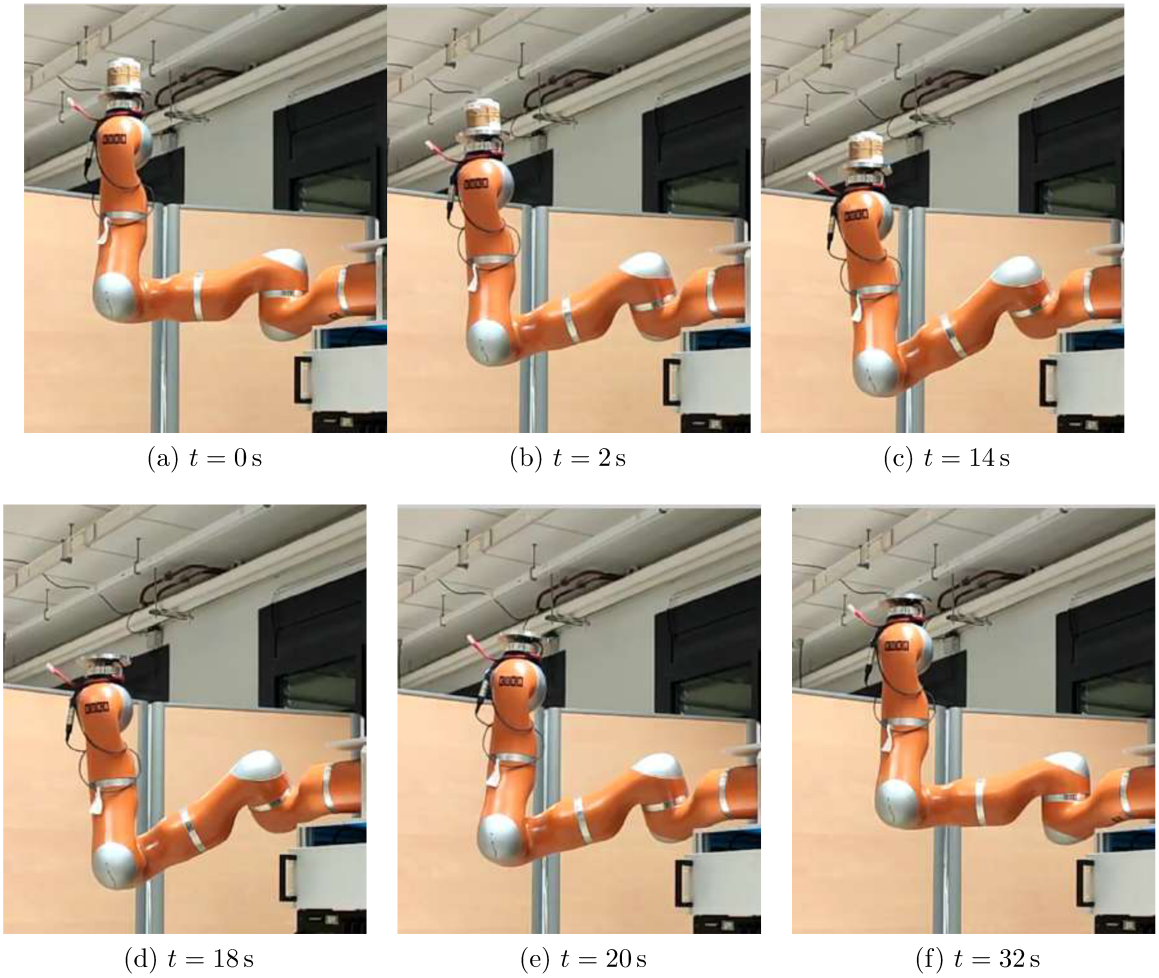

(a) $t = 0\,\mathrm{s}$ (b) $t = 2\,\mathrm{s}$ (c) $t = 14\,\mathrm{s}$

(d) $t = 18\,\mathrm{s}$ (e) $t = 20\,\mathrm{s}$ (f) $t = 32\,\mathrm{s}$

Figure 5.16: Snapshots of the experiment with an object exerting a wrench at the end-effector. In the first row, the object is on the end-effector, which moves complacently due to the gravitational force. In the second row, the object is removed and the end-effector returns to the desired pose.

object with mass of 0.44kg was placed onto the end-effector, which moved complacently due to the gravitational force exerted on the object. To ensure the desired apparent impedance, the compliant reference pose $\underline{\boldsymbol{x}}_c$ deviated from $\underline{\boldsymbol{x}}_d$ but the inner-loop controller ensured the end-effector tracking of the trajectory given by $\underline{\boldsymbol{x}}_c(t)$. After 35 s the object was removed and because there was no external wrench acting at the end-effector, it returned to the desired pose, as shown in the snapshots of Figure 5.16.

The external wrench for all three controllers are shown in Figure 5.17. The larger force in the z-axis, close to $-4.5\,\mathrm{N}$, corresponds to the force exerted by the object due to gravity. Because the end-effector moves slightly differently depending on the controller used in the inner-loop, the measured wrenches are different for each one of them.

Given the DQ of the current end-effector pose $\underline{\boldsymbol{x}}$, the compliant pose $\underline{\boldsymbol{x}}_c$, and the desired pose $\underline{\boldsymbol{x}}_d$, the corresponding axis-angle and translation components (e.g., $\phi\boldsymbol{n} =$

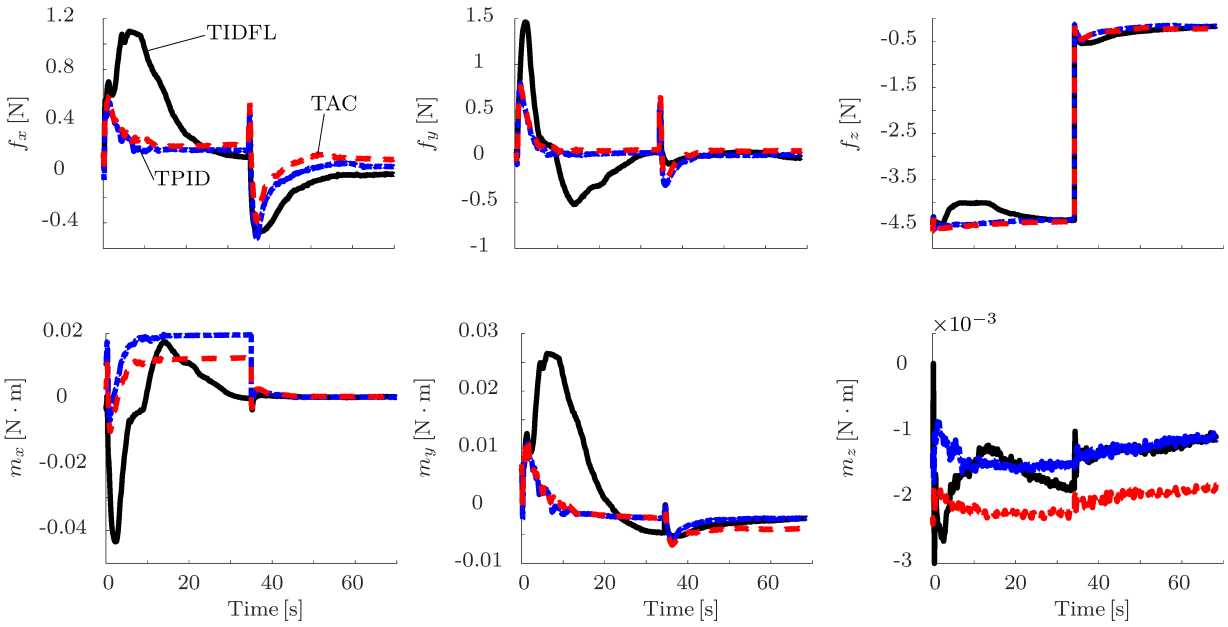

Figure 5.17: External wrench acting at the end-effector.

$\phi n_x\hat{\imath}+\phi n_y\hat{\jmath}+\phi n_z\hat{k}$ and $\boldsymbol{p} = p_x\hat{\imath}+p_y\hat{\jmath}+p_z\hat{k}$) are shown in Figure 5.18, for all three controllers. (Given $\underline{\boldsymbol{x}}$, the axis-angle and translation information are obtained as $2\log\underline{\boldsymbol{x}} = \boldsymbol{n}\phi+\varepsilon\boldsymbol{p}$—the same is done for $\underline{\boldsymbol{x}}_c$ and $\underline{\boldsymbol{x}}_d$.) As predicted by the theory, the compliant trajectory is different from the desired one when a wrench acts at the end-effector.

By inspection, the TIDFL controller performed worst as the current end-effector pose, and especially the translational component, did not track $\underline{\boldsymbol{x}}_c$ as well as the other two controllers. The error norm for all controllers is shown in Figure 5.19 and indicates that the TIDFL had a larger error norm during the whole experiment, which corroborates the worst behavior in Figure 5.18.

Similar to Figure 5.15 at section 5.3.5, Figure 5.20 shows that the conditioning of $\boldsymbol{M} + \bar{\boldsymbol{D}}$ is always better than the conditioning of $\boldsymbol{M}$, but in this case for the task-space controller.

5.4.3 Experiments in Free-Motion

The analysis of the movement under an external wrench is limited since it requires the same applied wrench for all compared controllers, which is difficult to achieve, as illustrated in Figure 5.17. Therefore, deeper analyses were made in free-motion, with the outer-loop controller being the same in all experiments, given by Equation (4.20).

As a way to see if there is a significant difference between the performance of the three controllers in the inner-loop—namely, Equations (4.57), (4.60), and (4.46)-(4.56)—, statistical analyses were performed, which consisted of:

1. analysis of the error;

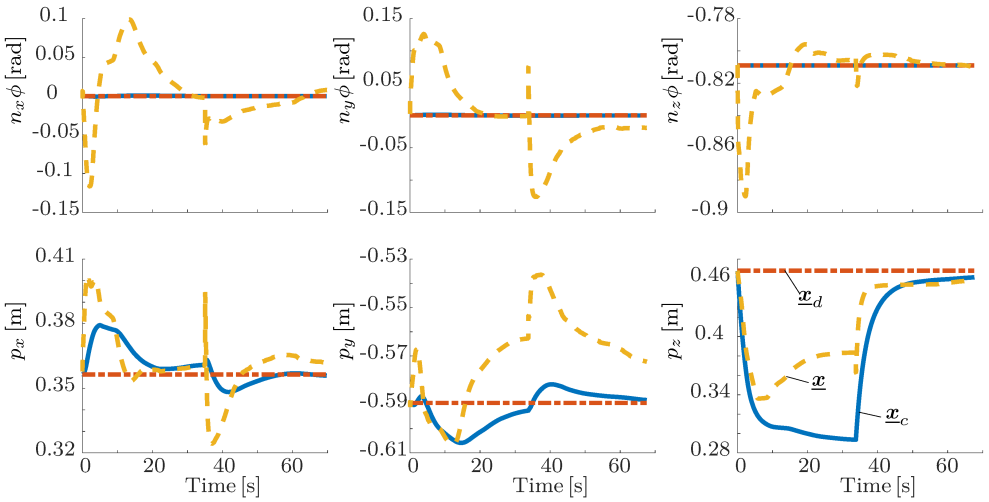

(a) TIDFL

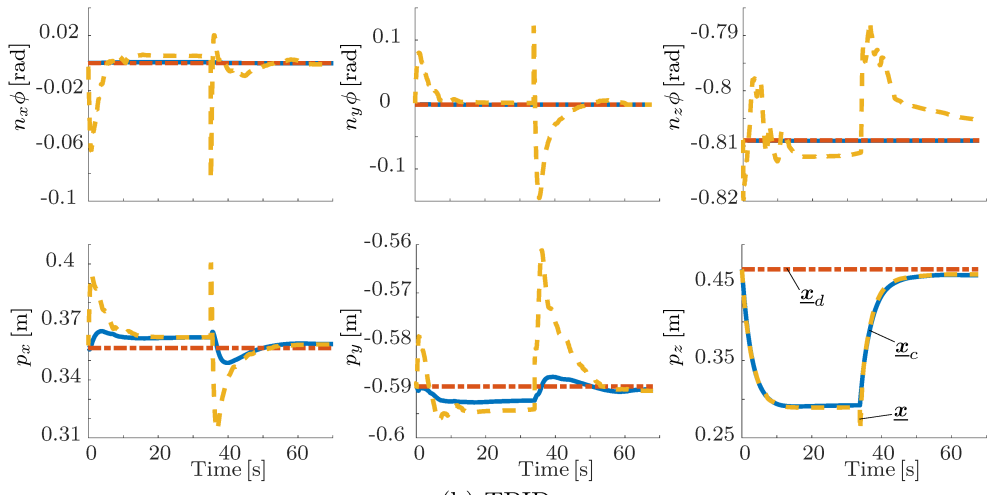

(b) TPID

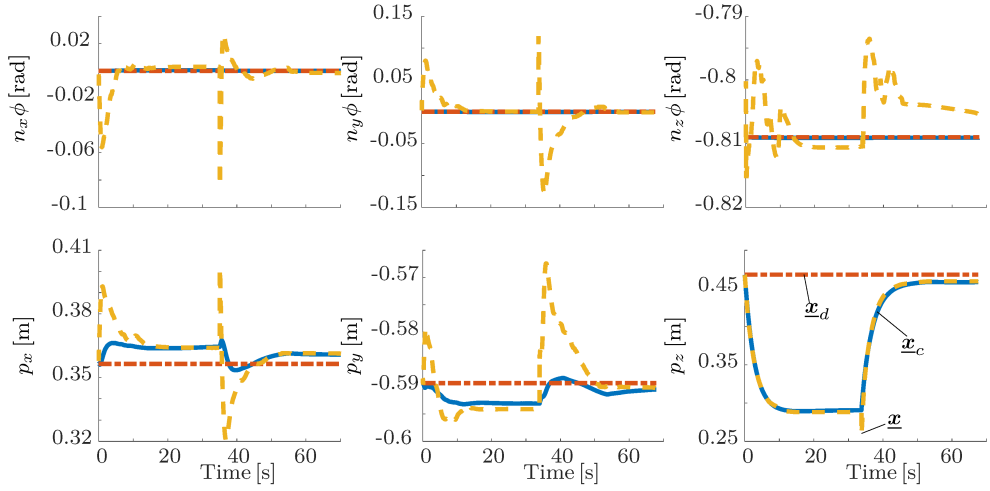

(c) TAC

Figure 5.18: Coefficients of $2\log \underline{\boldsymbol{x}}$, $2\log \underline{\boldsymbol{x}}_c$, and $2\log \underline{\boldsymbol{x}}_d$, indicating the rotation around the axes x, y, and z (first row), and the translation along each axis (second row).

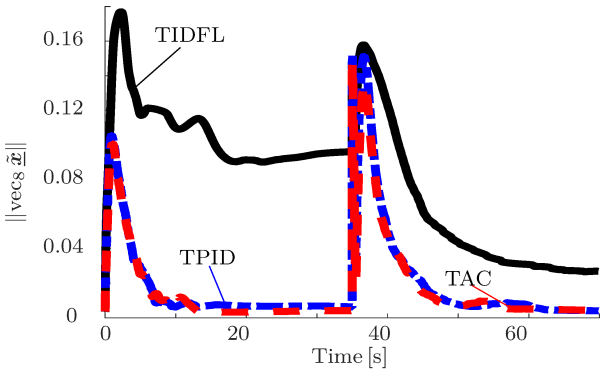

Figure 5.19: Error norm for all controllers.

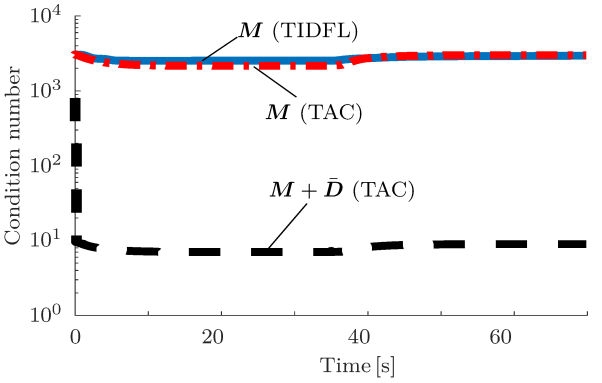

Figure 5.20: Condition number of the nominal $\boldsymbol{M}$ for the TIDFL and the TAC, and of the resultant matrix $\boldsymbol{M}+\bar{\boldsymbol{D}}$. The smaller the condition number, the better.

Table 5.5: Minimally interesting effect for each analysis.

Error discrepancy	Control signal of inner-loop
$\delta_{\int d} = 15$	$\delta_{\int \|\boldsymbol{u}\|} = 50$
$\delta_{\mu(d)} = 0.03$	$\delta_{\mu(\|\boldsymbol{u}\|)} = 1$
$\delta_{\max(d)} = 0.04$	$\delta_{\max(\|\boldsymbol{u}\|)} = 20$

2. analysis of the control signal.

5.4.3.1 Statistical Methodology

In order to compare each controller and identify which one presents the best performance, we performed three t-tests, all against all, for each analyses 1 and 2. The desired power for the analyses were chosen equal to the analyses shown in section 5.3.1. However, since the previous experiments resulted in p-values much bigger or much smaller than α_{analysis}, we decided to relax the tests and increase the value of the significance level to $\alpha_{\text{analysis}} = 0.05$, which would not change the results of the statistical analyses. The minimally interesting effect were chosen as described in Table 5.5, where $\delta_{\int}$,δ_{μ},$\delta_{\max}$ are, respectively, the minimally interesting effect for the total, the mean, and the maximum values of the error discrepancy and the control signal.

Similarly to the previous analyses, each of the three controllers was initially run 30 times. Given an initial pose $\underline{\boldsymbol{x}}(0) = \underline{\boldsymbol{x}}_c(0) \neq \underline{\boldsymbol{x}}_d$, different desired poses were generated randomly, but being the same for each controller to allow a fair comparison. Thus, to generate these 30 pairs of initial/final poses, first, three different initial configurations $\boldsymbol{q}_0$ were arbitrarily chosen and, for each one, ten desired joint configurations were generated according to a normal distribution $\mathcal{N}(\boldsymbol{q}_0, 0.5)$, and the initial and desired end-effector poses were found using the robot forward kinematics.

After using the Fligner-Killeen Test of homogeneity of variances (Crawley, 2007) in the collected data, we concluded that the variances for all the controllers were not the same,

Table 5.6: Fligner-Killeen test of homogeneity of variances.

p-values for the error discrepancy			p-values for the control signal
$\int d$	$\mathbf{5.15\times10^{-13}}$	$\int \|\boldsymbol{u}\|$	0.88
$\mu(d)$	$\mathbf{1.32\times10^{-13}}$	$\mu(\|\boldsymbol{u}\|)$	0.58
$\max(d)$	$\mathbf{5.73\times10^{-11}}$	$\max(\|\boldsymbol{u}\|)$	$\mathbf{2.67\times10^{-12}}$

since the p-values for each analysis are very small, as shown in Table 5.6, except for the control effort and the mean value of the control signal. Therefore, the null-hypothesis that the variances are equal is false and thus Student's t-test is not adequate.

Hence, we used the *Welch Two Sample t-test,* which is a modification of the *Student's t-test* used when the variance is not equal among all the populations. In this test, the null hypothesis and the alternative one are defined as (Montgomery, 2001)

$$\begin{cases} H_0: & \mu_1 = \mu_2, \\ H_1: & \mu_1 \neq \mu_2. \end{cases}$$

where μ_1 and μ_2 are the population distribution means.

Considering the comparison for each pair of controllers, resulting in three *Welch Two Sample t-tests*, the computation of the number of samples was done using the mean value of the standard deviation of all three controllers results and the significance level adjusted for three comparisons, according to the Bonferroni correction for the value of α_{analysis}, that is, (Montgomery, 2001)

$$\alpha_{\text{adj}} = \frac{\alpha_{\text{analysis}}}{K} = 0.0167,$$

where $K = a(a-1)/2$, with a being the number of controllers, which in our case is 3. Finally, the number of samples was calculated using the two-sample t-test power calculation available in R, resulting in a value lower than 30. Hence, the analyses were made with the 30 samples already collected.

5.4.3.2 Statistical Analyses of the Error

Given a discrepancy function defined as $d(t) \triangleq \|\text{vec}_8\, \underline{\boldsymbol{x}}_e(t)\|$, with $\underline{\boldsymbol{x}}_e(t) \triangleq \underline{\boldsymbol{x}}(t) - \underline{\boldsymbol{x}}_c(t)$, the first analysis concerns the total discrepancy, given by $\sqrt{\int_0^{t_{\text{end}}} \boldsymbol{d}(t)^2\, dt}$, for $t_{\text{end}} = 75\,\text{s}$. Figure 5.21a shows the boxplot of the total discrepancy, in which the TIDFL presents the largest value compared to the other controllers. The TPID and the TAC present similar values, although the error for the TAC is slightly larger. The same is observed for the mean value (Figure 5.21b) and maximum discrepancy values (Figure 5.21c).

The p-values for all the comparisons are described in Table 5.7, in which bold values mean that the p-values were smaller than the adjusted significance level $\alpha_{\text{adj}} = 0.0167$,

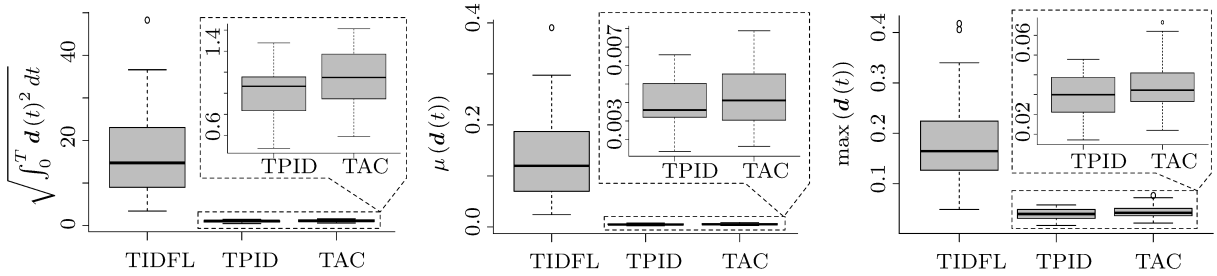

Figure 5.21: Error discrepancy: *(a)* integral of the discrepancy function along the motion, *(b)* mean value of the function, and *(c)* its maximum.

Table 5.7: p-values for the Welch t-test all against all, regarding the error discrepancy.

	Total discrepancy		Mean value		Max. value	
	TIDFL	TPID	TIDFL	TPID	TIDFL	TPID
TIDFL	-	$\mathbf{1.80\times10^{-9}}$	-	$\mathbf{1.41\times10^{-9}}$	-	$\mathbf{9.60\times10^{-10}}$
TAC	$\mathbf{2.05\times10^{-9}}$	0.15	$\mathbf{1.50\times10^{-9}}$	0.28	$\mathbf{2.13\times10^{-9}}$	0.07

indicating that the null-hypothesis is rejected; that is, the difference in performance is statistically significant in these cases. Therefore, both TPID and TAC had different performances when compared to TIDFL. However, when comparing the TPID to the TAC, the p-values were larger than α_{adj} for all criteria, which means that there is no statistically significant difference between TPID and TAC with respect to trajectory tracking.

We conclude that the TPID and the TAC are statistically equivalent since the null-hypotheses are not rejected when those two controllers are compared, as shown in Table 5.7. Moreover, both controllers presented a better performance than the TIDFL, which is indicated by the large discrepancy values for the later, as shown in Figure 5.21, and by the rejection of the null-hypotheses when comparing all controllers versus the TIDFL. These results corroborate the work of Shen and Featherstone (Shen & Featherstone, 2003) and our previous experiments, in which the controller that uses the nominal JSIM has a poor behavior regarding the error dynamics.

In the TIDFL, the control input for the linearized task-space dynamics, $\boldsymbol{a}_x$ (Equation (4.59)), is mapped to the joint-space through Equation (4.39) and then multiplied by the JSIM. Therefore, the torque applied to some joints may be attenuated if the inertia along these joints is very small, which may explain the poor closed-loop response when using the TIDFL. For the TPID and TAC, $\boldsymbol{a}_x$ is mapped to the joint space without being multiplied by the JSIM, and therefore the control signal is not weakened, enhancing the closed-loop error dynamics.

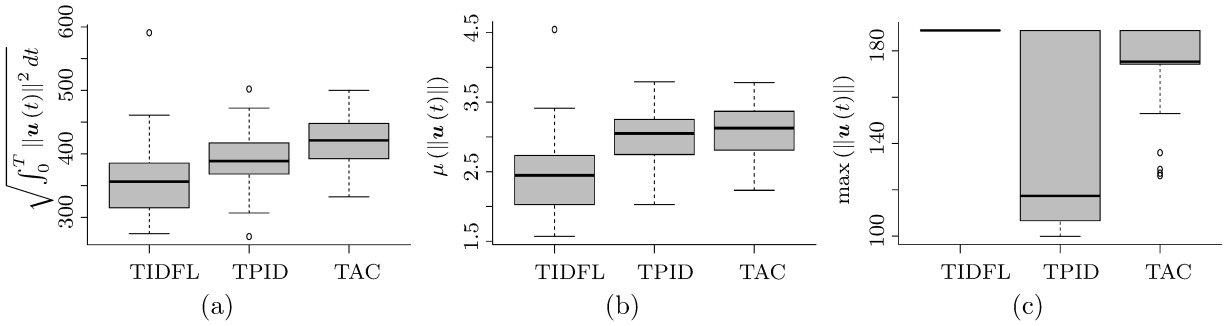

Figure 5.22: Inner-loop control signal: *(a)* control effort throughout the motion, *(b)* mean, and *(c)* its maximum value.

5.4.3.3 Statistical Analyses of the Control Signal

Similar analyses were done for the control signal $\boldsymbol{u}(t)$ of the inner-loop controllers, where we evaluated the control effort given by $\sqrt{\int_0^{t_{\text{end}}} \|\boldsymbol{u}(t)\|^2 dt}$, for $t_{\text{end}} = 75\,\text{s}$.

Figure 5.22a shows that the TAC presented the largest value, followed by the TPID and then the TIDFL. However, the TIDFL presented an outlier that is the largest value of all controllers. Figure 5.22b indicates similar values for the mean value of $\|\boldsymbol{u}(t)\|$ for both TPID and TAC, but smaller values for the TIDFL, although the difference was not so significant as for the error discrepancy. Regarding the maximum value of $\|\boldsymbol{u}(t)\|$, shown in Figure 5.22c, the TPID presented the smallest median, although the largest variation, followed by the TAC and then the TIDFL.

Again, since the TIDFL generates a low-level control input that is multiplied by the JSIM, the control signal may be attenuated for some joints, which does not happen for the TPID and the TAC. This may explain the larger control signals generated by both TPID and TAC than the ones generated by the TIDFL, as observed in Figures 5.22a-5.22b.

Regarding Figure 5.22c, the largest variation of the maximum value of the control signal for the TPID may be related to the absence of the JSIM in the control law. More specifically, the controller generates the control signal by using only partial information about the robot's dynamic behavior, which may explain a larger variance of the maximum value for the control input throughout the configuration space.

Table 5.8 shows the comparisons regarding the control signal of the inner motion controllers, in which bold values indicate that the p-values were smaller than the adjusted significance level $\alpha_{\text{adj}} = 0.0167$. When the maximum control signal is considered, all null-hypotheses were rejected, which means that there is a statistical difference between all controllers. On the other hand, in terms of the mean value, there is no significant difference between the TPID and the TAC. Lastly, when the total discrepancy is considered, there is a statistical difference only between the TIDFL and the TAC. These results indicate that, although the error discrepancy is the worst for the TIDFL, the same cannot be said about the control signal. Indeed, Figures 5.22a and 5.22b suggest that, in general, the TIDFL

Table 5.8: p-values for the Welch t-test all against all, regarding the control signal.

	Control effort		Mean value		Max. value	
	TIDFL	TPID	TIDFL	TPID	TIDFL	TPID
TIDFL	-	0.06	-	$\mathbf{7.19\times10^{-4}}$	-	$\mathbf{2.53\times10^{-8}}$
TAC	$\mathbf{6.20\times10^{-4}}$	0.05	$\mathbf{5.56\times10^{-5}}$	0.30	$\mathbf{5.19\times10^{-5}}$	$\mathbf{4.65\times10^{-5}}$

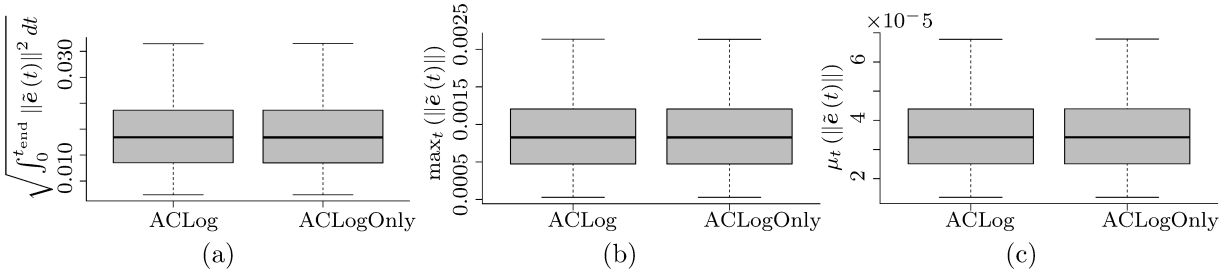

Figure 5.23: Error discrepancy: *(a)* total discrepancy, *(b)* maximum value, and *(c)* mean.

generates smaller control signals. This can be related to the use of the JSIM in the control law, which attenuates the control signal along joints that have smaller equivalent inertia.

5.4.4 Comparison Between Admittance Controllers

In the previous experiment, the proposed admittance controller using only the logarithmic mapping of the DQ displacement $\underline{\boldsymbol{x}}_d^c$ (ACLogOnly), given by Equation (4.2), was used. We also performed experiments with the proposed task-space adaptive controller with the ACLog. The impedance matrices used for these experiments were the same of the previous one, that is, $\boldsymbol{M}_d = 1.5\boldsymbol{I}_{6\times6}$, $\boldsymbol{B}_d = 300\boldsymbol{I}_{6\times6}$, and $\boldsymbol{K}_p = \boldsymbol{K}_\phi = 100\boldsymbol{I}_{3\times3}$.

We compared the two proposed admittance controllers, and the results are shown in Figures 5.23-5.25. The values of all boxplots show that both admittance controllers' behaviors were very similar, since the error discrepancy was very similar for both controllers, as well as the control signal. This result was corroborated by the Pairwise Wilcoxon Rank Sum Test, in which the p-values were all larger than the significance level $\alpha_{\text{analysis}} = 0.05$, as described in Table 5.9.

Although the ACLogOnly does not have a physical meaning, for the experiments done, its behavior is satisfactory and equivalent to the ACLog.

Table 5.9: p-values of the Wilcoxon Rank Sum Test, for comparison between the ACLogOnly and ACLog.

	Total	Max. value	Mean value
Error Discrepancy	0.9824	1	0.9824
Outer-Loop Control signal	0.9474	0.9474	0.8776
Inner-Loop Control signal	0.328	0.5096	0.4492

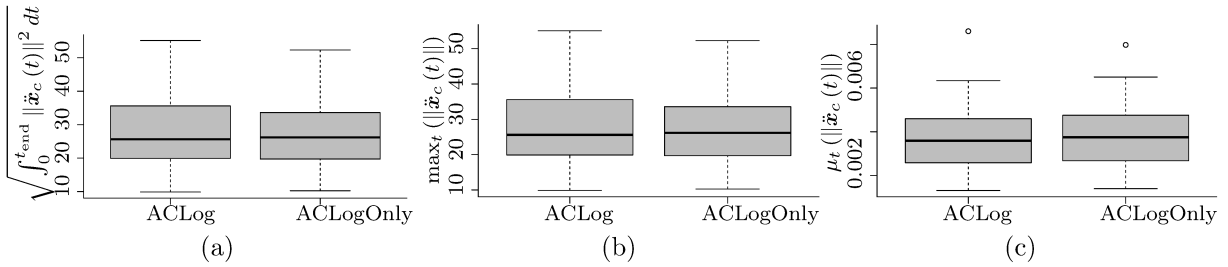

Figure 5.24: Outer-loop control signal: *(a)* control effort, *(b)* maximum value, and *(c)* mean.

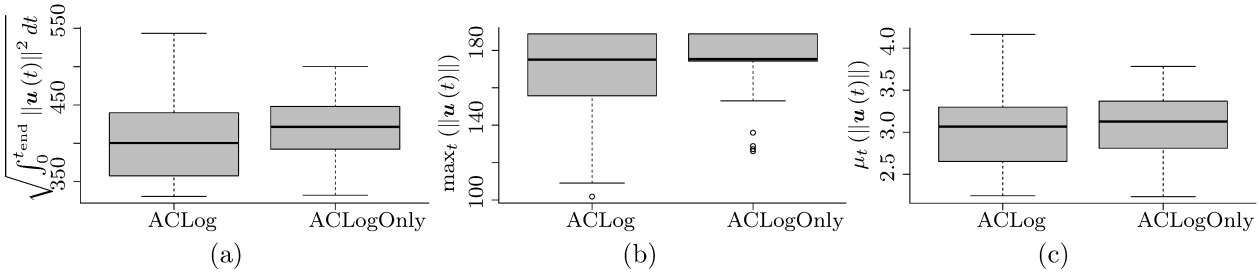

Figure 5.25: Inner-loop control signal: *(a)* control effort, *(b)* maximum value, and *(c)* mean.

5.5 Simulation and Experiments with Physically Meaningful Admittance Controller

An improvement of the controller of Equation (4.2) is the Equation (4.20), which have a physical meaning. Thus, more elaborated simulations and experiments were performed with this improved controller. First, a simulation to show the unwinding phenomenon; then, experiments with and without an external wrench acting on the robot end-effector. Moreover, statistical analyses were performed to compare this controller with one of the state-of-art controllers given by Equation (D.1).

For the following simulations and experiments, the architecture illustrated in Figure 4.1 is used, which consists of the admittance controller given by Equation (4.20) in the outer-loop and the kinematic controller Equation (4.37) in the inner-loop. The experiments were run on the KUKA LWR4+ (see Appendix B) robot manipulator with a force/torque sensor located at its end-effector. Since the KUKA LWR4+ is actuated in position, the control input of Equation (4.37) is numerically integrated twice, using Newton's first-order approximation, to obtain velocity and position signals. Moreover, to prevent reaching the joints maximum velocities, they were saturated in 0.2 rad/s. For all simulations and experiments, unless explicitly said otherwise, the matrices in Equation (4.20) were chosen as $\boldsymbol{M}_d = 1.5\boldsymbol{I}_{6\times6}$, $\boldsymbol{B}_d = 300\boldsymbol{I}_{6\times6}$, $\boldsymbol{K}_p = 80\boldsymbol{I}_{3\times3}$, and $\boldsymbol{K}_\phi = 80\boldsymbol{I}_{3\times3}$, whereas in Equation (4.37) they were chosen as $\boldsymbol{K}_P = 25\boldsymbol{I}_{6\times6}$, $\boldsymbol{K}_D = 10\boldsymbol{I}_{6\times6}$, and $k_{\text{dis}} = 1$.

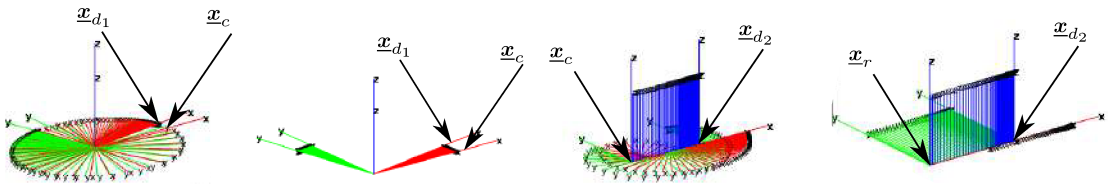

(a) (b) (c) (d)

Figure 5.26: Simulation of a free-flying rigid body under the unwinding phenomenon *(a* and *c)*, and path using solution Equation (4.24) (*b* and *d)*.

5.5.1 Simulation of Unwinding

We performed a simulation of a free-flying rigid body to show that, when using Equation (4.20) together with Equation (4.24), the end-effector follows the smallest spatial distance towards the desired pose, whereas without considering Equation (4.24), the end-effector performs an unnecessary rotation. Figure 5.26 shows the simulation for two different initial displacements between $\underline{\boldsymbol{x}}_c$ and $\underline{\boldsymbol{x}}_d$, namely $\underline{\boldsymbol{x}}_{d_1}^c$ and $\underline{\boldsymbol{x}}_{d_2}^c$. In the first case, (Figures 5.26a-5.26b), $\underline{\boldsymbol{x}}_{d_1}^c = \cos(\pi + 0.1) + \hat{k}\sin(\pi + 0.1)$ is closer to -1 than to 1. Thus, without using Equation (4.24), the body executes a rotation of almost 2π to reach the desired pose (Figure 5.26a) whereas when considering Equation (4.24), the rotation is much smaller (Figure 5.26b). In the second case (Figures 5.26c-5.26d), $\underline{\boldsymbol{x}}_{d_2}^c = -1 - \varepsilon\,(1/2)\,0.3\hat{\imath}$ is closer to -1 than to 1 and consists of a pure translation. In this case, without the solution for the unwinding problem, the body executes a rotation of 2π, whereas with the solution it only translates, while keeping its orientation.

5.5.2 Experimental Setup

Similar to the previous experiment, consider $\underline{\boldsymbol{x}}_c(0) = \underline{\boldsymbol{x}}_d(0) \triangleq \underline{\boldsymbol{x}}\,(0)$. When an external contact wrench acts on the end-effector, the reference pose $\underline{\boldsymbol{x}}_c$ becomes different from $\underline{\boldsymbol{x}}_d$ to ensure the desired apparent impedance, and the end-effector follows the trajectory given by $\underline{\boldsymbol{x}}_c(t)$. This situation is illustrated in the movement from 1 to 2 in Figure 5.27. When the contact is released, $\underline{\boldsymbol{x}}_c$ (and consequently $\underline{\boldsymbol{x}}$) returns to the desired pose $\underline{\boldsymbol{x}}_d$, thanks to the dynamics determined by the admittance controller, as illustrated by movement from 2 to 3 in Figure 5.27.

Two different experiments were performed: first, an external wrench acts on the end-effector (first part of Figure 5.27); second, the robot performs a free motion (second part of Figure 5.27).

The following analyses were made to compare our proposed controller (Equation (4.19)), named ACLog, with one of the main admittance controllers in the state of art, given by Equation (D.1), named here as ACIm (see Appendix D). The inner-loop controller was the same for both cases and both admittance controllers, being the second-order kinematic controller Equation (4.37).

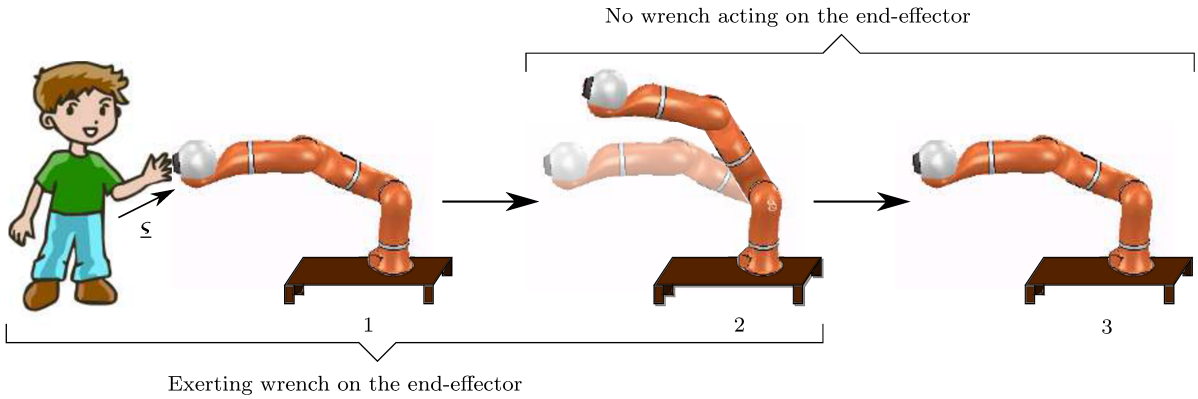

Figure 5.27: The experiments are divided in two parts: from 1 to 2, where a wrench is applied to the end-effector, which makes $\underline{\boldsymbol{x}}_c$ be different from a constant $\underline{\boldsymbol{x}}_d$; and from 2 to 3, where the controllers are applied in free-motion, such that $\underline{\boldsymbol{x}}_c$ returns to $\underline{\boldsymbol{x}}_d$.

5.5.3 Experiments with an External Wrench

To apply a wrench at the end-effector, a person pushed the manipulator, which moved complacently, as shown in the snapshots of Figure 5.28. The translation and orientation of the current end-effector pose $\underline{\boldsymbol{x}}$, the reference pose $\underline{\boldsymbol{x}}_c$, and the desired pose $\underline{\boldsymbol{x}}_d$ are shown in Figure 5.29a, for both controllers. Since the force is exerted by a human, it is not exactly the same for the two controllers, as shown in Figure 5.29b. However, both controllers generated a reference trajectory $\underline{\boldsymbol{x}}_c$ different from $\underline{\boldsymbol{x}}_d$, as expected, to ensure a compliant behavior according to the desired impedance, and this trajectory was followed by the end-effector, thanks to the inner-loop controller. Moreover, the results showed a control signal $\boldsymbol{u}$ with similar magnitude for both controllers, as depicted in Figure 5.29c.

Another experiment was executed in which an object with mass of 0.74kg was placed onto the end-effector, and removed after some seconds. For this experiment, the impedance matrices were chosen empirically as $\boldsymbol{M}_d = 1.5\boldsymbol{I}_{6\times6}$, $\boldsymbol{B}_d = 200\boldsymbol{I}_{6\times6}$, $\boldsymbol{K}_p = 20\boldsymbol{I}_{3\times3}$, and $\boldsymbol{K}_\phi = 20\boldsymbol{I}_{3\times3}$, and the kinematic controller gains were $\boldsymbol{K}_P = 25\boldsymbol{I}_{6\times6}$, $\boldsymbol{K}_D = 10\boldsymbol{I}_{6\times6}$, and $k_{\text{dis}} = 1$. The results are shown in Figure 5.30. Although in this case the wrench is due to an object, it was placed onto and removed from the end-effector by a human, which also inserts uncertainties to the contact wrench, as observed in Figure 5.30b, in which the wrenches of each execution are not exactly the same. Despite this difference, both controllers produced a compliant trajectory $\underline{\boldsymbol{x}}_c$ different from the desired one $\underline{\boldsymbol{x}}_d$ when the end-effector is under a contact wrench. After about 30 s the object is removed and thus the trajectory $\underline{\boldsymbol{x}}_c$ tends to the desired one $\underline{\boldsymbol{x}}_d$ for both controllers. The current end-effector pose follows the compliant one in all situations, thanks to the inner-loop kinematic controller.

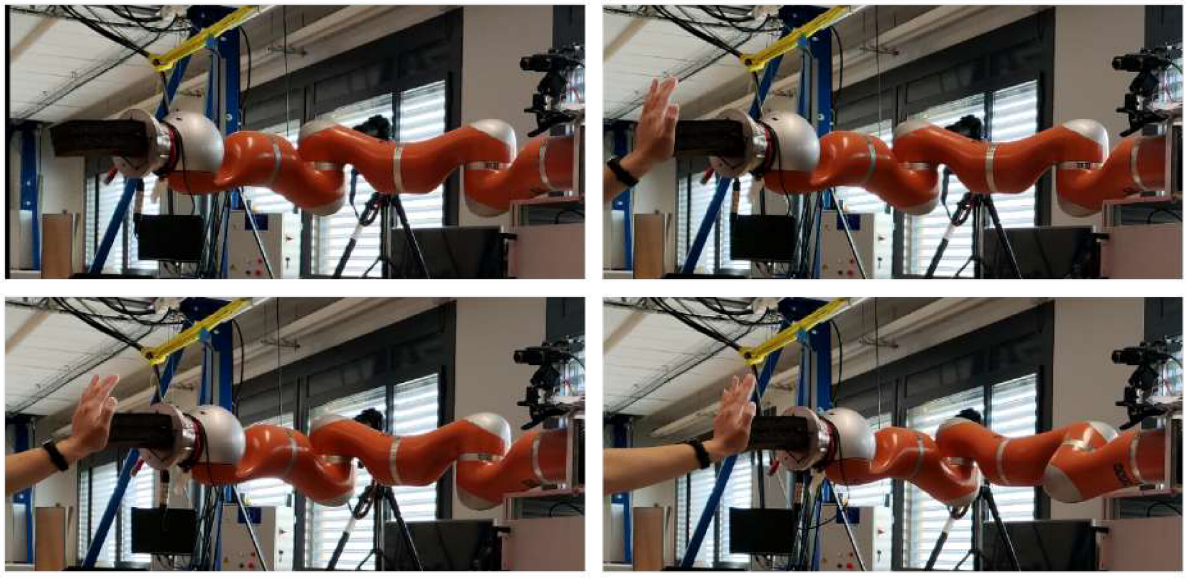

Figure 5.28: The person pushes the robot, exerting a wrench at the end-effector, and the robot moves complacently according to the wrench measured by the force/torque sensor.

5.5.4 Experiments in Free-Motion

Since the experiment of pHRI with a contact wrench is limited for comparison, as it is more susceptible to variations in the interaction wrench, deeper analyses were made in the second part of the movement, that is, when there is no wrench acting on the end-effector. As a way to see if there is a significant difference between the performance of the two controllers (Equation (4.19) and Equation (D.1)), statistical analyses were performed considering

1. the difference between the desired error dynamics and the experimental one;
2. the control signal regarding the admittance controller;
3. the control signal regarding the kinematic controller.

Given an initial pose, different desired poses are generated randomly and each generated pose is the same for each controller to allow for a fair comparison.

5.5.4.1 Statistical Methodology

For this case, we used the Wilcoxon Rank Sum Test (Hollander et al., 1999). The power and the significance level were the same as section 5.4.3.1, and the minimally interesting effects as shown in Table 5.10. Similarly to the previous analyses, each controller was run 30 times. With the variance of the collected data for each analyses 1, 2, and 3, for each controller, the the desired parameters chosen, the number of samples was calculated using

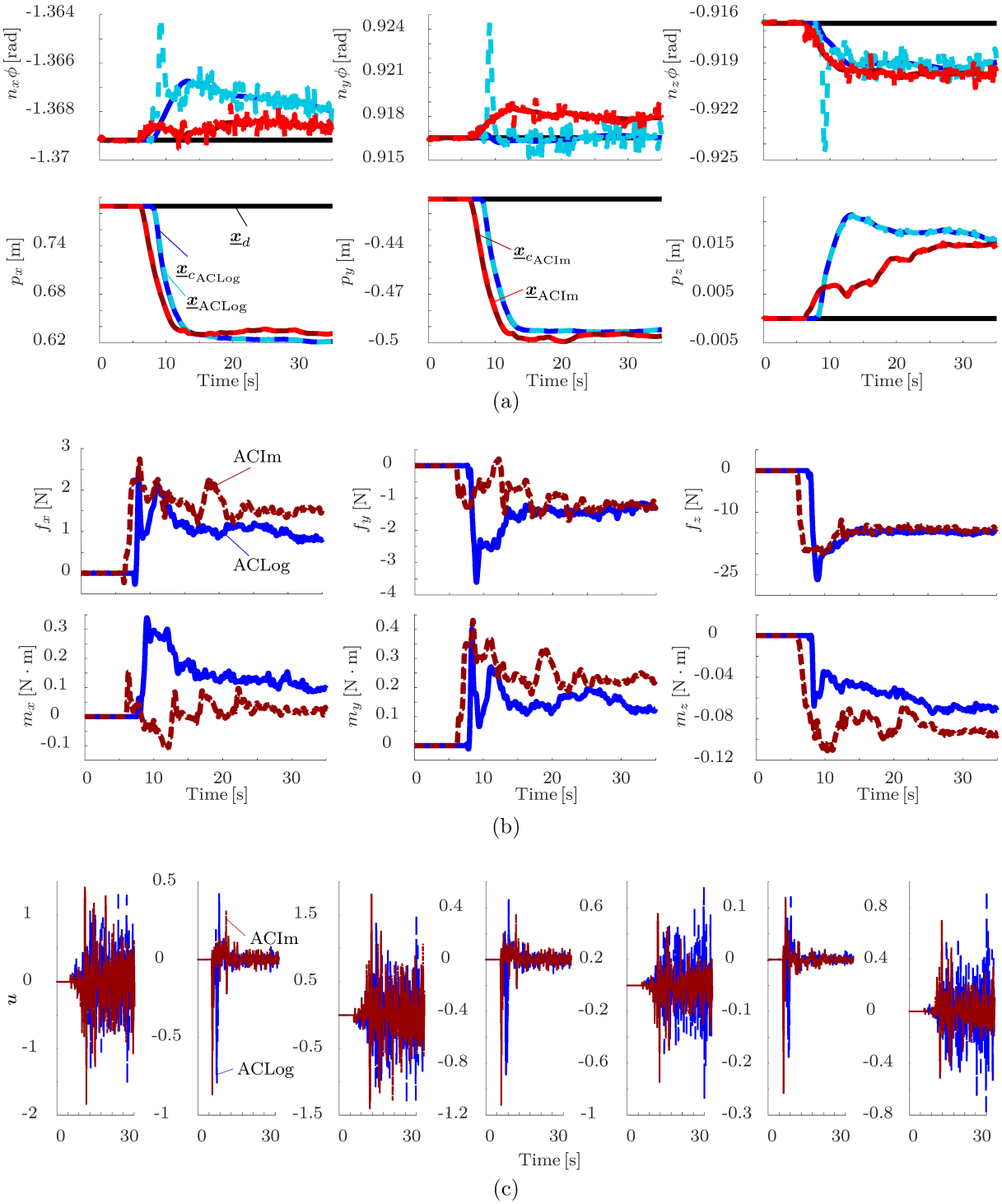

Figure 5.29: Results for the experiment in which a contact wrench acts on the robot end-effector. *(a)* Position and orientation of current, reference, and desired poses, *(b)* exerted wrench at the end-effector, and *(c)* control signal $\boldsymbol{u}$, for each controller.

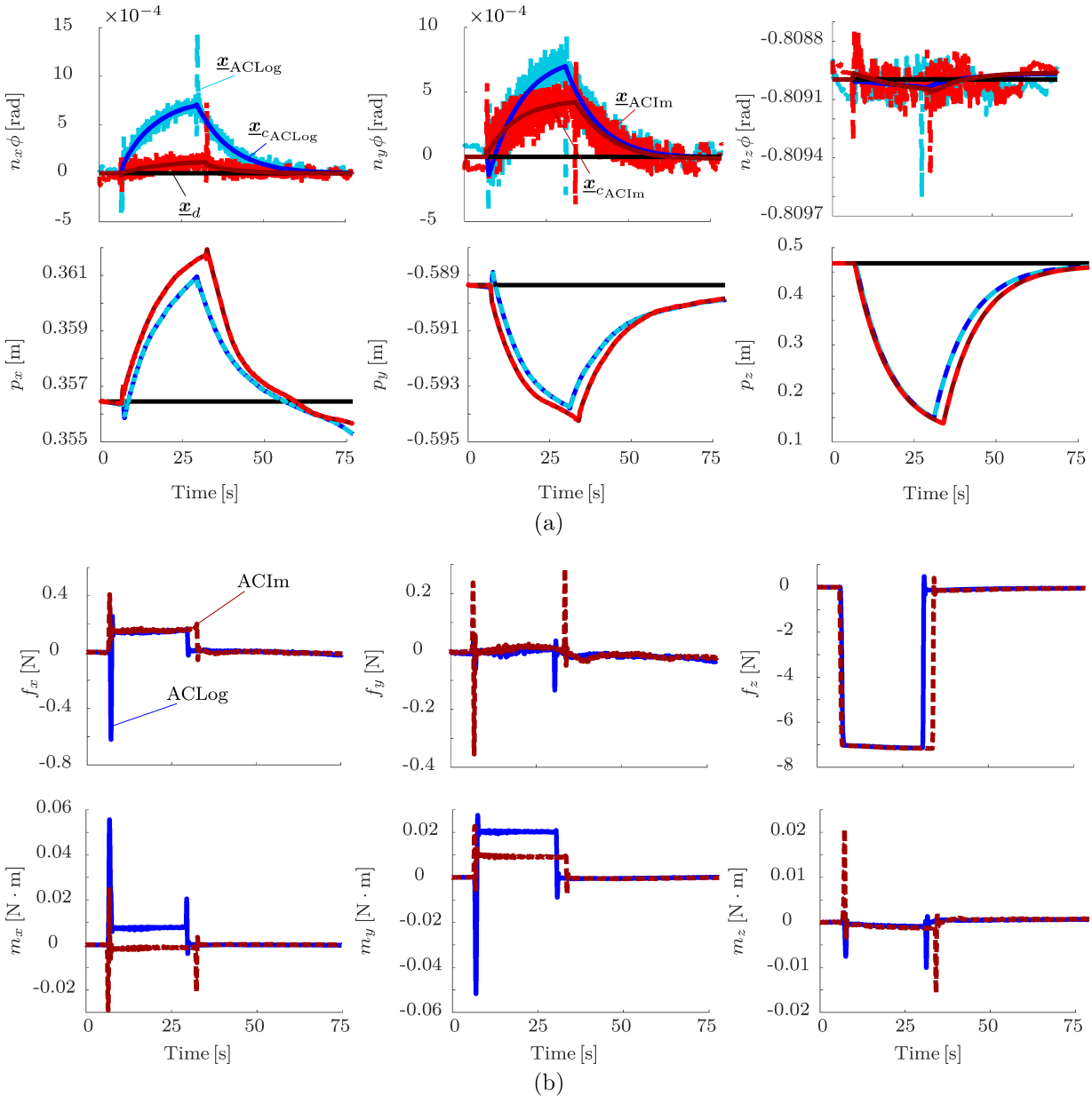

Figure 5.30: Results for the experiment in which a contact wrench acts on the robot end-effector as a result of the interaction with an object. *(a)* Position and orientation of current, reference, and desired poses and *(b)* exerted wrench at the end-effector.

Table 5.10: Minimally interesting effect, for each comparison.

Error discrepancy	Control signal of outer-loop	Control signal of inner-loop
$\delta_{\int \tilde{\boldsymbol{e}}} = 20$	$\delta_{\int \|\ddot{\boldsymbol{x}}_c\|} = 10$	$\delta_{\int \|\boldsymbol{u}\|} = 25$
$\delta_{\mu_{\tilde{\boldsymbol{e}}}} = 0.01$	$\delta_{\mu_{\|\ddot{\boldsymbol{x}}_c\|}} = 0.01$	$\delta_{\mu_{\|\boldsymbol{u}\|}} = 0.1$
$\delta_{\max(\tilde{\boldsymbol{e}})} = 0.02$	$\delta_{\max(\|\ddot{\boldsymbol{x}}_c\|)} = 10$	$\delta_{\max(\|\boldsymbol{u}\|)} = 25$

Table 5.11: p-values for the Wilcoxon Rank Sum Test.

Discrepancy		Outer control signal		Inner control signal	
$\int \tilde{\boldsymbol{e}}$	$\mathbf{1.67 \times 10^{-12}}$	$\int \ddot{\boldsymbol{x}}_c$	0.328	$\int \boldsymbol{u}$	0.7412
$\mu(\tilde{\boldsymbol{e}})$	$\mathbf{5.99 \times 10e^{-13}}$	$\mu(\ddot{\boldsymbol{x}}_c)$	0.3817	$\mu(\boldsymbol{u})$	0.8776
$\max(\tilde{\boldsymbol{e}})$	$\mathbf{2.75 \times 10^{-9}}$	$\max(\ddot{\boldsymbol{x}}_c)$	0.328	$\max(\boldsymbol{u})$	0.7191

the two-sample t-test power calculation available in R[6], resulting in a value lower than 30 for all cases. Hence, the analyses were made with the 30 samples already collected.

5.5.4.2 Statistical Analyses of the Error Dynamics

We first analyzed the difference between the desired and the actual error norm decay. More specifically, the error is given by $\boldsymbol{e} \triangleq 2\,\mathrm{vec}_6(\log \underline{\boldsymbol{x}}_d^c) = \left[(\mathrm{vec}_3(\boldsymbol{n}_{cd}^c \phi_d^c))^T \quad (\mathrm{vec}_3\, \boldsymbol{p}_{cd}^c)^T\right]^T$, and the desired error dynamics $\boldsymbol{e}_d(t)$ is given by the solution of the equation $\boldsymbol{M}_d\ddot{\boldsymbol{e}} + \boldsymbol{B}_d\dot{\boldsymbol{e}} + \boldsymbol{K}_d\boldsymbol{e} = \boldsymbol{0}$, with $\boldsymbol{K}_d = \mathrm{diag}(\boldsymbol{K}_\phi, \boldsymbol{K}_p)$. Therefore, given a discrepancy function defined as $\tilde{\boldsymbol{e}}(t) \triangleq \left|\|\boldsymbol{e}_d(t)\| - \|\boldsymbol{e}(t)\|\right|$,[7] the first analysis concerns the total discrepancy, given by $\sqrt{\int_0^{t_{\text{end}}} \tilde{\boldsymbol{e}}(t)^2\, dt}$, for $t_{\text{end}} = 35\,\text{s}$, along the trajectory. Figure 5.31 shows that the total discrepancy is very small for the ACLog, but this difference presents larger values for the ACIm. The same is observed for the maximum value $\max_t(\|\tilde{\boldsymbol{e}}(t)\|)$ of the discrepancy function (Figure 5.31a) and its mean value $\mu_t(\|\tilde{\boldsymbol{e}}(t)\|)$ (Figure 5.31a). Moreover, the ACIm presents outliers in all three cases, indicating an even larger discrepancy for some cases. The p-values for the Wilcoxon Rank Sum Test are described in Table 5.11, and are all smaller than the significance level $\alpha_{\text{analysis}} = 0.05$, therefore the null hypothesis that the populations are of the same type is rejected. By the boxplot and the Wilcoxon Rank Sum Test, we conclude that the ACLog obtained a better performance. The larger error discrepancy of the ACIm over the ACLog may be partially explained by the non-linearity of the former, as described in section 5.5.4.8. Nonetheless, this difference may not be critical for general applications.

[6] https://www.r-project.org/

[7] Since we use a coupled controller with positive definite gain matrices, the *norm* of the error has an exponential decay, but the same is not always true for each individually coefficient of the error. Therefore, the discrepancy function is defined as the difference between the error norms instead of the norm of the difference between the errors.

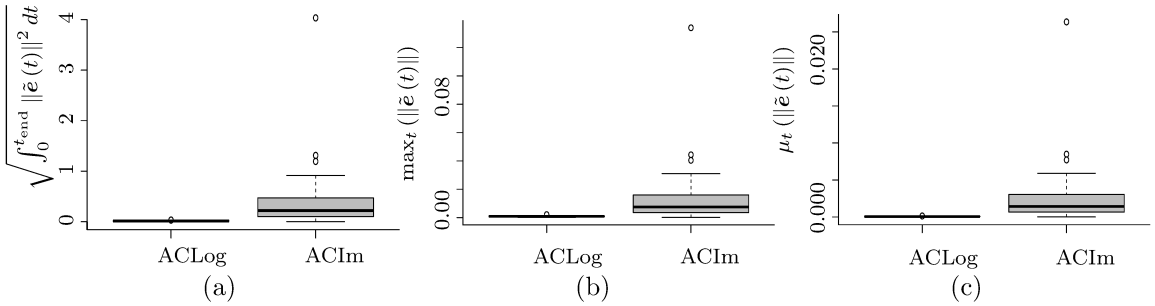

Figure 5.31: Error dynamics: *(a)* integral of the discrepancy function along the motion, *(b)* maximum value of the discrepancy function, and *(c)* its mean for each controller.

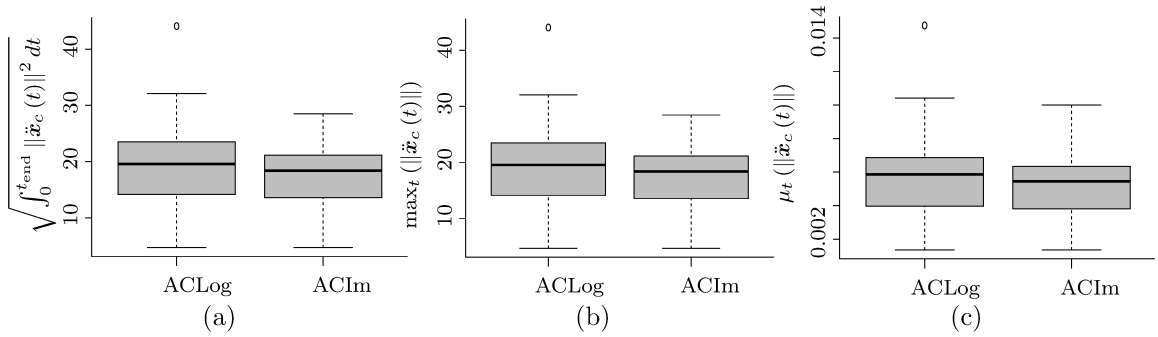

Figure 5.32: Outer-loop control signal: *(a)* control effort, *(b)* maximum value, and *(c)* mean.

5.5.4.3 Statistical Analyses of the Outer-Loop Control Signal

A similar analysis was done for the control signal of the admittance controller. We considered the control signal as the DQ acceleration $\underline{\ddot{\boldsymbol{x}}}_c$, since it represents the trajectory passed to the inner-loop, and is directly related to the $\dot{\boldsymbol{\zeta}}_{cd}^c$ through the Equations (3.19), (3.14), $\underline{\boldsymbol{x}}_d^c = \underline{\boldsymbol{x}}_c^* \underline{\boldsymbol{x}}_d$, and their derivatives. Figures 5.32a-5.32c show the control effort $\sqrt{\int_0^{t_{end}} \|\ddot{\boldsymbol{x}}_c(t)\|^2 dt}$, the maximum value of the control signal $\max_t(\|\ddot{\boldsymbol{x}}_c(t)\|)$, and its mean value $\mu_t(\|\ddot{\boldsymbol{x}}_r(t)\|)$, respectively. The hypothesis tests resulted in the p-values depicted in Table 5.11, which are all greater than the significance level $\alpha_{\text{analysis}} = 0.05$. Therefore, the null-hypothesis cannot be rejected and there is no significant statistical difference between the control signals of the two controllers.

5.5.4.4 Statistical Analyses of the Inner-Loop Control Signal

The same analyses were made for the control signal of the kinematic controller, that is, control effort $\sqrt{\int_0^{t_{end}} \|\boldsymbol{u}(t)\|^2 dt}$, maximum value of the control signal $\max_t(\|\boldsymbol{u}(t)\|)$, and its mean value $\mu_t(\|\boldsymbol{u}(t)\|)$. Figures 5.33a-5.33c show that the control signals for the kinematic controller were very similar for both ACLog and ACIm. The p-values for the Wilcoxon Rank Sum Test are the ones in Table 5.11. Again, all the values were larger than α_{analysis}, indicating that there is no significant statistical difference between the control

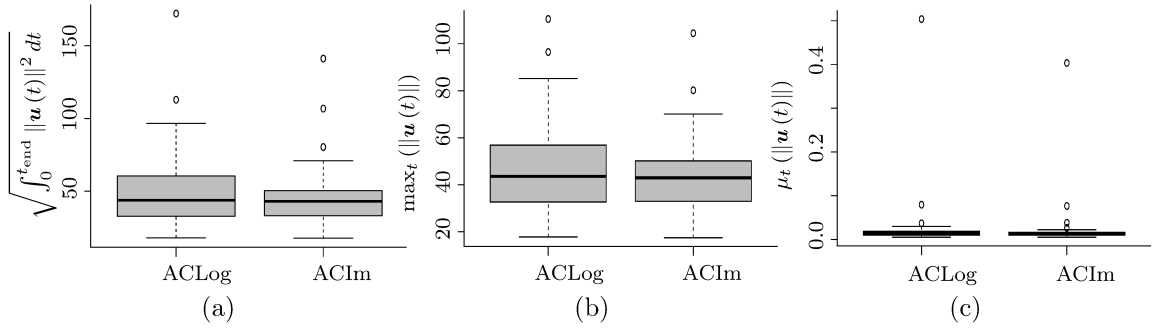

Figure 5.33: Inner-loop control signal: *(a)* control effort, *(b)* maximum value, and *(c)* mean.

signal of both controllers. This is expected because the reference signal for the inner-loop is generated by the outer-loop, and the outer-loop generates statistically equivalent control signals for both ACLog and ACIm, as shown in section 5.5.4.3.

5.5.4.5 Analyses of Special Cases

Besides the statistical analyses with 30 different samples, we also analyzed four special cases:

1. the closed-loop system under the admittance controller ACIm starts in the unstable equilibrium set (i.e., when $\phi(0) = \pi$);
2. the closed-loop system starts near this unstable equilibrium point;
3. a situation where the unwinding phenomenon appears ($\underline{\boldsymbol{x}}_d^c = -1$);
4. a situation where $\underline{\boldsymbol{x}}_d^c$ is closer to -1 than to 1.

For case 1, we considered an initial displacement of $\underline{\boldsymbol{x}}_d^c = \cos(\pi/2) + \hat{k}\sin(\pi/2)$, which consists of a pure rotation of π around the z axis. Figure 5.34a shows that, whereas the error norm decays when using the ACLog, it remains unchanged for the ACIm, which is undesirable as the current pose is different from the desired one. This is due to the topological obstruction (Bhat & Bernstein, 1998), as discussed in section 4.1.2.2.

For case 2, we initialize the displacement near the unstable equilibrium point (i.e., $\underline{\boldsymbol{x}}_d^c = \cos(\pi/2 - 0.002) + \hat{k}\sin(\pi/2 - 0.002)$). In that case, the closed-loop error decays when using the ACIm, but much slower than when the ACLog is used, as shown in Figure 5.34b, because the control signals near the unstable equilibrium point tend to be very small.

In case 3, the initial pose already equals the desired one, but the closed-loop system under the control law ACLog is in the PIS -1. Figure 5.34c shows that the error is always zero, indicating that the end-effector does not move for any controller. More specifically,

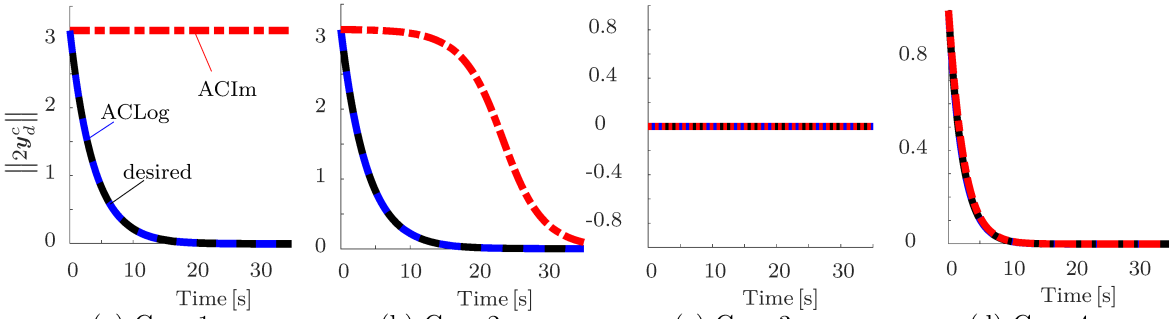

(a) Case 1 (b) Case 2 (c) Case 3 (d) Case 4

Figure 5.34: Closed-loop system during free-motion: time-evolution of the error norms in the four special cases.

the ACLog does not drive the system towards the PIS 1, which would make the end-effector move. Therefore, there is no unwinding.

Lastly, we considered $\underline{\boldsymbol{x}}_d^c = \cos(\pi + 0.5) + \hat{k}\sin(\pi + 0.5)$ to represent case 4. In this case the error norm for both controllers decay at the same rate, which indicates that the end-effector is converging to -1 instead of 1, performing the smallest path, as desired.

5.5.4.6 Simulation with an External Wrench

As observed by previously discussed results, experiments with a contact wrench is susceptible to variations, which does not allow a fair comparison. Nonetheless, a comparison between the two controllers, under the influence of external wrenches with very large rotations, may be interesting. Therefore, simulations were performed under these conditions and the results were exactly the same as predicted by the theory:

- when the initial error $\underline{\boldsymbol{x}}_d^c$ has an angle of rotation equal to π rad around a rotation axis parallel to any eigenvector of $\boldsymbol{K}_\phi$, the topological obstruction occurs if $\boldsymbol{\zeta}_{cd}^c = \mathbf{0}$ and $(1/2)\boldsymbol{K}_p^{''}\operatorname{vec}_3 \boldsymbol{p}_{cd}^c = -\operatorname{vec}_3 \boldsymbol{m}_{\text{eff,eff}}^c$, and $\boldsymbol{K}_p^{'}\operatorname{vec}_3 \boldsymbol{p}_{cd}^c = -\operatorname{vec}_3 \boldsymbol{f}_{\text{eff,eff}}^c$, where $\operatorname{vec}_3 \boldsymbol{f}_{\text{eff,eff}}^c$ and $\operatorname{vec}_3 \boldsymbol{m}_{\text{eff,eff}}^c$ are the force and the torque at the end-effector with respect to the frame $\mathcal{F}_c$ (see Appendix D);

- when the system starts near the unstable equilibrium set, the error starts to decay very slowly for the ACIm, similar to the behavior depicted in Figure 5.34b.

In the first simulation, which represents the case 1, the following parameters were used:

- a constant wrench $\boldsymbol{\varsigma}_{\text{eff,eff}}^{\text{eff}} = \begin{bmatrix} 4 & 0.8 & 0.8 & 0 & 0 & 0 \end{bmatrix}^T$ is applied at the end-effector;

- the initial error is $\underline{\boldsymbol{x}}_d^c = \boldsymbol{r}_d^c + \varepsilon(1/2)\boldsymbol{p}_{cd}^c \boldsymbol{r}_d$, with $\boldsymbol{r}_d^c = \cos(\pi/2) + \hat{k}\sin(\pi/2)$ and $\boldsymbol{p}_d^c = 0.05\hat{\imath} + 0.01\hat{\jmath} + 0.01\hat{k}$;

- the initial velocities are zero;

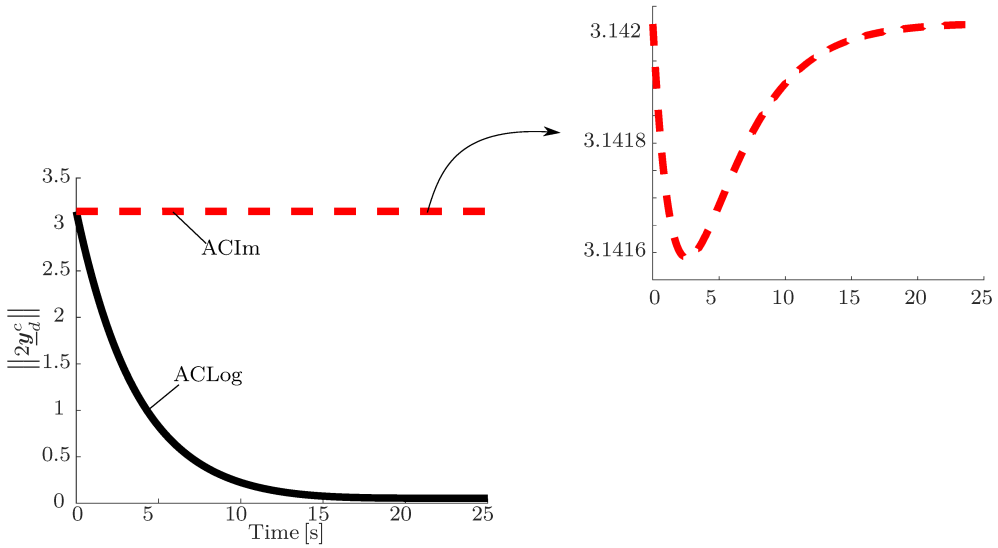

Figure 5.35: Two times the norm of the error $\underline{\boldsymbol{y}}_d^c$. The error for the ACLog decays until a small expected stationary error is perceived due to the presence of an external wrench, which makes $\underline{\boldsymbol{x}}_c \neq \underline{\boldsymbol{x}}_d$ to enforce the desired impedance. For the ACIm, however, the error decay is negligible due to the topological obstruction. Even though it slightly changes due to the variation of $\boldsymbol{p}_c$, the greatest contribution to the norm value comes from the rotational part, and therefore the error is almost constant.

- and $\boldsymbol{M}_d = 1.5\boldsymbol{I}_{6\times6}$, $\boldsymbol{B}_d = 300\boldsymbol{I}_{6\times6}$, $\boldsymbol{K}_p = \boldsymbol{K}_\phi = 80\boldsymbol{I}_{3\times3}$ are the inertial, damping, and stiffness matrices, respectively.

Figures 5.35-5.36 show that the rotational term of $\underline{\boldsymbol{x}}_c$ remained the same during all the simulation for the ACIm, characterizing the topological obstruction, whereas it approached to the rotational term of $\underline{\boldsymbol{x}}_d$ when the ACLog was used.

The second simulation shows a situation where the initial state of the closed-loop system starts near the topological obstruction, which represents case 2. Again, the closed-loop system response when using the ACIm is much slower than the one when using the ACLog, as shown in Figures 5.37-5.38. The following parameters were used:

- a constant wrench $\boldsymbol{\varsigma}_{\text{eff,eff}}^{\text{eff}} = \begin{bmatrix} 4 & 0.8 & 0.8 & 0 & 0 & 0 \end{bmatrix}^T$ is applied at the end-effector;
- the initial error is $\underline{\boldsymbol{x}}_d^c = \boldsymbol{r}_d^c + \varepsilon(1/2)\boldsymbol{p}_{cd}^c \boldsymbol{r}_d$, with $\boldsymbol{r}_d^c = \cos(\pi/2 - 0.002) + \hat{k}\sin(\pi/2 - 0.002)$ and $\boldsymbol{p}_{cd}^c = -0.05\hat{\imath} - 0.01\hat{\jmath} - 0.01\hat{k}$;
- the initial velocities are zero;
- and $\boldsymbol{M}_d = 1.5\boldsymbol{I}_{6\times6}$, $\boldsymbol{B}_d = 300\boldsymbol{I}_{6\times6}$, $\boldsymbol{K}_p = \boldsymbol{K}_\phi = 80\boldsymbol{I}_{3\times3}$ are the inertial, damping, and stiffness matrices, respectively.

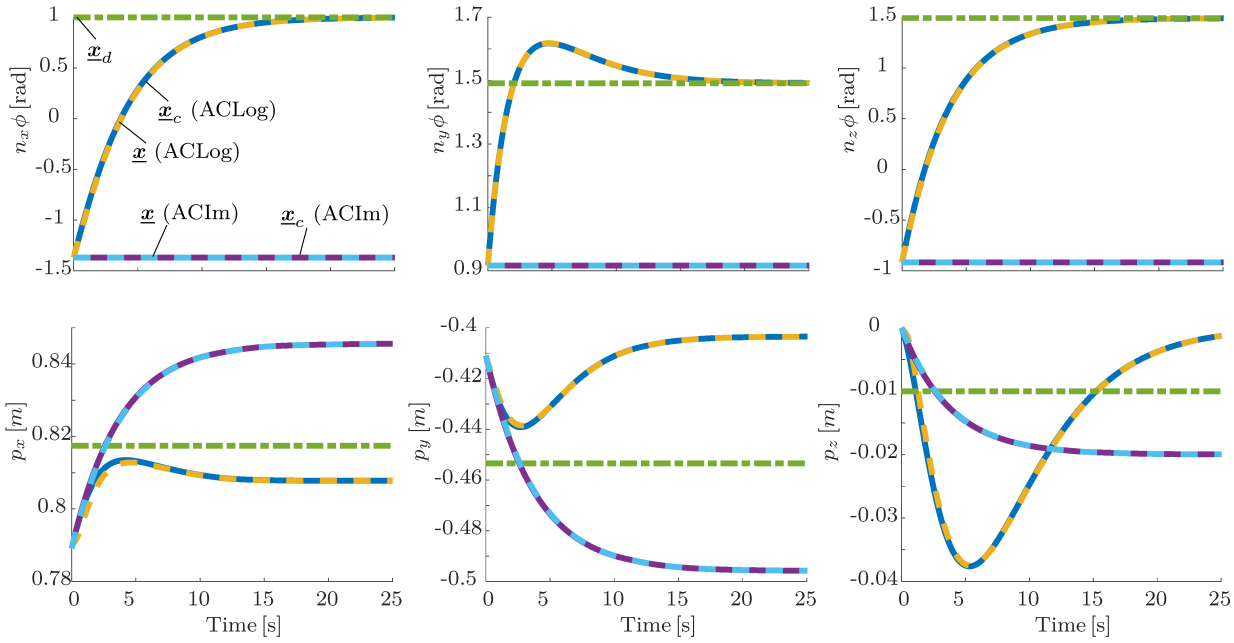

Figure 5.36: Orientation and position of the current $\underline{\boldsymbol{x}}$, compliant $\underline{\boldsymbol{x}}_c$, and desired $\underline{\boldsymbol{x}}_d$ poses. The kinematic controller follows the trajectories generated by both admittance controllers. However, due to the topological obstruction that affects the ACIm, the trajectory's rotational components remain constant throughout the robot's movement, which does not happen when ACLog is used.

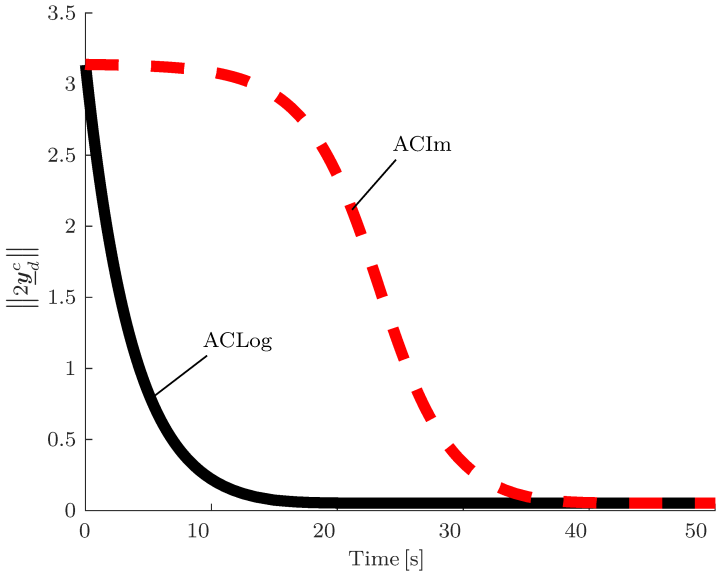

Figure 5.37: Two times the norm of the error $\underline{\boldsymbol{y}}_d^c$, when starting close to the topological obstruction. The error for the ACLog decays until a small expected stationary error is perceived due to the presence of an external wrench, which makes $\underline{\boldsymbol{x}}_c \neq \underline{\boldsymbol{x}}_d$ to enforce the desired impedance. For the ACIm, the error also decays until that small stationary error, but this decay is much slower than for the ACLog.

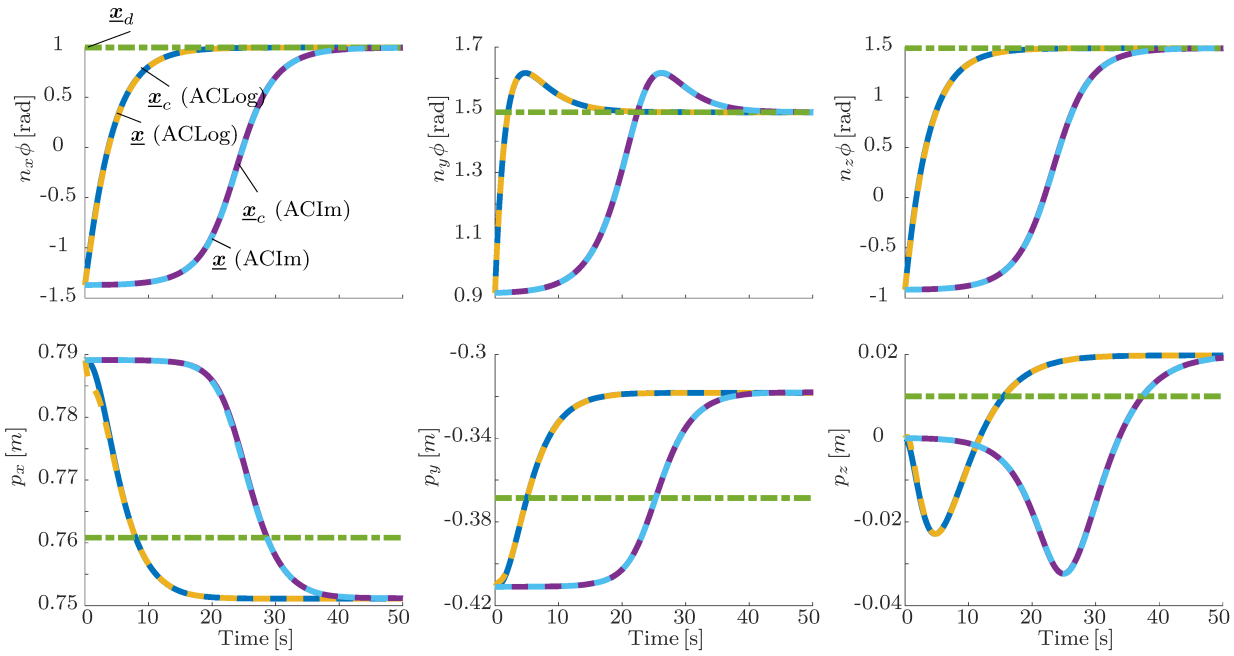

Figure 5.38: Orientation and position of the current $\underline{\boldsymbol{x}}$, compliant $\underline{\boldsymbol{x}}_c$, and desired $\underline{\boldsymbol{x}}_d$ poses. The kinematic controller follows the trajectories generated by both admittance controllers, achieving the same values for each coefficient of the logarithm in the end. However, the convergence of the ACIm is much slower than the one of the ACLog.

As a conclusion, the simulation results show that when there is an external wrench applied at the end-effector under special cases 1–2, both controllers behave analogously to when they are in free-motion. More specifically, the ACIm suffers from the problem of topological obstruction and loses performance near the unstable equilibrium set, whereas the ACLog do not suffers from topological obstruction.

5.5.4.7 Experiments in Free-Motion with Non-Isotropic Stiffness

The previous experiments and simulations were executed with isotropic stiffness matrices. However, it is also interesting to analyze the behavior of the admittance controllers using non-isotropic stiffness matrices. Therefore, the experiments were re-done with the same 30 pairs of initial/final end-effector poses, but now with $\boldsymbol{M}_d = 1.5\boldsymbol{I}_{6\times6}$, $\boldsymbol{B}_d = \text{diag}\,(300, 300, 300, 200, 200, 200)$, $\boldsymbol{K}_p = \text{diag}\,(95, 95, 100)$, and $\boldsymbol{K}_\phi = \text{diag}\,(92, 92, 90)$ as the desired apparent impedance matrices.

Statistical Analyses of the Error Dynamics As in the previous experiment, we first analyzed the difference between the desired and the actual error norm decay. Figure 5.39 shows that the total discrepancy, the maximum value of the discrepancy function, and its mean are, overall, similar for both admittance controllers. All three boxplots present outliers, which values are larger for the ACLog in the maximum and

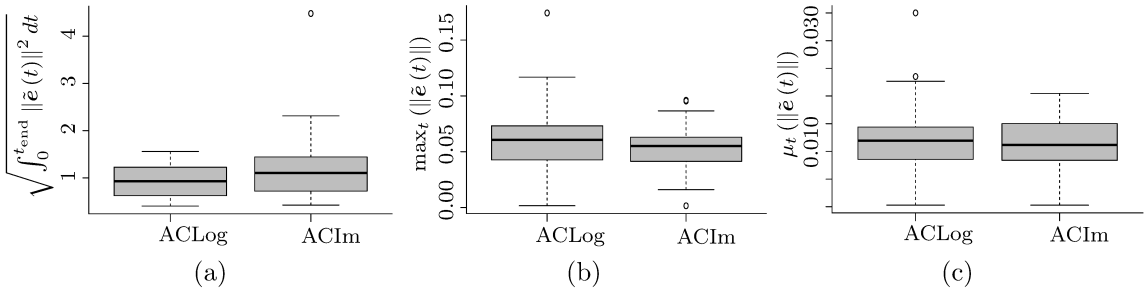

Figure 5.39: Error dynamics: *(a)* integral of the discrepancy function along the motion, *(b)* maximum value of the discrepancy function, and *(c)* its mean for each controller, using non-isotropic stiffness matrices.

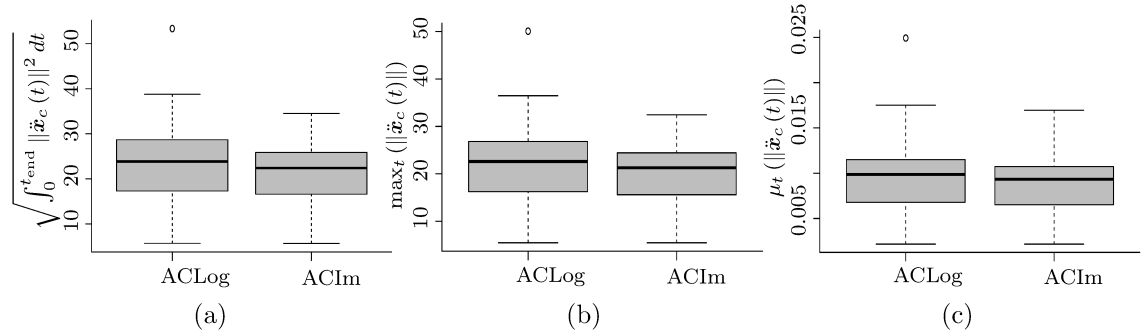

Figure 5.40: Outer-loop control signal when using non-isotropic stiffness matrices: *(a)* control effort, *(b)* maximum value, and *(c)* mean.

mean values, and for ACIm in the total discrepancy.

The p-values for the Wilcoxon Rank Sum Test are described in Table 5.12, begin all greater than the significance level $\alpha_{\text{analysis}} = 0.05$. Hence, the null hypothesis that the population are of the same type cannot be rejected.

Statistical Analyses of the Outer-loop Control Signal Again, a similar analysis was done for the control signal of the admittance controller. The hypothesis tests resulted in the p-values of Table 5.12, which are all greater than the significance level $\alpha_{\text{analysis}} = 0.05$. Therefore, the null-hypothesis cannot be rejected and there is no significant statistical difference between the control signals of the two controllers, which is corroborated by the boxplots of Figure 5.40.

Statistical Analyses of the Inner-Loop Control Signal Also, the p-values for the Wilcoxon Rank Sum Test for the control signal of the kinematic controller are depicted in Table 5.12. Again, all the values were larger than α_{analysis}, indicating that there is no significant statistical difference between the control signal of both controllers, as shown in Figure 5.41.

The p-values given by the Wilcoxon Rank Sum Test and also the boxplots of Figures 5.31-

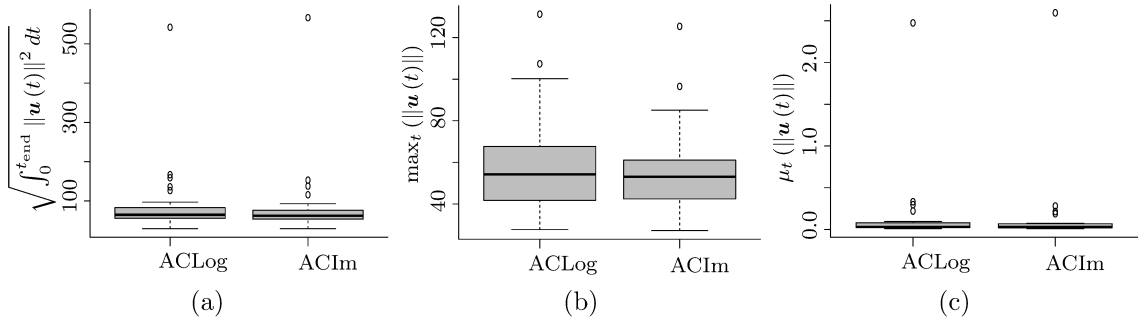

Figure 5.41: Inner-loop control signal when using non-isotropic stiffness matrices: *(a)* control effort, *(b)* maximum value, and *(c)* mean.

Table 5.12: p-values for the Wilcoxon Rank Sum Test for non-isotropic matrices.

Discrepancy		Outer control signal		Inner control signal	
$\int \tilde{\boldsymbol{e}}$	0.1058	$\int \ddot{\boldsymbol{x}}_c$	0.3208	$\int \boldsymbol{u}$	0.6022
$\mu(\tilde{\boldsymbol{e}})$	0.4853	$\mu(\ddot{\boldsymbol{x}}_c)$	0.5133	$\mu(\boldsymbol{u})$	0.5422
$\max(\tilde{\boldsymbol{e}})$	0.2928	$\max(\ddot{\boldsymbol{x}}_c)$	0.3354	$\max(\boldsymbol{u})$	0.6973

5.33 and Figures 5.39-5.41 show that the difference between the results of the experiments with the isotropic stiffness matrices and the non-isotropic is the error discrepancy, which is not statistically different for the non-isotropic matrices, but presents some disparity when using isotropic matrices. To try to explain this difference, a deeper analysis is made in the next section. Concerning the control signal, in both situations (isotropic and non-isotropic matrices) the statistical tests do not reject the null-hypothesis. However, the boxplots show a larger value of the control signal when using the non-isotropic matrices (Figures 5.40a-5.41c) over the isotropic case (Figures 5.32a-5.33c), which can be explained by the larger values of gains in the stiffness matrices, not necessarily being related to the nature of the matrix (i.e., isotropic or non-isotropic).

5.5.4.8 Qualitative Comparison Between ACLog and ACIm

Besides the problem of topological obstruction in the ACIm (Equation (D.1)), which is not present in the ACLog (Equation (4.19)), the main difference in both formulations is the stiffness term. More specifically, the stiffness term in the ACLog is given by

$$\begin{aligned}\boldsymbol{K}'_d \boldsymbol{y}^c_d &= \boldsymbol{K}'_d \begin{bmatrix} \left(\operatorname{vec}_3\left(\boldsymbol{n}^c_{cd}\frac{\phi}{2}\right)\right)^T & \left(\operatorname{vec}_3\left(\boldsymbol{p}^c_{cd}\frac{\phi}{2}\right)\right)^T \end{bmatrix}^T \\ &= \begin{bmatrix} 4\boldsymbol{W}^{-T}(\boldsymbol{r}^c_d)\,\boldsymbol{K}_\phi \operatorname{vec}_3 \boldsymbol{n}^c_{cd}\frac{\phi}{2} + \frac{1}{2}\boldsymbol{S}^T(\operatorname{vec}_3 \boldsymbol{p}^c_{cd})\,\boldsymbol{R}^c_d \boldsymbol{K}_p \boldsymbol{R}^{cT}_d \operatorname{vec}_3 \boldsymbol{p}^c_{cd} \\ \frac{1}{2}\left(\boldsymbol{K}_p + \boldsymbol{R}^c_d \boldsymbol{K}_p \boldsymbol{R}^{cT}_d\right)\operatorname{vec}_3 \boldsymbol{p}^c_{cd} \end{bmatrix}, \end{aligned} \tag{5.6}$$

whereas the stiffness term in the ACIm is given by

$$\begin{aligned}\boldsymbol{K}_d''\boldsymbol{h}_d^c &= \boldsymbol{K}_d''\left[\left(\operatorname{vec}_3\left(\boldsymbol{n}_{cd}^c\sin\left(\tfrac{\phi}{2}\right)\right)\right)^T \quad \left(\operatorname{vec}_3\boldsymbol{p}_{cd}^c\right)^T\right]^T \\ &= \begin{bmatrix} 2\boldsymbol{E}'^T\left(\boldsymbol{r}_d^c\right)\boldsymbol{K}_\phi\operatorname{vec}_3\boldsymbol{n}_{cd}^c\sin\frac{\phi}{2} + \frac{1}{2}\boldsymbol{S}^T\left(\operatorname{vec}_3\boldsymbol{p}_{cd}^c\right)\boldsymbol{R}_d^c\boldsymbol{K}_p\boldsymbol{R}_d^{cT}\operatorname{vec}_3\boldsymbol{p}_{cd}^c \\ \frac{1}{2}\left(\boldsymbol{K}_p + \boldsymbol{R}_d^c\boldsymbol{K}_p\boldsymbol{R}_d^{cT}\right)\operatorname{vec}_3\boldsymbol{p}_{cd}^c \end{bmatrix}, \end{aligned} \tag{5.7}$$

with $\boldsymbol{K}_d'$ and $\boldsymbol{K}_d''$ defined as Equation (4.17) and Equation (D.2), respectively. Comparing Equation (5.6) and Equation (5.7), the only term that differs between the two equations is the term in the left of the addition symbol, in the first row, that is,

$$\underbrace{4\boldsymbol{W}^{-T}\left(\boldsymbol{r}_d^c\right)\boldsymbol{K}_\phi\operatorname{vec}_3\boldsymbol{n}_{cd}^c}_{\mathbb{K}_{\text{Log}}}\frac{\phi}{2}$$

for the ACLog and

$$\underbrace{2\boldsymbol{E}'^T\left(\boldsymbol{r}_d^c\right)\boldsymbol{K}_\phi\operatorname{vec}_3\boldsymbol{n}_{cd}^c}_{\mathbb{K}_{\text{Im}}}\sin\frac{\phi}{2}$$

for the ACIm. The term related to the orientation in the ACIm is nonlinear due to the sine function, differently from the stiffness term in the ACLog, which is linear in the orientation angle ϕ. Moreover, the stiffness matrices for both controllers vary according to $\boldsymbol{r}_d^c$. To verify if these matrices influence the decay of the error, we analyzed the norm of $\mathbb{K}_{\text{Log}}$ and $\mathbb{K}_{\text{Im}}$ with and without an eigenvector parallel to the rotation axis, for different values of $\boldsymbol{K}_\phi$, ϕ, and $\boldsymbol{n}_{cd}^c$. One example of the result is shown in Figure 5.42, where the norm of $\mathbb{K}_{\text{Log}}$ and $\mathbb{K}_{\text{Im}}$ are shown for a specific $\boldsymbol{K}_\phi$ and $\boldsymbol{n}_{cd}^c$, for 100000 different values of ϕ, varying from 0 to π. If $\boldsymbol{K}_\phi$ has an eigenvector parallel to the rotation axis $\operatorname{vec}_3\boldsymbol{n}_{cd}^c$, then $\boldsymbol{K}_\phi\operatorname{vec}_3\boldsymbol{n}_{cd}^c = \lambda_\phi\operatorname{vec}_3\boldsymbol{n}_{cd}^c$, with λ_ϕ being one eigenvalue of $\boldsymbol{K}_\phi$. To have an eigenvector parallel to the rotation axis, we choose an isotropic matrix, that is, $\boldsymbol{K}_\phi = \lambda_\phi\boldsymbol{I}_{3\times3}$. The results for other values of $\boldsymbol{K}_\phi$ and $\boldsymbol{n}_{cd}^c$ presented the same type of curve, differing only in the magnitude. For instance, the norm of $\mathbb{K}_{\text{Log}}$ for the isotropic $\boldsymbol{K}_\phi$ have shown to be constant, with value equal to $2\lambda_\phi$, so it depends on the eigenvalue of $\boldsymbol{K}_\phi$. The isotropic matrix used to generate Figure 5.42 was $\boldsymbol{K}_\phi = 100\boldsymbol{I}_{3\times3}$, the non-isotropic was $\boldsymbol{K}_\phi = \operatorname{diag}(250, 92, 0)$, and the rotation axis $\boldsymbol{n}_{cd}^c$ was generated randomly by a normal function $\mathcal{N}(0,1)$, and then normalized to have an unit norm.

Figure 5.42 shows that for an isotropic matrix, the norm of $\mathbb{K}_{\text{Log}}$ is constant, differently from $\mathbb{K}_{\text{Im}}$. This gives a clue why the error discrepancy is smaller for ACLog than for the ACIm when an isotropic $\boldsymbol{K}_\phi$ is used, as depicted in Figure 5.31a. Since we evaluate the norm of the error, and the norm of $\mathbb{K}_{\text{Log}}$ has shown to be constant in all simulations done, the dynamics of the system approaches to the situation in which we have the error multiplied by a constant gain, and thus it decays exponentially. For the $\mathbb{K}_{\text{Im}}$ this does not occur, and thus the error discrepancy is larger. Moreover, in case 2 of section 5.5.4.5, the

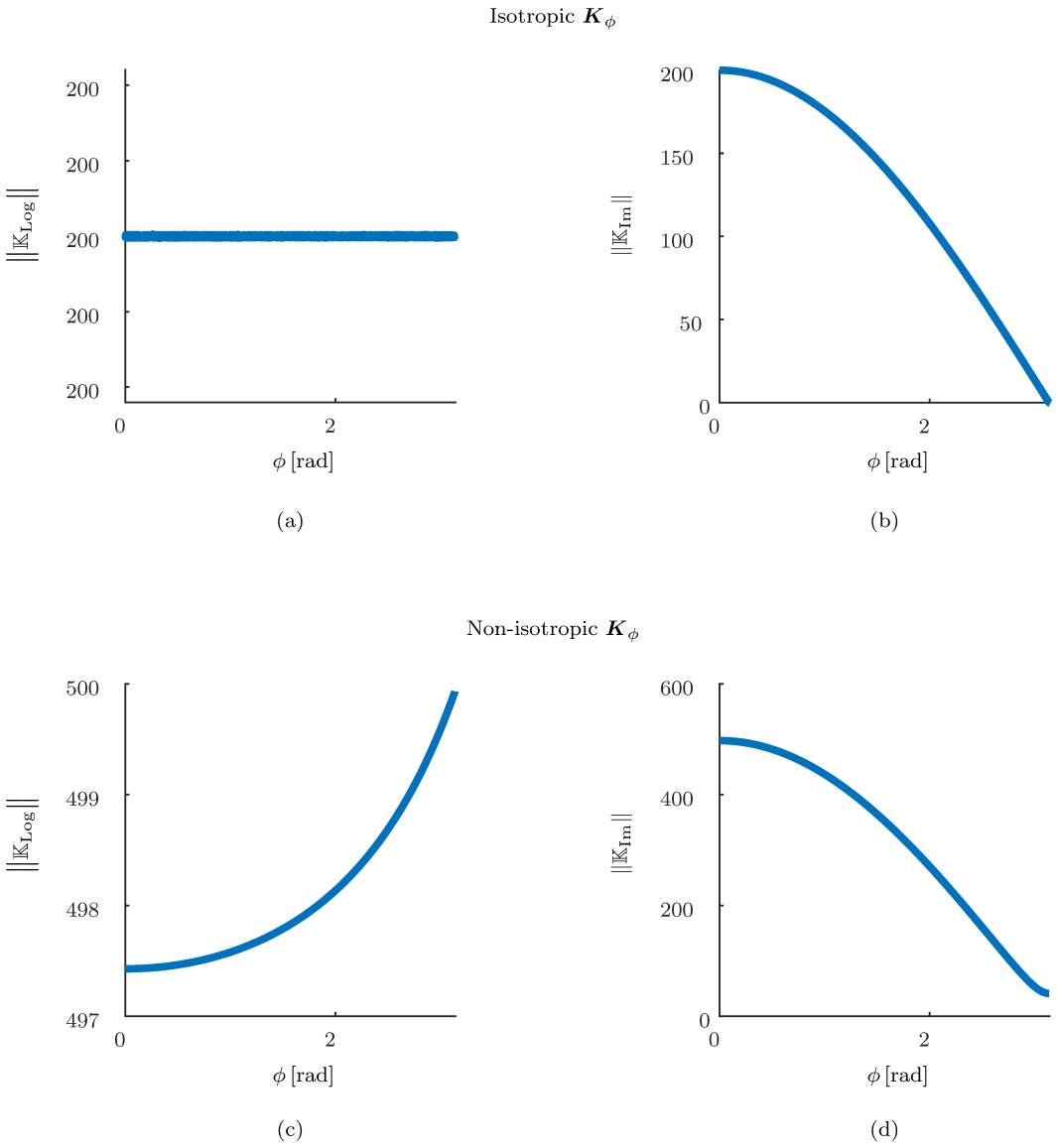

Figure 5.42: Norm of $\mathbb{K}_{\text{Log}}$ and $\mathbb{K}_{\text{Im}}$for *(a)*, *(b)* isotropic and *(c)*, *(d)* non-isotropic $\boldsymbol{K}_\phi$.

error decay is slower for the ACIm than the ACLog due to the small values of the control signal close to the unstable equilibrium point, which is influenced by the value of the angle ϕ but also of the norm of $\mathbb{K}_{\text{Im}}$.

Notwithstanding, in the case we do not have an eigenvalue of $\boldsymbol{K}_\phi$ parallel to the rotation axis, as in the case of the non-isotropic matrix, the norm of $\mathbb{K}_{\text{Log}}$ varies, and thus the error decay may not be exponential, which may explain the larger discrepancy of the ACLog in Figure 5.39a in relation to Figure 5.31a, and a similar one when compared to the ACIm, in Figure 5.39a.

5.6 Simulation Results for Whole-Body Admittance Controller

All the previous experiments have taken in consideration only one arm of the BAZAR robot. The proposed admittance controller can also be used considering the whole-body of the robot. For this, a small adaptation is done, as described in sections 4.1.4 and 4.2.3.

A simulation is therefore performed in MATLAB considering the whole-body of the BAZAR model (see Appendix B) for a task of cooperative manipulation of an object. The two arms of the robot are rigidly holding an object in a parallelepiped format, with negligible mass, so no gravity effect due to the object affects the movement of the arms. The initial configuration of the robot was $\boldsymbol{q}_{\text{base}}(0) = \begin{bmatrix} 0 & 0 & 0 \end{bmatrix}^T$, $\boldsymbol{q}_{\text{right}}(0) = \boldsymbol{q}_{\text{left}}(0) = \begin{bmatrix} 0 & 0.8726 & 0 & -2 & 0 & 0 & 0 \end{bmatrix}^T$, and the desired pose for the absolute and relative variables were equal to the initial ones, that is, $\underline{\boldsymbol{x}}_{\text{abs}_c}(0) = \underline{\boldsymbol{x}}_{\text{abs}_d}(0) \triangleq \underline{\boldsymbol{x}}_{\text{abs}}(0)$, and $\underline{\boldsymbol{x}}_{\text{rel}_c}(0) = \underline{\boldsymbol{x}}_{\text{rel}_d}(0) \triangleq \underline{\boldsymbol{x}}_{\text{rel}}(0)$. Moreover, a constant wrench $\underline{\boldsymbol{\psi}}^0_{0,\text{right}} = \underline{\boldsymbol{\psi}}^0_{0,\text{left}} = 10\hat{\imath}$ is applied to both arms until half of the simulation (25 s), and thereafter the wrench is zero. The initial configuration was chosen so the robot could grasp the object. Moreover, since we wanted to prevent internal wrenches so the object is not damaged, the desired relative pose was chosen equal to the initial one. The desired absolute pose and the applied wrenches was chosen so the robot would remain at its initial pose until a wrench is applied. The applied wrench would pull the robot forward, and then, when the robot is released, it would return to its original pose.

The simulated wrenches measured by the sensor at both end-effectors are depicted in Figure 5.46, as well as the external and internal wrenches with reference to the inertial frame $\mathcal{F}_0$. Although the applied wrenches only have the linear component, they are shown with reference to the inertial frame, and there is a transformation between the inertial frame $\mathcal{F}_0$ and the frames of the end-effectors, as illustrated in Figure 5.43. Therefore, torques appear in the wrenches measured at the end-effectors, with respect to the end-effectors.

The norm of the error of the whole-body admittance controller is shown in Figure 5.47. When the wrench is applied to the robot end-effectors, the norm increases, indicating

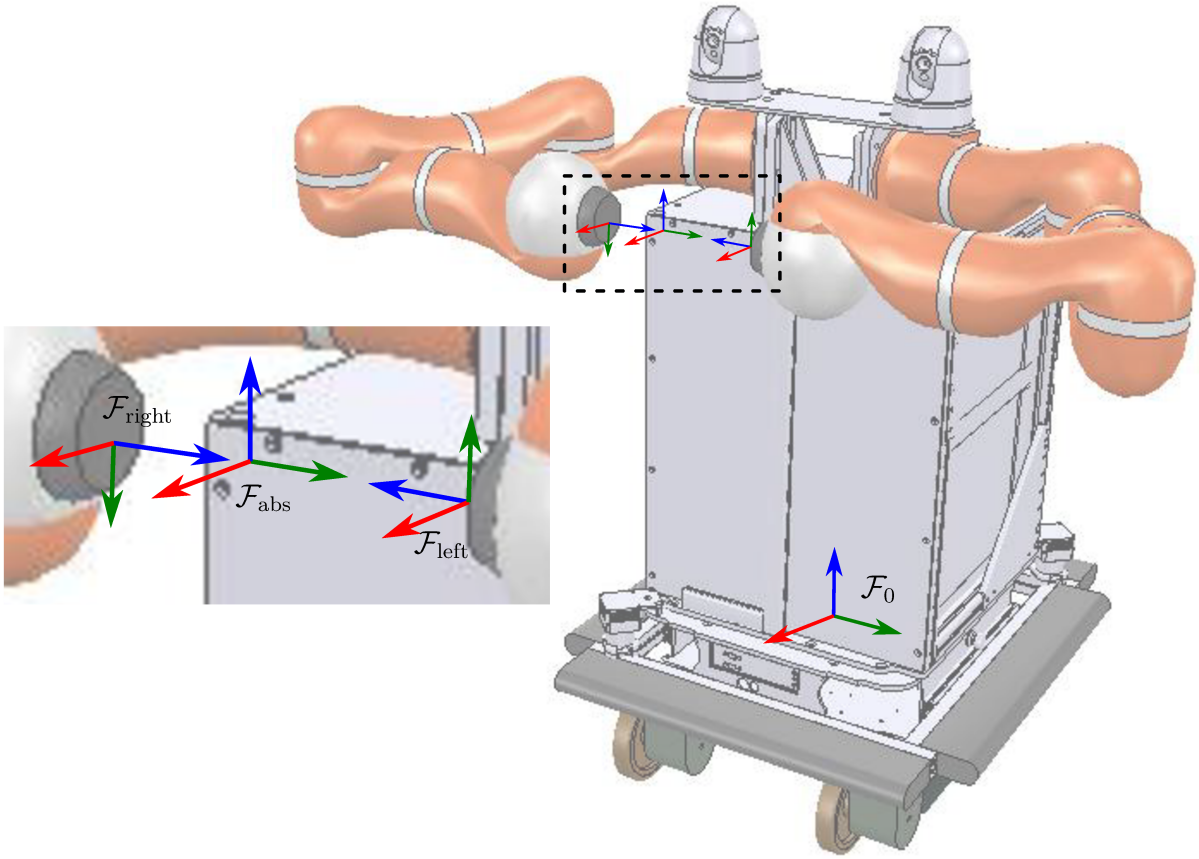

Figure 5.43: Inertia, absolute, right, and left end-effector frames.

that the reference compliant pose for the absolute and/or relative variables becomes different from the desired one. When the wrenches become zero, the norm of the error starts to decrease until the robot return to the original and desired pose. The position and orientation of the absolute and the relative desired, compliant, and current poses are presented in Figure 5.48. Again, the curves show the absolute compliant pose $\underline{\boldsymbol{y}}_{\text{abs}_c}$ diverging from the desired one $\underline{\boldsymbol{y}}_{\text{abs}_d}$ until 25 s, and then approaching to $\underline{\boldsymbol{y}}_{\text{abs}_d}$ again. In both cases, the current absolute pose $\underline{\boldsymbol{y}}_{\text{abs}}$ follows the compliant one. During all the simulation the relative variables remain practically the same, since the internal wrench is equal to zero. Figure 5.44 show some snapshots of the simulation. The robot moves forward until 25 s, when the wrench becomes zero, and then the robot moves backward to its original pose. Figure 5.45 shows both end-effector poses during the first half of the simulation, illustrating the forward movement of the robot.

The results show the efficiency of the whole-body controller, presenting a behavior equal to the previous experiments using just one arm.

Remark 5.2. Since the simulation was performed in MATLAB, the wrenches measured at the end-effector were calculated according to Equation (3.32), and therefore only the imposed wrench of $\underline{\boldsymbol{\psi}}^0_{0,\text{right}} = \underline{\boldsymbol{\psi}}^0_{0,\text{left}} = 10\hat{\imath}$ was considered. Any wrench originated by inaccuracy of the robot and/or the object model, or by modifications of the relative pose during the movement were not taken into account. This is the reason why the internal wrench in 5.46 is always zero, as

$$\begin{aligned}\underline{\boldsymbol{\psi}}^0_{\text{int}} &= \frac{1}{2}\left(\underline{\boldsymbol{\psi}}^0_{0,\text{right}} - \underline{\boldsymbol{\psi}}^0_{0,\text{left}}\right) \\ &= \frac{1}{2}\left(10\hat{\imath} - 10\hat{\imath}\right) = 0.\end{aligned}$$

This is a limitation of this simulation, and a more realistic simulation or experiment must be done in the future.

5.7 Conclusion

In this chapter, different simulations and experiments were presented to highlight the performance of the proposed controllers and also to compare them to controllers from the literature.

Since some robots are actuated in torque, a control law based on its dynamic model is more suitable, and in this case, the JSIM has an important role, which is depicted in section 5.1. Considering the robot manipulator KUKA LBR4+, simulations were run in order to study its behavior under zero torque, based on its dynamic model. The simulated robot did not perform well, presenting an unstable behavior due to high velocities in the joints, which were caused by the ill-conditioning of the inertia matrix. Since the condition

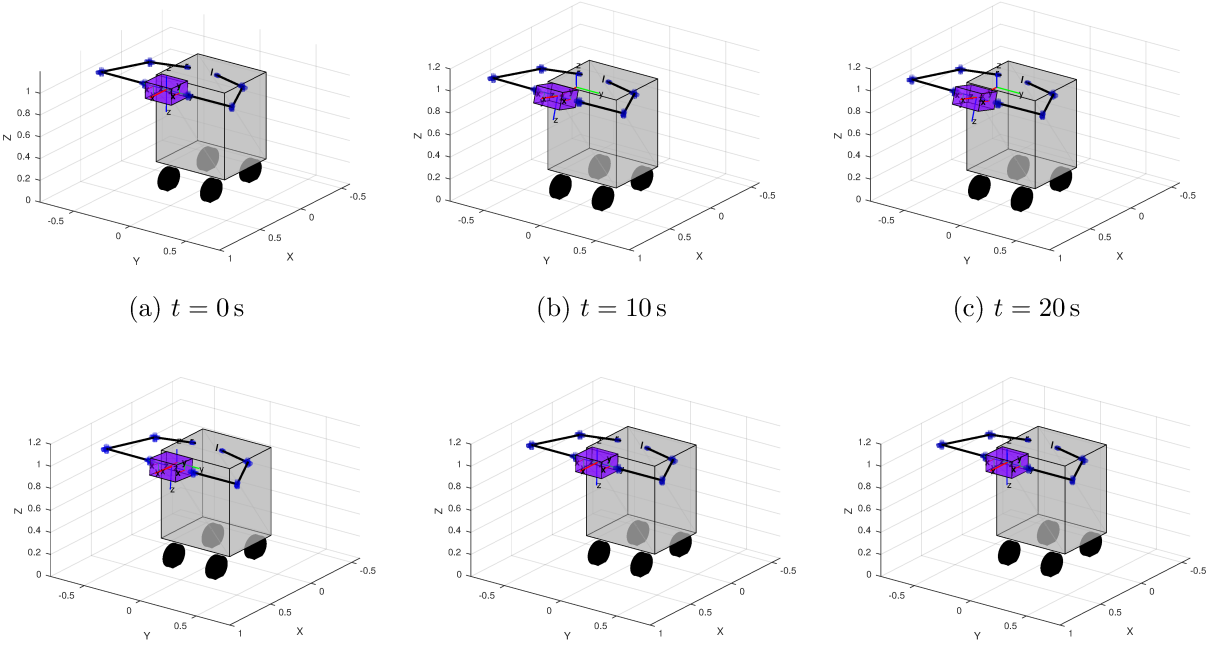

(a) $t = 0\,\mathrm{s}$ (b) $t = 10\,\mathrm{s}$ (c) $t = 20\,\mathrm{s}$

(d) $t = 30\,\mathrm{s}$ (e) $t = 40\,\mathrm{s}$ (f) $t = 50\,\mathrm{s}$

Figure 5.44: Snapshots of the BAZAR.

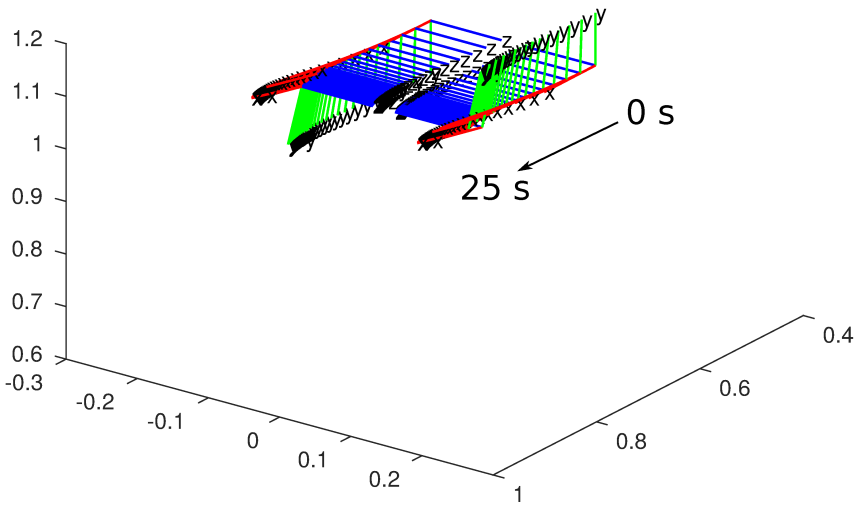

Figure 5.45: Bazar's end-effector poses during the first half of the simulation. The arrow indicates the direction of the movement.

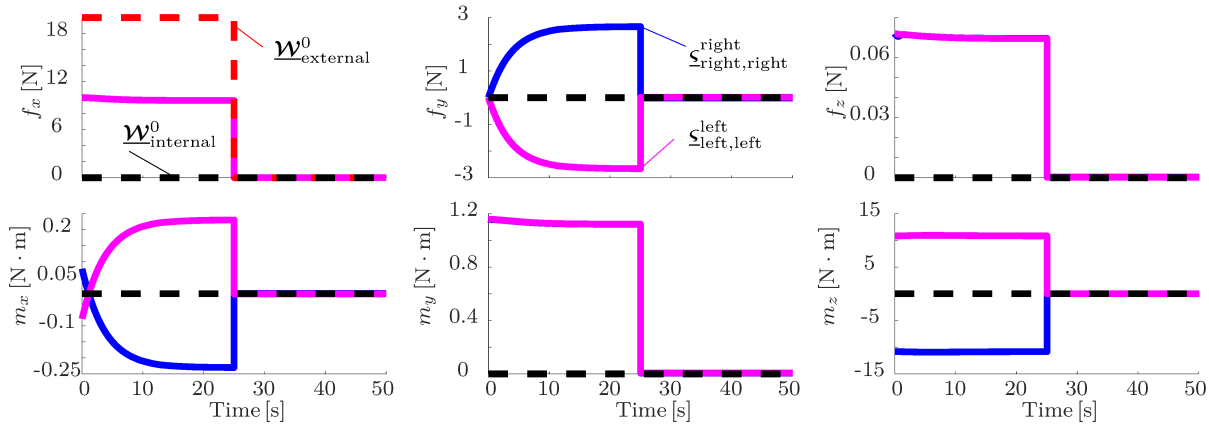

Figure 5.46: Wrenches read by the force/torque sensors attached to the BAZAR end-effectors, and the external and internal wrenches with reference to the inertial frame.

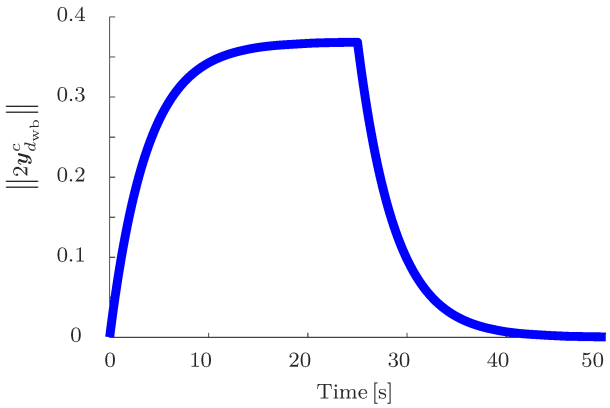

Figure 5.47: Norm of $2\boldsymbol{y}^c_{d_{\text{wb}}}$, where $\boldsymbol{y}^c_{d_{\text{wb}}}$ represents the displacement between the desired and the compliant frames, concerning both absolute and relative variables.

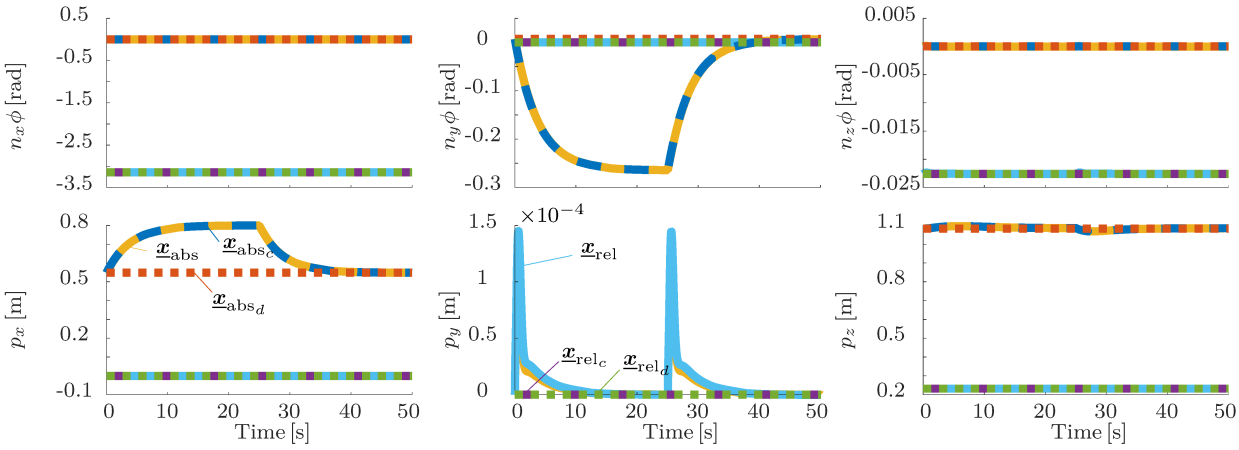

Figure 5.48: Position and orientation of the absolute and relative desired, compliant, and current poses.

number of the matrix is very high, the inversion of the matrix has a very large Frobenius norm, resulting in large joint accelerations, and thus the joints velocities obtained by integrating the acceleration will be also large. Other simulations with a robot with the last links locked together corroborated the results showed by Featherstone (2004), since robots with fewer links had a smaller condition number during all the simulation when compared to the original robot.

The problem of ill-conditioning of the inertia matrix is intrinsic to multi-link open kinematic chains. This phenomenon is reflected not only in simulations but also when controlling the robot. Furthermore, since it makes the control and simulation of the robot difficult, it is important to find solutions to mitigate the effects of the ill-conditioning of $\boldsymbol{M}(\boldsymbol{q})$. In the previous chapter we proposed some controllers to mitigate this problem, and in this chapter we presented a comparison of the proposed adaptive controllers (Equation (4.46)) with the IDFL (Equation (4.38)), which is a classic controller that present problems due to the ill-conditioning of the JSIM, and with the PID (Equation and (4.41)). First, we showed the comparison of the controllers in joint-space, and then in task-space (Equations (4.61), (4.57), and (4.60)). This last comparison involved not only the motion controller in the inner-loop but also the admittance controller (Equation (4.2)) in the outer-loop. Statistical analyses showed that, in all cases, the IDFL presented the worst behavior, whereas the PID with gravity compensation and the proposed adaptive controller showed similar performance.

We also run experiments with the ACLogOnly (Equation (4.2)) in the outer loop, with the same inner-loop controllers. We compared the performance of the controllers concerning the error discrepancy, the outer and the inner loop control signals, and we conclude that both are statistically equivalent, regarding the experiments done. Since the ACLogOnly is simpler and presented the same performance than the ACLog, the former can be used in simple tasks, especially the ones including only translations of the end-effector. However, since the ACLogOnly does not have the stiffness matrix consistent with the task geometry, and the ACLog does, the latter may perform better concerning tasks involving rotations.

For those robots actuated in position or velocity, a kinematic controller is more appropriate. In addition, as kinematic controllers tend to be simpler than the ones based on the robot dynamics, and also do not suffer from the JSIM ill-conditioning problem, they were used as the inner motion controller to evaluate the proposed admittance controllers. First, simulations and experiments were performed to show the performance of the admittance controllers designed using the DQ logarithmic mapping. Both controllers (Equation (4.2) and Equation (4.20)) were run in the KUKA LWR4+ robot, together with the second order kinematic controller (Equation (4.36)) that also uses the logarithmic mapping. Again, the controllers presented satisfactory performance: the robot's end-effector followed the desired pose in the absence of a wrench acting on it, and followed the

compliant pose returned by the admittance controller otherwise. Moreover, the solution for the unwinding problem, used in the ACLog, showed a good behavior. The end-effector did not perform unnecessary rotations to achieve the desired pose.

The ACLog (Equation (4.20)) was also statistically compared with the ACIm (Equation (D.1)), emphasizing the good performance of the proposed controller. When using non-isotropic stiffness matrices, the results are statistically equivalent concerning the error discrepancy and the control signal, but the ACLog presented a better behavior concerning the error discrepancy when using isotropic stiffness matrices. This difference in the error is not so significant for general tasks. However, when the tasks require big rotations, the ACLog performs better than the ACIm, since the latter presents the problem of topological obstruction.

The controller of Equation (4.31) was used in a simulation considering the whole-body of the BAZAR robot in a bimanual manipulation task. The control laws described by Equations (4.31) and (4.36) were extended to consider the absolute and relative variables, taking into consideration the external and internal wrenches acting on the manipulated object. No statistical comparison was done for this controller, but since it considers the changes in the lever arms in the twist and the wrench, it may lead a better behavior of the robot when performing tasks, especially when considering external and internal wrenches, as in the case of a bimanual manipulation.

6

Conclusions and Future Works

"A painting is never finished, it simply stops in an interesting place."

- Paul Gardner

This chapter presents the final discussion concerning the proposed Ph.D. work and what has already been done, together with some conclusions according to the theoretical, simulation, and experimental results. In addition, a proposal for future works and the corresponding methodologies is presented.

6.1 Conclusions

The use of robots in human environments has been increasing in the last years. With robots working together with humans, it is important to keep the safety for the humans, the environment, and also the robot.

This thesis has focused on control strategies for safe manipulation tasks subject to contacts. We have proposed different control laws for this purpose and we also compared it with other classic controllers. As seen in Chapter 2, the admittance controller is appropriate to enforce the desired interaction impedance, especially for velocity-actuated robots, allowing to change the way the human partner *feels* the robot. Usually, admittance controllers are used in a control architecture together with a motion controller, in which the admittance controller is in the outer-loop and changes the desired robot end-effector

trajectory to ensure the desired apparent impedance, and the motion controller is in the inner-loop to control the robot end-effector, so it can follow this new reference (compliant) trajectory, as illustrated in Figure 4.1.

With respect to the outer admittance loop, we firstly have designed an admittance controller using the DQ logarithmic mapping, which assures that the unit DQ group properties are satisfied. This controller is simple, does not have the problem of topological obstruction, and is efficient since it has responded compliantly when a wrench is applied to the robot's end-effector. However, it has the problem of unwinding and its stiffness term is not geometrically consistent with the six-DOF tasks. Thus, we have improved by using the energy of the system to design a second control law that has a physical meaning and its stiffness term is geometrically consistent with six-DOF tasks. Moreover, we also proposed a solution for the unwinding problem based on a switching error function in which the two PIS of the space of unit DQ are mapped into a single PIS in the image of the logarithmic mapping.

Although this controller presents the previously cited characteristics and showed to have a performance at least as good as one of the main admittance controllers of the state of art, namely ACIm, and outperforms it near the unstable equilibrium set of the ACIm, it does not use all information available regarding wrenches and twists. The controller does not take into account the effects of the lever arms (see discussion in section 4.1.3), that is, ignore the term $\varepsilon\left(\boldsymbol{p} \times \boldsymbol{f}\right)$ in the wrenches and the $\varepsilon\left(\boldsymbol{p} \times \boldsymbol{\omega}\right)$ in the twist. Therefore, we improved it once more, so the new controller uses the DQ twist and the DQ wrench, considering the lever arm when performing transformations regarding wrenches and twists. This controller has the same characteristics as the previous one but also contemplates the effects of the lever arm in the system. The control law is later extended to cover the whole-body case of a bimanual mobile manipulator, considering not only the external wrenches but also the internal ones that arise in bimanual manipulation.

Concerning the inner motion loop, two types of controllers can be used: a controller that generates velocity inputs, based on the robot kinematic model; and a controller that generates torque inputs, based on the robot dynamic model. Regarding the former, first and second order kinematic controllers were proposed, both using the DQ logarithmic mapping. Concerning the latter, the JSIM plays an important role, since it can be ill-conditioned in some regions of the configuration space, and this property can lead to undesired stationary error and even instability, as discussed in sections 2.1.2 and 5.1. To mitigate this problem, we proposed an adaptive controller that adapts the JSIM conditioning online so the performance of the closed-loop system is improved. For this, a positive definite matrix is added to the nominal JSIM, in the Euler-Lagrange equation, and this matrix is adapted according to the proposed adaptation law. We have firstly presented a joint-space controller with an adaptation law that guarantees that the added matrix is always positive definite, and tends to improve the final JSIM conditioning. However, this improvement is not

guaranteed. Secondly, we improved this algorithm so the added matrix always decreases the JSIM condition number. Lastly, we designed a task-space adaptive controller, using DQ, which has the same adaptation law as in the joint-space controller.

Thanks to the advantages described in section 3.1, the DQ algebra has been used in all modeling and task-space controllers, resulting in compact formulations. Moreover, the simulations, experiments, and statistical analyses made have shown that the proposed controllers present a performance equal or better than other classic approaches of the literature. For instance, the adaptive controller showed better results concerning the error decay and stationary error when compared to controllers based on the inverse dynamics with feedback-linearization, and similar performance when compared to a PID with gravity compensation. Furthermore, the proposed admittance controller ACLog has shown to have analogous performance concerning the error decay when compared to the ACIm, for general cases. For some specific cases the ACLog outperforms the ACIm, especially when the system is close to an unstable equilibrium set.

6.2 Future Works

Despite the good results of the proposed architecture, a lot of improvements can be done. The admittance controller, for example, modifies the desired trajectory so the desired apparent impedance can be imposed on the robot. However, no constraints are added to this new trajectory, so it can reach, for instance, the maximum joint velocities and joint limits. Furthermore, self-collisions can occur, collision with other objects and some desired task-designed constraints are ignored in the current control laws. A solution is to re-write the admittance controller as an optimization problem, so we can generate a trajectory that will obey the desired constraints (Marinho et al., 2019; Quiroz-Omana & Adorno, 2019).

Considering that the robot has physical contacts with the environment, its dynamic model can be affected by the dynamics of the tools and/or other objects with which the robot is in contact. Thus, an adaptive controller can be used to compensate for the unknown parameters of the system model (Slotine & Li, 1987; Cheah et al., 2006a). This would solve both the problems of lack of information of the robot model and changes in the dynamics of the system produced by the interaction with the environment, including humans. One could argue that we could use identification techniques first to estimate the unknown parameters and then control the robot normally. However, when the robot picks a tool in the middle of task execution, the parameters must be updated online. Besides, a positive feature of adaptive control is that the error will converge regardless of whether the trajectory is persistently exciting or not, which is not true using identification algorithms (Cheah et al., 2006b). In our approach, we used the adaptive controller only to improve the JSIM conditioning. An enhancement is to put together this algorithm and the ones that estimate the kinematic and dynamic parameters of the system, and thus

the controller would be able to adapt to modifications due to physical interactions with the environment. Moreover, we have not proven that the closed-loop system under the proposed algorithm that guarantees the better conditioning of the JSIM is stable, and this is left as future works. Also, all controllers (admittance and kinematic) were designed using the DQ logarithmic mapping. A more direct improvement of the task-space adaptive controller is to also use in it the DQ logarithmic mapping, so that all task-space controllers would use the same error definition, which respects the properties of the unit DQ group.

Concerning stability, it is also necessary to prove the stability of the closed-loop system under the proposed kinematic controllers, which was not the focus of this thesis. Furthermore, the stability of the whole cascade system, including the inner and the outer loop must be formally proven.

6.2.1 Estimation of Human Intention

In addition to developing control strategies aiming at the safety in the pHRI, the cognitive part is also important since understanding the human's intentions increase the autonomy of the system and makes the cooperative tasks more effective. Without knowing the human's intention, the robot can perform the task in such a way that it conflicts with the action the human takes, which can endanger the person or damage the object with which the robot interacts. Even if the task is fully defined, unforeseen events may occur during its execution, such as obstacles that require a change in the previous nominal trajectory. Therefore, it would be more efficient for the human to retrace the trajectory, so the robot would understand its intention, allowing it to complete the desired task.

Humans have generally well-developed cognitive abilities, being able to communicate with their partners, whether by speech, tact, or sight. Thus, one of the challenges of HRI is to design a procedure to establish similar communication between humans and robots, so the robot can understand the human's intention (Bauer et al., 2008). In this sense, for robots to share human-centered environments, it is indispensable to equip them with manipulation, perception, and communication skills necessary for the interaction with the environment and humans beings (Asfour et al., 2006). Although many sensors are already available in most robots, it is necessary to define a kind of language to decode the data from the sensors in meaningful information that indicates the human's intention (Ajoudani et al., 2018).

Bauer et al. (2008) presented a human-robot collaboration survey in which they discuss the communication between humans and robots. Figure 6.1 shows some of the ways to communicate the human intention to the robot, explicitly, implicitly, and also unconsciously. Speech, gestures, haptic signals, and also physiological signals are some of the possible ways to communicate. Explicit communication includes words, sentences, pointing gestures, sign-language gestures, applied forces and torques, angles, or orientations. Some of the

implicit communication consists of heart rate, brain activity, and muscle activity. There is also the unconscious communication given by emotion in speeches and facial expressions, for example.

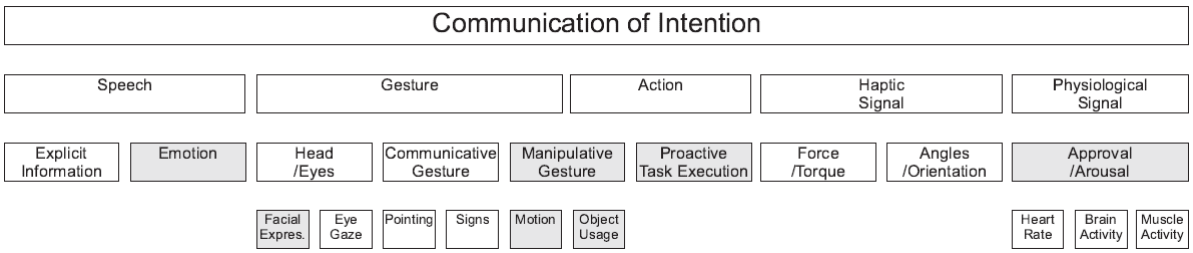

Figure 6.1: Main ways of communicating intentions. Unconsciously communication is marked in gray. Source: (Bauer et al., 2008)

The information used to provide hints of the human's intention is gathered from different type of sensors, as for example haptic sensors (Dumora et al., 2012), RGB-D sensors (Gonzalez et al., 2012; Cherubini et al., 2013; Zimmermann et al., 2018), wearable motion sensors (Cehajic et al., 2015), force sensors (Caccavale et al., 2008), Inertia Measurement Unit (IMU) (de Brito, 2016), and bio-signals as EEG and EMG (Bell et al., 2008). Many works have stood out the multi-modal sensory information in the estimation of human's intention (Ajoudani et al., 2018). According to Ajoudani et al., over 76% of the publications in the field of HRI used multi-modal interfaces in 2015. Thus, multi-modal information is promising and can be used in our architecture, for instance, to recognize the configuration of the kinematic chain of the human partner, and also the exerted force in the manipulated object. Then, it is necessary to decode this information to understand the human's intention.

We already use force/torque sensors at the robot end-effector to measure the wrenches that are used by the admittance controller. However, this information can also be used, together with other sensors such as the IMU and RGB-D sensors, to assist in the estimation of the human posture. The RGB-D sensors can be used to capture the kinematic chain of the human being, or the pose of the person's hand, as done by Cherubini et al. (2013); Gonzalez et al. (2012, 2013). Figure 6.2 shows the image returned by the low-cost Microsoft Kinect RGB-D sensor. This image shows the skeleton of two people identified by the sensor from which it is possible to extract information of the human kinematic chain.

An IMU can also be used to assist in capturing human pose data. IMUs are usually equipped with an accelerometer and a gyroscope, and may also have a magnetometer, barometer, or temperature sensor. With the help of these sensors, the rotation and acceleration of the measuring unit can be detected. If an IMU is placed on the arm of the person with which the robot is interacting, the arm pose can be determined and this information can be used in the robot control law (de Brito, 2016). Also, inertia sensors measurements can be combined with the ones from a RGB-D sensor, using a Kalman filter,

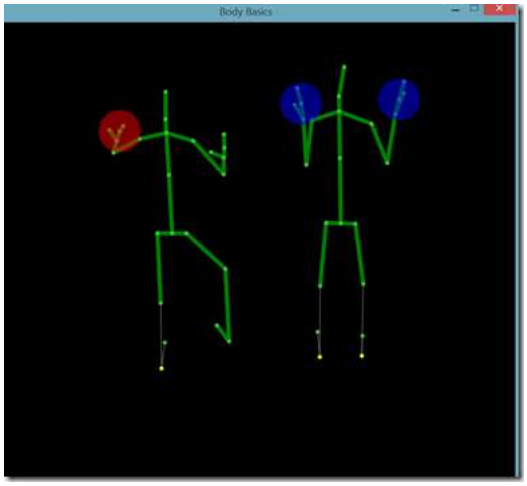

Figure 6.2: Image returned by the Kinect RGB-D sensor, identifying the skeleton of two people.[1]

to estimate the joints angle of a human body (Bo et al., 2011).

This sensor information can be used not only to estimate the human's posture but also to identify its movement. Baptista et al. (2017) proposed an approach to segment discrete movements (movements that have an unambiguously identifiable start and end) using a Switching Linear Dynamic System (SLDS), which is "a stochastic approach suitable for modeling and tracking aspects in time series." According to Baptista et al. (2017), a movement can be described by breaking it down into elements according to the change in angular motion of each body joint, such as flexion and extension, and its effects in posture changes. Thus, by identifying the changes in joints angle and posture, it is possible to recognize the phases of the movement (e.g., sit, rising, stand), and then, from the period that each phase was executed and the temporal sequence of the phases, the complete movement can be identified (e.g., sit-to-stand). This approach can be used to recognize the human's movement, helping in the identification of its intention.

In addition to providing information of the human's current postures and their hand poses (concerning the robot end-effector), it is possible to use information from the sensors to create a communication language with the robot, so that it can understand the human's intention in the execution of a certain task. Dumora et al. (2012) use haptic sensors to create implicit communication between human and robot. Given a variety of movements, these are mapped into torque and force measurements, in addition to the displacement of the human operator's hand. Thus, changes in the sensors' measurements indicate the human's intention and the robot then acts accordingly. Therefore, one idea for a prospective work is to map certain human's intentions, considered more relevant in the execution of cooperation tasks, into measurements in the available sensors, similar to what Dumora et al. have done. This mapping will allow the robot to understand the intent of

[1]Source: http://www.imaginativeuniversal.com/blog/2013/11/26/kinect-for-windows-v2-first-look/

its human partner, and thus optimize the execution of the cooperation task. Different from what Dumora et al. have done, the idea is to consider complete movements (translation and rotation) on all axes, not just movements in the horizontal plane.

Another work that can be used as an inspiration is the one of Unhelkar et al. (2018). The authors used a Multiple-Predictor System (MPS) to predict the motion of the human so the robot adapts its behavior according to this motion. A Safe-Interval Path Planner (SIPP) is used to plan robot trajectories. The human motion predictions together with the path planning "allow the robot to make intelligent decisions about how to move towards its own goal" (Unhelkar et al., 2018). Unhelkar et al. use this approach to avoid collision between the robot and the human in a collaborative factory environment where both human and robot have a common shared operating region. However, a similar approach can be used in pHRI, not only to prevent collisions between robot and person but for the robot to follow its human partner in a locomotion task.

The whole process including the understanding of human intentions and the control strategies for a safe interaction is described in Figure 6.3. Given a cooperation task to be executed, the multi-modal information will be used to recognize the human's intention. Once the intention is discovered, it is necessary to find the desired end-effectors pose to better execute the task. This desired pose will be provided to the admittance controller, which will regulate the desired apparent inertia, damping, and stiffness of the robot, and will return a reference pose for the motion controller to control.

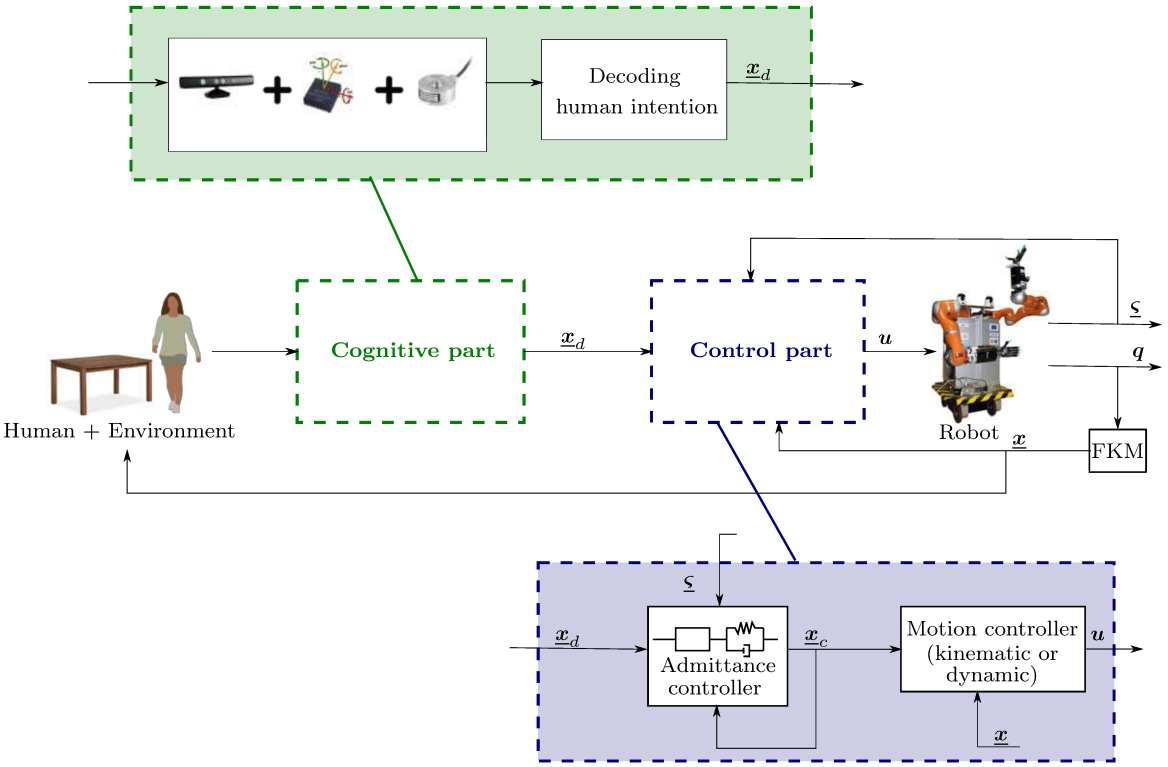

Figure 6.3: HRI scheme to accomplish a cooperative task. The human's intention must be recognized and then control strategies are applied to control the robot end-effector to ensure the safety of the ones involved in the task.

A

Kinematic and Dynamic Model of KUKA LBR4+

The model of the KUKA LBR4+ was the one used in simulations related to the torque control and dynamic behavior. Both kinematic and dynamic model were retrieved from V-REP, and are detailed here.

A.1 Kinematic Model

The KUKA LBR4+ has seven DOFs. The standard DH parameters that describe the kinematic model of the robot are described in Table A.1 and illustrated in Figure A.1.

Besides the DH parameters, which gives us the end-effector pose $\underline{\boldsymbol{x}}_7^0 = \underline{\boldsymbol{x}}_{\text{eff}}^0$, the kinematic model also considers the transformation of the first DH frame to the robot's base, that is given by

$$\begin{aligned}
\boldsymbol{r}_0^{\text{base}} &= 1 \\
\boldsymbol{p}_0^{\text{base}} &= 0.31\hat{k} \\
\underline{\boldsymbol{x}}_0^{\text{base}} &= \boldsymbol{r}_0^{\text{base}} + 0.5\varepsilon \boldsymbol{p}_0^{\text{base}} \boldsymbol{r}_0^{\text{base}}.
\end{aligned}$$

Thus, the complete kinematic model is

$$\underline{\boldsymbol{x}}_{\text{eff}}^{\text{base}} = \underline{\boldsymbol{x}}_0^{\text{base}} \underline{\boldsymbol{x}}_{\text{eff}}^0.$$

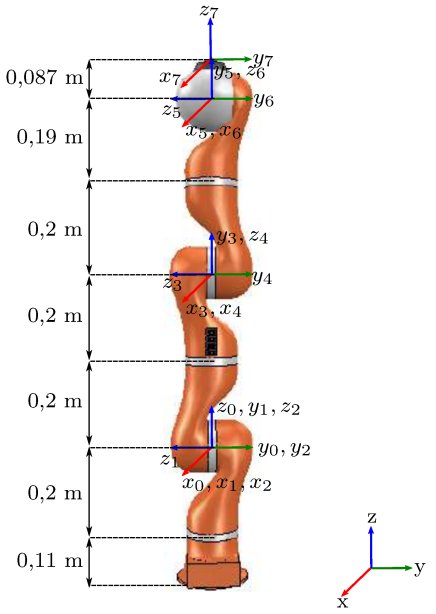

Figure A.1: Standard DH parameters of KUKA LBR4+.

Table A.1: Standard DH parameters of KUKA LBR4+.

Link	θ (rad)	d (m)	a (m)	α (rad)
1	0	0	0	$\pi/2$
2	0	0	0	$-\pi/2$
3	0	0.4	0	$\pi/2$
4	0	0	0	$-\pi/2$
5	0	0.39	0	$\pi/2$
6	0	0	0	$-\pi/2$
7	0	0.087	0	0

A.2 Dynamic Model

To derive the dynamic model, even using Newton-Euler or Euler-Lagrange method, some parameters are important, as the mass, the inertia tensor, and the center of mass (COM) of each link of the robot. The dynamic parameters that were gotten from V-REP are shown in Tables A.2-A.4.

Table A.2: Mass of each link.

Link	Mass (Kg)
1	2.7
2	2.7
3	2.7
4	2.7
5	1.7
6	1.6
7	0.3

Table A.3: Position of the center of mass of each link, related to its DH frame.

	COM		
Link	x	y	z
1	0.0000781	−0.0599002	0.0255518
2	0.0101166	0.0278437	0.1066027
3	0.0100804	−0.0626202	−0.0278332
4	−0.0192432	−0.0255866	0.0958104
5	−0.0192526	−0.0887392	0.0252519
6	−0.0190836	0.0089009	0.0011072
7	−0.0192717	−0.0004046	−0.0126029

Table A.4: Inertia tensor of each link, at its center of mass and related to the DH frame of the link.

Link	Inertia tensor			
1	$\begin{bmatrix} 0.0163405 & -0.0000029 & -0.0000007 \\ -0.0000029 & 0.0050261 & -0.0035343 \\ -0.0000007 & -0.0035343 & 0.0161729 \end{bmatrix}$			
2	$\begin{bmatrix} 0.0163404 & -0.0000008 & 0.0000035 \\ -0.0000008 & 0.0161732 & 0.0035339 \\ 0.0000035 & 0.0035339 & 0.0050272 \end{bmatrix}$			
3	$\begin{bmatrix} 0.0163404 & 0.0000029 & -0.0000008 \\ 0.0000029 & 0.0050276 & 0.0035334 \\ -0.0000008 & 0.0035334 & 0.0161727 \end{bmatrix}$			
4	$\begin{bmatrix} 0.0163404 & -0.0000005 & -0.0000025 \\ -0.0000005 & 0.0161734 & -0.0035336 \\ -0.0000025 & -0.0035336 & 0.0050257 \end{bmatrix}$			
5	$\begin{bmatrix} 0.0098192 & 0.0000016 & 0.0000009 \\ 0.0000016 & 0.0037085 & -0.0030943 \\ 0.0000009 & -0.0030943 & 0.0090912 \end{bmatrix}$			
6	$\begin{bmatrix} 0.0030112 & 0.0000000 & -0.0000001 \\ 0.0000000 & 0.0030224 & -0.0000192 \\ -0.0000001 & -0.0000192 & 0.0034144 \end{bmatrix}$			
7	$\begin{bmatrix} 0.1017180 & 0.0000000 & -0.0000014 \\ 0.0000000 & 0.1017179 & -0.0000033 \\ -0.0000014 & -0.0000033 & 0.1584360 \end{bmatrix}$			$\times 10^{-3}$

B

Kinematic and Dynamic Model of BAZAR Arms

The BAZAR is a bimanual mobile manipulator that consists of 2 KUKA LWR4+ arms and a mobile base. The kinematic and dynamic model of each arm are described here. The modified DH parameters and the dynamic model was obtained from (Katsumata et al., 2019).

B.1 Kinematic Model

The KUKA LWR4+ has seven DOFs. The modified DH parameters that describe the kinematic model of the robot are described in Table B.1 and illustrated in B.1 on the following page.

The transformation to the tip of the end-effector is given by

$$\underline{\boldsymbol{x}}^7_{\text{eff}} = 1 + \varepsilon \frac{1}{2} \left(0.078 \hat{k} \right).$$

Thus, the kinematic model is given by

$$\underline{\boldsymbol{x}}^0_{\text{eff}} = \underline{\boldsymbol{x}}^0_7 \underline{\boldsymbol{x}}^7_{\text{eff}},$$

where $\underline{\boldsymbol{x}}^0_7$ is the kinematic model given by the modified DH parameters.

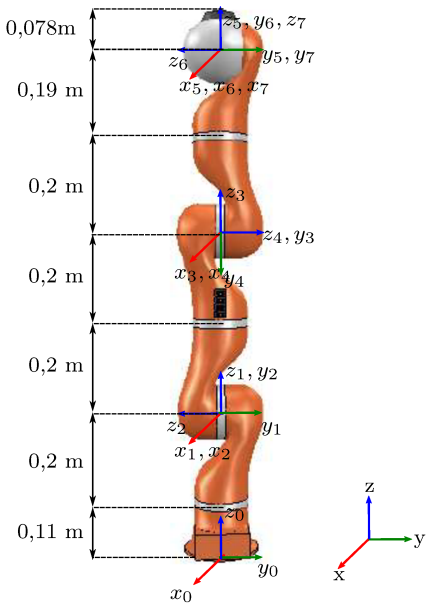

Figure B.1: Frames and sizes of the KUKA LWR4+ used in the modified DH parameters.

Table B.1: Modified DH parameters of KUKA LWR4+.

Link	θ (rad)	d (m)	a (m)	α (rad)
1	0	0.3105	0	0
2	0	0	0	$\pi/2$
3	0	0.4	0	$-\pi/2$
4	0	0	0	$-\pi/2$
5	0	0.39	0	$\pi/2$
6	0	0	0	$\pi/2$
7	0	0	0	$-\pi/2$

The arms are located differently in the BAZAR robot. Thus, the transformation of the base of each arm is differently, and described as follow.

B.1.1 Right Arm Base

The rotation of the base of the right arm is given by

$$\begin{aligned} \boldsymbol{r}_z &= \cos \pi/24 + \hat{k} \sin \pi/24 \\ \boldsymbol{r}_y &= \cos \pi/2 + \hat{\jmath} \sin \pi/2 \\ \boldsymbol{r}_x &= \cos \pi/4 + \hat{\imath} \sin \pi/4 \\ \boldsymbol{r}_0^{\text{base}} &= \boldsymbol{r}_z \boldsymbol{r}_y \boldsymbol{r}_x, \end{aligned}$$

and the translation is

$$\boldsymbol{p}_{\text{base0}}^{\text{base}} = 0.10193\hat{\imath} - 0.11472\hat{\jmath} + 0.4582\hat{k}.$$

Thus, the complete base transformation is

$$\underline{\boldsymbol{x}}_0^{\text{base}} = \boldsymbol{r}_0^{\text{base}} + \varepsilon \frac{1}{2} \boldsymbol{p}_{\text{base0}}^{\text{base}} \boldsymbol{r}_0^{\text{base}}. \tag{B.1}$$

B.1.2 Left Arm Base

For the left arm, the rotation of the base is

$$\begin{aligned} \boldsymbol{r}_z &= \cos {}^{-\pi}/_{24} + \hat{k} \sin {}^{-\pi}/_{24} \\ \boldsymbol{r}_y &= \cos {}^{\pi}/_{2} + \hat{\jmath} \sin {}^{\pi}/_{2} \\ \boldsymbol{r}_x &= \cos {}^{3\pi}/_{4} + \hat{\imath} \sin {}^{3\pi}/_{4} \\ \boldsymbol{r}_0^{\text{base}} &= \boldsymbol{r}_z \boldsymbol{r}_y \boldsymbol{r}_x, \end{aligned}$$

and the translation is

$$\boldsymbol{p}_{\text{base0}}^{\text{base}} = 0.10193\hat{\imath} + 0.11472\hat{\jmath} + 0.4582\hat{k}.$$

The complete transformation of the base is given by Equation (B.1).

The complete kinematic model of each arm is given by

$$\underline{\boldsymbol{x}}_{\text{eff}}^{\text{base}} = \underline{\boldsymbol{x}}_0^{\text{base}} \underline{\boldsymbol{x}}_7^0 \underline{\boldsymbol{x}}_{\text{eff}}^7.$$

B.2 Dynamic Model

The dynamic parameters of the KUKA LWR4+ identified at LIRMM (Katsumata et al., 2019) are the following:

Table B.2: Mass of each link.

Link	Mass (Kg)
1	2.70
2	2.70
3	2.68
4	2.68
5	1.67
6	1.57
7	0.27

Table B.3: Position of the center of mass of each link, related to its modified DH frame.

	COM		
Link	x	y	z
1	0.0036	0.0708	−0.2370
2	−0.0261	0.2089	0.0708
3	0.0176	−0.0849	−0.3195
4	0.0030	−0.2477	0.0567
5	−0.0006	0.0460	−0.2591
6	−0.0042	0.0475	0.0094
7	0.0138	−0.0032	0.1059

Table B.4: Inertia tensor of each link, at its center of mass and related to the modified DH frame of the link.

Link	Inertia tensor
1	$\begin{bmatrix} 0.0848 & -0.0000 & 0.0001 \\ -0.0000 & 0.0825 & 0.0009 \\ 0.0001 & 0.0009 & 0.0039 \end{bmatrix}$
2	$\begin{bmatrix} 0.1813 & -0.0152 & 0.0532 \\ -0.0152 & 0.2576 & 0.2629 \\ 0.0532 & 0.2629 & 0.2955 \end{bmatrix}$
3	$\begin{bmatrix} 0.0315 & 0.0020 & 0.0084 \\ 0.0020 & 0.0858 & -0.0123 \\ 0.0084 & -0.0123 & 0.0214 \end{bmatrix}$
4	$\begin{bmatrix} 0.0542 & 0.0001 & 0.0035 \\ 0.0001 & 0.0220 & 0.0262 \\ 0.0035 & 0.0262 & 0.0501 \end{bmatrix}$
5	$\begin{bmatrix} 0.0613 & 0.0023 & -0.0088 \\ 0.0023 & 0.0659 & 0.0022 \\ -0.0088 & 0.0022 & 0.0023 \end{bmatrix}$
6	$\begin{bmatrix} 0.0075 & 0.0003 & -0.0008 \\ 0.0003 & 0.0015 & 0.0015 \\ -0.0008 & 0.0015 & 0.0057 \end{bmatrix}$
7	$\begin{bmatrix} 0.0062 & -0.0001 & 0.0003 \\ -0.0001 & 0.0066 & -0.0001 \\ 0.0003 & -0.0001 & 0.0010 \end{bmatrix}$

C

General Mathematical Properties

Lemma C.1. *If a matrix* $\boldsymbol{A} \in \mathbb{R}^{n\times n}$ *is skew-symmetric* $\left(\boldsymbol{A} = -\boldsymbol{A}^T\right)$*, then* $\boldsymbol{s}^T\boldsymbol{A}\boldsymbol{s} = 0,\ \forall \boldsymbol{s} \in \mathbb{R}^n$*.*

Proof. Consider $\boldsymbol{s} \in \mathbb{R}^n$, $\boldsymbol{A} \in \mathbb{R}^{n\times n}$, with $\boldsymbol{A} = -\boldsymbol{A}^T$, and $b \in \mathbb{R}$, with $b = \boldsymbol{s}^T\boldsymbol{A}\boldsymbol{s}$. Thus,

$$b = \boldsymbol{s}^T\boldsymbol{A}\boldsymbol{s} = \boldsymbol{s}^T\left(-\boldsymbol{A}^T\right)\boldsymbol{s} = -\boldsymbol{s}^T\boldsymbol{A}\boldsymbol{s} = -b.$$

Therefore, $b = 0$, which concludes the proof. □

Lemma C.2. *The rotation matrix* $\boldsymbol{R} \in SO(3)$ *is related to the rotation quaternion* $\boldsymbol{r} \in \mathbb{S}_3$ *by the relationship*

$$\boldsymbol{R} = \bar{\boldsymbol{I}}\overset{+}{\boldsymbol{H}}_4(\boldsymbol{r})\,\bar{\boldsymbol{H}}_4(\boldsymbol{r}^*)\,\bar{\boldsymbol{I}}^T.$$

Proof. Considering $\boldsymbol{r} = r_1 + \hat{\imath}r_2 + \hat{\jmath}r_3 + \hat{k}r_4$, the direct calculation of $\bar{\boldsymbol{I}}\overset{+}{\boldsymbol{H}}_4(\boldsymbol{r})\,\bar{\boldsymbol{H}}_4(\boldsymbol{r}^*)\,\bar{\boldsymbol{I}}^T$

yields

$$\begin{aligned}
\bar{\boldsymbol{I}}\overset{+}{\boldsymbol{H}}_4(\boldsymbol{r})\,\bar{\boldsymbol{H}}_4(\boldsymbol{r}^*)\,\bar{\boldsymbol{I}}^T &= \begin{bmatrix}\boldsymbol{0}_{3\times1} & \boldsymbol{I}_{3\times3}\end{bmatrix}\begin{bmatrix} r_1 & -r_2 & -r_3 & -r_4 \\ r_2 & r_1 & -r_4 & r_3 \\ r_3 & r_4 & r_1 & -r_2 \\ r_4 & -r_3 & r_2 & r_1 \end{bmatrix}\begin{bmatrix} r_1 & r_2 & r_3 & r_4 \\ -r_2 & r_1 & -r_4 & r_3 \\ -r_3 & r_4 & r_1 & -r_2 \\ -r_4 & -r_3 & r_2 & r_1 \end{bmatrix}\begin{bmatrix}\boldsymbol{0}_{1\times3} \\ \boldsymbol{I}_{3\times3}\end{bmatrix} \\
&= \begin{bmatrix} r_2 & r_1 & -r_4 & r_3 \\ r_3 & r_4 & r_1 & -r_2 \\ r_4 & -r_3 & r_2 & r_1 \end{bmatrix}\begin{bmatrix} r_2 & r_3 & r_4 \\ r_1 & -r_4 & r_3 \\ r_4 & r_1 & -r_2 \\ -r_3 & r_2 & r_1 \end{bmatrix} \\
&= \begin{bmatrix} r_2^2 + r_1^2 + -r_4^2 - r_3^2 & r_2r_3 - r_1r_4 - r_4r_1 + r_3r_2 & r_2r_4 + r_1r_3 + r_4r_2 + r_3r_1 \\ r_3r_2 + r_4r_1 + r_1r_4 + r_2r_3 & r_3^2 - r_4^2 + r_1^2 - r_2^2 & r_3r_4 + r_4r_3 - r_1r_2 - r_2r_1 \\ r_4r_2 - r_3r_1 + r_2r_4 - r_1r_3 & r_4r_3 + r_3r_4 + r_2r_1 + r_1r_2 & r_4^2 - r_3^2 - r_2^2 + r_1^2 \end{bmatrix} \\
&= \begin{bmatrix} 2\left(r_1^2 + r_2^2\right) - 1 & 2\left(r_2r_3 - r_1r_4\right) & 2\left(r_2r_4 + r_1r_3\right) \\ 2\left(r_2r_3 + r_1r_4\right) & 2\left(r_1^2 + r_3^2\right) - 1 & 2\left(r_3r_4 - r_1r_2\right) \\ 2\left(r_2r_4 - r_1r_3\right) & 2\left(r_3r_4 + r_1r_2\right) & 2\left(r_1^2 + r_4^2\right) - 1 \end{bmatrix},
\end{aligned}$$

which is the equation to transform a quaternion $\boldsymbol{r}$ to a rotation matrix $\boldsymbol{R}$ (Siciliano et al., 2009, section 2.6, Equation (2.33)). □

Lemma C.3. *The matrix* $\overline{\boldsymbol{W}}(\boldsymbol{r}) = 2\bar{\boldsymbol{H}}_4(\boldsymbol{r}^*)\,\boldsymbol{Q}_4(\boldsymbol{r})$ *is given by*

$$\overline{\boldsymbol{W}}(\boldsymbol{r}) = \begin{bmatrix}\boldsymbol{0}_{1\times3} \\ \boldsymbol{W}(\boldsymbol{r})\end{bmatrix}$$

for all $\boldsymbol{r} \in \mathbb{S}^3$*, where* $\boldsymbol{W}(\boldsymbol{r}) \in \mathbb{R}^{3\times3}$*.*

Proof. By direct calculation of $\bar{\boldsymbol{H}}_4(\boldsymbol{r}^*)\,\boldsymbol{Q}_4(\boldsymbol{r})$ we have

$$\frac{1}{2}\overline{\boldsymbol{W}}(\boldsymbol{r}) = \bar{\boldsymbol{H}}_4(\boldsymbol{r}^*)\,\boldsymbol{Q}_4(\boldsymbol{r}) = \begin{bmatrix} r_1 & r_2 & r_3 & r_4 \\ -r_2 & r_1 & -r_4 & r_3 \\ -r_3 & r_4 & r_1 & -r_2 \\ -r_4 & -r_3 & r_2 & r_1 \end{bmatrix}\begin{bmatrix} -r_2 & -r_3 & -r_4 \\ \Gamma n_x^2 + \Theta & \Gamma n_x n_y & \Gamma n_x n_z \\ \Gamma n_y n_x & \Gamma {n_y}^2 + \Theta & \Gamma n_y n_z \\ \Gamma n_z n_x & \Gamma n_z n_y & \Gamma {n_z}^2 + \Theta \end{bmatrix},$$

where r_i is the i-th coefficient of $\boldsymbol{r}$, Γ and Θ are given by Equations (3.15) and (3.16), respectively, and n_x, n_y, n_z are the coefficients of the rotational axis $\boldsymbol{n}$.

Therefore, the first row of this multiplication is given by

$$\frac{1}{2}\begin{bmatrix} w_{1,1} & w_{1,2} & w_{1,3}\end{bmatrix},$$

where

$$\begin{aligned}
\frac{1}{2}w_{1,1} &= -r_1 r_2 + r_2\left(\Gamma n_x^2 + \Theta\right) + r_3\Gamma n_y n_x + r_4\Gamma n_z n_x,\\
\frac{1}{2}w_{1,2} &= -r_1 r_3 + r_2\Gamma n_x n_y + r_3\left(\Gamma n_y^2 + \Theta\right) + r_4\Gamma n_z n_y,\\
\frac{1}{2}w_{1,3} &= -r_1 r_4 + r_2\Gamma n_x n_z + r_3\Gamma n_y n_z + r_4\left(\Gamma n_z^2 + \Theta\right).
\end{aligned}$$

Hence,

$$\begin{aligned}
\frac{1}{2}w_{1,1} &= -\cos\frac{\phi}{2}n_x\sin\frac{\phi}{2} + n_x\sin\frac{\phi}{2}\left[\left(\cos\frac{\phi}{2}-\Theta\right)n_x^2+\Theta\right]\\
&+ n_y\sin\frac{\phi}{2}\left(\cos\frac{\phi}{2}-\Theta\right)n_y n_x + n_z\sin\frac{\phi}{2}\left(\cos\frac{\phi}{2}-\Theta\right)n_z n_x\\
&= -\cos\frac{\phi}{2}\sin\frac{\phi}{2}n_x + \sin\frac{\phi}{2}\cos\frac{\phi}{2}n_x^3 - \sin\frac{\phi}{2}\Theta n_x^3 + \sin\frac{\phi}{2}\Theta n_x\\
&+ \sin\frac{\phi}{2}\cos\frac{\phi}{2}n_y^2 n_x - \sin\frac{\phi}{2}\Theta {n_y}^2 n_x + \sin\frac{\phi}{2}\cos\frac{\phi}{2}{n_z}^2 n_x - \sin\frac{\phi}{2}\Theta n_z^2 n_x\\
&= \left(-\cos\frac{\phi}{2}\sin\frac{\phi}{2} + \sin\frac{\phi}{2}\Theta\right)n_x + \left(\sin\frac{\phi}{2}\cos\frac{\phi}{2} - \sin\frac{\phi}{2}\Theta\right)n_x^3\\
&+ \left(\sin\frac{\phi}{2}\cos\frac{\phi}{2} - \sin\frac{\phi}{2}\Theta\right){n_y}^2 n_x + \left(\sin\frac{\phi}{2}\cos\frac{\phi}{2} - \sin\frac{\phi}{2}\Theta\right){n_z}^2 n_x\\
&= \left(-\cos\frac{\phi}{2}\sin\frac{\phi}{2} + \sin\frac{\phi}{2}\Theta + \left(\sin\frac{\phi}{2}\cos\frac{\phi}{2} - \sin\frac{\phi}{2}\Theta\right)n_x^2\right.\\
&\left.+ \left(\sin\frac{\phi}{2}\cos\frac{\phi}{2} - \sin\frac{\phi}{2}\Theta\right){n_y}^2 + \left(\sin\frac{\phi}{2}\cos\frac{\phi}{2} - \sin\frac{\phi}{2}\Theta\right){n_z}^2\right)n_x\\
&= \left(-\cos\frac{\phi}{2}\sin\frac{\phi}{2} + \sin\frac{\phi}{2}\Theta + \left(\sin\frac{\phi}{2}\cos\frac{\phi}{2} - \sin\frac{\phi}{2}\Theta\right)\left(n_x^2 + {n_y}^2 + {n_z}^2\right)\right)n_x.
\end{aligned}$$

Since $n_x^2 + {n_y}^2 + {n_z}^2 = 1$, thus $\frac{1}{2}w_{1,1} = 0$. Similarly, $\frac{1}{2}w_{1,2} = \frac{1}{2}w_{1,3} = 0$. Therefore, the first row of the matrix $\overline{\boldsymbol{W}}(\boldsymbol{r})$ is a row of zeros, which concludes the proof. □

Lemma C.4. *Considering the positive definite matrices $\boldsymbol{K}_\phi \in \mathbb{R}^{3\times3}$ and $\boldsymbol{K}_p \in \mathbb{R}^{3\times3}$ that represent the rotational and translational stiffness matrices, respectively, and that there is no coupling between translation and rotation, the elastic potential energy given by*

$$\mathcal{U} = \left(\operatorname{vec}_6 \underline{\boldsymbol{y}}_d^c\right)^T \boldsymbol{K}_d \operatorname{vec}_6 \underline{\boldsymbol{y}}_d^c$$

is port-symmetric if $\boldsymbol{K}_d = 2\operatorname{diag}\left(\boldsymbol{K}_\phi, \boldsymbol{K}'_p\right)$, with $\boldsymbol{K}'_p \triangleq \frac{1}{2}\boldsymbol{K}_p + \frac{1}{2}\boldsymbol{R}_d^c\boldsymbol{K}_p\boldsymbol{R}_d^{cT}$, and $\underline{\boldsymbol{y}} = \boldsymbol{n}\phi/2 + \varepsilon\boldsymbol{p}/2$.

Proof. The potential energy is port-symmetric if it is the same whether seen from either

$\mathcal{F}_c$ or $\mathcal{F}_d$. Therefore, consider the energy seen from $\mathcal{F}_c$ as

$$\begin{aligned}
\mathcal{U}^c &= \left(\operatorname{vec}_6 \underline{\boldsymbol{y}}_d^c\right)^T \boldsymbol{K}_d \operatorname{vec}_6 \underline{\boldsymbol{y}}_d^c \\
&= \begin{bmatrix} \left(\operatorname{vec}_3 \frac{\boldsymbol{n}_d^c \phi}{2}\right)^T & \left(\operatorname{vec}_3 \frac{\boldsymbol{p}_{cd}^c}{2}\right)^T \end{bmatrix} \begin{bmatrix} 2\boldsymbol{K}_\phi & \boldsymbol{0} \\ \boldsymbol{0} & 2\boldsymbol{K}'_p \end{bmatrix} \begin{bmatrix} \operatorname{vec}_3 \frac{\boldsymbol{n}_d^c \phi}{2} \\ \operatorname{vec}_3 \frac{\boldsymbol{p}_{cd}^c}{2} \end{bmatrix} \\
&= \underbrace{\left(\operatorname{vec}_3 \frac{\boldsymbol{n}_d^c \phi}{2}\right)^T 2\boldsymbol{K}_\phi \operatorname{vec}_3 \frac{\boldsymbol{n}_d^c \phi}{2}}_{\mathcal{U}_r^c} + \underbrace{\left(\operatorname{vec}_3 \frac{\boldsymbol{p}_{cd}^c}{2}\right)^T \left(\boldsymbol{K}_p + \boldsymbol{R}_d^c \boldsymbol{K}_p \boldsymbol{R}_d^{cT}\right) \operatorname{vec}_3 \frac{\boldsymbol{p}_{cd}^c}{2}}_{\mathcal{U}_p^c}.
\end{aligned}$$

Manipulating $\mathcal{U}_p^c$ gives

$$\begin{aligned}
\mathcal{U}_p^c &= \left(\operatorname{vec}_3 \frac{\boldsymbol{p}_{cd}^c}{2}\right)^T \boldsymbol{K}_p \operatorname{vec}_3 \frac{\boldsymbol{p}_{cd}^c}{2} + \left(\operatorname{vec}_3 \frac{\boldsymbol{p}_{cd}^c}{2}\right)^T \boldsymbol{R}_d^c \boldsymbol{K}_p \boldsymbol{R}_d^{cT} \operatorname{vec}_3 \frac{\boldsymbol{p}_{cd}^c}{2} \\
&= \left(\operatorname{vec}_3 \frac{\boldsymbol{p}_{cd}^c}{2}\right)^T \boldsymbol{K}_p \operatorname{vec}_3 \frac{\boldsymbol{p}_{cd}^c}{2} + \left(\boldsymbol{R}_d^{cT} \operatorname{vec}_3 \frac{\boldsymbol{p}_{cd}^c}{2}\right)^T \boldsymbol{K}_p \boldsymbol{R}_d^{cT} \operatorname{vec}_3 \frac{\boldsymbol{p}_{cd}^c}{2} \\
&= \left(\operatorname{vec}_3 \frac{\boldsymbol{p}_{cd}^c}{2}\right)^T \boldsymbol{K}_p \operatorname{vec}_3 \frac{\boldsymbol{p}_{cd}^c}{2} + \left(\operatorname{vec}_3 \frac{\boldsymbol{p}_{cd}^d}{2}\right)^T \boldsymbol{K}_p \operatorname{vec}_3 \frac{\boldsymbol{p}_{cd}^d}{2}.
\end{aligned}$$

Similarly, the energy seen from $\mathcal{F}_d$ is

$$\begin{aligned}
\mathcal{U}^d &= \left(\operatorname{vec}_6 \underline{\boldsymbol{y}}_c^d\right)^T \boldsymbol{K}_d \operatorname{vec}_6 \underline{\boldsymbol{y}}_c^d \\
&= \begin{bmatrix} \left(\operatorname{vec}_3 \frac{\boldsymbol{n}_c^d \phi}{2}\right)^T & \left(\operatorname{vec}_3 \frac{\boldsymbol{p}_{cd}^d}{2}\right)^T \end{bmatrix} \begin{bmatrix} 2\boldsymbol{K}_\phi & \boldsymbol{0} \\ \boldsymbol{0} & 2\boldsymbol{K}'_p \end{bmatrix} \begin{bmatrix} \operatorname{vec}_3 \frac{\boldsymbol{n}_c^d \phi}{2} \\ \operatorname{vec}_3 \frac{\boldsymbol{p}_{cd}^d}{2} \end{bmatrix} \\
&= \underbrace{\left(\operatorname{vec}_3 \frac{\boldsymbol{n}_c^d \phi}{2}\right)^T 2\boldsymbol{K}_\phi \operatorname{vec}_3 \frac{\boldsymbol{n}_c^d \phi}{2}}_{\mathcal{U}_r^d} + \underbrace{\left(\operatorname{vec}_3 \frac{\boldsymbol{p}_{cd}^d}{2}\right)^T \left(\boldsymbol{K}_p + \boldsymbol{R}_c^d \boldsymbol{K}_p \boldsymbol{R}_c^{dT}\right) \operatorname{vec}_3 \frac{\boldsymbol{p}_{cd}^d}{2}}_{\mathcal{U}_p^d}.
\end{aligned}$$

Again, manipulating the translation energy $\mathcal{U}_p^d$ yields to

$$\begin{aligned}
\mathcal{U}_p^d &= \left(\operatorname{vec}_3 \frac{\boldsymbol{p}_{cd}^d}{2}\right)^T \boldsymbol{K}_p \operatorname{vec}_3 \frac{\boldsymbol{p}_{cd}^d}{2} + \left(\operatorname{vec}_3 \frac{\boldsymbol{p}_{cd}^d}{2}\right)^T \boldsymbol{R}_c^d \boldsymbol{K}_p \boldsymbol{R}_c^{dT} \operatorname{vec}_3 \frac{\boldsymbol{p}_{cd}^d}{2} \\
&= \left(\operatorname{vec}_3 \frac{\boldsymbol{p}_{cd}^d}{2}\right)^T \boldsymbol{K}_p \operatorname{vec}_3 \frac{\boldsymbol{p}_{cd}^d}{2} + \left(\boldsymbol{R}_c^{dT} \operatorname{vec}_3 \frac{\boldsymbol{p}_{cd}^d}{2}\right)^T \boldsymbol{K}_p \boldsymbol{R}_c^{dT} \operatorname{vec}_3 \frac{\boldsymbol{p}_{cd}^d}{2} \\
&= \left(\operatorname{vec}_3 \frac{\boldsymbol{p}_{cd}^d}{2}\right)^T \boldsymbol{K}_p \operatorname{vec}_3 \frac{\boldsymbol{p}_{cd}^d}{2} + \left(\operatorname{vec}_3 \frac{\boldsymbol{p}_{cd}^c}{2}\right)^T \boldsymbol{K}_p \operatorname{vec}_3 \frac{\boldsymbol{p}_{cd}^c}{2}.
\end{aligned}$$

Therefore, $\mathcal{U}_p^c = \mathcal{U}_p^d$.

Moreover, since $\boldsymbol{n}_c^d = -\boldsymbol{n}_d^c$, thus

$$\begin{aligned}\mathcal{U}_r^d &= \left(-\operatorname{vec}_3 \frac{\boldsymbol{n}_d^c \phi}{2}\right)^T 2\boldsymbol{K}_\phi \left(-\operatorname{vec}_3 \frac{\boldsymbol{n}_d^c \phi}{2}\right) \\ &= \left(\operatorname{vec}_3 \frac{\boldsymbol{n}_d^c \phi}{2}\right)^T 2\boldsymbol{K}_\phi \left(\operatorname{vec}_3 \frac{\boldsymbol{n}_d^c \phi}{2}\right) \\ &= \mathcal{U}_r^c,\end{aligned}$$

which concludes the proof. □

D

Admittance Using the Imaginary Part of the Rotation Quaternion (ACIm)

Caccavale et al. (2008) propose a similar controller as Equation (4.19), but they used the imaginary part of a unit quaternion to represent the rotational displacement in the stiffness term. More specifically, their admittance controller is given by[1]

$$\dot{\boldsymbol{\zeta}}_{cd}^{c} = \boldsymbol{M}_{d}^{-1}\left(-\boldsymbol{I}^{\#}\boldsymbol{\varsigma}_{\text{eff,eff}}^{c} - \boldsymbol{B}_{d}\boldsymbol{\zeta}_{cd}^{c} - \boldsymbol{K}_{d}^{\prime\prime}\boldsymbol{h}_{d}^{c}\right), \tag{D.1}$$

where $\boldsymbol{h}_{d}^{c} \triangleq \left[\left(\text{vec}_3\,\text{Im}\left(\boldsymbol{r}_{d}^{c}\right)\right)^{T} \quad \left(\text{vec}_3\,\boldsymbol{p}_{cd}^{c}\right)^{T}\right]^{T}$, with $\text{Im}\left(\boldsymbol{r}_{d}^{c}\right) = \boldsymbol{n}_{cd}^{c}\sin\left(\phi/2\right)$, and

$$\boldsymbol{K}_{d}^{\prime\prime} = \begin{bmatrix} 2E^{\prime T}\left(\boldsymbol{r}_{d}^{c}\right)\boldsymbol{K}_{\phi} & \frac{1}{2}\boldsymbol{K}_{p}^{\prime\prime} \\ \boldsymbol{0}_{3\times 3} & \boldsymbol{K}_{p}^{\prime} \end{bmatrix}, \tag{D.2}$$

with $E^{\prime}\left(\boldsymbol{r}_{d}^{c}\right) = \text{Re}\left(\boldsymbol{r}_{d}^{c}\right)\boldsymbol{I}_{3\times 3} - \boldsymbol{S}\left(\text{vec}_3\,\text{Im}\left(\boldsymbol{r}_{d}^{c}\right)\right)$ and $\text{Re}\left(\boldsymbol{r}_{d}^{c}\right) = \cos\left(\phi/2\right)$ (Caccavale et al., 2008), $\boldsymbol{K}_{\phi} \in \mathbb{R}^{3\times 3}$ being the rotational stiffness matrix, and $\boldsymbol{K}_{p}^{\prime}$ and $\boldsymbol{K}_{p}^{\prime\prime}$ being the matrices defined in Equations (4.11) and (4.13).

As shown by Caccavale et al. (1999), the closed-loop system has two sets of equilibrium points, one stable and the other one unstable. The latter consists of rotations of π rad around a rotation axis parallel to any eigenvector of $\boldsymbol{K}_{\phi}$. If the initial state is inside this unstable set, the system gets trapped. This is the so-called topological obstruction (Bhat

[1] We changed the order of the rotational and translation terms in $\boldsymbol{h}_{d}^{c}$ and $\boldsymbol{\zeta}_{cd}^{c}$ to be consistent with our notation.

& Bernstein, 1998).

More specifically, if $\boldsymbol{\zeta}_{cd}^{c} = \mathbf{0}$, Equation (D.1) becomes

$$\dot{\boldsymbol{\zeta}}_{cd}^{c} = \boldsymbol{M}_{d}^{-1}\left(-\boldsymbol{I}^{\#}\boldsymbol{\varsigma}_{\text{eff,eff}}^{c} - \boldsymbol{K}_{d}''\boldsymbol{h}_{d}^{c}\right).$$

Having $\phi = \pi$ and a rotation axis parallel to any eigenvector of $\boldsymbol{K}_{\phi}$ yields to $E'\left(\boldsymbol{r}_{d}^{c}\right) = -\boldsymbol{S}\left(\operatorname{vec}_3 \boldsymbol{n}_{cd}^{c}\right)$ and $\boldsymbol{K}_{\phi}\operatorname{vec}_3 \boldsymbol{n}_{cd}^{c} = \lambda_{\phi}\operatorname{vec}_3 \boldsymbol{n}_{cd}^{c}$. Hence,

$$\boldsymbol{K}_{d}''\boldsymbol{h}_{d}^{c} = \begin{bmatrix} 2\boldsymbol{S}\left(\operatorname{vec}_3 \boldsymbol{n}_{cd}^{c}\right)\lambda_{\phi}\operatorname{vec}_3 \boldsymbol{n}_{cd}^{c} + \frac{1}{2}\boldsymbol{K}_{p}''\operatorname{vec}_3 \boldsymbol{p}_{cd}^{c} \\ \boldsymbol{K}_{p}'\operatorname{vec}_3 \boldsymbol{p}_{cd}^{c} \end{bmatrix}.$$

Since $\boldsymbol{S}\left(\operatorname{vec}_3 \boldsymbol{n}_{cd}^{c}\right)\operatorname{vec}_3 \boldsymbol{n}_{cd}^{c} = \mathbf{0}$, thus

$$\boldsymbol{K}_{d}''\boldsymbol{h}_{d}^{c} = \begin{bmatrix} \frac{1}{2}\boldsymbol{K}_{p}''\operatorname{vec}_3 \boldsymbol{p}_{cd}^{c} \\ \boldsymbol{K}_{p}'\operatorname{vec}_3 \boldsymbol{p}_{cd}^{c} \end{bmatrix}.$$

Therefore, if

$$-\boldsymbol{I}^{\#}\boldsymbol{\varsigma}_{\text{eff,eff}}^{c} = \boldsymbol{K}_{d}''\boldsymbol{h}_{d}^{c} \implies -\begin{bmatrix} \operatorname{vec}_3 \boldsymbol{m}_{\text{eff,eff}}^{c} \\ \operatorname{vec}_3 \boldsymbol{f}_{\text{eff,eff}}^{c} \end{bmatrix} = \begin{bmatrix} \frac{1}{2}\boldsymbol{K}_{p}''\operatorname{vec}_3 \boldsymbol{p}_{cd}^{c} \\ \boldsymbol{K}_{p}'\operatorname{vec}_3 \boldsymbol{p}_{cd}^{c} \end{bmatrix},$$

with $\boldsymbol{f}_{\text{eff,eff}}^{c}$ and $\boldsymbol{m}_{\text{eff,eff}}^{c}$ the force and moment with respect to $\mathcal{F}_c$, then $\dot{\boldsymbol{\zeta}}_{cd}^{c} = \mathbf{0}$ and the system gets trapped.

Bibliography

Adorno, B. V. (2011). *Two-arm Manipulation: From Manipulators to Enhanced Human-Robot Collaboration [Contribution à la manipulation à deux bras : des manipulateurs à la collaboration homme-robot]*. PhD thesis, Université Montpellier II.

Adorno, B. V. (2017). *Robot Kinematic Modeling and Control Based on Dual Quaternion Algebra - Part I : Fundamentals*.

Adorno, B. V., Bó, A. P. L., & Fraisse, P. (2011a). Interactive manipulation between a human and a humanoid: When robots control human arm motion. In *2011 IEEE/RSJ International Conference on Intelligent Robots and Systems* (pp. 4658–4663).: IEEE.

Adorno, B. V., Bo, A. P. L., Fraisse, P., & Poignet, P. (2011b). Towards a cooperative framework for interactive manipulation involving a human and a humanoid. In *2011 IEEE International Conference on Robotics and Automation* (pp. 3777–3783).: IEEE.

Adorno, B. V., Fraisse, P., & Druon, S. (2010). Dual position control strategies using the cooperative dual task-space framework. In *IEEE/RSJ 2010 International Conference on Intelligent Robots and Systems, IROS 2010 - Conference Proceedings* (pp. 3955–3960). Taipei: IEEE.

Adorno, B. V. & Marinho, M. M. (2020). DQ Robotics: A Library for Robot Modeling and Control. *IEEE Robotics & Automation Magazine*, (pp. 1–15).

Agarwal, A., Shah, S. V., Bandyopadhyay, S., & Saha, S. K. (2014). Dynamics of serial kinematic chains with large number of degrees-of-freedom. *Multibody System Dynamics*, 32(3), 273–298.

Agravante, D. J., Cherubini, A., Bussy, A., Gergondet, P., & Kheddar, A. (2014). Collaborative human-humanoid carrying using vision and haptic sensing. In *2014 IEEE International Conference on Robotics and Automation (ICRA)* (pp. 607–612).: IEEE.

Ajoudani, A., Zanchettin, A. M., Ivaldi, S., Albu-Schäffer, A., Kosuge, K., & Khatib, O. (2018). Progress and prospects of the human-robot collaboration. *Autonomous Robots*, 42(5), 957–975.

Alban, D. S. & Adorno, B. V. (2017). External hybrid force/pose controller for manipulator robots using dual quaternion algebra. In *2017 Latin American Robotics Symposium (LARS) and 2017 Brazilian Symposium on Robotics (SBR)*, volume 2017-Decem (pp. 1–6).: IEEE.

Ambrose, R., Askew, S., Bluethmann, W., & Diftler, M. (2001). Humanoids designed to do work. In *Proceedings of the IEEE International Conference on Humanoid Robots (Humanoids 2001)* (pp. 173–180).: IEEE.

Asfour, T., Regenstein, K., Azad, P., Schröder, J., Bierbaum, A., Vahrenkamp, N., & Dillmann, R. (2006). ARMAR-III: An integrated humanoid platform for sensory-motor control. *Proceedings of the 2006 6th IEEE-RAS International Conference on Humanoid Robots, HUMANOIDS*, (pp. 169–175).

Badeau, N., Gosselin, C., Foucault, S., Laliberte, T., & Abdallah, M. E. (2018). Intuitive Physical Human-Robot Interaction: Using a Passive Parallel Mechanism. *IEEE Robotics & Automation Magazine*, 25(2), 28–38.

Bainbridge, W. S., Ed. (2004). *erkshire Encyclopedia of Human-computer Interaction*. Berkshire Publishing Group.

Baptista, R. d. S., Bo, A. P. L., & Hayashibe, M. (2017). Automatic Human Movement Assessment With Switching Linear Dynamic System: Motion Segmentation and Motor Performance. *IEEE Transactions on Neural Systems and Rehabilitation Engineering*, 25(6), 628–640.

Bauer, A., Wollherr, D., & Buss, M. (2008). Human-Robot Collaboration: a Survey. *International Journal of Humanoid Robotics*, 05(01), 47–66.

Bell, C. J., Shenoy, P., Chalodhorn, R., & Rao, P. R. (2008). Control of a humanoid robot by noninvasive brain-computer interface in humans. *Journal of Neural Engineering*, 5(2), 214.

Bernstein, D. S. (2009). *Matrix mathematics: theory, facts, and formulas*. Princeton University Press, 2nd ed. edition.

Bhat, S. & Bernstein, D. (1998). A topological obstruction to global asymptotic stabilization of rotational motion and the unwinding phenomenon. In *Proceedings of the 1998 American Control Conference. ACC (IEEE Cat. No.98CH36207)*, volume 5 (pp. 2785–2789 vol.5).: IEEE.

Bo, A. P. L., Hayashibe, M., & Poignet, P. (2011). Joint angle estimation in rehabilitation with inertial sensors and its integration with Kinect. In *2011 Annual International*

Conference of the IEEE Engineering in Medicine and Biology Society (pp. 3479–3483).: IEEE.

Borst, C., Wimböck, T., Schmidt, F., Fuchs, M., Brunner, B., Zacharias, F., Giordano, P. R., Konietschke, R., Sepp, W., Fuchs, S., Rink, C., Albu-Schäffer, A., & Hirzinger, G. (2009). Rollin' Justin - Mobile platform with variable base. *Proceedings - IEEE International Conference on Robotics and Automation*, (pp. 1597–1598).

Caccavale, F., Chiacchio, P., Marino, A., & Villani, L. (2008). Six-DOF Impedance Control of Dual-Arm Cooperative Manipulators. *IEEE/ASME Transactions on Mechatronics*, 13(5), 576–586.

Caccavale, F., Natale, C., Siciliano, B., & Villani, L. (1999). Six-DOF impedance control based on angle/axis representations. *IEEE Transactions on Robotics and Automation*, 15(2), 289–300.

Caccavale, F. & Villani, L. (2000). Impedance control for multi-arm manipulation. In *Proceedings of the 39th IEEE Conference on Decision and Control (Cat. No.00CH37187)*, volume 4 (pp. 3465–3470).: IEEE.

Cehajic, D., Erhart, S., & Hirche, S. (2015). Grasp pose estimation in human-robot manipulation tasks using wearable motion sensors. In *2015 IEEE/RSJ International Conference on Intelligent Robots and Systems (IROS)* (pp. 1031–1036).: IEEE.

Cheah, C., Liu, C., & Slotine, J. (2006a). Adaptive Jacobian Tracking Control of Robots With Uncertainties in Kinematic, Dynamic and Actuator Models. *IEEE Transactions on Automatic Control*, 51(6), 1024–1029.

Cheah, C. C., Liu, C., & Slotine, J. J. E. (2006b). Adaptive Tracking Control for Robots with Unknown Kinematic and Dynamic Properties. *The International Journal of Robotics Research*, 25(3), 283–296.

Chen, C.-T. (1999). *Linear System Theory and Design*. New York: Oxford University Press, 3 edition.

Cherubini, A., Crosnier, A., Fraisse, P., Navarro, B., Passama, R., & Sorour, M. (2017). Research on cobotics at the LIRMM IDH group. In *ICRA Workshop IC3 - Industry of the future: Collaborative, Connected, Cognitive*, volume hal-015233 (pp. 1–5). Singapore.

Cherubini, A., Passama, R., Crosnier, A., Lasnier, A., & Fraisse, P. (2016). Collaborative manufacturing with physical human-robot interaction. *Robotics and Computer-Integrated Manufacturing*, 40, 1–13.

Cherubini, A., Passama, R., Meline, A., Crosnier, A., & Fraisse, P. (2013). Multimodal control for human-robot cooperation. In *2013 IEEE/RSJ International Conference on Intelligent Robots and Systems* (pp. 2202–2207).: IEEE.

Cherubini, A., Passama, R., Navarro, B., Sorour, M., Khelloufi, A., Mazhar, O., Tarbouriech, S., Zhu, J., Tempier, O., Crosnier, A., Fraisse, P., & Ramdani, S. (2019). A Collaborative Robot for the Factory of the Future: BAZAR. *International Journal of Advanced Manufacturing Technology*, 105(9), 3643–3659.

Chiacchio, P., Chiaverini, S., & Siciliano, B. (1996). Direct and inverse kinematics for coordinated motion tasks of a two-manipulator system. *Journal of Dynamic Systems, Measurement, and Control*, 118(4), 691–697.

Chiaverini, S. & Sciavicco, L. (1993). The Parallel Approach to Force/Position Control of Robotic Manipulators. *IEEE Transactions on Robotics and Automation*, 9(4), 361–373.

Clifford (1873). Preliminary Sketch of Biquaternions. *Proceedings of the London Mathematical Society*, s1-4(1), 381–395.

Colgate, E. & Hogan, N. (1989). An analysis of contact instability in terms of passive physical equivalents. In *Proceedings, 1989 International Conference on Robotics and Automation* (pp. 404–409 vol.1).

Crawley, M. J. (2007). *The R Book*. John Wiley & Sons Ltd.

de Brito, R. P. (2016). *Consenso Utilizando Álgebra de Quatérnios Duais em Sistemas Compostos por Manipuladores Móveis*. Master's thesis, Universidade Federal de Minas Gerais.

de Gea, J. & Kirchner, F. (2008). Modelling and Simulation of Robot Arm Interaction Forces Using Impedance Control. *IFAC Proceedings Volumes*, 41(2), 15589–15594.

De Santis, A., Siciliano, B., De Luca, A., & Bicchi, A. (2008). An atlas of physical human-robot interaction. *Mechanism and Machine Theory*, 43(3), 253–270.

Dietrich, A. M. (2015). *Whole-Body Impedance Control of Wheeled Humanoid Robots*. Phd thesis, Technische Universitat Munchen.

Ding, L., Wu, H., Yao, Y., & Yang, Y. (2015). Dynamic Model Identification for 6-DOF Industrial Robots. *Journal of Robotics*, 2015, 1–9.

Dumora, J., Geffard, F., Bidard, C., Brouillet, T., & Fraisse, P. (2012). Experimental study on haptic communication of a human in a shared human-robot collaborative task. In *2012 IEEE/RSJ International Conference on Intelligent Robots and Systems* (pp. 5137–5144).: IEEE.

Erhart, S. & Hirche, S. (2015). Internal Force Analysis and Load Distribution for Cooperative Multi-Robot Manipulation. *IEEE Transactions on Robotics*, 31(5), 1238–1243.

Erhart, S., Sieber, D., & Hirche, S. (2013). An impedance-based control architecture for multi-robot cooperative dual-arm mobile manipulation. In *2013 IEEE/RSJ International Conference on Intelligent Robots and Systems* (pp. 315–322). Tokyo: IEEE.

Featherstone, R. (2004). An Empirical Study of the Joint Space Inertia Matrix. *The International Journal of Robotics Research*, 23(9), 859–871.

Ferraguti, F., Talignani Landi, C., Sabattini, L., Bonfè, M., Fantuzzi, C., & Secchi, C. (2019). A variable admittance control strategy for stable physical human-robot interaction. *International Journal of Robotics Research*, 38(6), 747–765.

Figueredo, L., Adorno, B., Ishihara, J., & Borges, G. (2013). Robust kinematic control of manipulator robots using dual quaternion representation. In *2013 IEEE International Conference on Robotics and Automation* (pp. 1949–1955). Karlsruhe: IEEE.

Fonseca, M. d. P. A. & Adorno, B. V. (2016). Whole-Body Modeling and Hierarchical Control of a Humanoid Robot Based on Dual Quaternion Algebra. In *Proceedings - 13th Latin American Robotics Symposium and 4th Brazilian Symposium on Robotics, LARS/SBR 2016* (pp. 103–108).

Fonseca, M. d. P. A., Adorno, B. V., & Fraisse, P. (2018). Design of an Adaptive Controller to Improve the Condition Number of the Inertia Matrix of Serial Manipulators. In *Proceedings XXII Congresso Brasileiro de Automática* (pp. 1–8).

Fonseca, M. d. P. A., Adorno, B. V., & Fraisse, P. (2019a). An Adaptive Controller with Guarantee of Better Conditioning of the Robot Manipulator Joint-Space Inertia Matrix. In *2019 19th International Conference on Advanced Robotics (ICAR)*, volume 111 (pp. 111–116).: IEEE.

Fonseca, M. d. P. A., Adorno, B. V., & Fraisse, P. (2019b). Task-Space Impedance Controller Using Dual Quaternion Logarithm. In *Workshop on Applications of Dual Quaternion Algebra to Robotics* (pp. 1–2).

Fonseca, M. d. P. A., Adorno, B. V., & Fraisse, P. (2020). Coupled Task-Space Admittance Controller Using Dual Quaternion Logarithmic Mapping. *IEEE Robotics and Automation Letters*, 5(4), 6057–6064.

Fonseca, M. d. P. A., Adorno, B. V., & Fraisse, P. (2021). Task-Space Admittance Controller with Adaptive Inertia Matrix Conditioning. *Journal of Intelligent & Robotics Systems*, (pp. 1–19).

Gonzalez, A., Hayashibe, M., & Fraisse, P. (2012). Estimation of the center of mass with Kinect and Wii balance board. In *2012 IEEE/RSJ International Conference on Intelligent Robots and Systems* (pp. 1023–1028).: IEEE.

Gonzalez, A., Hayashibe, M., & Fraisse, P. (2013). Online identification and visualization of the statically equivalent serial chain via constrained Kalman filter. *Proceedings - IEEE International Conference on Robotics and Automation*, (pp. 5323–5328).

Goodrich, M. A. & Schultz, A. C. (2007). Human-robot interaction: A survey. *Foundations and Trends in Human-Computer Interaction*, 1(3), 203–275.

Haddadin, S., Albu-SchäCurrency Signffer, A., & Hirzinger, G. (2009). Requirements for safe robots: Measurements, analysis and new insights. *International Journal of Robotics Research*, 28(11-12), 1507–1527.

Hamilton, W. R. (1844). On Quaternions, Or On a New System of Imaginaries in Algebra. *Philosophical Magazine Series 3*, 25(163), 10–13.

Hanlei, W. (2010). On the Recursive Implementation of Adaptive Control for Robot Manipulators. In *Proceedings of the 29th Chinese Control Conference* (pp. 2154–2161).

Higa, F. Y. G., Lahr, G. J. G., Caurin, G. A. P., & Boaventura, T. (2019). Joint kinematic configuration influence on the passivity of an impedance-controlled robotic leg. In *2019 International Conference on Robotics and Automation (ICRA)* (pp. 9516–9522).

Hinds, P., Roberts, T., & Jones, H. (2004). Whose Job Is It Anyway? A Study of Human-Robot Interaction in a Collaborative Task. *Human-Computer Interaction*, 19(1), 151–181.

Hoffman, E. M., Laurenzi, A., Muratore, L., Tsagarakis, N. G., & Caldwell, D. G. (2018). Multi-Priority Cartesian Impedance Control Based on Quadratic Programming Optimization. In *2018 IEEE International Conference on Robotics and Automation (ICRA)* (pp. 309–315). Brisbane: IEEE.

Hogan, N. (1985). Impedance Control: An Approach to Manipulation. *Journal of Dynamic Systems, Measurement, and Control*, 107(1), 1–7.

Hollander, M., A. Wolfe, D., & Chicken, E. (1999). *Nonparametric Statistical Methods*. Wiley Series in Probability and Statistics. Wiley, second edition.

Ju, Z., Yang, C., & Ma, H. (2014). Kinematics Modeling and Experimental Verification of Baxter Robot. In *Proceedings of the 33rd Chinese Control Conference, CCC 2014* (pp. 8518–8523).

Katsumata, T., Navarro, B., Bonnet, V., Fraisse, P., Crosnier, A., & Venture, G. (2019). Optimal exciting motion for fast robot identification. Application to contact painting tasks with estimated external forces. *Robotics and Autonomous Systems*, 113, 149–159.

Keemink, A. Q., van der Kooij, H., & Stienen, A. H. (2018). Admittance control for physical human-robot interaction. *International Journal of Robotics Research*, 37(11), 1421–1444.

Kelly, R., Santibáñez, V., & Loría, A. (2005). *Control of Robot Manipulators in Joint Space*. Leipzig: Springer.

Kemp, C. C., Fitzpatrick, P., Hirukawa, H., Yokoi, K., Harada, K., & Matsumoto, Y. (2008). *Handbook of Robotics*, chapter 56. Humanoids, (pp. 1307–1333). Springer.

Kimmel, M. & Hirche, S. (2015). Active safety control for dynamic human-robot interaction. In *2015 IEEE/RSJ International Conference on Intelligent Robots and Systems (IROS)* (pp. 4685–4691).: IEEE.

Kussaba, H. T., Figueredo, L. F., Ishihara, J. Y., & Adorno, B. V. (2017). Hybrid kinematic control for rigid body pose stabilization using dual quaternions. *Journal of the Franklin Institute*, 354(7), 2769–2787.

Landi, C. T., Ferraguti, F., Sabattini, L., Secchi, C., & Fantuzzi, C. (2017). Admittance control parameter adaptation for physical human-robot interaction. In *2017 IEEE International Conference on Robotics and Automation (ICRA)* (pp. 2911–2916).: IEEE.

Lange, F., Jehle, C., Suppa, M., & Hirzinger, G. (2012). Revised force control using a compliant sensor with a position controlled robot. In *2012 IEEE International Conference on Robotics and Automation* (pp. 1532–1537).

Lee, J., Chang, P. H., & Jamisola, R. S. (2014). Relative Impedance Control for Dual-Arm Robots Performing Asymmetric Bimanual Tasks. *IEEE Transactions on Industrial Electronics*, 61(7), 3786–3796.

Leite, A. C. & Lizarralde, F. (2016). Passivity-based adaptive 3d visual servoing without depth and image velocity measurements for uncertain robot manipulators. *International Journal of Adaptive Control and Signal Processing*, 30(8-10), 1269–1297.

Liegeois, A. (1977). Automatic Supervisory Control of the Configuration and Behavior of Multibody Mechanisms. *IEEE Transactions on Systems, Man and Cybernetics*, SMC-7(12), 868–871.

Liu, C., Cheah, C. C., & Slotine, J. J. E. (2006). Adaptive Jacobian tracking control of rigid-link electrically driven robots based on visual task-space information. *Automatica*, 42(9), 1491–1501.

Magrini, E., Flacco, F., & De Luca, A. (2014). Estimation of contact forces using a virtual force sensor. *IEEE International Conference on Intelligent Robots and Systems*, (Iros), 2126–2133.

Magrini, E., Flacco, F., & De Luca, A. (2015). Control of generalized contact motion and force in physical human-robot interaction. *Proceedings - IEEE International Conference on Robotics and Automation*, 2015-June(June), 2298–2304.

Marinho, M. M., Adorno, B. V., Harada, K., & Mitsuishi, M. (2019). Dynamic active constraints for surgical robots using vector-field inequalities. *IEEE Transactions on Robotics*, 35(5), 1166–1185.

Mitsantisuk, C., Katsura, S., & Ohishi, K. (2010). Force control of humanrobot interaction using twin direct-drive motor system based on modal space design. *IEEE Transactions on Industrial Electronics*, 57(4), 1383–1392.

Montgomery, D. C. (2001). *Design and Analysis of Experiments*. John Wiley & Sons, Inc., 5th ed. edition.

Navarro, B. (2017). *Solutions for safe human-robot collaboration*. Phd, Université d'Orléans.

Navarro, B., Cherubini, A., Fonte, A., Passama, R., Poisson, G., & Fraisse, P. (2016). An ISO10218-compliant adaptive damping controller for safe physical human-robot interaction. In *2016 IEEE International Conference on Robotics and Automation (ICRA)* (pp. 3043–3048).: IEEE.

Navarro, B., Cherubini, A., Fonte, A., Poisson, G., & Fraisse, P. (2017). A framework for intuitive collaboration with a mobile manipulator. *IEEE International Conference on Intelligent Robots and Systems*, 2017-Septe, 6293–6298.

Navarro, B., Fonte, A., Fraisse, P., Poisson, G., & Cherubini, A. (2018). In Pursuit of Safety: An Open-Source Library for Physical Human-Robot Interaction. *IEEE Robotics & Automation Magazine*, 25(2), 39–50.

Okie, S. (2002). Robots make the rounds to ease hospitals' costs. The Washington Post. (pp. A03).

Pedro, L. M., Fernandes, G., StÃŒecheli, M., Siqueira, A. A. G., & Caurin, G. A. P. (2013). A robust manipulation strategy based on impedance control parameters changes and smooth trajectories. In *2013 16th International Conference on Advanced Robotics (ICAR)* (pp. 1–7).

Peng, R. D. (2016). *R Programming for Data Science*. Lean Publishing.

Pham, H., Adorno, B., Perdereau, V., & Fraisse, P. (2018). Set-point control of robot end-effector pose using dual quaternion feedback. *Robotics and Computer-Integrated Manufacturing*, 52(May 2016), 100–110.

Pratt, G. A., Williamson, M. M., Dillworth, P., Pratt, J., & Wright, A. (2005). Stiffness isn't everything. In O. Khatib & J. K. Salisbury (Eds.), *Experimental Robotics IV* (pp. 253–262). London: Springer-Verlag.

Quiroz-Omana, J. J. & Adorno, B. V. (2019). Whole-Body Control With (Self) Collision Avoidance Using Vector Field Inequalities. *IEEE Robotics and Automation Letters*, 4(4), 4048–4053.

Rohmer, E., Singh, S. P. N., & Freese, M. (2013). V-REP: A versatile and scalable robot simulation framework. In *IEEE International Conference on Intelligent Robots and Systems* (pp. 1321–1326).

Roveda, L., Iannacci, N., Vicentini, F., Pedrocchi, N., Braghin, F., & Tosatti, L. M. (2016). Optimal Impedance Force-Tracking Control Design With Impact Formulation for Interaction Tasks. *IEEE Robotics and Automation Letters*, 1(1), 130–136.

Santis, A. D. (2007). *Modelling and control for human-robot interaction*. PhD thesis, Università degli Studi di Napoli Federico II.

Savino, H. J., Pimenta, L. C., Shah, J. A., & Adorno, B. V. (2020). Pose consensus based on dual quaternion algebra with application to decentralized formation control of mobile manipulators. *Journal of the Franklin Institute*, 357(1), 142–178.

Selig, J. M. (2005). *Geometric Fundamentals of Robotics*. Springer-Verlag New York Inc.

Shah, S. V., Saha, S. K., & Dutt, J. K. (2018). A new perspective towards decomposition of the generalized inertia matrix of multibody systems. *Multibody System Dynamics*, 43(2), 97–130.

Shen, Y. & Featherstone, R. (2003). The Effect of Ill-conditioned Inertia Matrix on Controlling Manipultor Robot. In *Proceedings of the 2003 Australasian Conference on Robotics & Automation* (pp. 1–6).: Australian Robotics and Automation Association.

Siciliano, B., Sciavicco, L., Villani, L., & Oriolo, G. (2009). *Robotics: Modelling, Planning and Control*. Advanced Textbooks in Control and Signal Processing. London: Springer London, 1 edition.

Siciliano, B. & Slotine, J.-j. E. (1991). A General Framework for Managing Multiple Tasks in Highly Redundant Robotic Systems. In *Fifth International Conference on Advanced Robotics, 1991. 'Robots in Unstructured Environments', 91 ICAR* (pp. 1211 – 1216 vol.2).

Sieber, D., Music, S., & Hirche, S. (2015). Multi-robot manipulation controlled by a human with haptic feedback. In *2015 IEEE/RSJ International Conference on Intelligent Robots and Systems (IROS)*, volume 2015-Decem (pp. 2440–2446).: IEEE.

Siino, R. & Hinds, P. (2004). Making sense of new technology: Organizational sensemaking of autonomous mobile robots as a lead-in to structuring. Unpublished work, Stanford University.

Silva, F. F. A. (2017). *Whole-Body Control of a Mobile Manipulator Using Feedback Linearization and Dual Quaternion Algebra*. Master's thesis, Universidade Federal de Minas Gerais.

Slotine, J.-J. E. & Li, W. (1987). On the Adaptive Control of Robot Manipulators. *The International Journal of Robotics Research*, 6(3), 49–59.

Slotine, J. J. E. & Li, W. (1991). *Applied Nonlinear Control*. Prentice Hall.

Spong, M. W., Hutchinson, S., & Vidyasagar, M. (2006). *Robot Modeling and Control*. John Wiley & Sons, Inc.

Squeo, A. (2001). Meet the newest recruits: Robots. The Wall Street Journal. (pp. B01).

Tarbouriech, S., Navarro, B., Fraisse, P., Crosnier, A., Cherubini, A., & Salle, D. (2020). Admittance control for collaborative dual-arm manipulation. (pp. 198–204).

Uchiyama, M. & Dauchez, P. (1988). A symmetric hybrid position/force control scheme for the coordination of two robots. In *Proceedings. 1988 IEEE International Conference on Robotics and Automation* (pp. 350–356).: IEEE Comput. Soc. Press.

Unhelkar, V. V., Lasota, P. A., Tyroller, Q., Buhai, R.-D., Marceau, L., Deml, B., & Shah, J. A. (2018). Human-Aware Robotic Assistant for Collaborative Assembly: Integrating Human Motion Prediction With Planning in Time. *IEEE Robotics and Automation Letters*, 3(3), 2394–2401.

Vanderborght, B. (2018). Humans and Robots Working Together. *IEEE Robotics & Automation Magazine*, 25(2), 4–4.

Villani, L. & de Schutter, J. (2008). Force Control. In B. Siciliano & O. Khatib (Eds.), *Siciliano B., Khatib O. (eds) Springer Handbook of Robotics*, volume 53 chapter Force Cont, (pp. 161–185). Berlin, Heidelberg: Springer.

Wang, H. & Xie, Y. (2009). Adaptive inverse dynamics control of robots with uncertain kinematics and dynamics. *Automatica*, 45(9), 2114–2119.

Wang, H. & Xie, Y. (2011). On the Uniform Positive Definiteness of the Estimated Inertia for Robot Manipulators. In *IFAC Proceedings Volumes*, volume 44 (pp. 4089–4094).: IFAC.

Yang, C., Ma, H., & Fu, M. (2016). Robot kinematics and dynamics modeling. In *Advanced Technologies in Modern Robotic Applications* (pp. 27–48). Springer, Singapore.

Zimmermann, C., Welschehold, T., Dornhege, C., Burgard, W., & Brox, T. (2018). 3D Human Pose Estimation in RGBD Images for Robotic Task Learning. In *2018 IEEE International Conference on Robotics and Automation (ICRA)* (pp. 1986–1992).